Project No. 09-781

Experimental Studies of NGNP Reactor Cavity Cooling System With Water

Reactor Concepts RD&D

Dr. Michael Corradini
University of Wisconsin, Madison

In collaboration with:
Texas A&M University
University of Idaho

Madeline Feltus, Federal POC
Thomas Wei, Technical POC

NEUP Nuclear Energy University Programs
U.S. Department of Energy

FINAL REPORT

Title: Experimental Studies of NGNP Reactor Cavity Cooling System with Water

Covering Period Nov 1, 2009 to Oct 30, 2012

Date of Report: December 22, 2012

Recipient: University of Wisconsin – Madison

Department of Engineering Physics 1500 Engineering Drive, Madison, WI, 53706

Technical Workscope: G4M-1 – Generation IV Methods

Project Number: 09-781

Principal Investigators: Michael Corradini: corradini@engr.wisc.edu
Co-PI's: Mark Anderson (UW), Yassin Hassan (TAMU), Akira Tokuhiro (UI)

Objectives: Our team investigated the flow behavior occurring in the Reactor Cavity Cooling System (RCCS) with a water coolant under a passive cooling-mode of operation. We conducted scaled tests and develop and developed system-level phenomenological and computational models that describe key flow phenomena during RCCS operation, for natural circulation, single-phase flow and two-phase flow and flashing.

Task 1: We conducted separate-effects, single-phase flow experiments and develop associate scaling analysis with comparison to system-level computational modeling for the RCCS design. These tests measured global flow behavior as well as developed instrumentation to measure void fractions and local velocities. These diagnostics can be used in larger scale experiments (e.g., at the ANL NSTF facility).

Task 2: We conducted separate-effects experiments for the RCCS design from single-phase to two-phase flow. As natural circulation cooling continues without an ultimate heat sink, water will heat up to temperatures approaching the saturation temperature within the system. Two-phase flashing and flow then begins. We developed models for these tests that describe the flashing and flow stability phenomena. We were also able to design a phase separation for the RCCS storage tank as the two-phase flashing phenomena ensues and the storage tank vents the steam produced.

Task 3: We developed a system-level computational model using both RELAP and MELCOR that describes the overall RCCS behavior as it transitions from forced flow to natural circulation single phase and eventually two-phase flow in the passive cooling-mode of operation. This modeling can then be used to in conjunction with Tasks 1 and 2 to test the phenomenological models developed as a function of scale.

Executive Summary

This report documents investigations into the thermal hydraulic behavior that can occur in a reactor cavity cooling system (RCCS) under passive cooling-mode of operation.

An 1/4 scale experimental facility was constructed at the University of Wisconsin - Madison, with a three riser tube and cooling panel test section representing a 5° sector slice of a prototype RCCS design. Derived similarity relations have preserved the nominal flow patterns and integral system response, ensuring relevant data and similarity among scales. System modeling with RELAP5-3D and FLUENT was performed to identify prototypic behavior, confirm scaling methodology, and serve as a comparison to experimental data. Characterization tests at single phase evaluated the steady-state behavior of the experimental facility, establishing linearity, repeatability, and heat removal performance. The transition to saturation and subsequent boiling conditions allowed investigations into the two-phase behavior during prototypic scenarios. High resolution data acquisition provided measurement of local and global flow behavior, and support suggestions that the RCCS will successfully remove decay heat during an accident scenario. The authors investigations indicate that a high level of performance can be expected at the full scale decay heat load of 1.5 MW_t regardless of axial or asymmetric power shaping. During two-phase conditions, flashing phenomena is anticipated to occur in the adiabatic chimney above the riser tubes, however we believe the heat removal performance to be unaffected. Inventory in the water storage tank was confirmed to maintain adequate cooling for the 72 hour criterion set by the NRC.

Acknowledgments

Financial support for this work was made possible by the Department of Energy Nuclear Energy University Programs (NEUP).

Student involvement

1. Angelo Frisani - PhD Nucl. Eng. TAMU, 2012
2. Christian Bakken - MS Mech. Eng. Univ. Idaho, 2012
3. Darius Lisowski - PhD Nucl. Eng. Univ. Wisc. (in progress)
4. Luigi Capone PhD Nucl. Eng. TAMU, 2012
5. Mark Albiston - MS Nucl. Eng. Univ. Idaho, 2011
6. Mike Gorman - MS Nucl. Eng. TAMU (in progress)
7. Moses Muci - MS Mech. Eng. Univ. Wisc. (in progress)
8. Olumuyiwa Omotowa - PhD Nucl. Eng. Univ. Idaho (in progress)
9. Robert Scherrer - MS Nucl. Eng. Univ. Wisc., 2011
10. Rodolfo Vaghetto - PhD Nucl. Eng. TAMU (in progress)
11. Saya Lee - PhD Nucl. Eng. TAMU (in progress)
12. Troy Haskin - PhD Nucl. Eng. Univ. Wisc. (in progress)

Published works

1. D. D. Lisowski et al., "Experimental Studies of NGNP Reactor Cavity Cooling System with Water", Proc. Of ICAPP 2011, Nice, France. May 5 11, 2011. ICAPP (2011).
2. R.Vaghetto, Y.A. Hassan, "Analysis of the Thermo-hydraulic Behavior of the New TEXAS AM RCCS Experimental Facility Using RELAP5-3D", Proc. of ICONE19, May 16-19, 2011, Chiba, Japan. ICONE (2011)
3. D. D. Lisowski, R. M. Scherrer, M. H. Anderson, M. L. Corradini, "Design and Construction of a Scaled Experimental Reactor Cavity Cooling System with Water", Proc. of ANS Annual 2011, Hollywood, FL, USA. June 26 30, 2011. ANS (2011).
4. R.Vaghetto, H. Wei, Y.A.Hassan, "Simulation of a Simple RCCS Experiment with RELAP5-3D System Code and Computational Fluid Dynamics Computer Program", NURETH-14, Toronto, Ontario, Canada, September 25-30, 2011. NURETH (2011)
5. D. D. Lisowski, S. M. Albiston, M. H. Anderson, M. L. Corradini, "Steady-State Data from a Scaled Experimental Reactor Cavity Cooling System with Water", Proc. of ANS Winter 2011, Washington DC, USA. October 30 November 5th, 2011. ANS (2011)
6. R.Vaghetto, Y.A.Hassan, "Scaling the NGNP Reactor Cavity Cooling System", Proc. of ANS Winter 2011, Washington DC, USA. October 30 November 5th, 2011. ANS (2011)
7. D. D. Lisowski, S. M. Albiston, A. Tokuhiro, M. H. Anderson, M. L. Corradini, "Results from a Scaled Reactor Cavity Cooling System with Water at Steady State", Proc. Of ICAPP 2012, Chicago, IL USA. June 24 28, 2011. ICAPP (2012)
8. D. D. Lisowski, M. H. Anderson, M. L. Corradini, "Numerical and experimental studies of heat transfer coefficients in a RCCS", Proc. of ANS Annual 2012, Chicago, IL, USA. June 24 38, 2012. ANS (2012)

9. R.Vaghetto, H. Wu, Y.A.Hassan, "RELAP5-3D Simulations of the Reactor Cavity Cooling System Experimental Facility", Proc. of ANS Annual 2012, Chicago, IL, USA. June 24 - 38, 2012. ANS (2012)
10. R.Vaghetto, S. Lee, Y.A.Hassan "Reactor Cavity Cooling System Experimental Facility Shakedown and RELAP5-3D Model Validation", ICONE20 July 30 - August 3, 2012, Anaheim, California, USA. ICONE (2012).
11. R.Vaghetto, S. Lee, Y.A.Hassan, "Analysis of the Steady-State Phase of the Reactor Cavity Cooling System Experimental Facility", Proc. of ANS Winter 2012, San Diego, CA, USA. Nov. 11 - 15, 2012. ANS (2012)
12. D. D. Lisowski, T. C. Haskin, A. Tokuhiro, M. H. Anderson, M. L. Corradini, "A Study on the Behavior of an Asymmetrically Heated Reactor Cavity Cooling System with Water in Single Phase", Nuclear Technology *accepted Aug. '12*
13. D. D. Lisowski, M. A. Moses, M. H. Anderson, M. L. Corradini, "Design Considerations for a Scaled Reactor Cavity Cooling System with Air for the VHTR", Proc. Of NURETH15, Pisa, Italy. May 12 15, 2013. NURETH (2013) *abstract accepted, paper in progress*
14. D. D. Lisowski, O. Omotowa, M. H. Anderson, M. L. Corradini, "Power Investigations on the Two-Phase Behavior and Instability in an Experimental Reactor Cavity Cooling System with Water", Proc. of NURETH15, Pisa, Italy. May 12 15, 2013. NURETH (2013) *abstract accepted, paper in progress*
15. R. Vaghetto, Y.H. Hassan, "Analysis of the Steady-State Phase of the Reactor Cavity Cooling System Experimental Facility and Comparison with RELAP5-3D Simulations", Proc. of NURETH15, Pisa, Italy. May 12 15, 2013. NURETH (2013) *abstract accepted, paper in progress*

Report preparation encompasses the works by primary investigator, collaborators, and student involvement over a period from Aug. '09 - Dec. '12. Compiled by D. Lisowski, submitted in final form to NEUP on Dec. 22nd, 2012.

Contents

Executive Summary

Acknowledgments

1 Introduction **1-1**
1.1 Motivation . . . 1-1
1.2 Passive Decay Heat Removal in the HTGR . . . 1-2
1.3 Flow Instabilities . . . 1-4
1.4 Generation IV Nuclear Reactors . . . 1-4
1.4.1 Technological Goals . . . 1-4
1.4.2 NGNP . . . 1-5
1.4.3 Reactor Cavity Cooling System . . . 1-5

2 Literature Review **2-7**
2.1 Classification of Flow Instabilities . . . 2-7
2.1.1 Single-Phase Subcooled . . . 2-8
2.1.2 Two-Phase Flow Instabilities . . . 2-11
2.2 Review of Previous Efforts & Experiments . . . 2-19
2.2.1 Small Scale Natural Circulation Loops . . . 2-19
2.2.2 Effects of Power and Multiple Channels . . . 2-22
2.2.3 Nuclear Focused Passive Cooling Systems . . . 2-24

3 Scaling **3-26**
3.1 Integral (Top Down) Scaling . . . 3-26
3.2 Water Storage Tank . . . 3-29
3.2.1 Single Phase Condensation . . . 3-30
3.2.2 Two-Phase Bubble Transport . . . 3-33
3.3 Combined Scaling . . . 3-34

4 CFD Simulations **4-36**
4.1 2D Benchmark . . . 4-36
4.1.1 CFD Methods and Models . . . 4-37
4.1.2 Benchmark Results . . . 4-39
4.2 Variable Cavity Height . . . 4-43
4.2.1 P/D = 5 Results . . . 4-46
4.2.2 P/D = 2,4 Results . . . 4-48

5 RELAP5-3D Model **5-50**
5.1 Tool Overview . . . 5-51
5.1.1 Input Structure . . . 5-51
5.1.2 Model Execution . . . 5-53
5.1.3 Uses with Natural Circulation Calculations . . . 5-54
5.2 Reactor (Full) Scale Model . . . 5-55
5.2.1 Choking Cases . . . 5-57
5.3 UW Experimental Scale . . . 5-64
5.3.1 Experimental Run Cases - Steady State . . . 5-68
5.4 Scaling Laws Validation . . . 5-71
5.5 Two - Phase Modeling . . . 5-74

6 Experimental Facility **6-78**
6.1 Construction Purpose . . . 6-78
6.2 Concept Design . . . 6-78
6.2.1 Facility Overview . . . 6-80
6.3 Structural Considerations . . . 6-86
6.3.1 Thermal Expansion . . . 6-86
6.3.2 High Temperature Supports . . . 6-88
6.3.3 Heater Spacing . . . 6-89
6.4 Data Acquisition . . . 6-90
6.4.1 Ultrasonic Velocity . . . 6-91
6.4.2 RBI Optical Probe . . . 6-95
6.4.3 Calibration . . . 6-97
6.5 Operation . . . 6-99

7 Experimental Results **7-101**
7.1 Characterization . . . 7-101
7.1.1 Heat Loss . . . 7-101
7.1.2 Repeatability . . . 7-106
7.1.3 Uncertainty . . . 7-109
7.1.4 Nominal Behavoir . . . 7-110
7.1.5 Heating Rate . . . 7-115
7.2 Single Phase Steady-State . . . 7-120
7.2.1 Integral Behavior at Varying Power . . . 7-121
7.2.2 Axial Power Shaping . . . 7-125
7.2.3 Asymmetric Power Shaping . . . 7-126
7.2.4 Initial System Inventory . . . 7-128
7.2.5 Sparger & Tank Mixing . . . 7-128

7.2.6 Steady State Summary 7-129
7.3 Two-Phase Conditions 7-132
7.3.1 Baseline Procedure & Conditions 7-132
7.3.2 Power Investigation 7-138
7.3.3 Inlet Restriction 7-142
7.3.4 Discussion 7-145

Bibliography **8-146**

Appendix **A.1**

List of Figures

1.1 GA-MHTGR RCCS configuration plan (HTGR-86-024) 1-6
1.2 RCCS concept. RPV, RCCS cooling tubes, Concrete containment 1-6
1.3 RCCS design overview 1-6

2.1 Theoretical stability maps for various cases at positive flow steady-state conditions . 2-11
2.2 Ball-and-hill analogy of equilibrium descriptions 2-13
2.3 Various natural circulation loops (Zvirin 1981) 2-20
2.4 Stability characteristics for toroidal loop (Zvirin, 1981) 2-21
2.5 Starting transient for an open loop, outlet and heater temperature (Zvirin, 1981) . . 2-21
2.6 Left: Full scale solar water heater, temperature decay. Right: Multiple steady state solutions for parallel tube systems. (Zvirin, 1981) 2-22
2.7 Stability map of CARR, inlet temperature vs power ratio (Yun, 2004) 2-25

3.1 Penetration length for a jet into a stagnant body of water 3-31

4.1 Boundary condition overview for Benchmark #2 4-37
4.2 Temperature [K] profile for Benchmark #1 4-40
4.3 Velocity [m/s] profile for Benchmark #1 4-40
4.4 Temperature [K] profile for Benchmark #2 4-41
4.5 Velocity [m/s] profile for Benchmark #2 4-41
4.6 Temperature [K] profile for Benchmark #3 4-42
4.7 Velocity [m/s] profile for Benchmark #3 4-42
4.8 Pitch/Diameter = 5. Cross Section of RCCS in Wedge of Reactor Cavity, with Dimensions, inches 4-44
4.9 Three-dimensional wedge representation with labels for BC 4-45

5.1 Reactor Scale Model Piping Nodalization 5-56
5.2 Henry-Fauske mass flow rate, reactor scale baseline model 5-59
5.3 Henry-Fauske Δ T across risers, reactor scale baseline model 5-60
5.4 Henry-Fauske tank water level 5-61
5.5 Henry-Fauske pipe node void fractions 5-61
5.6 Unmodified Ransom-Trapp mass flow rate 5-62
5.7 INL Modified Ransom-Trapp mass flow rate 5-63
5.8 UW experimental model, pipe and heat structure nodalization 5-65
5.9 UW experimental model, cavity nodalization diagram 5-66
5.10 9.91 kW steady state, experimental vs RELAP5 5-68

5.11 4.63 kW steady state, experimental vs RELAP5 5-70
5.12 7.27 kW steady state, experimental vs RELAP5 5-70
5.13 Predictive reactor scale simulation into two-phase 5-75
5.14 Predictive reactor scale void fraction into two-phase 5-75
5.15 RELAP5 power level parametric study. Mass flow rate [kg/s] is plotted versus time [hours] for varying power levels 5-76
5.16 Matched power levels (12.55 kW) for RELAP5 and experiments 5-77
5.17 Unequal power, RELAP5 (7.27 kW) and experiments (12.55 kW) 5-77

6.1 Thermal Fin Concept Design, dimensions in cm 6-79
6.2 Thermal Shield design, dimensions in cm 6-79
6.3 Concept design plan view. Original GA-MHTGR air cooled RCCS cavity and RPV, with air ducting replaced with water cooling tubes. 6-80
6.4 UW RCCS facility overview 6-81
6.5 Dimensions of riser tubes and cooling fins, with heaters and cavity walls 6-82
6.6 CAD model of heated interior, test ection and radiant heaters shown 6-82
6.7 TE10P phase angle firing mode 6-84
6.8 Steady state energy removal network diagram 6-85
6.9 316 Stainless steel yield stress versus temperature 6-88
6.10 Internal water temperature, tube and surface temperature TC 6-91
6.11 UVP instrument (left) and standard ultrasonic transducers (right) 6-91
6.12 Averaging post-processing technique for UDV 6-93
6.13 Dual tip RBI probe, 0.5mm sapphire tips visible 6-95
6.14 AutoCAD drawing of tank, RBI installation 6-96
6.15 Intalled RBI at vertical section into tank 6-96
6.16 Deviation from measured value, Optiflux 1000 6-98

7.1 Temperature profile of heated enclosure 7-102
7.2 Resistance network for network heat loss 7-103
7.3 Flow chart for heat loss calculation 7-105
7.4 Repeatability of single phase experiments. Mass flow rate, Run004,005,010 7-107
7.5 Repeatability of two phase experiments. Mass flow rate, Run052,058 7-108
7.6 Energy balance and uncertainty, Run010. 9.91kW linear 7-110
7.7 Analysis of time lagged inlet temperature 7-111
7.8 Cool down behavior, temperatures in riser tubes. 150 minutes after heater shutdown, from a steady-state power of 9.91kW 7-112
7.9 Spike in mass flow rate due to initiation of HXG 7-113
7.10 Oscillations in TC readings near exit of riser tubes, turbulent regime 7-113

7.11 Time evolution of the frictional pressure through through the adiabitc chimney, outlet header to tank inlet . . . 7-114
7.12 Radiant heater surface temperatures, with maximum steady state values noted . . . 7-115
7.13 Riser interior water temperatures during a fast power rate, 0-15kW in 4 minutes . . 7-116
7.14 Left: Radial dependence on convective heat transfer coefficient Right: Interior tube wall temperature (color), riser tube and fin geometry (gray), heat flux direction (arrows) . . . 7-119
7.15 Sample log from steady state experiments . . . 7-120
7.16 Comparison of temperature rise for steady state power variations . . . 7-123
7.17 Comparison of test section energy for steady state power variations . . . 7-123
7.18 True vs actual cosine power profile . . . 7-125
7.19 Fin surface temperature, steady state with linear and cosine power shoping . . . 7-126
7.20 Comparison of steady state with and without sparger in mixing tank . . . 7-129
7.21 Linearity of mass flow rate and Δ T with increasing power . . . 7-130
7.22 Primary measured system parameters for 15.19 kW baseline two-phase . . . 7-134
7.23 Mass flow rate vs time. a) Chaotic nucleate boiling at initiation of boiling, b) multimode nucleate / flashing, c) flashing dominated. 15.19 kW baseline experiment . . 7-135
7.24 Void fraction averaged over 10 second period, shown with mass flow rate overlay . . 7-136
7.25 Void fraction histogram, 15.19 kW . . . 7-136
7.26 Gas bubble velocity histogram, 15.19 kW . . . 7-137
7.27 Coupling of pressure drop and mass flow rate for baseline conditions . . . 7-137
7.28 Growing amplitude of system flow rate excursions at varying powers . . . 7-138
7.29 Growing amplitude of system flow rate excursions at increasing powers . . . 7-139
7.30 Phase portraits, pressure drop and mass flow rate at varying powers . . . 7-140
7.31 Orifice plate installed at inlet header . . . 7-142
7.32 Mass flow rate and upper network pressure drop, Run066 (Basline+orifice). Saturation of pressure drop was due to exceeding range of the device . . . 7-143
7.33 Mass flow rate detail. Orifice installation resulted in non-regular, sharp spike in the flow rate. Occasional flow reversal observed. Baseline exhibited periodic sinusoidal shape oscillations. . . . 7-144
7.34 Orifice plate installed . . . 7-144
7.35 Baseline (no orifice plate) . . . 7-144

List of Tables

1.1 RCCS examples in existing or previous HTGR designs 1-2

2.1 Summary of static flow instabilities 2-16
2.2 Summary of dynamic flow instabilities 2-17
2.3 Effects of parametric variation on instability 2-18

3.1 Similarity relationship summary for system level scaling 3-29
3.2 Summary of scaling, with details of water storage tank 3-35

4.1 Comparison of Benchmark #2, #3 for heat transfer modes 4-43
4.2 Names of Faces for reference on Figure 4.9 and Boundary Conditions 4-46
4.3 P/D = 5 Results for each height configuration 4-47
4.4 P/D = 5, results for each height configuration 4-47
4.5 P/D=2 and P/D=4 Results for each pitch configuration, 22' cavity height 4-48

5.1 Log of experimental conditions for input into RELAP5 5-67
5.2 Scaling validation RELAP5 test matrix 5-71
5.3 Reactor scale results RELAP5, similarity parameters applied and new values at $\ell_R = 0.25$ calculated, and compared to reduced reactor RELAP5 results 5-72
5.4 Reduced reactor (3 riser tubes) vs experimental 5-73
5.5 Times to tank depletion from loss of inventory due to steaming 5-73

6.1 Cavity insulation properties 6-83
6.2 Thermal induced stress for varying P/D ratios, Analytical vs ANSYS 6-87
6.3 Goal driven optimization results for heating geometry and position 6-89
6.4 Validation results for UDV testing 6-94
6.5 Data aquisition measurement uncertainty 6-97

7.1 Heat losses during steady state and two-phase conditions. Percent heat losses from total energy at various integral powers. Contributions from facility components. . . . 7-105
7.2 Initial conditions and test parameters for single phase repeatability 7-107
7.3 Test conditions and results from two-phase repeatability tests 7-108
7.4 Uncertainty in calculated energy balance 7-109
7.5 Initial Conditions and Test Parameters for Power Level Variation Runs 7-122
7.6 Summary of power level investigation at steady state 7-122
7.7 Ultrasonic velocity compared to magnetic flow meter, linear heating 7-125
7.8 Comparison of flow rates in individual riser tubes during asymmetric heating 7-127

7.9 Analytical view factors from Heater A to Riser N 7-128
7.10 Fluctuations with and without sparger in tank 7-129
7.11 Summary of single phase, steady-state experiments 7-130
7.12 Summary of steady state values and energy balance from UDV testing 7-131
7.13 Summary of flow rate measurements from UDV and magnetic flow rate meter 7-131
7.14 Results from two-phase testing, power investigation 7-141

Chapter 1

Introduction

1.1 Motivation

Passive heat removal systems have become one of the primary focus areas for meeting the technological goals of the Generation IV International Forum. In the event of an accident scenario, where power is lost and subsequent failure of the cooling pumps occur, passive systems provide an ultimate heat sink for the decay power to leave the system, thus preventing temperatures from reaching dangerous levels and ultimately preventing a core meltdown. Of these passive systems, natural circulation water loops have the potential to offer a high level of performance, with relative simplicity and inherent safety characteristics. The reactor cavity cooling system (RCCS) has emerged as the leading concept for passive decay heat removal, with recent developments tailored to the latest generation of very high temperature reactors (VHTR).

Passive heat removal systems provide the opportunity to remove decay heat from a RPV to an ultimate heat sink without the need for off-site AC or on-site DC power. With a robust design, these systems become an integral part of the power plant that require no human intervention during an accident transient. While offering an extensive array of benefits, these systems often exhibit complex and uncertain thermal hydraulic behavior. A primary concern is the development of flow instabilities, both global (e.g. continual and increasing flow oscillations) and local (e.g. variations in individual tube flow directions). With real systems exhibiting multiple parallel channels, skewed heating profiles, and power transients, the instabilities are further reinforced and made more complicated. To ensure a successful application of these systems to a full sized reactor design, these instabilities must be under-

stood. This includes, but not limited to, knowledge of their behavior and magnitude over a broad range of conditions, with an ultimate goal of creating a shift from uncertainty to predictability. Thus, the thermal hydraulic performance and stability characterization of passive decay heat removal systems for applications to nuclear reactors will be the primary scope of this work.

1.2 Passive Decay Heat Removal in the HTGR

Passive cooling for high temperature gas reactors (HTGR) has been designed and researched since the early 1950s. While each are unique in geometric design, they all share one fundamental ideal: with an extremely high vessel wall temperature of HTGR RPV (nominally 400°C), they can take advantage of radiative heat transfer to accomplish their purpose. Table 1.1 summarizes a few of the most recent designs under development.

Table 1.1: RCCS examples in existing or previous HTGR designs

Reactor	**RCCS Coolant Type**		**Country**	**Power**
HTTR	Water	Forced	Japan	30 MW
HTR-10	Water	Natural	China	10 MW
PBMR	Water	Natural	South Africa	265 MW
GT-MHR	Air	Natural	Russia	600 MW
MHTGR	Air	Natural	USA	450 MW

The HTTR, the first HTGR to be build in Japan, is a 30 MWt engineering test reactor that utilizes graphite moderation, helium coolant, and prismatic TRISO fuel (Oh, 2006). Their RCCS design relies on forced cooling with water through a set of water stand pipes and radiant fins. While not a truly passive design, their vessel cooling system are used as a residual heat removal system when forced circulation in the primary coolant loop cannot be maintained due to a rupture of piping, and boast high reliability and redundancy (Shiozawa, 2004).

The HTR-10, a 10 MWt module pebble bed type reactor from the People's Republic of China, adopts two independent water cooled RCCS loops which rely completely on natural

circulation (Wu, 2002). In the event of loss of coolant, decay heat would dissipate via the core structure by means of conduction and radiation to a cavity cooler installed on the walls of the concrete containment. While the primary working fluid is water, the exchange to the ultimately heat sink (atmosphere) is by means of air. The design of the cooling tubes consists of thermal shields that lie tangent to the cooling tubes.

The South African 265 MWt pebble bed module reactor (PBMR) adds an additional level of redundancy, with 3 independent systems of natural circulation drive water flow. As with the HTR-10, they rely ultimately on an external water to air heat exchanger to reject heat to the atmosphere. The design of the cooling panels, or curtains, consists of approximately 60 large standpipes, with an oval cross section of 0.25x1.0 m (IAEA-1198).

The Russian GT-MHR, a 600 MWt gas turbine modular helium reactor planned for construction in the near future, will be the first to test the performance of a full scale RCCS design with air (IAEA-1198). As with previous designs, a bare vessel conducts heat from the fuel elements to a set of cooling panels by radiation and convection. However, unlike the previous designs, the working fluid in the cooling panels and ultimately into the atmosphere, will consist entirely of air.

The last design under active development is the General Atomics module high temperature gas reactor (MHTGR). Development in the United States, this air cooled RCCS design will reject heat from a 450 MWt RPV by a set of air ducts that line the cavity walls. Each duct, with a cross section of 10x2 cm and total length of 19.2 m, will be a part of 227 total ducts that act in two redundant circuits (HTGR-86-024). The design basis calls for air entering the system at 43°C through an inlet plenum, continuing down a set of downcomers and up the riser ducts before, being discharged out from the chimney. The total elevation, from the chimney inlet to the bottom of the air ducts, is planned to extend over 55 m.

1.3 Flow Instabilities

Due to the inherent nature of buoyancy driven natural circulation loops, flow instabilities must be considered when designing and analyzing a system. At a stable steady state condition, the driving forces (buoyancy) and losses (frictional) balance in an equilibrium. However, when a perturbation occurs in the system, this balance is skewed and oscillations or instabilities can arise and propagate.

These instabilities are most commonly found in the form of mass flow rate and pressure drop, tightly coupled to boundary conditions, such as power input, heat flux, and level of subcooling. Additionally, many secondary effects are present, such as geometry and boundary conditions. These instabilities are extremely undesirable in process systems, since a continued oscillation may cause forced mechanical vibrations, effect local and integral heat transfer characteristics, and even induce boiling crises, such as CHF, burn out, dry out, etc. (Boure, 1973).

1.4 Generation IV Nuclear Reactors

1.4.1 Technological Goals

Eight technological goals have been defined for the Gen IV systems in four primary areas: sustainability, economics, safety and reliability, and proliferation resistance and physical protection (Abram, 2008). These goals aim at responding to the economic, environmental, and social requirements of the 21st century

1. Systems operations will excel in safety and reliability
2. Nuclear energy systems will have a very low likelihood and degree of core damage
3. Nuclear energy systems will eliminate the need for off site emergency response

1.4.2 NGNP

The Next Generation Nuclear Plant (NGNP) is a Gen IV version of the VHTR. Sponsored by a Department of Energy (DOE) initiative, the NGNP design allows for a multipurpose facility, producing not only electricity, but process heat for industrial applications and a coupled hydrogen production assembly. Based on the VHTR, the NGNP uses a graphite-moderated reactor core (pebble bed or prismatic blocks) with a once-through uranium fuel cycle. Using helium as the primary coolant, outlet temperature reach up to 700°C, though similar designs reach temperatures upward of 1,000°C

1.4.3 Reactor Cavity Cooling System

While HTGRs have been designed and operated since the early 1950s, the RCCS design is unique to the recent generation of gas-cooled reactors as a passive decay heat removal system. Both air and water-cooled designs are under consideration. Air-cooled RCCS designs, such as for the General Atomics Modular High Temperature Gas-Cooled Reactor (MHTGR), Figure 1.1, have been used in sodium-cooled fast reactor designs, but many aspects of the newer water cooled design are still to be investigated. This paper focuses on the water-cooled design, Figure 1.2 which has some advantages over an air-cooled system, given its superior cooling capability and less intricate piping network that is required for a natural circulation driven air system. Using water as the working fluid, the RCCS operates in passive mode during an accident condition, rejecting heat from the RPV to the atmosphere via a system of water tubes, cooling panels, and water storage tanks, Figure 1.3. The Nuclear Regulatory Commission (NRC) has indicated that for passive safety system, a 72-hour cooling inventory must be available before water storage tanks can be replenished. Since the NGNP design is under development, a concept design has been created using previous work and openly available literature.

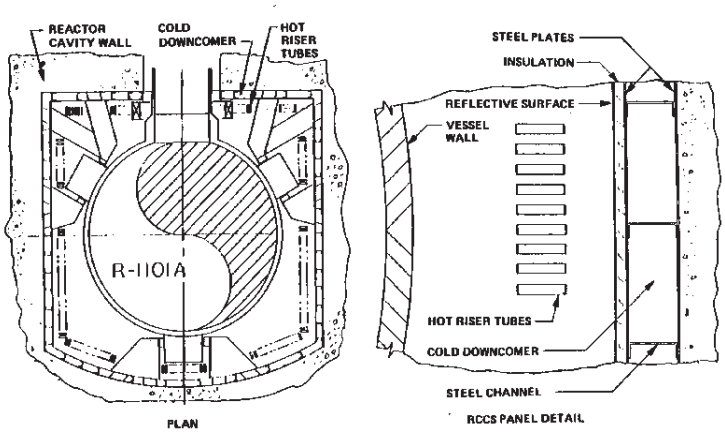

Figure 1.1: GA-MHTGR RCCS configuration plan (HTGR-86-024)

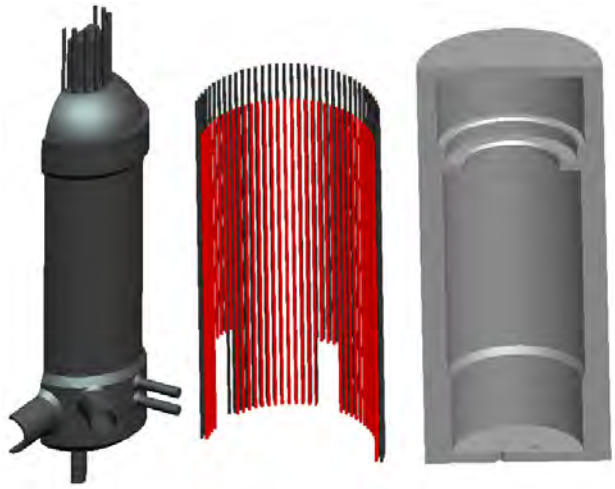

Figure 1.2: RCCS concept. RPV, RCCS cooling tubes, Concrete containment

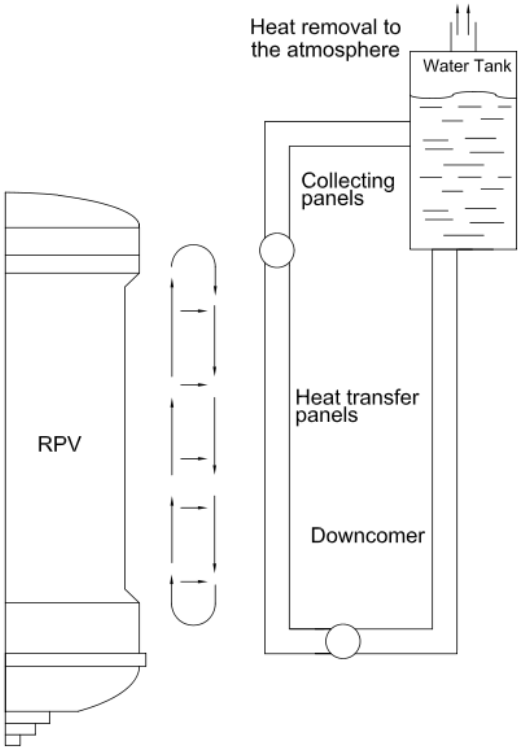

Figure 1.3: RCCS design overview

Chapter 2

Literature Review

To understand the flow instabilities associated with natural circulation loops in both single and two-phase conditions, an extensive literature review was conducted. A classification and definition of common forms of instabilities will be presented, followed by examples of previous work.

2.1 Classification of Flow Instabilities

Two-phase flow instabilities have been extensively studied for numerous industrial applications, including thermosiphons and power cycle loops. Therefore, the literature of two-phase flow instabilities is extensive. It should be noted that single phase instabilities do exist and are researched, but an in-depth overview of those mechanisms will not be given. As such, an overview of two-phase instabilities, classifications, and definitions will be given. Then, specific discussion of efforts and techniques in the analysis will be discussed.

For clarity, key terms will be defined. If a system at steady-state is perturbed and eventually returns to its initial equilibrium, the system is described as stable. If a system at steady-state is perturbed into a neighborhood where no equilibrium exists near the initial state, the system possesses a static instability. A system has dynamic instabilities if there are inherently transient feedback mechanisms that may lead to a steady-state, though there is no guarantee of uniqueness. An instability that arises from another is referred to as a secondary phenomenon (the instigator being the primary).

2.1.1 Single-Phase Subcooled

During normal subcooled conditions, the driving forces (buoyancy) present due to the differences in elevation of the hot and cold leg temperatures are balance by frictional losses. However, for a given disturbance, such as a small increase in buoyancy, an increase mass flow rate will follow suit. Jain et al (2005) observed that at off normal parameters, for example certain heat flux condition, instabilities become present and have integral consequences.. They are commonly found in the form of oscillations in mass flow rate, with a few cases leading to flow reversals. These oscillations can perturb heat transfer performance and expected flow behavior. P.K. Vijayan et al. (2006) observed three distinct mechanisms for instability development during single phase flow in a natural circulation loop.

1. start up from rest
2. power raising from stable steady state
3. power step back from initially unstable state

In the first mechanism, the oscillation growth terminates after a few cycles and near periodic uniform directional oscillations. In the second, he observed at higher power, a switch from unidirectional to bi-directional pulsing which terminated the oscillation growth. Both were found only for start up from rest. The third was observed when power increased to an unstable value from a stable steady state.

Additionally, he observed a unique behavior in the hysteresis region, with an instability threshold that depended on the heat addition path. The implications of the hysteresis region is that a stability map obtained from convectional methods, such as linear analysis, is not sufficient by itself to guarantee stability, and a nonlinear analysis must be performed.

Misale et al. (2010) constructed an experimental apparatus that consisted of a rectangular loop with the heater at the bottom and HXG at the top. By comparing the temperature differences across the hot and cold legs, they were able to recognize different flow regimes. The regimes they observed are summarized below:

- Stable steady-state. After an initial transient by a power excursion, the dT between the hot and cold legs reached a constant value, and experienced small perturbations.

- Bidirectional pulsing flow: This unstable state is seen with a pulsing flow from opposite directions. They characterized the oscillations as chaotic, with the flow alternating from either direction.

At these two flow ranges, they observed unstable behavior with periodic and bidirectional flow patterns. Flow reversals were more frequent at low heat fluxes, but became rare when the system approach the turbulent regime. At high heat fluxes, a smooth transition was observed between unstable and stable behavior, with limit conditions which could be considered "meta-stable".

They characterized a linear stability analysis of their natural circulation system by following Vijayans (Vijayans, 2006) model. They defined a modified Stanton and Nusselt number number, Eq. 2.1:

$$St_m = \frac{4Nu_m}{RePr}, \qquad Nu_m = \frac{U_i L_t}{k} \tag{2.1}$$

With these parameters, they placed their experimental data into stable or unstable regions. They concluded that the theoretical Stanton number, needed to reach the stability of the system, is much higher than their experiment values. They offered the following explanation of the discrepancies: the main effect of the increase of the heat sink temperature is the raise of the mean working fluid temperature. At low power, where the heat exchanger at the cooler is easily achieved, the main effect of the increase in working fluid temperature is a reduction of the shear stresses, which have a stabilizing effect, thus bringing the system in instability. On the contrary, at high power, where the cooling is more critical, the most important consequence of the reduction of the shear stresses, is the increase of the flow velocity, which make the heat exchanger at the cooler more efficient, thus stabilizing the system. Maiani et al. (2003) formulated an analytical model for the stability bounds in a

natural circulation single phase thermosyphon loop. These loops are often characterized as non-linear systems, which experience extremely complex and chaotic behavior. They derived mathematical models for an ideal system, comprising of a closed loop of total length L, with two vertical adiabatic legs joined by top and bottom horizontal runs of length S. It was at these horizontal runs that heat transfer, either power supplied, or power removed, took place. An effort to quantify the stability was made by linearizing the momentum and energy equations along with the associated boundary conditions. They arrive at the following equation to assess the stability of the system, where $\overline{\alpha} = \frac{\alpha n}{\overline{q}}$ and $\Theta = \frac{\Theta}{\overline{q}}$.

$$\frac{e^z + m}{e^z - 1} + \frac{\overline{\alpha}}{z(z + \Theta)} = 0 \tag{2.2}$$

The previous equation can be solved with respect to z to determine the dynamic behavior of the system: the stable, unstable, or neutral regions are given by $Re(z_1) < 0$, $Re(z_1) > 0$, $Re(z_1) = 0$ where z_1 is the solution with the largest real part. They found that a systems stability criteria is strongly dependent on the initial conditions, with the onset of instabilities occur at higher values of α. Additionally, they define two dimensionless numbers, α^*, Φ^*, which the authors strongly believe can 'completely determine a steady state solution' (for the authors natural circulation single phase thermosyphon loop). The dimensionless number in Eq. 2.2, depend exclusively on the geometrical and physical characteristics of the system, and thus can be applied universally to all thermosyphon systems. Lengthy in their derivation, details can be found in their paper (Maiani, 2003). A theoretical stability map for the authors single phase thermosyphon loop is given in Figure 2.1.

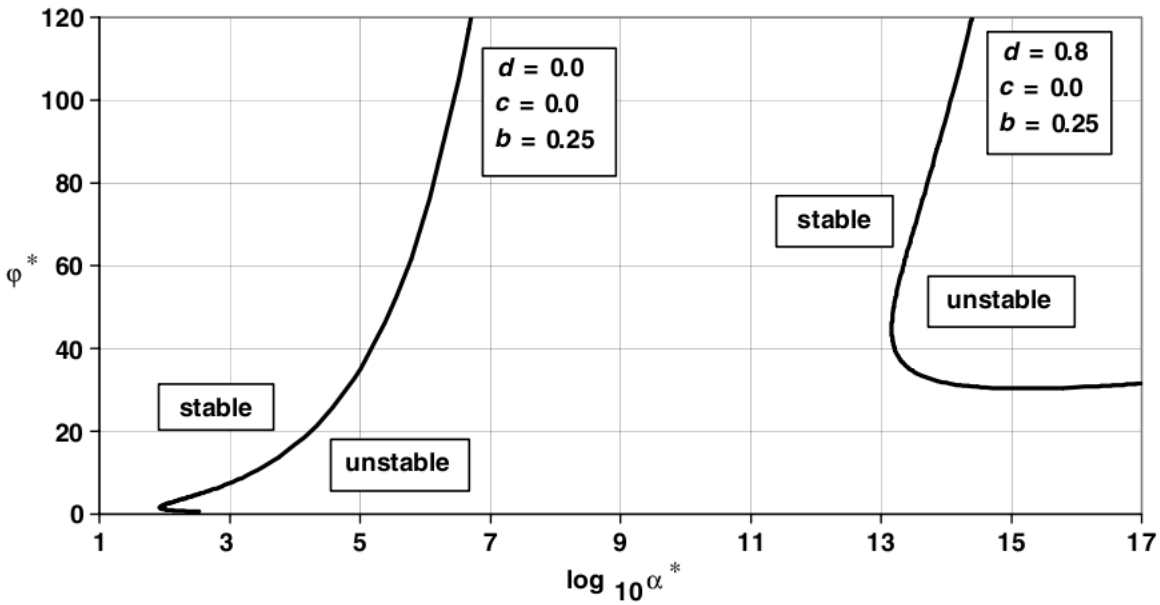

Figure 2.1: Theoretical stability maps for various cases at positive flow steady-state conditions

2.1.2 Two-Phase Flow Instabilities

There are a variety of ways to classify two-phase flow instabilities depending on geometry, spatial/temporal dependence, multiphase models, etc. Difficulties also arise when real world applications see a convergence of all of these parameters. Both Boure and Kakac provide extensive discussions of general two-phase flow instability characterization (Boure et al., 1973; Kakac Bon, 2008) and their similar systems for describing two-phase will be used throughout this section. 2.1, 2.2 present a summary of general two-phase instabilities presented by the above authors; however, not all of them will be discussed in detail. (Durga Prasad et al., 2007) and (A. K. Nayak Vijayan, 2008), while overlapping somewhat with the generic descriptions of instabilities, present and classify certain instabilities as natural circulation specific that should be described. Most of the following discussion concerns a flowing fluid undergoing phase transition in a channel which may require some familiarity with two-phase flow regimes; explanation of these regimes is left to the literature, (Thome, 2004; Tong Tang,

1997; Ghiaasiaan, 2007).

For clarity, key terms will be defined. If a system at steady-state is perturbed and eventually returns to its initial equilibrium, the system is described as stable. If a system at steady-state is perturbed into a neighborhood where no equilibrium exists near the initial state, the system possesses a static instability. A system has dynamic instabilities if there are inherently transient feedback mechanisms that may lead to a steady-state, though there is no guarantee of uniqueness. An instability that arises from another is referred to as a secondary phenomenon (the instigator being the primary).

A compound instability is one that incorporates two or more mechanisms that confound analysis; fundamental instabilities are the opposite. Using a standard physical analogy, 2.2(c) is a stable system while 2.2(d) is an example of a system with a static instability.

One aspect of the stability the above definitions do not discuss is the magnitude of the system perturbations. The strength of the perturbation is important since it determines how much energy is imparted into the system and, therefore, how far the system will travel from its initial state. The importance can be seen in **??** where both systems exhibit different behavior depending how hard the system is "hit." 2.2(e) shows a linear instability while actually being nonlinearly stable with multiple equilibria. 2.2(f) exhibits linear stability while being nonliearly stable These concepts are important to consider when looking at linear stability because the behavior beyond the system's linear boundary is technically *terra incognita*. Actually performing a nonlinear analysis, if possible, is the only surefire tool for assessing stability.

Static Instabilities

Static instabilities are characterized by either a pure steady-state analysis or an analysis that foresees dynamic feedback from the steady-state system. The analysis tools used to derive stability boundaries for these instabilities will be discussed in later sections.

A flow excursion, also known as a Ledinegg instability, is the sudden drop in a steady flow rate to a lower, steady value. This jump occurs when the pressure losses in a system

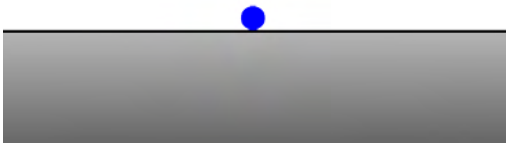

((a)) Neutral equilibrium (infinitely many steady-states)

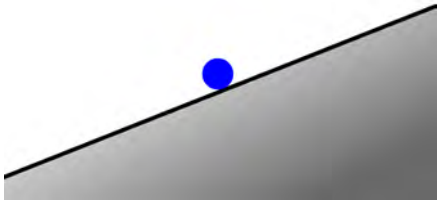

((b)) No equilibrium (no steady-state)

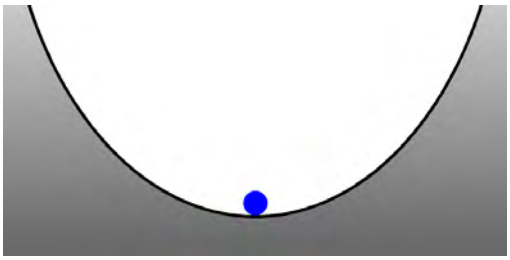

((c)) Stable equilibrium

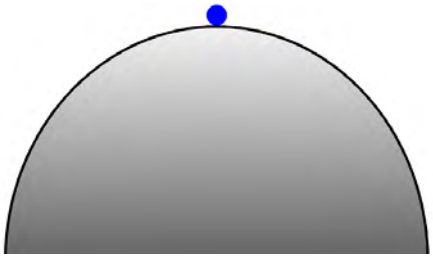

((d)) Unstable equilibrium

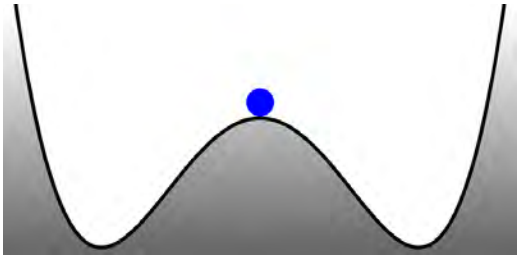

((e)) Linearly unstable, nonlinearly stable equilibrium

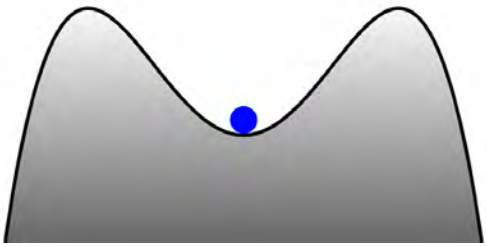

((f)) Linearly stable, nonlinearly unstable equilibrium

Figure 2.2: Ball-and-hill analogy of equilibrium descriptions. The ball represents some state at a given time and place, and the shapes supporting the ball dictate how the state moves when subjected to a perturbation. Troughs are considered stable while crests/runoffs are unstable.

decrease with increasing flow rate. For a liquid undergoing phase change in a channel, there is a complex, internal relationship between the buoyancy, friction, and acceleration momentum terms that must be taken into account for steady flow. If the flow is forced by external sources and the internal forces of the flow are not properly taken into account, then the pressure drop could rise with increasing flow; this is especially true for slightly sub-cooled flows entering a heated region where a sudden change in void fraction can have a large impact on the flow behavior with the system.

Fundamental relaxation instabilities occur when two or more flow regimes have state equilibriums close to each other. For example, a bubbly flow that experiences a small change in flow rate could transition to the annular regime. Then, the flow rate will experience an increase since annular flow has a relatively low pressure drop, and the flow regime transitions back to the bubbly regime. Given the right situation, this cycle could continue ad infinitum. The flow regime transitions act as a relaxation mechanism (in the dynamical system sense) that causes persistent, periodic behavior.

Chugging is an instability associated with the jetting of large vapor structures from a flow channel into larger space. This instability typically occurs with low velocities and moderate void fractions (Tong Tang, 1997). A flowing liquid receiving heat may development large vapor bubbles in a coolant channel; this increases the flow rate due to the vapor-to-liquid ratio. After the bubbles have been expelled, and possibly quenched, at the channel exit, the flow rate will return to the pre-slug rate. As with the relaxation instability, this mechanism also has a periodic nature (Aritomi et al., 1993).

Dynamic Instabilities

Dynamic instabilities, unlike static, are inherently transient and primarily involve the transmission of information via waves. Thermal hydraulic systems typically possess a material (or density) wave and an acoustic (or pressure) wave. For a non-ideal fluid, the acoustic wave's speed is primarily a function of the system's density and temperature while the material wave travels near the physical speed of the system.

Acoustic instabilities are typically of high frequency (10Hz–10kHz) and have been observed in various boiling regimes. The acoustic waves were found to cause large pressure drop oscillations relative to steady-state values. Even in situations where the lower frequency density waves were present, there was a clear superposition of high frequency acoustic waves with the material waves. At high pressure-and-temperature water experiments, the acoustic waves reached frequencies that were clearly audible (so-called whistler modes).

Material wave instabilities are the most common in two-phase flow and are a highly physical phenomenon that occur from a complex coupling of equations, constitutive relations, and geometry. These waves have also been described as "flow-void feedback instabilities" for boiling systems (Neal et al., 1967) and "time-delay oscillations" due to the relatively slow transmission of information at material speed (Bour Mihaila, 1966). Since the oscillation has its roots in the differing densities of a fluid's liquid and gas phases, vertical channel height (where the system pressure changes greatly with position), inlet conditions (thermodynamic and kinematic), and total heat transfer between the fluid and the surroundings are extremely important in the control and appearance of these flow oscillations. It has been found that by increasing the system pressure these oscillations can be mitigated or eliminated since the density ratio of the competing phases approach one another as the pressure increases.

These material oscillations can lead to oscillations in the boiling heat transfer processes at the wall and results in a compound thermal instability. The emphasis here is put on the highly variable nature of the two-phase heat transfer coefficient at the wall and how the information being propagated from the wall interacts with material wave oscillations. The effects of this interaction can be as bad as an oscillating dry point in the channel with large temperature oscillations.

Natural Circulation Instabilities

There are two natural circulation instabilities of primary interest: flashing and compound natural circulation. Flashing occurs when a high temperature liquid flows into a region of lower pressure such that it enters a saturated or superheated state and immediately bursts

into a two-phase mixture. This mechanism is a primary cause of material wave instabilities in natural circulation loops at low pressures or long vertical channels. This type of instability is currently under examination for one and two protypic fuel channels (Marcel et al., 2009, 2010).

The final instability is the compound natural circulation instability. This instability is the confluence of vertical channel heating, material wave oscillations (possibly due to flashing), chugging phenomenon, and flow regime transitions. Since the system's flow rate is not subject to any mechanical head contributions, all of these instabilities can occur concurrently and must be carefully analyzed to discern which of the mechanisms are present and which is dominate. These instabilities are extremely important for all types of nuclear reactors and are under continuously under investigation (DAuria Galassi, 1990; Aritomi et al., 1992; Yun et al., 2005)

Table 2.1: Summary of static flow instabilities

Name	**Class**	**Mechanism**	**Characteristics**
Flow excursion	Fundamental	$\left(\frac{\partial \Delta P}{\rho u}\right)_{int} \leq \left(\frac{\partial \Delta P}{\rho u}\right)_{ext}$	Sudden, large flow change to a new, stable state
Boiling crisis	Fundamental	Ineffective cooling	Wall temperature excursion and flow oscillation
Flow Regime Transition	Fundamental Relaxation	Varying Δ P between regimes	Cyclic flow pattern transitions and flow rate variations
Bumping, geysering, or chugging	Compound Relaxation	Periodic adjustment of metastable conditions	Periodic superheat and violent evaporation

Table 2.2: Summary of dynamic flow instabilities

Name	**Class**	**Mechanism**	**Characteristics**
Acoustic Oscillations	Fundamental	Resonance of pressure waves	High frequency oscillations near the acoustic speeds
Density Wave Oscillations	Fundamental	Coupled mass, momentum, and energy feedback	Low frequency oscillations near the material speed
Thermal Oscillations	Compound	Variable heat transfer coefficient interacting with flow	Occurs during film boiling
BWR Instability	Compound	Hydraulic-neutronic coupling	Strong only for a small fuel time constant and low pressure
Parallel Channel Instability	Compound	Interaction among parallel channels	Various modes of flow redistribution
Pressure drop Oscillations	Secondary Compound	Flow excursions initiate interactions between channels and compressible volumes	Very low frequency, periodic process

Table 2.3: Effects of parametric variation on instability for a flow entering a vertical channel sub-cooled or saturated

Parameter Increased	**Effect**	**Reason**
System pressure	Stability increases	Phase density difference lessens thus reducing the gravitational head gain.
Mass flow rate	Stability increases	Critical power for oscillation generation increases and avoids chugging.
Inlet sub-cooling	Destabilizes at small sub-coolings but stabilizes otherwise	For small sub-coolings,due to significant response delay in void formation with an increase in transit time. Otherwise, it reduces void fraction and increases non-boiling length.
Inlet resistance	Stability increases	Increases the single phase friction which has a damping effect upstream.
Exist resistance	Stability reduces	Increases two-phase friction which amplifies instabilities upstream
Riser height	Stability reduces	Increases two-phase gravitational pressure drop and phase transition as static head decreases

2.2 Review of Previous Efforts & Experiments

2.2.1 Small Scale Natural Circulation Loops

Zvirin (1981) conducted a review of small scale natural circulation loops, detailing their behavior and subsequent instability, with examples given for seven different types of pressurized water reactors and other systems in small scale loops, Figure 5. The theoretical investigations of natural circulation loops show three different types of possible instabilities

1. one associated with the onset of motion (either in the body or in a stagnant branch)
2. the growth of flow and temperature oscillations, which may lead to flow reversals
3. the multiple steady-state solutions

The first instability, the onset of motion, was observed in the open loop, Figure 2.3d, where the outlet temperature begun to change long after activation of the heaters, Figure 2.5. Analysis of experimental data and analytical comparisons showed the general trend of the transient observed; including the first strong oscillation in temperature and subsequent weaker oscillations. In a similar open loop, Figure 2.3e which is relevant to a pressure water reactor (PWR), flow reversals occurred suddenly in the previous inactive, or stagnant loop. It was concluded that the mechanisms for these flow onsets is the build up of buoyancy differences due to the heaver (colder) fluid resting on top of the lighter (hotter) fluid. At some critical threshold, a condition is reached where the buoyancy force was strong enough to drive a flow around the loop.

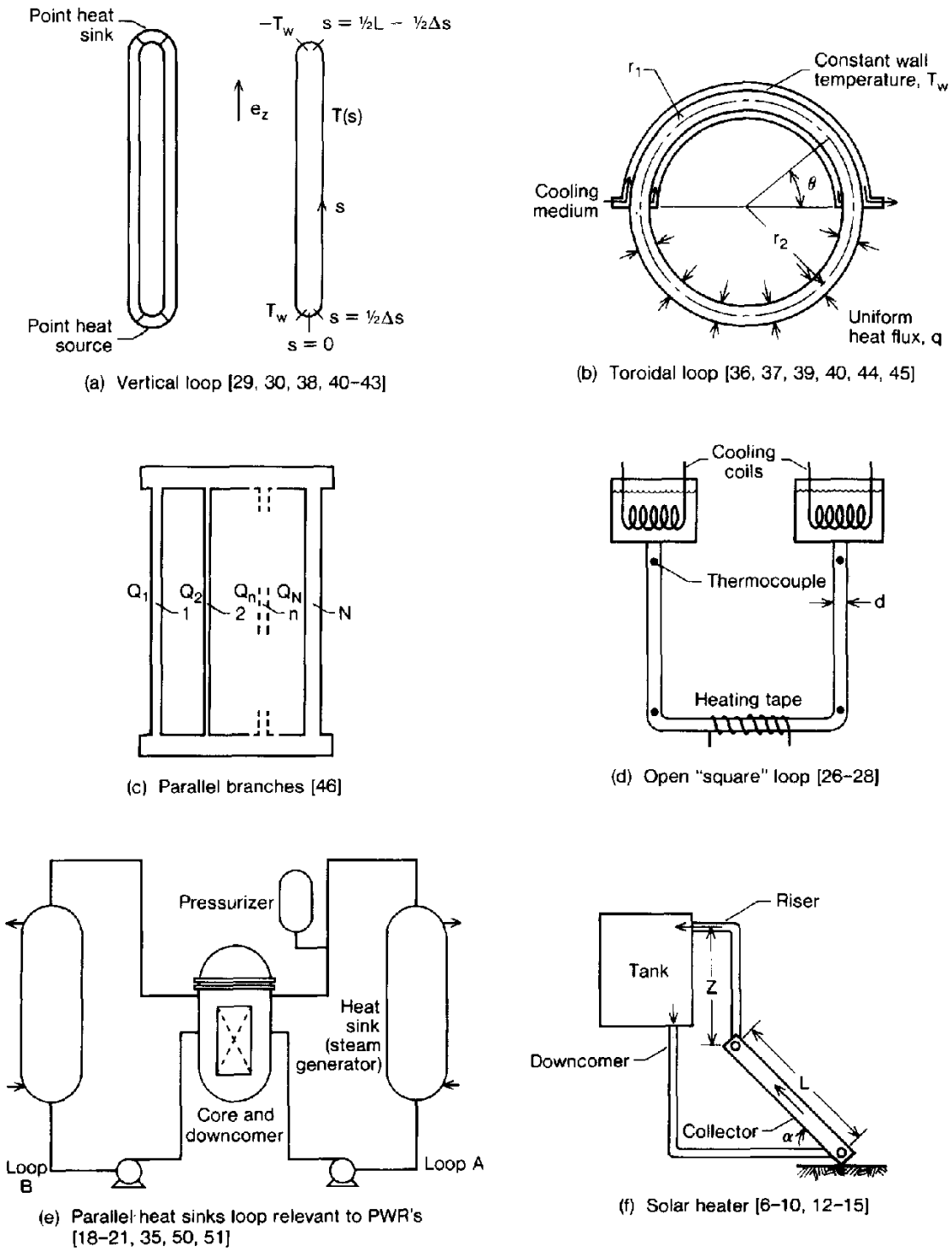

Figure 2.3: Various natural circulation loops (Zvirin 1981)

The second type of instability was observed in the toroidal loop, Figure 2.3b and the simple vertical loop, Figure 2.3a. Typical behavior of the growing temperature oscillations led to flow reversals, allowing for collection of data points for a stability map, Figure 2.4. It was observed that for Figure 2.3a, a simple vertical loop, that there is no relation between the two-types of flow instabilities in the loop and the small-amplitude stability. The general effect of the through flow, however, is the stabilization of flow in the loop.

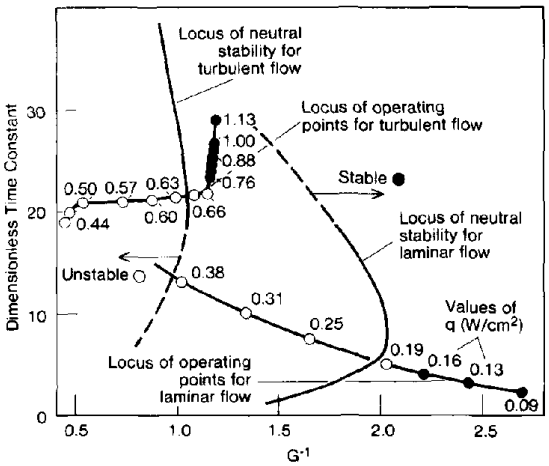

Figure 2.4: Stability characteristics for toroidal loop (Zvirin, 1981)

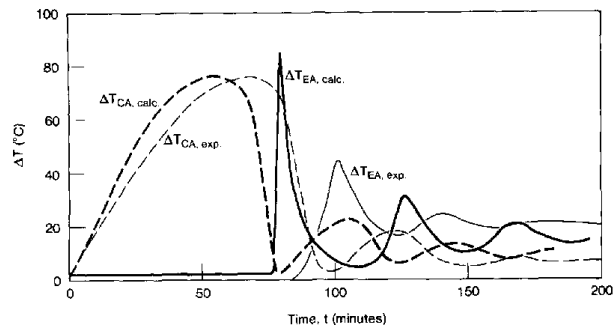

Figure 2.5: Starting transient for an open loop, outlet and heater temperature (Zvirin, 1981)

Oscillations in the flow rate and temperature have also been observed in solar water heaters, Figure 2.3f. The oscillations in the flow rate exhibited a slow decay, with a period of approximately 1,500 seconds, Figure 2.6, left. However, no instabilities and no flow reversals were observed. Thus, this system, under the experimental test conditions, was considered stable with a slowly decay oscillation modes. The third type of instability is associated with multiple steady state solutions, Figure 2.6, right. In the experiments of Figure 2.3c, it was observed that a critical heat input exists in a second channel for a fixed input in the first channel. Above the critical value, the flow in the second channel was always upward. However, below it the flow in the second channel could be reversed by disturbances such as a temporary restriction of the third channel or a short injection of a falling jet in the second channel.

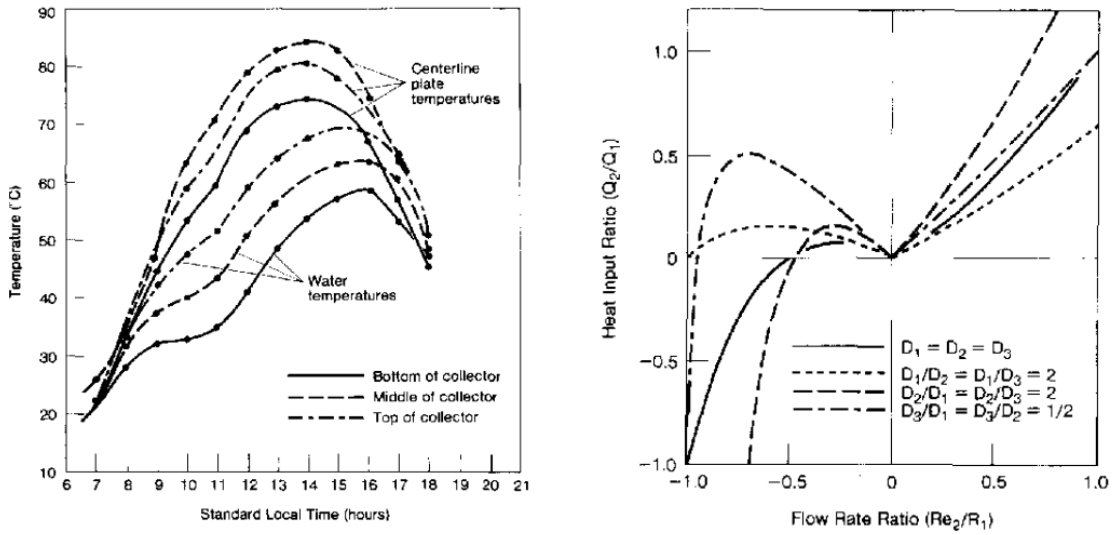

Figure 2.6: Left: Full scale solar water heater, temperature decay. Right: Multiple steady state solutions for parallel tube systems. (Zvirin, 1981)

The authors point out that the rest state of a thermosyphon is always unstable (when the heat source is applied). There is always an unstable mode (or a disturbance will grow), and they suggested that these predicted instabilities are local in nature and probably cause only closed convection cells (of the Benard type) while other critical condition must be reached prior to the initiation of a flow in the loop.

2.2.2 Effects of Power and Multiple Channels

With natural circulation boiling loops already susceptible to flow instabilities, the presence of multiple channels further complicates the problem as it can lead to multiple modes of instability.

The problem of two-phase flow instabilities in parallel channels and the modes of oscillation were analytically studied by Fukuda and Hesegawa (1979). It was found that it was very difficult to recognize the mode of oscillation as the number of parallel channels increased. Additionally, the occurrence of a particular mode of instability was found to strongly depend on the slight differences in the channel characteristic, such as heat flux, geometry, or inlet conditions. In multiple path systems that do not exhibit equal path lengths, this problem is

further augmented.

Jain et al. (2010) constructed a facility with relevance to pressure-tube type natural-circulation based boiling water reactors, such as the Indian Advanced Heavy Water Reactor (AHWR). Their facility was comprised of four parallel channels, which are direct electrically heated tubular sections. They experimented with varying pressures (1 - 10 bar), power (0.1 - 12 kW), number of parallel channels (1 - 4), and skewed heating profiles.

They found several interesting results at their range of system parameters. At lower pressures (1 bar), they observed minimal variation in behavior between the channels, which was a stark contrast from higher pressures (9 bar), where individual channels showed a preference for initiation of oscillatory flow. Additionally, lower pressure conditions were characterized by flow reversals, whereas high pressures show behavior that was purely unidirectional.

Stable two-phase regimes were only observed with intermediate power, and becoming unstable at the onset of higher powers. This was found to be lie in two power regimes, the first with a buoyancy dominated at low powers, and other with friction dominated at high powers. The low power regime showed that with an increase in system power, an increase in flow was observed, immediately followed by a Type-I instability (Fukuda, 1979). In the high power regime, the increase in system power caused a decrease in flow, followed by a Type-II instability.

Finally, the range of stable flow was found to increase with rise in pressure, confirming the stabilizing effects of high pressure systems. Interestingly enough, they found that even though their heating profiles were uniform across all the channels, the flow distribution was not. In general, the oscillations could not be characterized as in or out of phase among channels. There was only a gradual shift among channels.

Jain et al. (1966) investigated the flow and pressure oscillations that occurred with boiling water natural circulation loops. They varied the pressure, power, inlet subcooling, and relative lengths of the riser and vertical test section channels. In negative sloping or plateau regions of the ΔP vs power curve, they confirmed the presence of flow oscillations.

Additionally, they observed flow reversals, a strong dependence on the geometry of the loop, and stronger subcooling effects at low pressures. They found that even the smallest increase in subcooling resulted in a more unstable system, until a threshold point where the trend was reserved. The reserving trend, they hypothesized, was due to an equivalent effect of reduction in power at lower subcooling. Finally, in regards to the geometry, they found that both longer risers and smaller test sections had a destabilizing effect on natural circulation loops.

2.2.3 Nuclear Focused Passive Cooling Systems

G. Yun (2004) studied the characteristics of natural-circulation instabilities and the unstable operating region of China's Advanced Research Reactor (CARR). He describes CARR as a safe, reliable, multipurpose research reactor with high performance. The system's stability was determined by the time evolutions of dependent variables following perturbation in mass flow rate at a given steady condition. In the observed regions corresponding to a Type-I instability, the two-phase density changes very quickly with an increase in equilibrium quality at low system pressures. Thus, they concluded that the gravitational pressure drop was very sensitive to a small perturbation that caused the initial oscillation. However, if the equilibrium quality is greater that 3 percent, the found the change to be very slow. Thus, the driven force that comes due to the density variation is stabler than former, suppressing the oscillation, and explaining their very narrow unstable region. With regards to the influence of power ratio and mass flow rate, Figure 2.7, they found an unstable region located in the low power region in the range of 0.05 and 0.2 kg/s, and in the middle range corresponding to 39 - 59 kg/s. Additionally, they found a very narrow band of stability with regards to the temperature at the inlet. With an increase in inlet temperature, the power ratio will cause an oscillation dampening.

The two-phase instability became a quasi limiting oscillation after initial perturbations, with an observed a frequency between 0.07 and 0.25 Hz. The amplitude of the mass flow rate

was found to be very large, reaching up to 130 kg/s. The oscillations in pressure drop were found to be out of phase with the mass flow rate, which they observed were characteristic of density wave oscillations. They results showed that a throttling behavior at the inlet had a stabilizing effect on Type-II inabilities, with no change observed in Type-I boundaries. Their study presented confirmed that the instabilities of CARR only occur in very low quality regions. Additionally, the instabilities of CARR show characteristics of geysering and Type-I density wave oscillations.

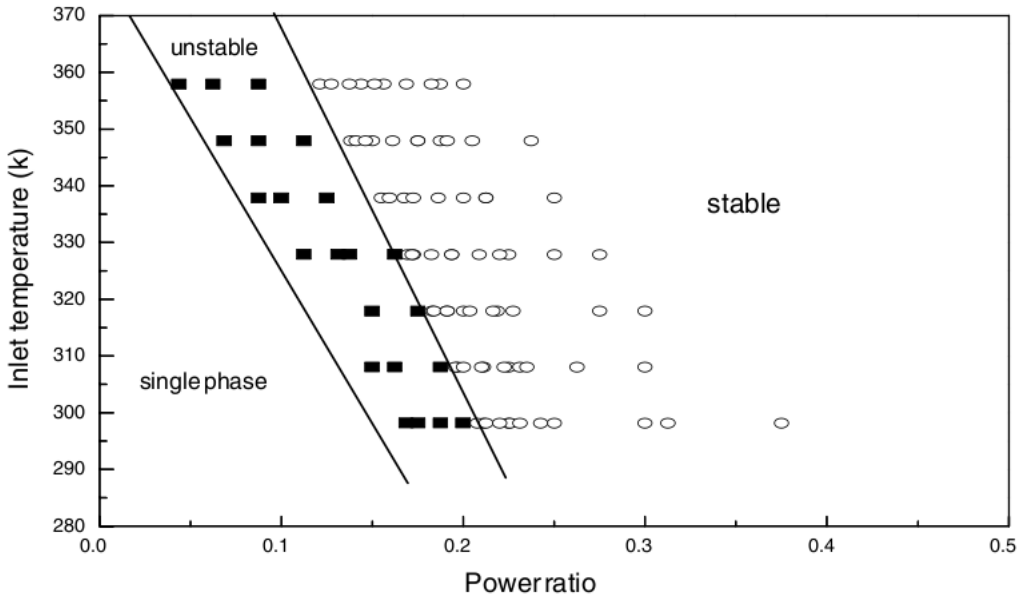

Figure 2.7: Stability map of CARR, inlet temperature vs power ratio (Yun, 2004)

Chapter 3

Scaling

To preserve key thermal hydraulic behavior and phenomena, a set of scaling laws were developed for system level integral performance, with another set of laws for single and two-phase criteria specific to the operation of the water storage tank. Each level of scaling serves a purpose that supports the broader scaling scope, with system scaling preserving key performance behavior such as temperature rise, system mass flow rates, etc. with respect to a given geometry. Water storage tank scaling preserve the baseline emptying, or depletion of system inventory, while ensuring good mixing and heat transfer from the working fluid to the ultimate heat sink. A detailed analysis follows.

3.1 Integral (Top Down) Scaling

Integral scaling of system level behavior and phenomena has been well documented by similar experimental facilities, in particular the Natural Shutdown Test Facility (NSTF) at ANL (Tzanos, 2006). Their scaling analysis was performed on generic information of the RCCS design for a PBMR. The first and foremost difference between the full scale and experimental scale is the reduced axial length scale, l_R, with all subsequent scaling laws affected by this parameter. We have chosen to preserve the temperatures between scales, as well as use water as our working fluid. Finally, the transient behavior of the RCCS under accident conditions will likely be quasi-steady in behavior, thus we hope to account for the overall accident timing. Similarity relationships, Eq. 3.1, will be noted in ratios of model parameters to prototype parameters, where model designates the experimental facility, and prototype designates the concept facility.

$$\Psi_R = \frac{\Psi_{model}}{\Psi_{prototype}} = \frac{\Psi_m}{\Psi_p} \tag{3.1}$$

The total heat transferred to the riser tubes during normal operation is the sum of the radiative and convective heat flux imposed on the riser tube walls and cooling panels inside the cavity.

$$Q = A\ h_{cavity}(T_{RPV} - T_{riser}) + A\ \epsilon\ \sigma_B({T_{RPV}}^4 - {T_{riser}}^4) \tag{3.2}$$

At steady state, this equals the total heat transferred to the water along the riser tubes

$$Q_o = A_o U_o \rho_o C_p (T_{out} - T_{in}) \tag{3.3}$$

Taking the heated section as a reference point, the total temperature rise along the heated section is a rearrangement of Eq. 3.4.

$$\Delta T_o = \frac{Q_o}{U_o A_o \rho_o C_p} \tag{3.4}$$

Assuming constant thermal properties, the similarity relationship for the temperature rise along the heat section section in given by Eq.3.5

$$\Delta T_{oR} = \frac{Q_R}{U_{oR} A_{oR}} \tag{3.5}$$

The non-dimensional Froude number desires a unity similarity relationship.

$$N_{fr} = \frac{{U_o}^2}{gL_r} = \frac{\rho_f}{\Delta\rho} = 1 \tag{3.6}$$

Assuming similar thermodynamic reference values, this reduces to the similarity relationship for a reference velocity, Eq.3.7.

$$U_{oR} = \sqrt{l_R} \tag{3.7}$$

The time ratio number also requires a similarity relationship of 1.

$$T_R{}^* = \frac{L_{hR}}{U_{oR}\delta_{ir}{}^2} = 1 \tag{3.8}$$

Scaling a reference thickness to the length scaling,, this reduces to the similarity relationship for the time ratio, Eq.3.9

$$T_R{}^* = \frac{l_R}{U_{oR}} = \sqrt{l_R} \tag{3.9}$$

The Richardson number, the dimensionless group that expresses the ratio of potential to kinetic energy, is given in Eq. 3.10 With previous similarity requirements, this is automatically satisfied.

$$Ri_R = \frac{g\ h}{u^2} = 1 \tag{3.10}$$

Inserting the velocity relationship, Eq.3.7. into the temperature rise similarity, Eq.3.5, and assuming a 1:1 radial scaling, a similarity group for the temperature rise can be found.

$$\Delta T_{oR} = \frac{Q_R}{U_{oR}A_{oR}} = 1 \tag{3.11}$$

A similarity relationship for the total power, Eq.3.12. and heat flux Eq.3.14. can then be found from the power and heat flux relationship, where W is the width (radial) and L is the height (axial scaling).

$$Q_r = U_{oR} = \sqrt{l_R} \tag{3.12}$$

$$Q = q^{''}\ W\ L \tag{3.13}$$

$$q^{''}{}_R = \frac{1}{sqrtl_R} \tag{3.14}$$

A summary of all the similarity groups and their values for the 1/4 and 1/6 length scaling are given in Table 3.1.

Table 3.1: Similarity relationship summary for system level scaling

Parameter	**Ratio**	**Values for length scale, l_R**	
-	-	$l_R = 0.25$	$l_R = 0.33$
Radial	A_{oR}	1	1
Axial	l_R	0.25	0.33
Q	$\sqrt{l_R}$	0.50	0.41
q"	${l_R}^{-0.5}$	2.00	2.45
Re	$\sqrt{l_R}$	0.50	0.41
U	$\sqrt{l_R}$	0.50	0.41
Δ T	1	1	1

3.2 Water Storage Tank

To begin the scaling analysis of the water storage tank, a baseline criteria will first be set on a system level basis. Following conservation of mass laws inside the tank, the following must hold.

$$\rho A_t \frac{dH_w}{dt} = \rho A_{out} U_o \tag{3.15}$$

For $H_w = h_w H_t$, where H_t is the water height in the tank at steady state conditions, the non-dimensional form of Eq. 3.15. is given in Eq. 3.16, where u_o is the tank outlet velocity and is only a function of the static hydraulic head.

$$\frac{dh_w}{d\tau} = \frac{A_{out} L_R}{A_t H_t} u_o \tag{3.16}$$

The similarity conditions for the mass and energy equations in the tank require Eq.3.17 to hold.

$$\left(\frac{A_{out} L_R}{A_t H_t}\right)_R = \left(\frac{A_{out} L_R}{V}\right)_R = 1 \tag{3.17}$$

For system wide scaling criteria of 1/4 height scale and 1:1 area scale, the volume of the

model tank scales as 1/4 that of the prototype.

$$V_R = l_R = 0.25 \tag{3.18}$$

Consisting of 227 tubes, the full scale prototype employs 8 water storage tanks to provide the required cooling inventory. Thus, the tank must also be scaled for the reduced inventory of 3 riser tubes and single water tank that will be used for the experimental facility. The volume of the experimental tank will then be scaled a 2nd time by conservation of mass and volume inventory ratios, Eq.3.19

$$\left(\frac{M_m}{V_m}\right)_m = \left(\frac{M_p}{V_p}\right)_p \tag{3.19}$$

Inventory ratios requires a new volume that is 0.105 times smaller than the full scale. This double wise scaling will be the basis for height and diameter dimensional search.

3.2.1 Single Phase Condensation

When a jet discharges into a bulk water volume, steam begins condenses shortly after entering the tank, and a heated turbulent jet continues to move towards the tank walls, eventually forming a buoyant bubble when all its momentum has been lost, Figure 3.1. At single phase conditions, the penetration length is simply that of the impinging jet, L_{min}. During two phase conditions, the penetration lengths vary between L_{min} and L_{max} due to incoming steam chugging and bubble cavities. During both conditions, the deepest penetration length is that of the bubble, L_b.During single phase conditions, there exists a penetration length of the jet created by the momentum of the injected fluid (Wang, 2010) This momentum penetration depth will be examined for its relative size to the bulk water storage tank.

$$\frac{L_j}{d_s} = 10.86\ Fr^{0.39} \left(\frac{H_o}{D_t}\right)^{-0.17} \left(\frac{u}{u_{mf}}\right)^{-0.11} (Re_f)^{-0.03} \tag{3.20}$$

where $Fr = \frac{\rho_g}{\rho_f - \rho_g} \frac{u^2{}_s}{g d_s}$ and $Re_f = \frac{d_p \rho_g u_s}{\mu}$

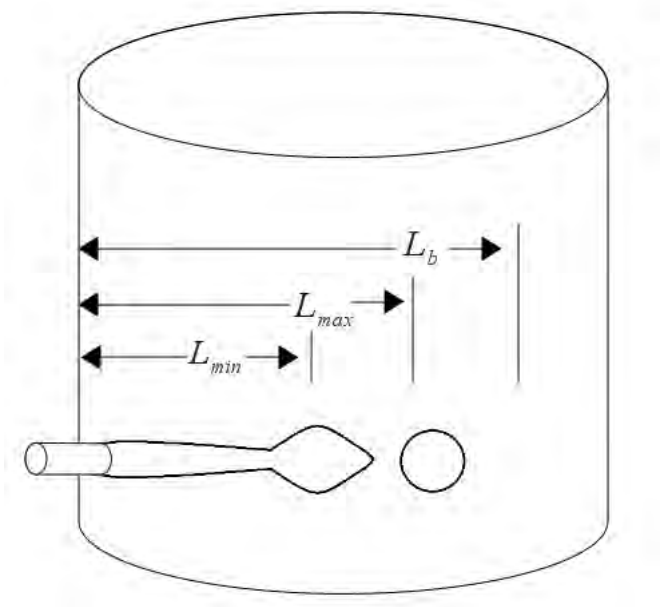

Figure 3.1: Penetration length for a jet into a stagnant body of water

There also exists a condensation penetration length (Liang, 1991), yielding a characteristic cavity length where condensation occurs before its rise up through the water tank from buoyancy forces.

$$\frac{2L_c}{dj} = \frac{1}{1.932} \frac{h_{fg}}{c_p \Delta T_{sub}} M^{0.5} \tag{3.21}$$

Jet penetration lengths were calculated for the full size prototype tank inlet geometry, velocity, and temperature. Both lengths proved to be insignificant when compared to the total diameter of the storage tank, on average of under 4 percent, and hence was assumed to be negligible in the scaling criteria search.

After the jet has lost its momentum, a transition to a buoyant plume occurs. During single phase, this buoyant plum will continue to condense. Ishii et al (1998) developed criteria for scaling of condensation phenomena in a suppression pool, with essential parameters a function of total interfacial area and vapor volumetric flow. The condensation potential of

the suppression pool and the vapor latent heat energy flux are given below.

$$\dot{Q}_c = a_i h_{cond}(T_{sat} - T_{pool}) \tag{3.22}$$

$$E_g = \rho_g Q_g h_{fg} \tag{3.23}$$

It was assumed that the condensation heat transfer coefficient and enthalpy will be similar for both designs, and thus a similarity relationship can be found

$$\left(\frac{\dot{Q}_c}{E_g}\right)_R = \frac{a_{iR}}{Q_{gR}} = 1 \tag{3.24}$$

The total bubble interfacial area is given in terms of the number of sparger holes, the number and diameter of the bubbles, n, N, and D_b, respectively.

$$a_i = \pi n N D^2{}_b \tag{3.25}$$

With a defined bubble frequency and geometric parameters of the tank and a prototypic bubble, Eq.3.26 can be reduced.

$$\left(\frac{\dot{Q}_c}{E_g}\right)_R = \frac{H_t}{(u_b)_R (D_b)_R} \tag{3.26}$$

And ultimately a similarity parameter for the scaling of sparger hole count inside the jet tube, Eq.3.27

$$n_R = Q_{gR}\ l_R{}^{-1.67} \tag{3.27}$$

Thus to match condensation areas and rates during single phase operation, the sparger holes inside the tank inlet can be modified to account for the reduced pool volume.

3.2.2 Two-Phase Bubble Transport

At tank saturation, the primary criterion for scaling now turns to the bubble rise time. At saturation, condensation is severely reduced to nearly negligible levels, and the buoyant plume rises to the surface where steam pockets are ultimately vented into the atmosphere. The rise time for the bubbles to reach the surface is of particular interest. 4 primary time constants will be presented and combined into a similarity relationship.

1. The transport time of the jet

$$\tau_{Jt} = \frac{n_j \pi / 4 d_j^2 H}{Q_o} \tag{3.28}$$

2. The jet entrainment constant, where α_T is Taylors jet entrainment constant

$$\tau_{Je} = \frac{n_j \pi / 4 d_j^3}{4\sqrt{2}\alpha_T Q_o} \tag{3.29}$$

3. The transport time of the surrounding fluid

$$\tau_{st} = \frac{V}{Q_o} \tag{3.30}$$

4. The entrainment time of the surrounding fluid

$$\tau_{se} = \frac{V}{n_j u \pi d_j H} \tag{3.31}$$

Peterson et al. (1998) choose to form a similarity group with the transport time and entrainment constant for the jet.

$$\pi_j = \frac{\tau_{Jt}}{\tau_{Je}} = 4\sqrt{2}\alpha_T \frac{H}{d_j} \tag{3.32}$$

And a similarity group for the transport time of the jet with respect to the transport time of the surrounding fluid.

$$\pi_s = \frac{\tau_{Jt}}{\tau_{st}} = \frac{n_j \pi / 4 d_j^2 H}{V} \tag{3.33}$$

Preservation of π_j requires $d_j/H = 1$, yielding a relationship for the number of jets for a given aspect ratio of tank.

$$n_{JR} = \frac{1}{(H/D)_R^2} \tag{3.34}$$

Thus, to match scaling criteria of bubble rise time during two phase, saturated conditions, the aspect ratio of the tank must be scaled to the number of jets.

3.3 Combined Scaling

The number of jets during two phase operation was picked to equal unity for the experimental facility to match the prototype, and hence the aspect ratio of the tank was scaled 1:1. Unable to scale the tank to satisfy both single and two phase conditions, the primary criterion was determined to be maintaining the aspect ratio to preserve buoyant plume rise times during tank saturation with a single jet. While investigating transients during single phase heat up, a sparger plate can be placed over the tank inlet to maintain condensation rate scaling. This removable orifice plate will be placed directly at the inlet to the water tank from the riser headers.

Simple algebraic manipulation yields the dimensions of the required scaled tank, given the previous requirements of volume and inventory scaling. This tank dimension will be true during 1/4 scale experiments, and will be skewed during the 1/6 experiments, with considerations made during the post experimental data reduction and analysis process. Table 3.2 gives a final summary of the scaling parameters, with details of the dimensions for the full and scaled water storage tanks.

Table 3.2: Summary of scaling, with details of water storage tank

Power	***Concept Full Scale***	***Concept 1/4 Scale***	***UW 1/4 Facility***
Full scale power	350 MW	175 MW	9.91 kW
Passive decay power	1.5 MW	0.75 MW	4.63 kW
Vessel peak heat flux	3 - 7 kW/m^2	6 - 14 kW/m^2	25 kW/m^2
Ducting	***Concept Full Scale***	***Concept 1/4 Scale***	***UW 1/4 Facility***
Total count	x227	x227	x3
Length	19.2 m	4.8 m	5.0 m
Tube Diameter	6 cm	6 cm	6 cm
Water Tank	***Concept Full Scale***	***Concept 1/4 Scale***	***UW 1/4 Facility***
Total count	x8	x8	x1
Height x Diameter	5.49 x 2.74 m	3.46 x 1.73 m	1.83 x 0.92 m
L/D	2	2	2
Volume	32.42 m^3	8.09 m^3	1.2 m^3
Total Inventory	260,000 L	65,000 L	1,200 L

Chapter 4

CFD Simulations

CFD modeling and simulation of phenomena related to the RCCS behavior were performed by both the University of Idaho and the University of Wisconsin team. A series of benchmark, 2D, and 3D simulations were run, with a primary objective to develop a physical sense of the anticipated natural convective flow with conduction and radiation heat transfer taking part, via simulations and as an aid in a coarse set-up to used to locally test instrumentation.

4.1 2D Benchmark

Prior to experimentation, and before attempting to simulate the RCCS on a larger scale, 2-dimensional benchmark simulations were performed to assess FLUENTs natural convection and radiation modeling capabilities. The same geometry was used for each of these benchmark tests in order to create a consistent basis for comparisons to be developed.

For these benchmark tests, three simulations were run. First, a natural convection simulation without radiation was analyzed where the uniform temperature hot wall of the air cavity was 50 °C warmer than the uniform temperature cold wall, meaning the hot fluid was set to a constant value of 50 °C, and the cold fluid was set to 0 °C. Second, a natural convection with radiation simulation with the same attributes as the first was run to see how the addition of radiation from the hot wall to the cold wall affected the heat transfer. Third, instead of a temperature difference, the previously "hot" wall was now assigned a heat flux into the air cavity, and the "cold" wall was assigned a heat flux out of the air cavity. Here, radiation was present within the cavity as well. This simulation would best show FLUENTs capabilities for our future CFD needs because it most accurately depicted the boundary condition settings and inputs for modeling of the RCCS. Figure 4.1 shows a

sample overview of one simulation, Benchmark #2.

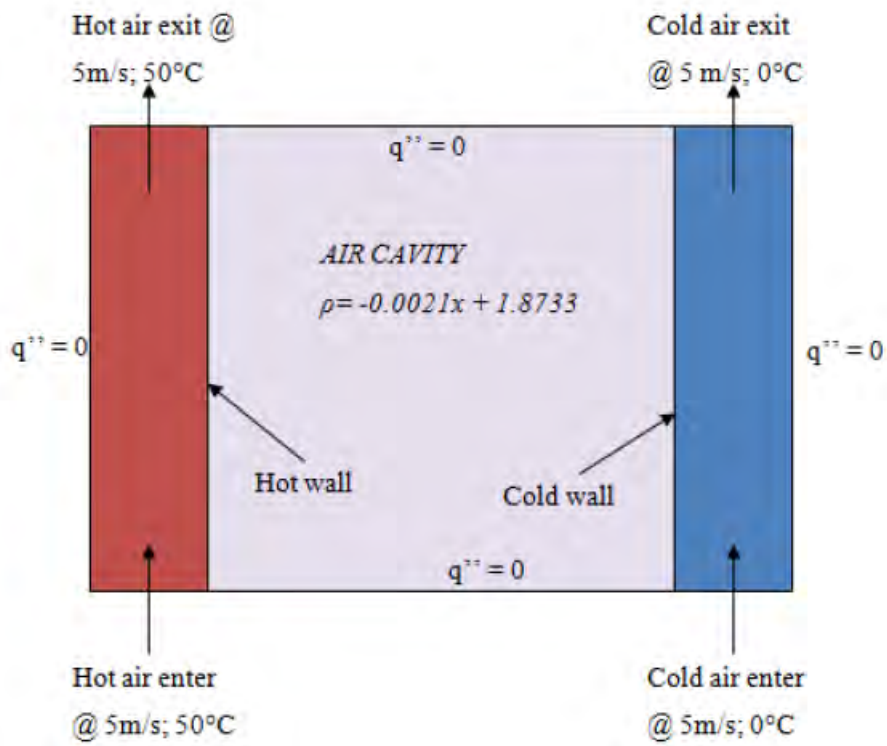

Figure 4.1: Boundary condition overview for Benchmark #2

4.1.1 CFD Methods and Models

For the computational component of this the 2D benchmark simulations, FLUENT version 6.2.16 was used, along with its accompanying meshing software, GAMBIT version 2.2.30. It was only intended for this researcher to become a competent user of these programs to run the necessary simulations; it was not imperative to become experienced and skilled in all facets of the programs. General procedures followed when performing simulations using these programs are summarized below.

Creating a mesh for an object begins with creating the object itself. Using GAMBIT, one begins by generating vertices, and then connecting those vertices with straight lines or arcs. After a wireframe model for the desired geometry has been produced, volumes are then defined to separate solids from fluids, and to classify what material each volume consists of.

Following volume generation, meshing can be completed. An object can be meshed in a number of ways. First, and perhaps most simply, a mesh interval size can be assigned for a volume, which produces an even mesh throughout the whole volume. Another method is to make the mesh finer near walls and larger in the center of volumes in an attempt to better analyze the phenomena happening near walls while not having too many mesh points to still be able to solve with limited computing power. Both of these methods were used at times for different CFD calculations discussed in this chapter, but limited computational resources restricted the maximum number of mesh nodes that could be used, so geometries typically had to suffer in mesh count near walls. Some things did not change about the mesh no matter if the mesh was consistent through the volume, or variable size. First, Tet/Hybrid elements were used for all three-dimensional meshes because they offer the most dynamic shapes to fit into the most unnatural volumes. Tet/Hybrid elements consist of mainly tetrahedral cells, but may also include hexahedral, pyramidal, and wedge elements where appropriate (Fluent, Inc., 2000). For all meshes created for this work, no matter what interval size was chosen, it was important to ensure that no elements were highly skewed, meaning none were above 0.98 on the distortion scale from 0 to 1. To even more confidently ensure that the mesh would be able to be solved successfully in FLUENT, it was decided that for this thesis study, no element should have a skew value higher than 0.9 on this same scale. This is important because the existence of highly skewed elements within a mesh has been known to produce a challenging simulation, and perhaps an inability to converge on a solution all together. After the mesh was successfully created, it was exported to FLUENT where boundary conditions and material properties could be added, and a solution could be found to the problem at hand.

FLUENT version 6.2.16 was the software used to perform all CFD simulations during this thesis research. The general boundary conditions, material inputs, and solving methods for all simulations discussed in this thesis were developed from the references noted previous, and adapted to best fit our specific problems. The standard k-ω turbulence and Discrete Or-

dinates radiation models were chosen, along with temperature dependent material properties for air and water.

4.1.2 Benchmark Results

Results will be examined for their agreement with expected physical phenomena and conformity to an analytical calculation for verification of truly buoyancy-driven natural circulation flow in the air cavity using dimensionless Nusselt and Rayleigh numbers of flow near the geometrys hot wall. They will also be compared to one another to explore the changes in heat transfer modes between their boundary condition configurations.

Benchmark #1

Benchmark test #1, with one hot wall and one cold wall and no radiation model, produced temperature and velocity profiles that look as they were physically expected to. The temperature distribution in the air cavity can be seen in Figure 4.2, and the velocity profile can be seen in Figure 4.3. The temperature distribution within the air cavity is as expected, showing thermal stratification, meaning the air is hotter at the top of the cavity, and cooler at the bottom. The velocity profile, showing the air circulating upwards along the hot wall as it warms, and traveling downwards along the cold wall as it cools, and leaving the air in the center of the cavity practically motionless was also expected. Moreover, the velocity magnitude along the hot vertical wall of the enclosure is verified to within the correct order of magnitude by using Eq. 4.1 (Bejan, 2004). In this equation, α is the fluids thermal diffusivity, H is the height along the vertical hot wall, Ra_H is the Rayleigh number at height H, and Pr is the fluid's Prandtl number.

$$v = \frac{\alpha}{H} {Ra_H}^{1/2} \tag{4.1}$$

This equation for velocity, U of low-Pr fluids returns a maximum velocity along the hot wall of approximately 5.3 cm/s, while the plot generated by FLUENT suggests a maximum velocity of approximately 7.5 cm/s. This order of magnitude agreement is well within reason

for this benchmark simulation development.

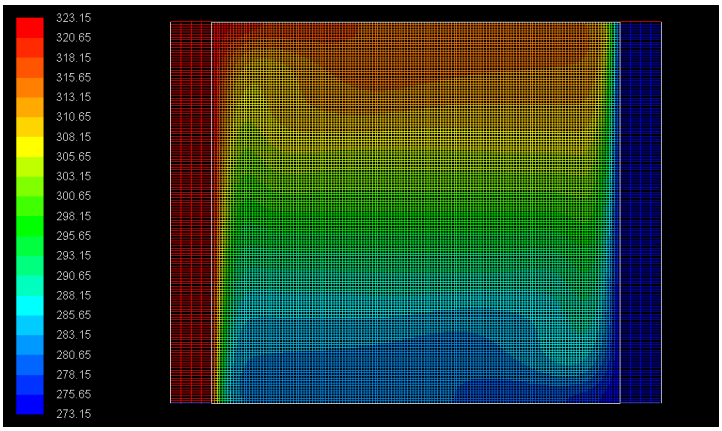

Figure 4.2: Temperature [K] profile for Benchmark #1

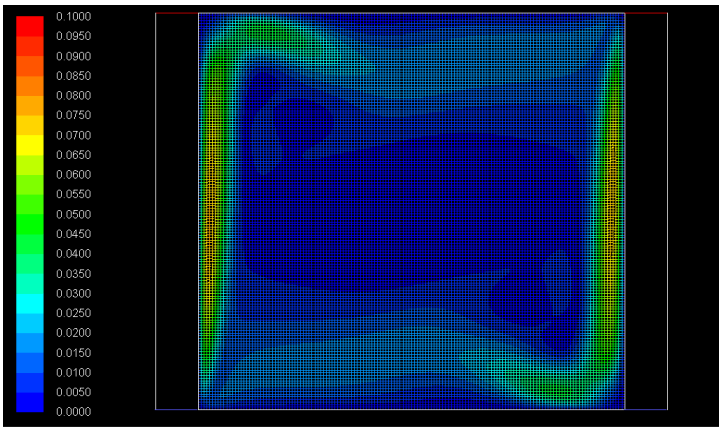

Figure 4.3: Velocity [m/s] profile for Benchmark #1

Benchmark #2

For the second benchmark test, radiation was added. The resulting temperature and velocity plots follow the same physical agreement as the first benchmark test. These temperature and velocity plots are depicted in Figures 4.4 and 4.5, respectively.

To compare the first two benchmark simulations, three horizontal lines were drawn across the two air cavities and temperatures were examined along those lines. One line was near the bottom of the cavity, one near the top, and one right in the middle. Along the top line,

it was found that with radiation present, the top of the cavity was on average 1.3% cooler. Along the bottom line, it was found that with radiation present, the bottom of the cavity was on average 1.8% warmer. The mid-height of the cavity proved to be 0.2% warmer with radiation present. From this analysis, it can be said that the presence of radiation allows for the heat in a closed cavity to be spread out slightly more than it is without radiation. The resulting increase in temperature at the bottom of the cavity, and decrease in temperature at the top of the cavity agrees with findings by Jaballah, Sammouda, Belghith (2007).

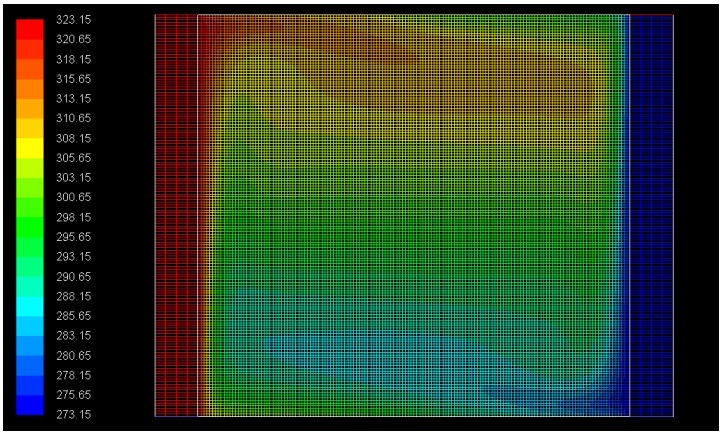

Figure 4.4: Temperature [K] profile for Benchmark #2

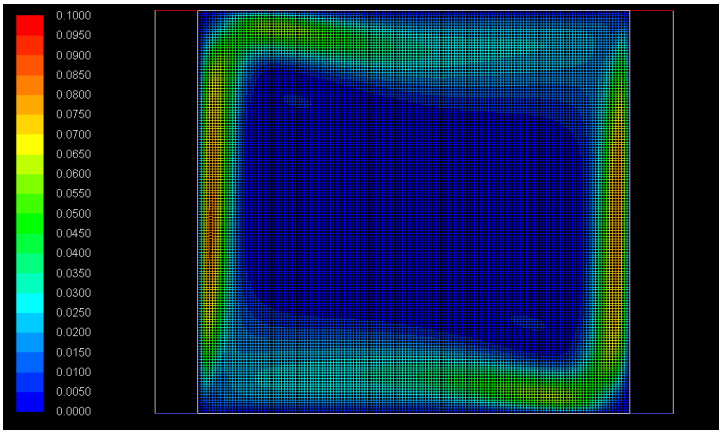

Figure 4.5: Velocity [m/s] profile for Benchmark #2

Benchmark #3

The third benchmark test employed a positive heat flux boundary condition into the air cavity instead of a constant temperature hot wall, and a negative heat flux boundary condition to remove heat from the air cavity instead of a constant temperature cold wall. Again, the resulting temperature and velocity profiles matched the physical expectations. They can be seen in Figures 4.6 and 4.7.

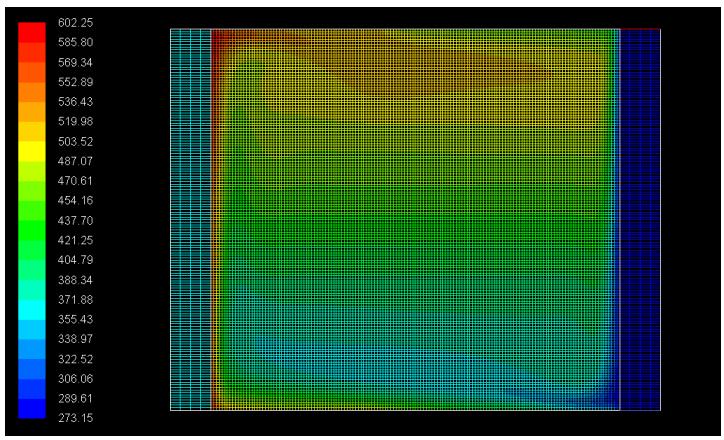

Figure 4.6: Temperature [K] profile for Benchmark #3

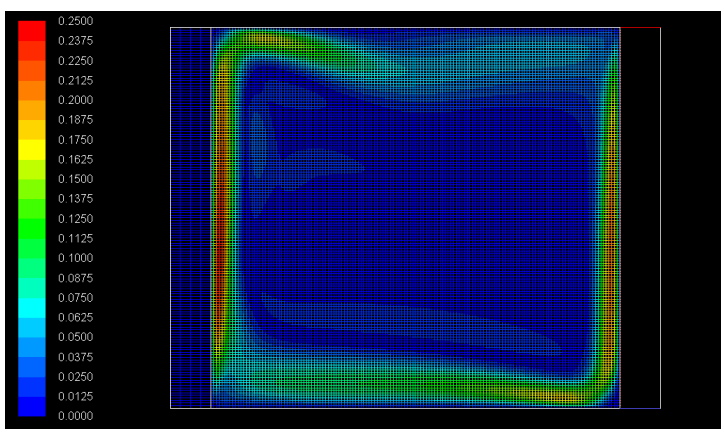

Figure 4.7: Velocity [m/s] profile for Benchmark #3

With a very large input heat flux of 5000 W/m2, comparing this simulation to Benchmark 1 and Benchmark 2 based on wall temperatures is not acceptable since heat transfer is much

higher here and thus, cavity temperatures are higher as well. Instead, comparisons were made between Benchmark 2 and Benchmark 3 using percentage values to determine the change in fractional heat transfer modes from the hot side to the cold side of the cavity. These results are depicted in Table 4.1

Table 4.1: Comparison of Benchmark #2, #3 for heat transfer modes

	Benchmark #2	Benchmark #3
Heat Transferred from hot wall	3.31 W	50.00 W
% Radiation	61.93%	80.49%
% Convection	38.07%	19.51%
Heat Transferred to cold wall	3.31 W	50.00 W
% Radiation	59.05%	71.92%
% Convection	40.05%	28.08%

From these results it is concluded that the percentage of heat transfer modes may change based on boundary conditions. When a heat flux boundary condition was used, the percentage of radiant heat transferred from the hot surface and to the cold surface increased. This can be attributed to the increased temperature on the hot wall from Benchmark #2 to Benchmark #3, because with increased temperature, radiative heat transfer increases as a function of the wall temperature to the 4th power.

4.2 Variable Cavity Height

A model was assembled that depicts a small wedge of the reactor cavity including the wall of the reactor vessel and one half of one riser tube filled with water, with fin connected. The cross section geometry of the reactor and surrounding cavity for this set of simulations was determined from the dimensions of the GA-MHTGR, provided by General Atomics (GA) as the reference design, and is depicted in Figure 4.8 below (Preliminary Safety Information Document for the Standard MHTGR, 1992). The geometry was simplified to basic circles from the true design for ease of modeling. Simulations at varying cavity heights between two and 22 feet were run using the wedge geometry for a pitch to diameter ratio of 5, with

additional simulations investigating P/D ratios of 2 and 4. Pitch-to-diameter ratio (P/D) is the ratio of the distance between riser tube centerlines to the outer diameter of one riser tube. Thus, examining the effects of a single tank failure that causes the spacing of riser tubes to change from P/D=2 to P/D=4 is of interest under postulated accident scenarios, and is described in this section. Simulations were run at 2' (0.61 m), 4' (1.22 m), 6' (1.8 3m), 8' (2.44 m), 10' (3.05 m), 12' (3.66 m), and 22' (6.71 m) high cavities. FLUENT version 6.2.16 was again used for this study. The interest of these simulations was to examine the change, if any, in heat transfer modes from the reactor vessel to the RCCS fin and tube, and the general air and water flow characteristics in the cavity and riser, respectively, when the height of the cavity is changed.

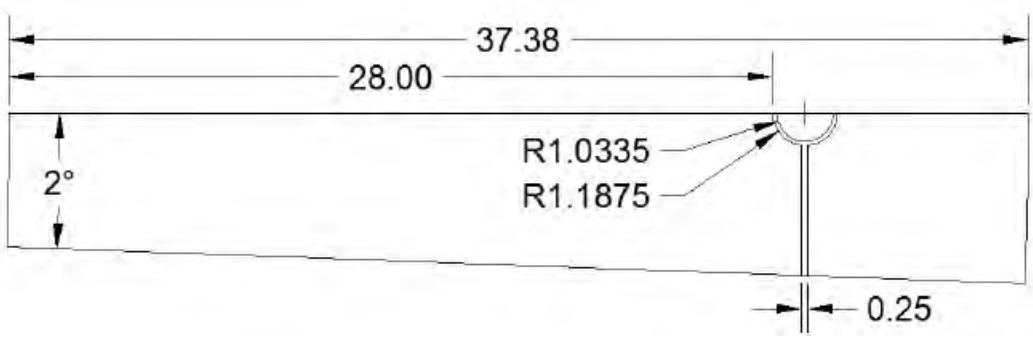

Figure 4.8: Pitch/Diameter = 5. Cross Section of RCCS in Wedge of Reactor Cavity, with Dimensions, inches

These simulations were performed with a water mass flow inlet of 0.11 kg/s and temperature inlet of 373K (99.85 °C) at the bottom of the riser, and a pressure outlet boundary condition at the top of the riser. The mass flow rate was determined from the assumed scenario in which water would flow collectively through the 227 riser tubes of the entire RCCS system at 25 kg/s.

In this ideal scenario, the top and bottom boundaries of both the front and rear air cavities were assumed to be adiabatic, as well as the outside cavity wall. Since this geometry is assumed to be a "wedge" of the reactor cavity surrounding the reactor vessel, all side walls were assigned to act as symmetry boundaries. Further, a boundary condition heat flux of

5230 W/m2 was radiated from the reactor vessel wall to correspond closely with the 1.5 MW accident scenario heat given off by the reactor vessel. This was also a design expectation provided by GA. This imposed heat flux boundary condition is not exact to the anticipated scenario. In the envisioned functioning reactor, the heat flux given off by the reactor vessel is not evenly spread out along its surface, but rather, would be better described by an axial temperature profile with the vessel being hottest near its mid-height (350 °C), and relatively cooler at the top and bottom, effectively resembling a vertical cosine shape. For the purpose of the simulations performed for this research, assigning a constant heat flux boundary condition at the reactor wall was determined efficient because the constant heat flux boundary condition is easier to create in experiments than a detailed temperature distribution, and it was important to create consistency between simulations and experiments. Figure 4.9 shows the general wedge used, labeling all prominent features, while Table 4.2 summarizes the boundary conditions imposed on the different faces. The boundary conditions in Table 4.2 are common for all wedge simulations described in this chapter.

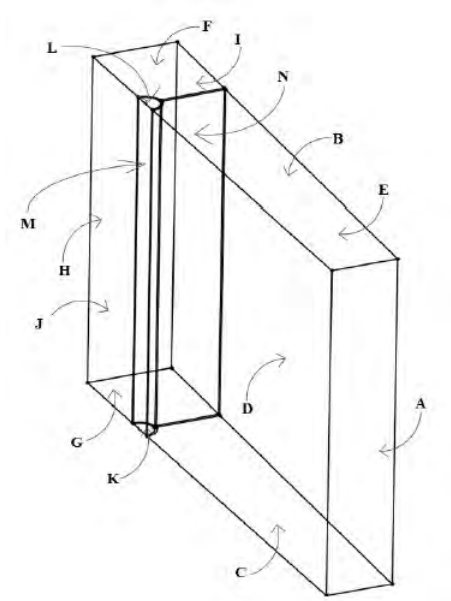

Figure 4.9: Three-dimensional wedge representation with labels for BC

The standard k-ω turbulence model was used again because of its effectiveness in sim-

Table 4.2: Names of Faces for reference on Figure 4.9 and Boundary Conditions

Label	Name	Boundary Condition
A	Reactor Vessel Wall	Wall, heat flux = 5230 W/m^2
B	Front air cavity top	Wall, heat flux = 0 W/m^2
C	Front air cavity bottom	Wall, heat flux = 0 W/m^2
D	Front air cavity left	Symmetry
E	Front air cavity right	Symmetry
F	Rear air cavity top	Wall, heat flux = 0 W/m^2
G	Rear air cavity bottom	Wall, heat flux = 0 W/m^2
H	Rear air cavity left	Symmetry
I	Rear air cavity right	Symmetry
J	Outside containment wall	Wall, heat flux = 0 W/m^2
K	Water in tube inlet	Mass flow inlet
L	Water in tube outlet	Pressure outlet
M	Water in tube side	Symmetry
N	Steel fin and tube assembly	Wall, emissivity = 0.7

ulating natural convective flow within the benchmark simulations. The fin and riser tube components of these simulations were treated as steel, while the water in the riser tube and the air in the front and rear cavities were assigned temperature-dependent-density polynomial functions.

4.2.1 P/D = 5 Results

Results from the P/D=5 variable cavity height simulations are summarized below in Table 4.3. From this table, fractional contributions of radiation, convection, and conduction heat transfer modes are seen to vary only slightly as cavity height increases.

Radiation dominates in all height scenarios, providing 85-90% of the heat entering the air cavity. Radiation also dominates accounting for 82-88% of the heat transferred to the front face of the RCCS fin and tube. From this, it is clear that radiation is the primary mode of heat transfer from the reactor vessel to the RCCS, dominating over natural convection. This conclusion agrees with the conclusion made by Charmeau et al. (2009) who noted that natural convection accounts for less than 25% of the total heat transfer. In looking at how the heat reaches the water in the riser tubes, conduction from the fin plays the largest

Table 4.3: P/D = 5 Results for each height configuration

	2ft	8ft	12ft	22ft
Heat flux from RPV [assigned] (W/m2)	5230	5230	5230	5230
Inlet water temp [assigned] (K)	373.13	373.12	373.12	373.11
Inlet water flow [assigned] (kg/s)	0.11	0.11	0.11	0.11
Inlet water velocity Z (m/s)	0.09	0.09	0.09	0.09
Outlet water temp (K)	375.44	378.12	379.86	384.20
Outlet water velocity Z (m/s)	0.10	0.10	0.10	0.10
Water Temp. Increase (K)	2.31	5.00	6.74	11.08
Heat flux on tube front (W/m2)	5426.23	5532.26	5513.73	5540.82
Heat flux on fin front (W/m2)	3316.14	3328.14	3334.35	3332.58

Table 4.4: P/D = 5, results for each height configuration

	2'	6'	10'	22'
Applied Heat Flux from Reactor Vessel (W/m2)	5230	5230	5230	5230
Heat Transfer from Reactor Vessel (W)	395	1185	1975	4346
%radiation	87.70%	88.20%	88.40%	88.80%
%convection	12.30%	11.80%	11.60%	11.20%
Heat Transfer to front of fin (W)	248	738	1226	2702
%of Total	62.70%	62.20%	62.10%	62.20%
%radiation	85.40%	89.80%	91.10%	92.30%
%convection	14.60%	10.20%	8.90%	7.70%
Heat Transfer to front of tube (W)	147	448	745	1642
%of Total	37.30%	37.80%	37.70%	37.80%
%radiation	75.90%	78.60%	79.50%	81.10%
%convection	24.10%	21.40%	20.50%	18.90%
Heat Conducted From Fin to Tube (W)	201	597	991	2180
Radiation Contribution % to RCCS	81.90%	85.60%	86.50%	88.00%
Convection Contribution % to RCCS	18.10%	14.40%	13.50%	12.00%
Conduction Contribution % (from fin to tube)	51.00%	50.40%	50.30%	50.20%

role. It accounts for, on average, 50.4% of the energy reaching the water. Radiation and convection on the riser tube face make up the remaining 49.6% with radiation contributing, on average, 37.7% and convection contributing, on average, 11.9%. From these results, it would be expected that full height simulations of the RCCS at this pitch configuration would show an even higher contribution by radiation within the air cavity, but retain conduction from the fin to tube as the major mode of heat transfer to the water.

4.2.2 P/D = 2,4 Results

Results from the P/D=2 and P/D=4 simulations are summarized Table **??**. Similar to the previous simulations discussed, radiation dominates in the air cavity from the reactor vessel, accounting for 80-84% of the heat entering the system. Radiation also dominates over convection on the front face of the RCCS assembly accounting for 79-83% of the heat transfer there.

Table 4.5: P/D=2 and P/D=4 Results for each pitch configuration, 22' cavity height

	P/D=2	P/D=4
Applied Heat Flux from Reactor Vessel (W/m2)	5230	5230
Heat Transfer from Reactor Vessel (W)	1738	3476
% radiation	80.10%	84.30%
% convection	19.90%	15.70%
Heat Transfer to front of fin (W)	658	2096
% of Total	37.80%	60.30%
% radiation	83.60%	88.80%
% convection	16.40%	11.20%
Heat Transfer to front of tube (W)	1069	1379
% of Total	61.50%	39.70%
% radiation	76.20%	74.70%
% convection	23.80%	25.30%
Heat Conducted From Fin to Tube (W)	638	1850
Radiation Contribution % to RCCS	78.50%	83.20%
Convection Contribution % to RCCS	21.50%	16.80%
Conduction Contribution % (from fin to tube)	37.00%	53.20%

The differences between the two simulated geometries begin when looking at the percentage of heat transferred to the fin versus the tube from the air cavity. For the P/D=4 geometry, where the fin has a much larger surface area than the tube, the majority of the heat is transferred to the fin rather than the riser tube, wherein for the P/D=2 case when the fin has less surface area than the riser tube, just the opposite is true, more heat is transferred to the tube. This proves what was expected, that as the risers become further spaced apart, and the size of the fin increases, the RCCS modes of heat removal will become dominated more and more by radiation to the fin, and subsequently, conduction through the fin to the water. Additionally, since for the P/D=4 case, 60% of the heat is transferred to the fin, it is logical that conduction serves as a greater contributor to the heat transfer to the water than for the P/D=2 case.

Chapter 5

RELAP5-3D Model

System modeling of the RCCS experiment was performed with RELAP5-3D, a thermal-hydraulics analysis code written by Idaho National Laboratory (INL) for the Nuclear Regulatory Commission (NRC). Originally designed for modeling light water reactor transients, this tool proves extremely powerful in a broad range of thermal-hydraulic applications. The primary objective of employing the use of RELAP5-3D is to render the behavior of the RCCS system as it transitions to two-phase flow in a natural circulation mode. This model can be verified with external calculations and experiments, and once verified can work in concert with an experimental facility.

A model was constructed in RELAP5-3D of the reactor scale system. This model contains one-eighth of the entire RCCS, with looped boundary conditions to represent the effects of the rest of the system. A loss of reactor coolant flow accident was modeled, assuming a failure of active RCCS cooling and pumping. It was found that the results became extremely unstable when the system transitioned to two-phase flow.

In examining the results in the unstable region, it was found that the system choked flow models had a significant effect on the stability of the results. Cases were run with the default choked flow model, as well as an alternate model. Idaho National Laboratory (INL) modeling guidelines suggest that in regions of low pressure, choking is disabled at all junctions that do not have an area change, and cases were run using these modifications with both choking models.

Using the more stable choked flow model, the system pressure, heat load, unheated piping length, and heated length were varied to determine the sensitivity of the system behavior to those properties.

5.1 Tool Overview

RELAP5-3D is a FORTRAN 77-based code designed to model light water reactor transients with focus on thermal hydraulic effects. The code is sufficiently generic and detailed to model one-dimensional fluid and thermal transients of any kind. It was developed at Idaho National Laboratory as a successor code to RELAP5-MOD3 in 1999. The current version is 2.4.3, with the beta version of 3.0.0 released which converts to FORTRAN 90. All simulations performed in this work have been done with version 2.3.6. (INL, 2005)

5.1.1 Input Structure

A model in RELAP5 is chiefly composed of hydrodynamic control volumes and solid heat structures. The hydrodynamic control volumes are connected by junctions to facilitate fluid flow. Volumes are independent of their containers, no physical component is necessary to be defined. Multiple control volumes connected by junctions compose a hydrodynamic system, which is filled with a single fluid in one or two phases, as well as an optional non-condensable gas.

Each control volume has a defined volume, flow area, and flow length which must be consistent. The volume also has a fixed hydraulic diameter and surface roughness for flow calculations, and these need not be related to the volume dimensions. The volume vertical angle is used to calculate pressure drop as well as using horizontal, vertical, or angled flow regime correlations. The user also inputs each volume's initial pressure, temperature, quality, and presence of noncondensable gases.

Control volume junctions consist of 'to' and 'from' pointers to the respective control volumes, a flow area, and a form loss coefficient. Junctions may also set the initial conditions as a volume, including an initial velocity or mass flow rate. A single volume can have any number of junctions, but the junctions can only attach to the front or back of a volume. Junctions can attach in non-physical ways, as long as the elevation change from vertical volumes remain consistent so that elevation-based pressure drop can be calculated.

For ease of input, a number of linked volumes of junctions can be defined as a single "pipe," allowing volumes and junctions with the same dimensions to be input as a single set of cards.

Hydrodynamic systems can be given boundary conditions through the inclusion of time-dependent volumes and junctions. These are similar to normal control volumes and junctions, but have properties dictated by a table rather than simulation. This allows for fluid to be lost to atmosphere, or representing an effectively infinite ocean, as well as simulating a system that is not modeled. Time dependent junctions allow for injections or suctions of a given mass flow rate.

For the solid components of a system, heat structures are used. These can be rectangular, cylindrical, or spherical. The thermal properties of the material defined for the structure are input by table. One-dimensional conduction within a heat structure occurs automatically in the radial direction.

es of a heat structure, along the axis used for conduction, can be set to convect with a fluid volume. This convection will be done with forced, natural, or mixed convection as determined by the code. Instead of setting a surface to convect with a fluid volume, it can instead be made adiabatic, or have a fixed temperature or heat flux via table.

Heat structures can be set to conduct to other heat structures or axially, as well as interact with other structures via radiation. This requires a radiation/conduction enclosure, in which the view factors or conduction areas between all heat structures in the enclosure are entered. Axial conduction can be mimicked by having axial nodes of a heat structure conduct to each other, but as the enclosures only allow heat to move between the temperature at the "left" and "right" sides, it will not be accurate for a heat structure with multiple radial nodes.

Every component contains numerous flags to enable or disable specific models. In general, the defaults are sufficient. There are also options to alter calculations for the entire input deck. Every component also contains cards to set initial conditions in pressure, temperature, flow rate, etc. as appropriate to the component.

For execution, a set of cards defines the timeframe to run in, the default maximum timestep, the minimum timestep, and the rate of data recording. The data recording rate defines the number of default timesteps between each entry in the restart file, minor edits, and major edits.

5.1.2 Model Execution

When an input deck is given to RELAP5 to run, it first performs a number of verification checks to ensure the deck is in the correct format, and that the elevations in a loop match up properly. Assuming the deck passes initial verification, the code begins to solve a partially implicit system of equations for the entire model. The user-input timestep is used as the delta t in solving the equations. If in solving the equations, the Courant-Friedrichs-Lewy (CFL) condition [2] is found to not be met, the code halves the timestep and attempts again. If this reduces the timestep below the user input minimum timestep, the code terminates.

Output is produced in the form of an output summary file with the file extension .p, and a sequential restart-plot file with the extension '.r'. The output summary file contains information about the execution of the code, including error messages should the code not function correctly. This file also contains all the major edit data in a user-readable form. Each major edit reports element properties such as temperature, pressure, flow rates, etc. for every component. Properties not normally returned can be requested in the input deck.

The restart-plot file contains data for the system in a non-readable condensed format. RELAP5 can interface with the restart-plot file in two ways. The first is to run a 'restart' input deck that just contains the desired starting time and timestep/execution control cards. This allows a simulation to be continued after a termination. The second is to run a 'strip' input deck, which contains pointers to desired system properties and locations. This will strip, or extract, the desired quantities from the restart-plot file in a format suitable for plotting.

RELAP5 can be run from the command line or from a GUI. If the GUI is used, it produces

an additional output file, a direct access restart-plot file with extension .rr. Unlike the sequential restart-plot file, this can be accessed during execution by the GUI to dynamically plot system characteristics. This direct-access file is significantly larger than the sequential file, and on systems with powerful processors, leads to a bottleneck in simulation speed arising from the hard-drive speed.

RELAP5 uses a sophisticated two-fluid flow model, with a flow regime map based on void fraction, slip velocity, and phasic temperature difference. Horizontal and vertical flows have separate flow regime maps. Each regime uses its own correlations for flow and frictional losses.

RELAP5's default choked flow model is based on a correlation developed by Ransom and Trapp (Trapp, 1982). As this correlation was developed for pressurized systems, it overpredicts choking at low pressures. An alternate, simpler, choking model developed by Henry and Fauske (Henry, 1971) can be employed by a global flag instead of the Ransom-Trapp model. This model is used for most cases run. INL modeling guidelines also suggest deactivating the choking model for all junctions without area change, and forcing a single-velocity calculation at those junctions under low pressure.

5.1.3 Uses with Natural Circulation Calculations

RELAP5 has previously been used in several natural circulation calculations. In general, these calculations fall into two categories: low pressure, single-phase calculations, or pressurized two phase calculations.

Analyses of natural circulation in a pressurized system with RELAP5 have been performed for BWR systems during reactor trips. These can be compared to actual reactor data, as done by Kaliatka and Uspuras for the Ignalina RBMK. [19] The RELAP5 results show good agreement with the system-level data in this and similar cases.

Single phase natural circulation experiments have also been modeled with RELAP5. While small discrepancies have been noted at atmospheric pressure, Mousavian et. al. show

the overall behavior matches that of experimental data, (Mousavian, 2004).

RELAP5 simulations of two-phase natural circulation at atmospheric pressure, however, have not been experimentally verified. On small timescales, large pressure gradients such as those caused by flashing have been shown to be handled poorly by RELAP5 by (Tiselj, 2000) As such, the model produced of the experimental system can verify the system-level behavior of RELAP5 in a two-phase atmospheric pressure natural circulation regime. By scaling, this can then be applied to the reactor scale model.

5.2 Reactor (Full) Scale Model

The full scale RCCS model is designed to closely mimic the actual geometry of the water based RCCS, while making the following simplifying assumptions to allow the simulations to execute on a reasonable timescale.

The deck contains one of the eight tanks, and 27 of the 227 risers. It was assumed that the extra banks of 5 and 6 risers in the corners absorbed minimal heat, and were ignored. With those 11 risers ignored, the 27 risers represent one-eighth of the system. It was then assumed that the heat loading averaged equally to the remaining risers. For simplicity, this heat loading was applied as a set heat flux to the riser piping in the heated zone, assuming that the heat removal predicted by van Staden of 700 kW in steady state and 1.5 MW peak in accident conditions is accurate. The system was conservatively assumed to be adiabatic, with the exception of venting of steam to the atmosphere. To represent the header connections with the rest of the RCCS, the left side of each header was connected to the right representing assumed flow from the other symmetric sections. Each group of 9 risers was represented in RELAP5 with a single 'pipe,' with flow area equivalent to the sum of the riser areas, but hydraulic diameter the same as a single riser. This was assumed to give sufficient resolution. The riser groups were junctioned to a manifold that was one-quarter of the full manifold length to add in the assumed average flow losses for entering the risers.

The nodal layout is shown in Figure 5.1. The details of the manifolding are all in the

horizontal plane, the rest is vertical. Each pipe shown consists of numerous nodes for more accurate modeling. The main body of each riser and the lower section of the tank are thermally connected to cylindrical heat structures representing the piping and outer tank wall, respectively. These are present to allow a heat flux to be imposed, both for the heat removed in operation by the risers, and the theoretical active cooling provided by the tank heat exchanger. The rest of the system does not require heat structures, as it is assumed to be adiabatic. The dimensions of each pipe correspond to the actual geometry, or as noted in the assumptions.

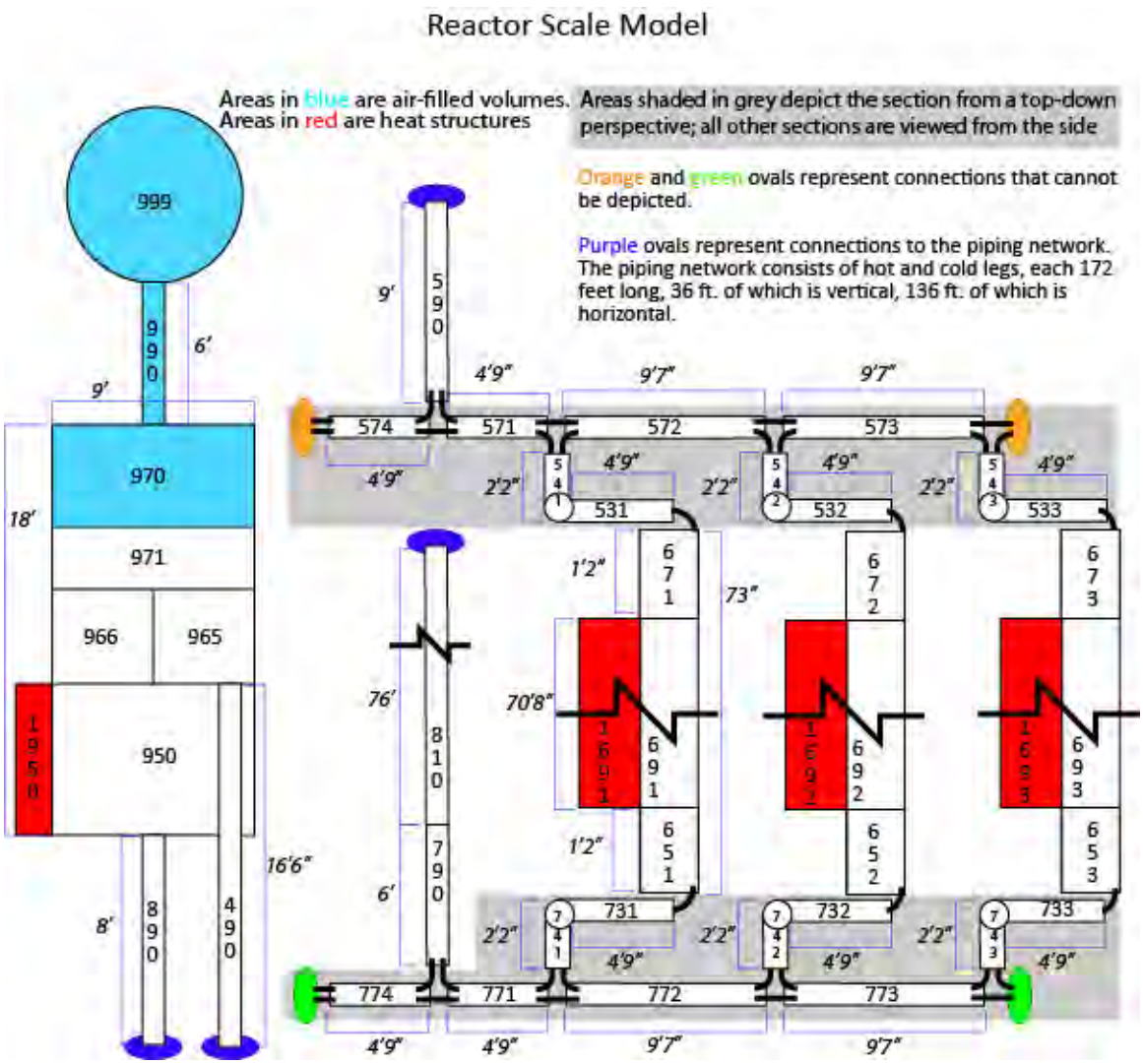

Figure 5.1: Reactor Scale Model Piping Nodalization

Due to the one-dimensional nature of RELAP5, the tank nodalization was required to be more complex. Using a single path of nodes does not allow the heated water from the loop to mix with the nodes above the tank inlet, since a junction can only have a single mass flow. As such, there are two nodes above the tank inlet, each node with the hydraulic diameter of the tank, but with half the flow area. This allows water in the tank to circulate within those nodes and the nodes above and below, keeping the tank well mixed and keeping the whole water mass active in the system.

The heat loading was configured to impose a heat load equivalent to one-eighth of the total system removal of 700 kW on the outside of the riser piping. In steady state operations, it was assumed that the active cooling of the tank heat exchanger removed the same amount of heat. As this set of boundary conditions contains no fixed temperature reference, the initial temperatures were set by setting the tank wall to a fixed temperature of 20 degrees C, and letting the system come to steady state with the 700kW equivalent heat load. The temperature data for that run was set as the initial temperature in future runs. In each run, the system was given 20,000 seconds to achieve a steady state. At the 20,000 second mark, the heat load would linearly ramp up to one-eighth of the 1,500 kW peak power expected to be removed in a LOFA over 3,000 seconds. The active cooling would likewise decrease to zero over the same interval. After the ramp, the heat load remained constant over the remainder of the simulation.

5.2.1 Choking Cases

Three cases were run with the baseline reactor scale geometry and heat loading. The first case is with all choking flags set to their default values, including the use of the Ransom-Trapp choking model. A case using the Ransom-Trapp model with the INL suggested modeling guidelines was also used. These guidelines disabled the choking model in every junction that did not have an area change. The junctions unaffected were the tank inlet, outlet, vent, and riser inlets and outlets. The junctions with choking enabled were also modified to use a

single velocity calculation for choking instead of a two-velocity calculation.

A case was run to directly compare choking models. This used the Henry-Fauske choking model with the INL modifications. It should be noted that the Henry-Fauske is intrinsically a single-velocity model, so the flag to force single-velocity calculations has no effect.

The single most distinguishing characteristic between these cases is the system mass flow rate. The rate is taken at the tank outlet and downcomer inlet junction, so direct two-phase effects are not present in the junction. Note that for all cases, the first 20,000 seconds are running in steady state, followed by a 3,000 second heat ramp up and cooling ramp down. Under these conditions, the system begins to transition to two-phase flow around 69,500 seconds. Note that all cases have identical behavior in steady state/single phase, as the choking models do not act on those flow regimes.

Henry-Fauske Model

It should be noted that the Henry-Fauske choking model in this case results in the exact same effects as disabling the choking model in all junctions. As such, flow does not meet the choking criteria. The INL modifications specifically deal with the effects of choking, and therefore do not affect the performance of the system with the Henry-Fauske model.

The mass flow rate for the simulation is shown in Figure 5.2. It follows the same steady state and single-phase behavior as the other baseline cases. The system mass flow has an inverse relation with the change in temperatures over the length of the riser tubes. The temperature change over time is shown in Figure 5.3. Since the change in temperature is directly dependant on mass flow, future cases will neglect this figure and simply display the system mass flow rate. Note the general similarities between the mass flow rate behavior of the predictive experimental case and this baseline case.

After the initial transition into two-phase, there is an approximate 10,000 second period in which the flow is perfectly stable. This is followed by a small increase in mass flow. This can be explained as a result of the tank modeling. As previously mentioned, the reservoir tank could not be modeled as a single pipe, as the heated water would not circulate to the

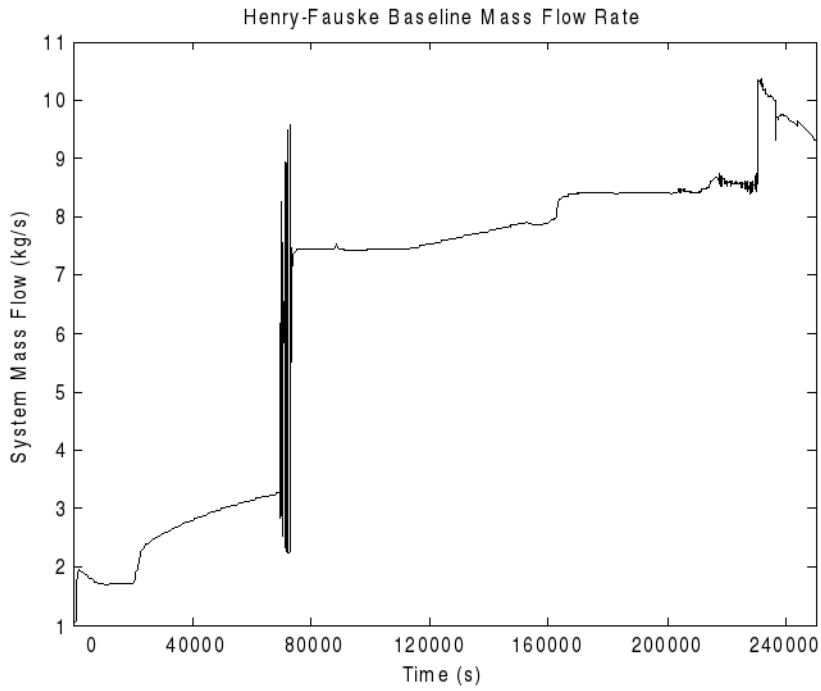

Figure 5.2: Henry-Fauske mass flow rate, reactor scale baseline model

nodes above the hot leg inlet, keeping the water in those nodes at the initial temperature. As such, two nodes with half the flow area are used as two components in a circulating flowpath, allowing the tank to heat up evenly. During the heat up to two-phase flow, the water in the system undergoes thermal expansion, which pushes water up to the first air-filled node at the top of the tank. This water does not thermally communicate with the rest of the tank, and as such is subcooled when the system begins to flash. Once this node empties, there is a small increase in mass flow. Figure 5.4 shows the tank water level over time. This is based on the void fractions in each water filled node. The dip in the beginning corresponds to the time dealt with the water in the air nodes, and it decreases linearly after this point as the water evenly boils out.

After the short spike in mass flow caused by the emptying of the air node, there is another period of stability, followed by a slow ramp up of mass flow. This corresponds to the movement of the point of flashing. The ramp begins when the flash point descends to

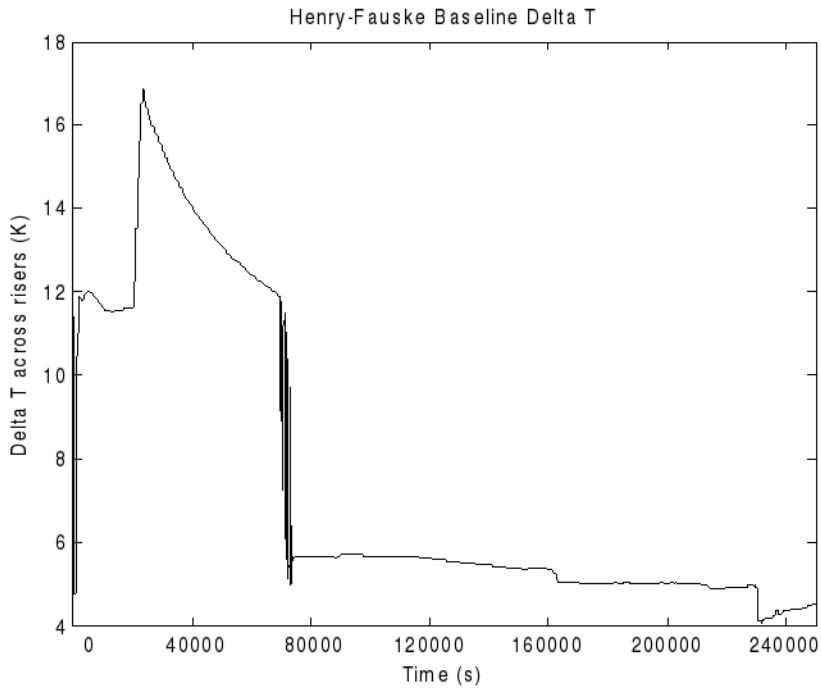

Figure 5.3: Henry-Fauske Δ T across risers, reactor scale baseline model

the 3rd node from the top, and the void fraction in the node continues to increase. Each of the first 5 piping nodes are 1.00584 m long. This can be seen in Figure 5.5.

The step change in mass flow shortly after 160,000 seconds is another artifact of the tank nodalization. This step change corresponds to the emptying upper water node. Similar effects can be seen as other nodes drain. The increase and oscillations after 200,000 seconds reflect the two circulation nodes emptying. The large step change at approximately 230,000 seconds corresponds to the first lower water node emptying. While these do correspond to modeling decisions, the large mass flow change after the first lower node empties also represents the physical change of the tank inlet being above the level of the water.

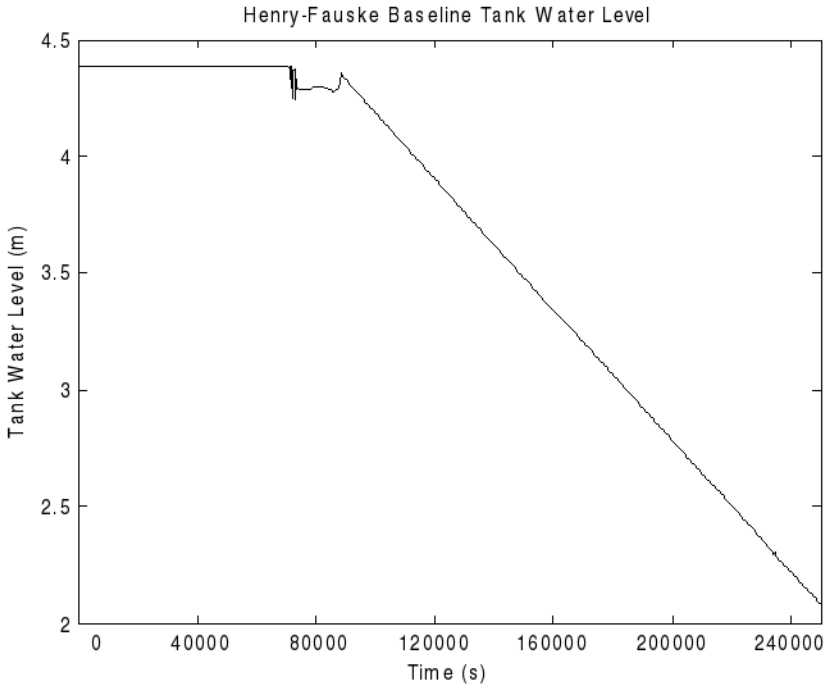

Figure 5.4: Henry-Fauske tank water level

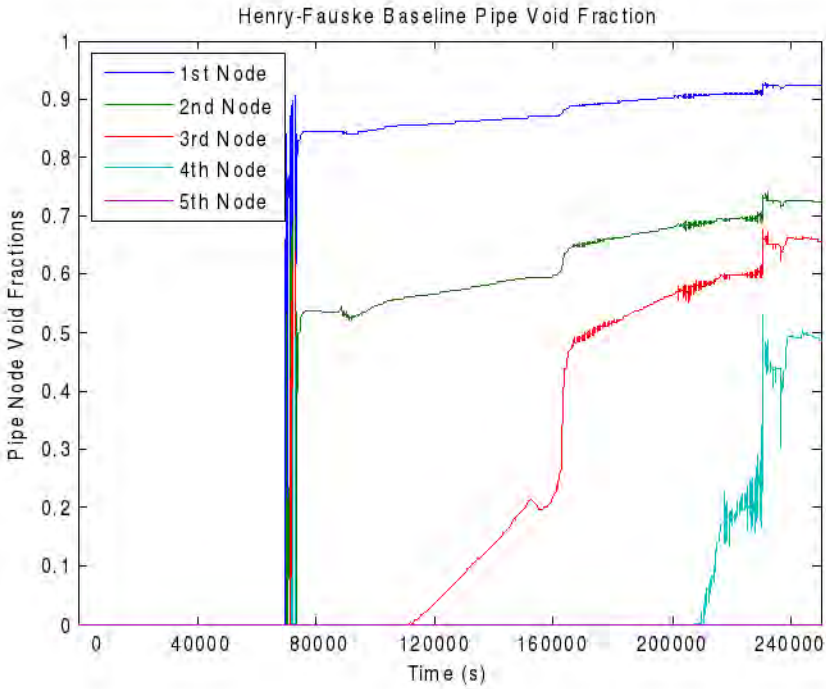

Figure 5.5: Henry-Fauske pipe node void fractions

Ransom-Trapp Model, unmodified

This case uses the default choking model and choking flags at all junctions. It should be noted that this case also neglects abrupt area change form losses in all junctions.

The system mass flow is shown below in Figure 5.6. The initial hump is simply the system equilibrating to a steady state condition. As the heat load is increased with corresponding decrease in active cooling, the mass flow rises as the change in density, and therefore driving force, is increased over the risers. As the riser inlet temperature continues to rise in the absence of any cooling, the mass flow rate continues to increase. The oscillatory spike in mass flow at approximately 70,000 seconds is due to the violent initial flashing event as the system moves to two-phase.

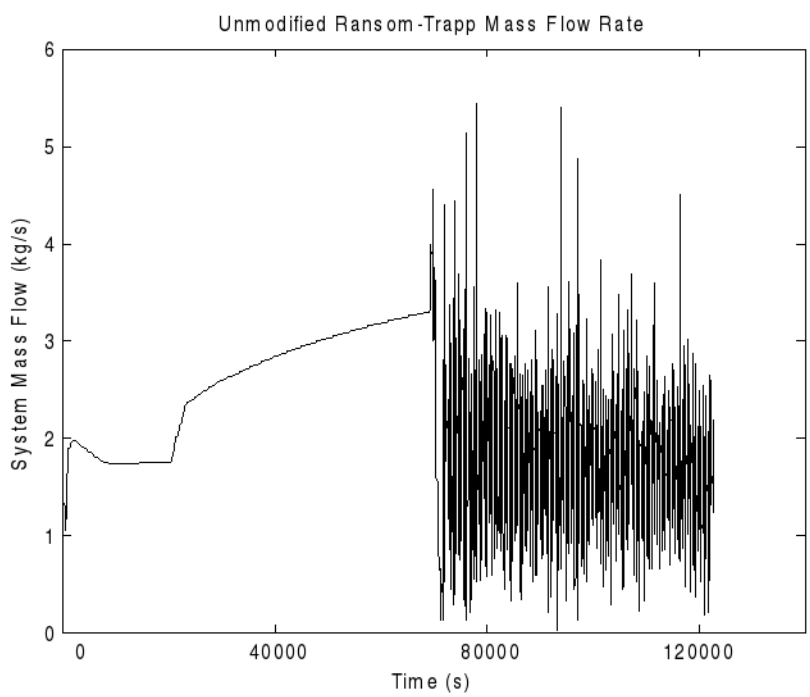

Figure 5.6: Unmodified Ransom-Trapp mass flow rate

After the transition to two phase flow, the system becomes highly unstable. By examining the system choking flags with a minor edit, it can be seen that choking is occurring throughout the top of the piping network. This is unlikely to be physical, and results in an

average decrease in flow contrary to expectations. This case was terminated early due to the instability of the flow.

Ransom-Trapp Model, INL modified

This case uses the default choking model, but disables choking at all junctions that do not have an area change. Each junction with choking active uses a single-velocity calculation, instead of a two velocity calculation.

The system mass flow can be seen in Figure 5.7. The system behavior is nearly identical to the Henry-Fauske model up to 170,000 seconds. After that point, the mass flow begins to decrease rather than staying level. This is due to choking in the tank inlet under the Ransom-Trapp choking criteria. This limits the change in mass flow as the tank level and flashpoint descend to new nodes, unlike the Henry-Fauske case.

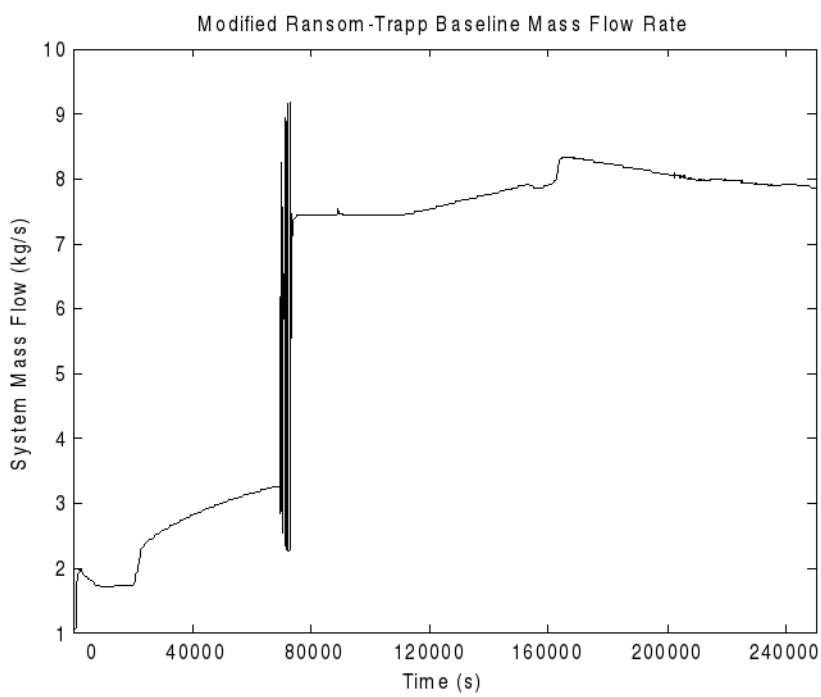

Figure 5.7: INL Modified Ransom-Trapp mass flow rate

The slight increases seen after approximately 200,000 appear to correspond to similar changes from the Henry-Fauske case based on the emptying of the circulation nodes and the

transition to the 3rd node in the tank inlet piping. The timing of these changes is effectively the same between cases, and effect on the mass flow is obviously much reduced.

The limitations of RELAP5-3D in creating a large mixing volume with an inlet in the side of the volume appear to account for the remainder of the non-uniformities. While the mass flow results appear to be more consistent using these modifications, this required disabling the physics modeling in places where the Ransom-Trapp choking criteria is met. This should not be necessary with a comprehensive choking model, and it cannot be verified short of experiments.

5.3 UW Experimental Scale

The RELAP5 model of the experimental system was designed to accurately reflect the actual facility as best as possible so that results of the simulation could be directly compared to results of the experiment.

The system was assumed to be adiabatic, though the system piping and tank are accurately modeled to preserve the thermal inertia. Despite the experiment's insulation, heat loss on the order of 15-20 % is occurring, [5] and this is modeled by assuming the heat is lost directly from the heaters, and never enters the system. Due to limitations of the conduction model, the heat structures representing the riser piping were combined with the fins in a single rectangular slab, in contact with the riser fluid on one side, and in contact with the heater box volume on the other. The mass of material and surface cross-section is conserved in this combination. The heater box space behind the risers and fins was assumed to be packed with insulation and treated as adiabatic. The heat exchanger piping and operation were assumed unimportant aside from the thermal effect, and as such it is represented by a heat flux removed from the tank wall when active. The thermal properties of the heaters were unknown, but were assumed to be generally unimportant, and thermal properties of alumina were used.

The nodal layout for the piping system is shown in Figure 5.8. Each component shown

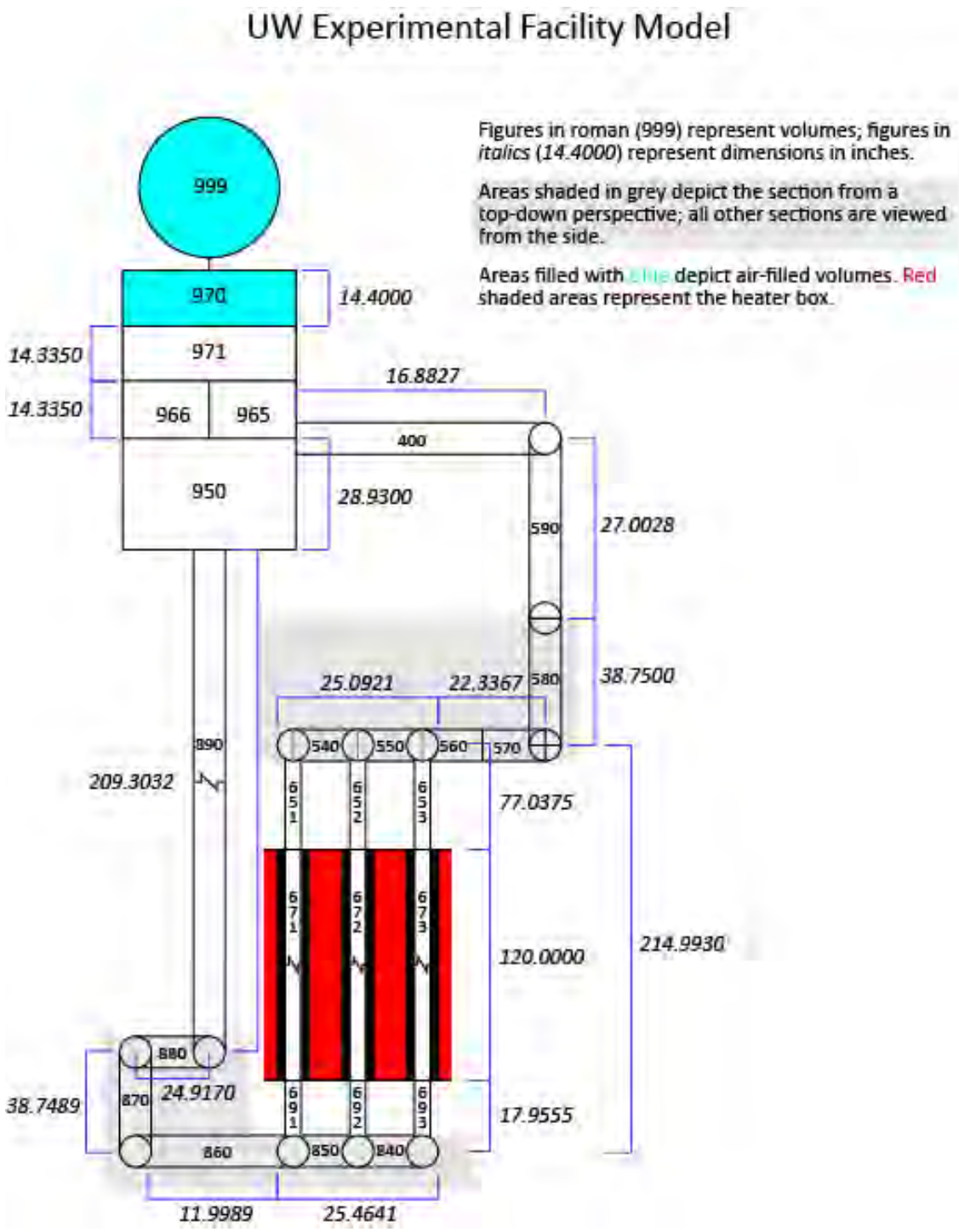

Figure 5.8: UW experimental model, pipe and heat structure nodalization

is wrapped in cylindrical heat structures representing the piping except for the risers. As in the full scale, each component is composed of multiple nodes. The same nodalization of the tank from the full scale model is used here.

The heater cavity is shown in Figure 5.9.The top, bottom, left, right, and back walls are all represented as single heat structures. The heaters are lumped together in 6 axial groups corresponding to the control limits of the experiment. The risers have 10 axial nodes each. The cavity volume consists of 4 nodes of air forming a loop, convecting with all heat structures. The radiation enclosure model was used here, with view factors between each surface calculated with MCNP. Heat loading was applied as a heat flux to the back of the heater surfaces, and the heat was communicated to the risers via radiation and convection.

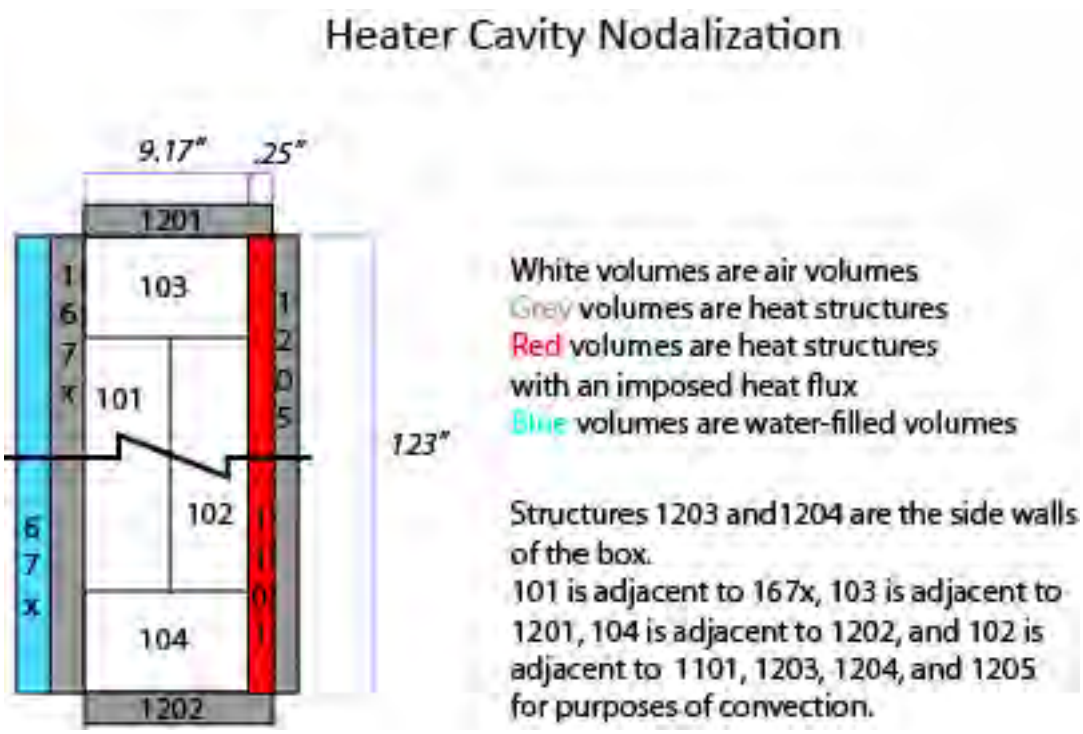

Figure 5.9: UW experimental model, cavity nodalization diagram

The specific heat loadings were set to match those of completed experimental runs. 5,000 seconds at the beginning of each run are set with no heat load in order for the system to reach equilibrium. The heat load is linearly ramped to scale with the experimental loading.

The heat load used, however, corresponds to the heat added to the test section calculated from the Δ T over the risers, instead of the heater power in order to account for the heat loss. The heat exchanger heat removal was assumed to be linear, starting at zero when the heat exchanger was first turned on, and leveling out at a steady state value equal to the heat added after a time equal to the actual experiment reaching an approximate steady state value. The Henry-Fauske choking model was used all experimental cases.

From experimental data logs, parameters that were modeled were ramp rate of electric heating, steady state power in the test section, time of HXG activation, and time history of HXG heat removal. The transcribing of actions, for a sample test, Run010, is given below in Table 5.1, with the translated RELAP5 inputs after.

Table 5.1: Log of experimental conditions for input into RELAP5

Action	Time	Heater	Test Section	HXG
1. Turn on heaters, begin ramp	02:30:00 PM	0 watts	0 watts	0 watts
2. Complete Ramp	03:30:00 PM	9,917 watts	4,324 watts	0 watts
3. Turn on HXG	04:45:00 PM	9,917 watts	7,710 watts	0 watts
4. Increase to half section energy	05:04:00 PM	9,917 watts	7,710 watts	4,162 watts
5. Increase to full section energy	05:20:00 PM	9,917 watts	7,710 watts	7,710 watts

```
    * Power Input Card
    20210000   htrnrate    0    1.0   -0.633171201 *W/m^2
    *
    20210001  -1.0       0.0
    20210002  0.0        0.0
1. - 20210003  5000.0     0.0
2. - 20210004  8600.0     7710.0
    20210005  31100.0    7710.0
    *
    *
    * Power Removal Card
    20220000   htrnrate    0    1.0   0.4201172723 *W/m^2
    *
    20220001  -1.0       0.0
    20220002  0.0        0.0
3. - 20220003  13200.0    0.0
4. - 20220004  14640.0    4162.0
5. - 20220005  15120.0    7710.0
    *
```

5.3.1 Experimental Run Cases - Steady State

Three cases were run to compare to existing single-phase and steady state data, at powers of 4.63, 7.27, and 9.91 kW. The experimental runs were chosen due to the consistent behavior and the variation in power between runs. The results for these three cases are generally similar, so the basline 9.91 kW will be examined in detail and the others summarized.

9.91 kW Steady State

In this case, the system began at room temperature with no heat load. Heat was increased linearly over the course of one hour to a peak of 7.91 kW. The actual run was performed with a peak power of 9.91 kW, but the excess energy was lost to the environment and is treated here as not generated. The heat exchanger was turned on at 12,500 seconds after the beginning of the heat ramp, with a 4,000 second linear ramp to match the generated power. The system mass flow rate is seen in Figure 5.10, alongside the experimental mass flow results.

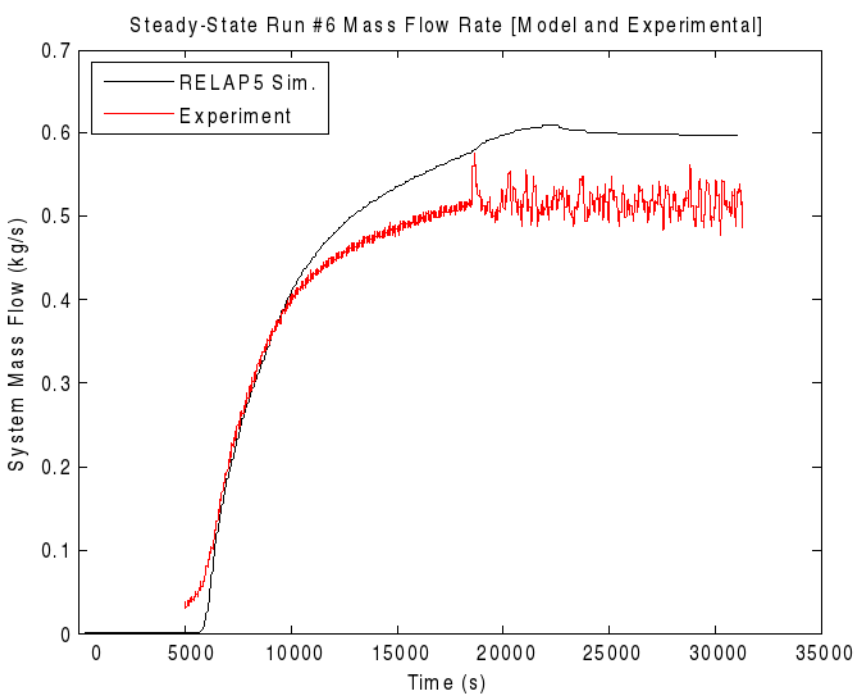

Figure 5.10: 9.91 kW steady state, experimental vs RELAP5

The model tracks the ramp of the mass flow quite accurately for the beginning of flow, but exceeds the experimental results. The increase in mass flow rate seen around 18,000 seconds is due to the activation of the heat exchanger increasing the change in temperature over the risers. The oscillatory behavior seen in the experimental results when approximating steady state is a result of imprecise control of the heat exchanger, as well as the effects of the heat exchanger inlet/outlets on the flow. The most likely source for the difference in magnitude between the experiment and model final mass flows is incorrect application of frictional and form losses from the experiment piping. RELAP5 default surface roughness for calculation is 9-10 times the volume hydraulic diameter, which is valid for large reactor piping but less so for the small diameter piping that the experiment consists of.

4.63 kW Steady State

This case was run with a power of 3.439 kW, with a one hour ramp for power, and a 1,775 second ramp for the heat exchanger beginning 25,000 seconds after the initiation of the heater ramp. The mass flow is shown in Figure 5.11. Behavior is similar to the experiment, with the same differences noted in the 9.91 kW run. The shorter ramp of the heat exchanger leads to a greater spike in mass flow rate.

7.27 kW Steady State

This case was run with a power of 5,559 kW, with a one hour heat ramp followed by a 3,780 second ramp of the heat exchanger beginning 15,320 seconds after the initiation of the heat ramp. The system mass flow is shown in Figure 5.12. The behavior is consistent with the previous two runs.

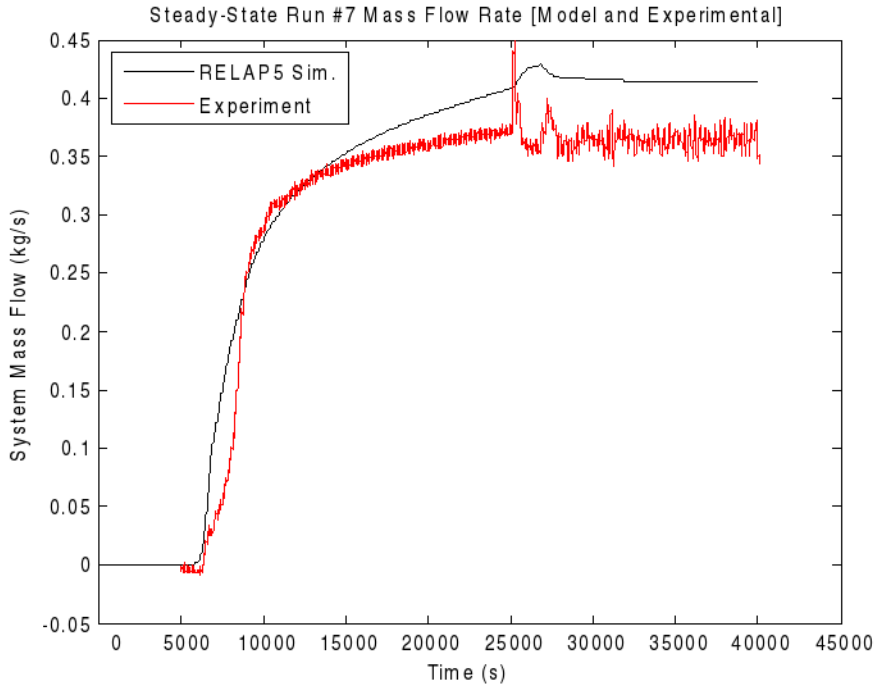

Figure 5.11: 4.63 kW steady state, experimental vs RELAP5

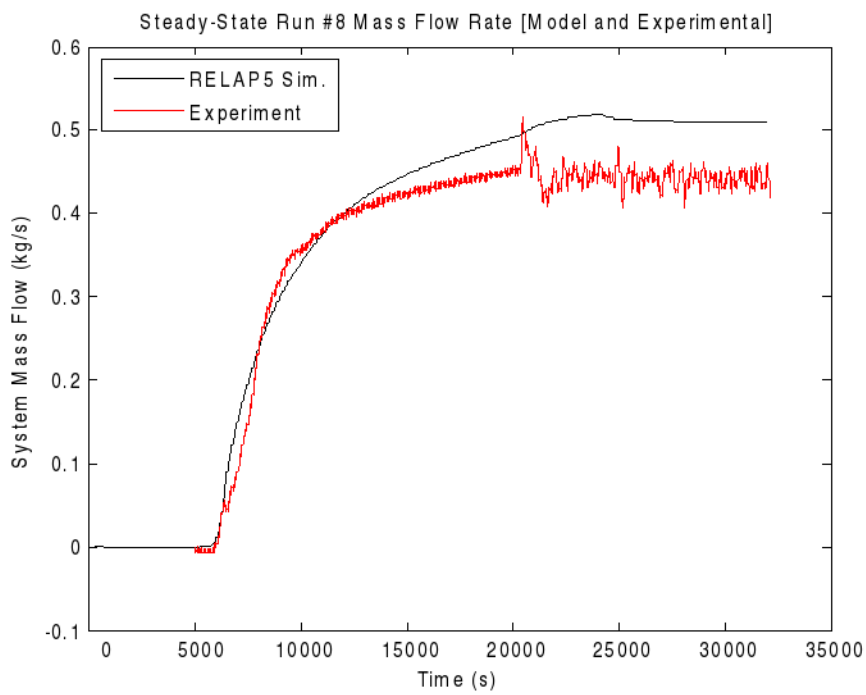

Figure 5.12: 7.27 kW steady state, experimental vs RELAP5

5.4 Scaling Laws Validation

The ultimate goal of the RELAP5 simulations serves several practical purposes: validating scaling laws for thermal hydraulic performance, and confirmation of the model will assist in data acquisition device selection criteria, such as expected void fraction and velocity ranges. Additionally, a confirmed model will allow for a high level of confidence when investigating off normal scenarios that would otherwise be unfeasible in an experimental facility.

A series of simulations were run for the 'reactor scale', 'reduced reactor', and 'experimental model'. The 'reactor scale' models the concept GA-MHTGR RCCS geometry to exact dimensions, while the 'reduced reactor' linearly downsizes the full reactor geometry and axial dimensions by 1/4. Integral power levels based off the decay heat load, or 1.5 MW for the full reactor, and scaled appropriately for the 'full reduced scale' with scaling laws. A reduced 27 riser tubes was selected to aid in computational efforts. For comparisons to the facility at UW-Madison, the 'reduced reactor' was reduced to only model 3 riser tubes to provide a similar mode of comparison to the 'experimental model'. Conditions for the test matrix are given below in Table 5.2

Table 5.2: Scaling validation RELAP5 test matrix

Run	Criteria	Scale	Power [kW]	Risers	Heated [m]
1	Reactor Scale	1:1	178.4	27	21.54
2	Reduced Reactor	1:4	89.2	27	5.39
3	Reduced Reactor	1:4	9.91	3	5.39
4	Experimental Model	1:4	9.91	3	3.05

At time 0, a reduced and uniform heat flux was imposed over the entire area of the heated section of the riser tubes, resulting in a slow and steady rise in system temperatures and mass flow rates. The water storage tank was given a fixed wall temperature boundary condition of 20 °C, with the remaining system components considered adiabatic. This single-phase regime was allowed to reach a steady state, where after the heat flux was gradually increased

to peak loss-of-flow conditions and the fixed water storage tank boundary condition was removed. A gradual rise in system temperatures and flow rates was again seen, and upon reaching system saturation, flashing began inside the top header, nearest the inlet to the water storage tank. This flashing settled as it began occurring lower and lower in the system, traveling further down the hot leg, with a distance proportional to the heat load. The flashing effects were capable of inducing temporary flow reversals in the system, as seen with negative velocity values. A transition to the final state was observed: highly oscillatory two-phase flow. Shortly after the establishment of this two-phase regime in the system; steam is continually vented at a constant rate into the atmosphere. As the tank water level falls below the downcomer inlet, flow reversals become less frequent. Even at later stages, the system does not significantly change in behavior, the density difference driven mass flow coupled with the flashing is sufficient to overcome the difference in water levels.

Numerical parameters from the 'reactor scale' were used to calculate the expected values at the 'reduced reactor', and compared against the actual results from RELAP5. The results from the 'reactor scale' and 'reduced reactor' are shown below in Table 5.3.

Table 5.3: Reactor scale results RELAP5, similarity parameters applied and new values at $\ell_R = 0.25$ calculated, and compared to reduced reactor RELAP5 results

	Reactor Scale	$\rightarrow \ell_R = 0.25$	Reduced Reactor
Axial Scale	1:1	1:4	1:4
Height [m]	21.54	5.39	5.39
Risers #	x27	x27	x27
Tank inlet velocity (fluid) [m/s]	1.759	0.879	0.998
Tank inlet velocity (gas) [m/s]	8.640	4.320	4.780
Riser Velocity [m/s]	0.036	0.018	0.024
Inlet Temp [K]	376.02	376.02	377.84
Outlet Temp [K]	398.68	398.68	393.86
Steam Vent Rate [kg/s]	0.083	0.041	0.043

Comparisons between the 'reduced reactor' and 'experimental scale' were finally made to examine the how accurately the experimental facilities design representing the concept RCCS design, Table 5.4

Table 5.4: Reduced reactor (3 riser tubes) vs experimental

	Height	Downcomer	Riser			
	[m]	$\dot{m}$ [kg/s]	#	$\dot{m}$ [kg/s]	V [m/s]	Δ T [°C]
Reduced Reactor	5.39	0.475	x3	0.154	0.076	2.411
Experimental Model	3.05	0.512	x3	0.165	0.082	2.235

The majority of the simulations were allowed to run to tank depletion, with computationally intensive runs allowed to reach steady state two-phase for a period of 10 hours, where after times to tank depletion were extrapolated. A summary of results is given below in Table 5.5. These results demonstrate satisfying a minimum 72 hour cooling criterion, with excellent agreement between the ideal and actual scaled models, validating the derived time ratio similarity of ${\ell_R}^{0.25}$.

Table 5.5: Times to tank depletion from loss of inventory due to steaming

	Vent Mass Flow Rate [kg/s]	Tank Depletion [hr]
Reactor Scale	8.29E-02	142.97
Reduced Reactor	4.29E-02	72.48
Experimental Model	4.36E-03	70.56

5.5 Two - Phase Modeling

In addition to the single-phase RELAP5 simulations, the behavior at two-phase was investigated. Previous simulations encountered unphysical flow oscillations and reversals. It was found that the system was unexpectedly entering a choked flow regime. By changing the choked flow model from the default Ransom-Trapp model to the alternate Henry-Fauske model, the flow stabilized and increased upon entering two-phase. Using Idaho National Lab (INL) modeling guidelines, deactivating the choking model in all junctions without area changes and using a single velocity calculation for choking with the Ransom-Trapp model provides similar results. Thus, the Henry-Fauske model was used for future cases.

Predictive Full Scale

A predictive two-phase case was run to mimic the accident condition of the full scale reactor. There is an initial 10,000 second steady state condition with a heat load of 4.63 kW. After this section, power is instantly increased to 9.91 kW, and the heat exchanger instantly deactivated. These power values are scaled to correspond to the normal operation heat removal and peak removal under a loss of flow accident as calculated by van Staden[1], 700kW and 1.5 MW respectively for the entire system. Power is held constant, and the case was run for a total of 140,000 seconds. The system mass flow is shown in Figure 5.13. The large step change at approximately 100,000 seconds is likely an artifact of the tank model, and is discussed further in chapter 6. The extremely oscillatory region in the beginning of the two-phase flow region has a physical basis, but the magnitudes calculated are higher than expected.

To determine the cause of the oscillations, the inlet pipe void fractions in a section of the oscillatory region were examined. This is shown in Figure 5.14. The horizontal node is the section of pipe entering the tank from the side. The 1st, 2nd, etc. nodes are the nodes in the vertical pipe connected to the horizontal section, in descending order. It is apparent that the system is not smoothly boiling off, but undergoing intermittent flashing events. Each

event increases the mass flow, which then decreases the Δ T across the risers. This decreased temperature rise results in a lack of flashing, decreasing the mass flow and causing the cycle to begin again. While the peak mass flow rate in the chugging region does ramp up, it does so very quickly.

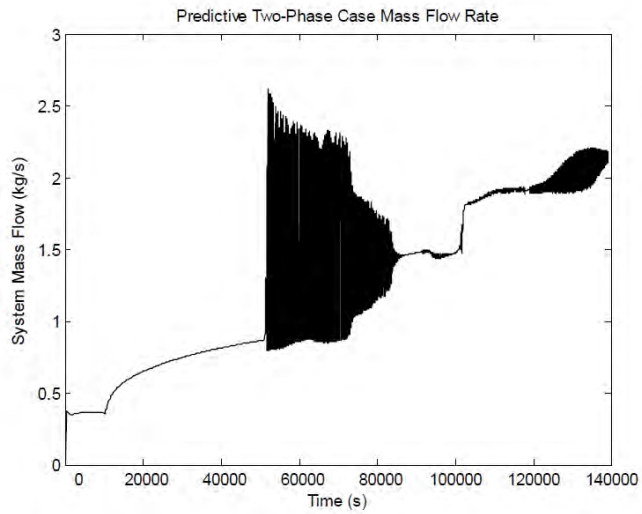

Figure 5.13: Predictive reactor scale simulation into two-phase

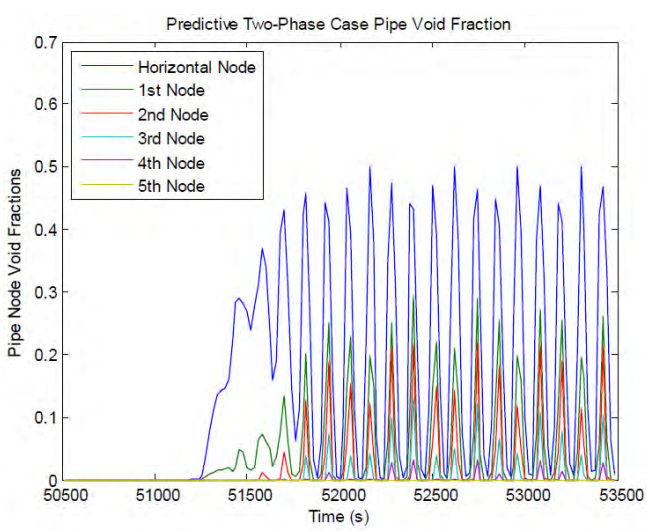

Figure 5.14: Predictive reactor scale void fraction into two-phase

Parametric Study

A parametric study of the influence of total power level was performed where the power was varied between 3 and 16 kW in 100 Watt intervals. An iterative Perl script automated the created of input files for RELAP5, executed the RELAP5 run program, saved and parsed the output data, then repeated the process. Over 36 hours of computation time was required for this parametric study, and the final result was in the form of an animated .gif file that showed the varying trends of the mass flow rate at each simulated power. A few key power levels are given in Figure 5.13.

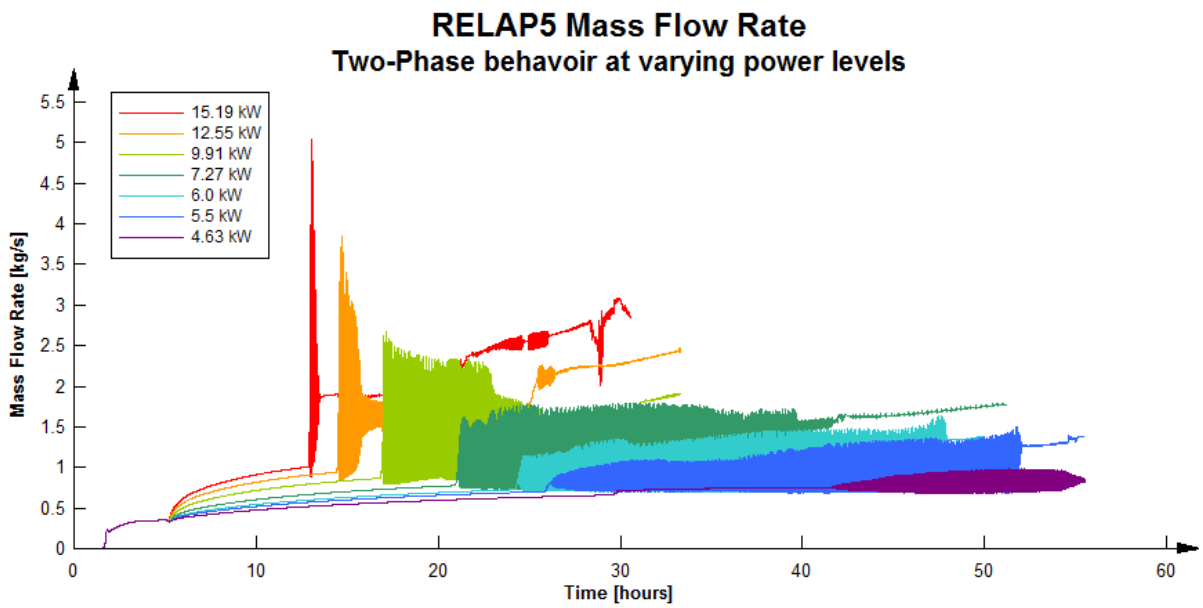

Figure 5.15: RELAP5 power level parametric study. Mass flow rate [kg/s] is plotted versus time [hours] for varying power levels

Experimental Comparison

A comparison was made with the two-phase RELAP5 simulations to experimental data. An initial model was created that matched the energies of experimental results exactly, that is the calculated energy balance in the test section (e.g. 12.55 kW for Run017) was programmed into the RELAP5 input deck. The result, Figure 5.16 indicated that RELAP5 was unable to match experimental conditions for similar initial and boundary conditions It was found that energy levels had to be significantly altered to reach similar data sets. The mass flow rate from a two-phase baseline experiment, with a supplied heater power of 15.19kW and test section energy of 12.25kW is compared to a RELAP5 simulation, Figure 5.17. The energy input had to be brought down to an extremely low 7.2kW to reach consistent data, an extremely low value that indicates major discrepancies between the experimental and RELAP5 two-phase behavior. Work is currently in progress to identify the cause, and will be the scope of future investigations.

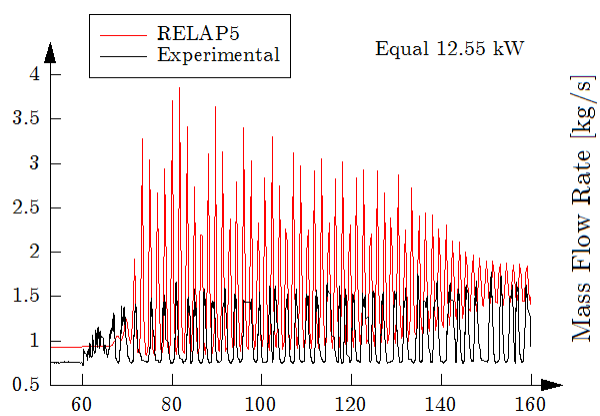

Figure 5.16: Matched power levels (12.55 kW) for RELAP5 and experiments

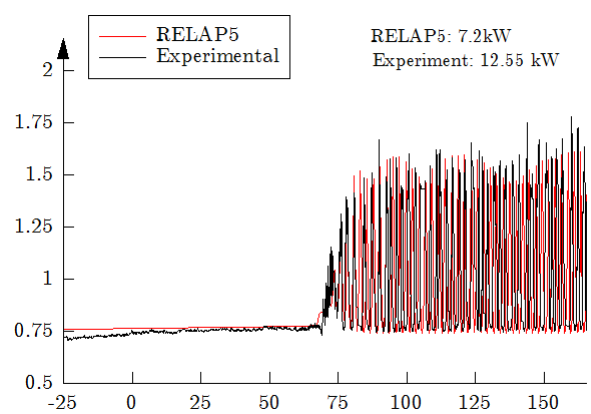

Figure 5.17: Unequal power, RELAP5 (7.27 kW) and experiments (12.55 kW)

Chapter 6

Experimental Facility

6.1 Construction Purpose

The design and construction of a scaled water cooled RCCS served to aid in the evaluation of thermal hydraulic behavior and heat removal performance, identification of characteristic behavior, and isolation of flow instabilities that arise during normal and off normal operation. To accomplish these goals, several criteria must be met:

1. Prove true to the General Atomic MHTGR / hybrid concept design
2. Allow for the recording of key parameters that will yield a complete and total evaluation of the thermal hydraulic response
3. Deliver a flexible design that will allow the investigation into a variety of scenarios, including modified scaling and power profiles at both steady state single and two-phase flow conditions.

6.2 Concept Design

The design of the experimental facility was an Argonne National Lab concept for passive decay heat removal of the NGNP whose design was based on available open literature of the HTR-10 and AVR reactor, sized to perform within a General Atomics MHTGR cavity and containment building.

The conceptual RCCS design, as developed by Argonne National Laboratory (ANL) and the authors, is a hybrid design from openly available literature. The selection process began with known dimensions of the air cooled GA-MHTGR cavity and RPV (HTGR-86-024).

The duct array for the GA RCCS design was then transformed, replacing each air duct with a water tube. Hydraulic diameters were preserved, and tube gaps filled with radiant cooling panels, based on the German HTR-Module design for water-cooling tubes and fins (IAEA-TECDOC-988). Two possible cooling panel designs were examined, the thermal fin option from the Japanese HTTR, Figure 6.1, and the thermal shield option from the Russian 20MWt VGM reactor, Figure 6.2. Unlike previous designs, this system does not utilize the standpipe curtain design of later PBMR designs. Remaining details were adopted from the legacy German FZ-Jülich design on the HTR-MODUL (IAEA-TECDOC-1198), early SA PBMR 265 MWt design work, and HTTR JAERI(JAEA) publications (IAEA-TECDOC-1163).

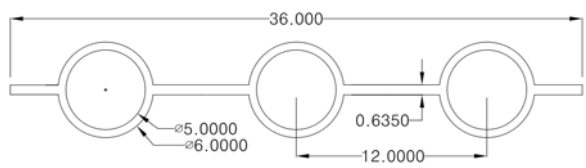

Figure 6.1: Thermal Fin Concept Design, dimensions in cm

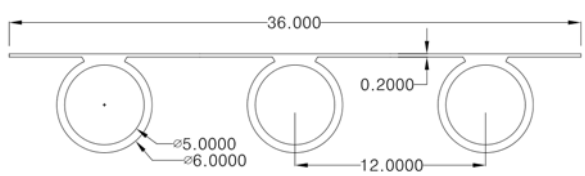

Figure 6.2: Thermal Shield design, dimensions in cm

The full-scale RCCS conceptual design must accommodate a steady-state heat loss of 0.75 MW_t from the RPV, rising to a decay heat level of 1.5 MW_t following a reactor SCRAM. The 227 riser tubes are fixed to the cavity walls, fully surrounding the RPV, and are placed at a minimum distance of 28 inches. In passive operating mode, without forced circulation, water flows by natural circulation through the downcomers and returns to the water storage tank via the riser tubes and heat transfer panels, Figure 6.3. Since there is no active cooling guaranteed under accident conditions, the water heats up and eventually reaches saturation

conditions and boiling commences. The decay heat is then rejected by venting steam in the tank to the outside atmosphere, and thus operating at near atmospheric pressures.

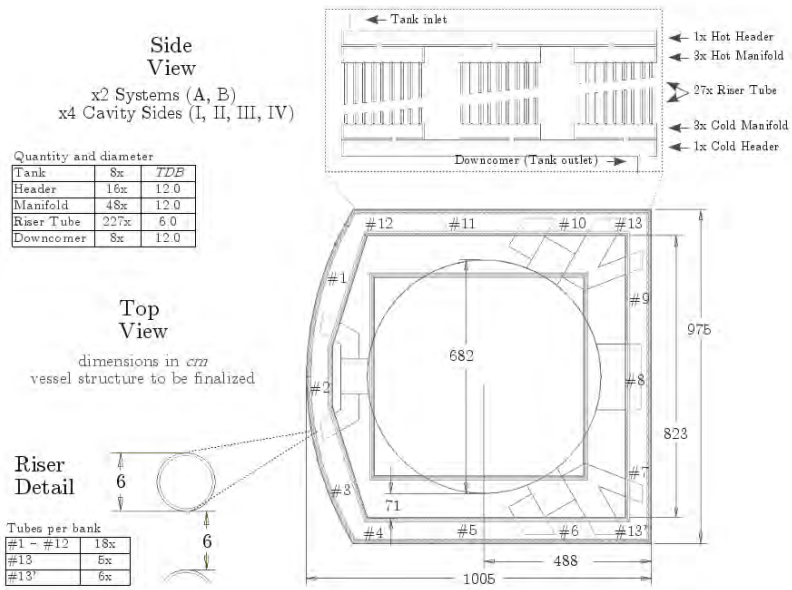

Figure 6.3: Concept design plan view. Original GA-MHTGR air cooled RCCS cavity and RPV, with air ducting replaced with water cooling tubes.

6.2.1 Facility Overview

The RCCS facility was built in the Shocktube laboratory of Mechanical Engineering in Madison, WI, and has been designed and constructed to accurately represent a 1/4 scale model of the full concept design. Fundamentally, it retains all aspects common to the typical water driven natural circulation loop: a downcomer to provide the driving head, heated section to supply the heat source, adiabatic chimney, and bulk mixing tank as the heat sink. A 7.6 m structure houses a 5 m tall test section and 1,200 liter water storage tank. Thirty four radiant heaters impose a heat flux onto a three riser tube test section, representing a 5°radial sector of the full scale. The maximum available heat flux and power levels are 25 kW/m^2 and 42.5 kW, respectively, and can be configured for linear, axial, or radial power profiles. An overview of key components is shown in Figure 6.4, with additional figures in Appendix A.

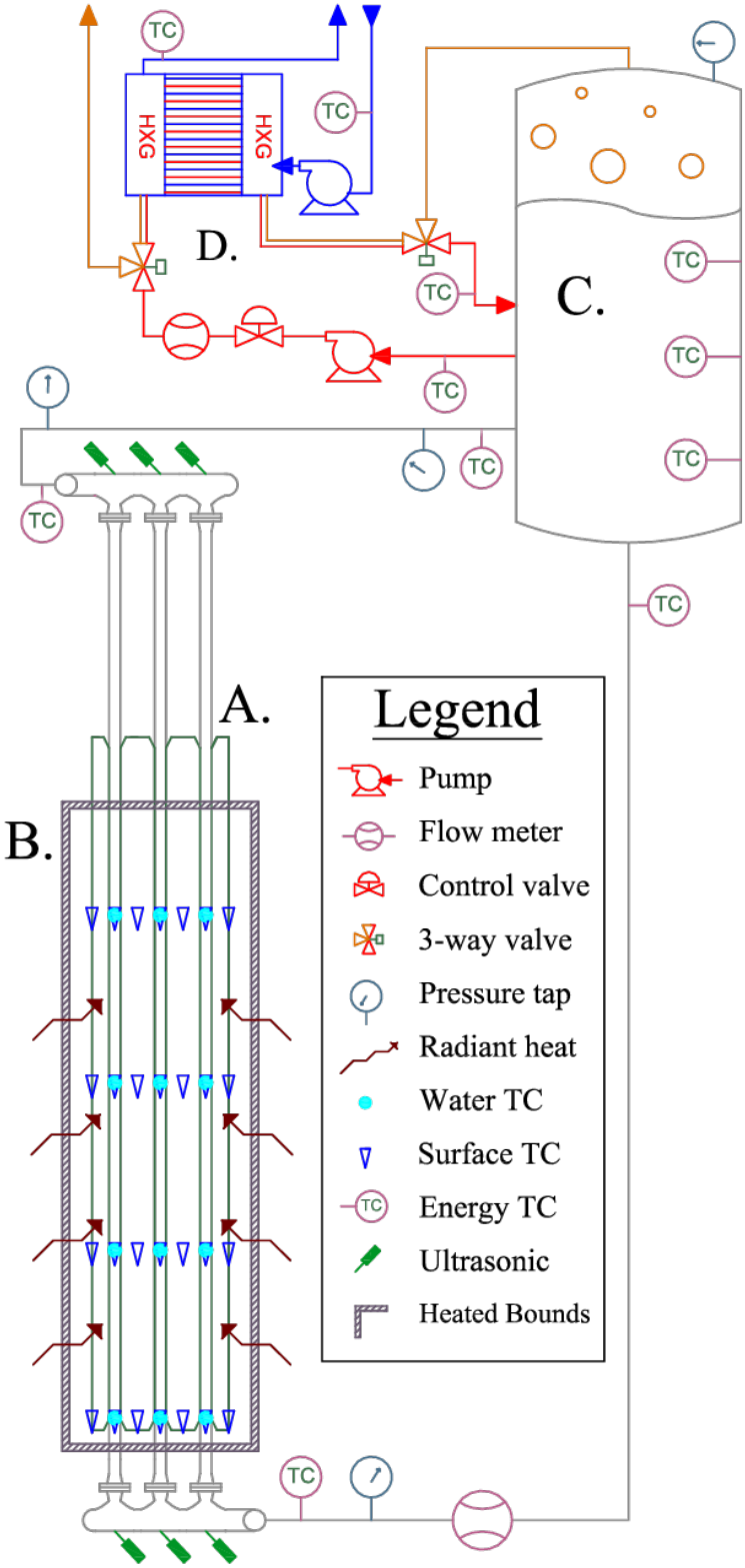

Figure 6.4: UW RCCS facility overview

The test section is comprised of three parallel riser tubes, separated by fins welded at their centerline, and is constructed entirely from Schedule 40 314L stainless steel tubing. Each fin, 17.8 cm wide and 6mm thick, results in a total pitch-to-diameter ratio of four among the three risers. The riser tubes extend 5m in length; however, the welded fins only join 3.6m of the riser length. An insulated enclosure contains the test section and heaters, and simulates the cavity of the GA-MHTGR that house the RPV and riser tubes. Figure 6.5 shows dimensions of the heated cavity, and Figure 6.6 provides a CAD image of the interior.

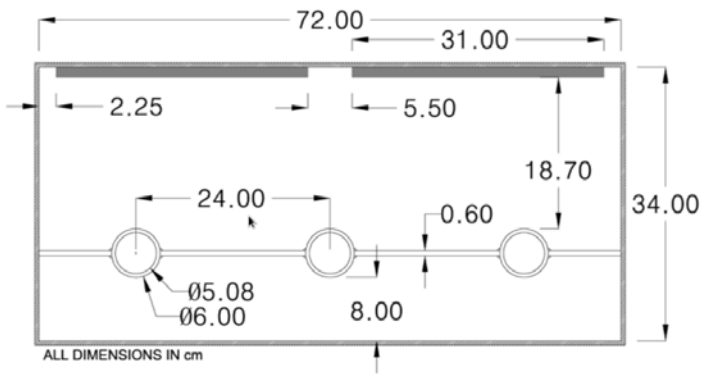

Figure 6.5: Dimensions of riser tubes and cooling fins, with heaters and cavity walls

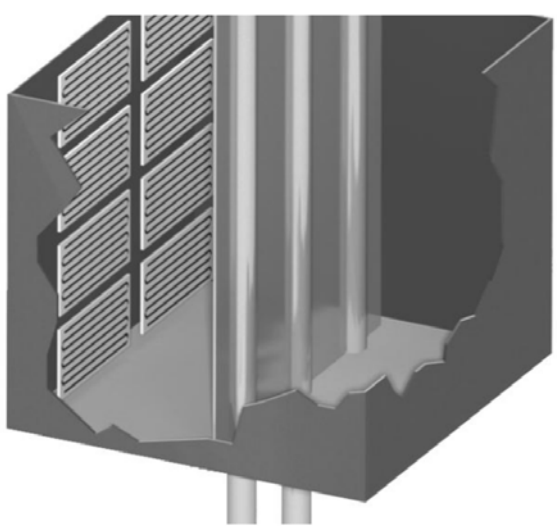

Figure 6.6: CAD model of heated interior, test ection and radiant heaters shown

Thermal Insulation

A strong effort was placed on thermal insulation of the entire RCCS facility, with a focus on the heated box. The network plumbing, inclusive of the water storage tank, downcomer, network connections, and headers, were insulated with industrial KFlex insulation, which has a thermal conductivity of 0.036 W/m-K. This closed cell elastomeric insulation is design for use in commercial and industrial HVAC applications, and can operate at a temperature range of -182 to 100 °C. This insulation was choose to due to its low price, high insulation performance. The low temperature limit was not a concern since the saturation temperature of water at atmospheric pressures is 100 °C.

The heated box was insulated by multiple types of fabrics, depending on the exact location and application. Immediately adjacent to the radiant heaters, 1.0 inch of Standard Block Microtherm insulation was used due to it's superior insulating performance. Immediately behind the heaters, 2.0 inch of Zircal-18 was used due to it's better structural integrity and high temperature tolerances. The back cavity and other low temperature areas were insulated with two layers of 0.25 inch Pyrogel. A table of the properties in Table **??**.

Table 6.1: Cavity insulation properties

Zircal-18		**Pyrogel-XT**		**Microtherm LWB**	
°C	W/m-K	°C	W/m-K	°C	W/m-K
200	0.07	200	0.028	200	0.022
400	0.09	400	0.046	400	0.024
600	0.10	600	0.089	600	0.028
Max:	*1100 °C*	*Max:*	*650 °C*	*Max:*	*1000 °C*

Power Supply

The power delivered to the test section is from thirty four radiant heaters, custom ordered from Mellen Heater Company. Each heater, 12”x6” in size, is capable of delivering up to 1,000 Watts at 1,100 °C. These heaters are mounted on a heater wall facing the test section, 2 columns wide by 17 rows high. The maximum total power available is 42 kW, with a heat flux of 25 kW/m2.

The heaters are grouped into 6 control zones, each with a separate Eurotherm power controller, model TE10P. These devices operate on 208V supply to the heaters, and analogue control signals. A 4-20mA signal can be sent to the controllers to specify a voltage, current, or true RMS power that is to be delivered to a given heater zone. A separate return signal, 0 - 5V, sends a value of any of the same parameters (current, voltage, true RMS power).

The controllers have been configured to operate on true RMS power, and perform this function by controlling the conduction of the thyristors for part of each half-cycle of the mains voltage, Figure 6.7. This ”Phase Angle” firing mode varies the firing angle in the same sense as the set point signal during each half cycle. Since the power delivered is not a linear function of the firing angle, online measurements of RMS voltage and current determine the returned RMS power.

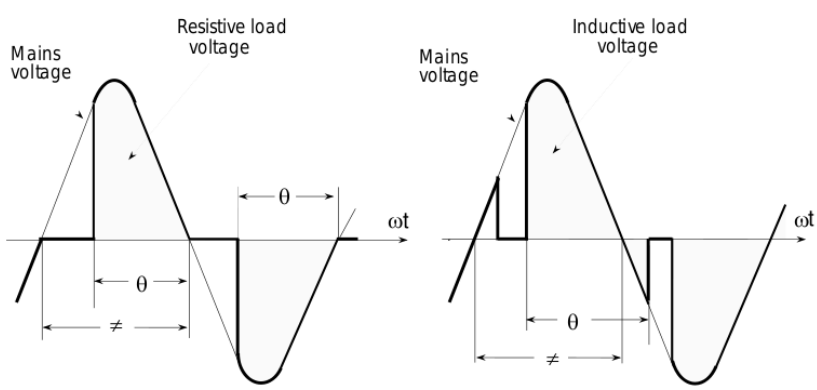

Figure 6.7: TE10P phase angle firing mode

Power Removal

Power is removed from the RCCS facility via a closed loop that pulls water out from the water storage tank, cooled via a heat exchanger (HXG), and pumped back into the tank, Figure 6.8.

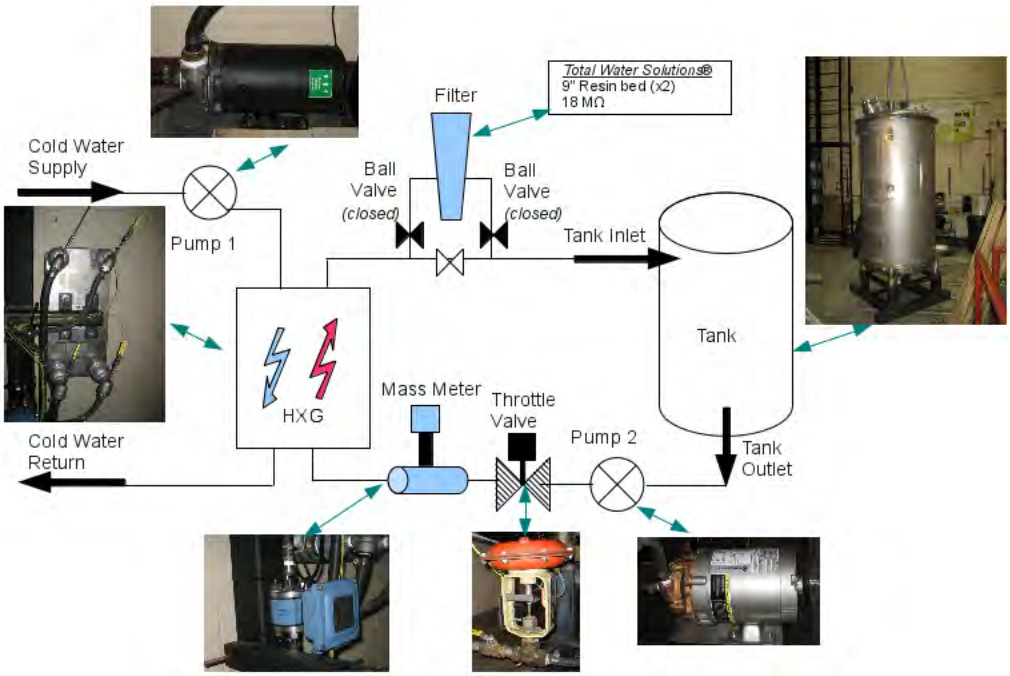

Figure 6.8: Steady state energy removal network diagram

Two legs comprise the HXG network, a cold and hot leg. The cold leg of the system operates by a 3 HP, 3 phase water pump, AMT Model 315D-98 that draws water from the chilled building supply at 5 °C, through one side of the HXG, and back into the building return. The pump operates at a constant power, and thus the removal by the cold leg cannot be changed. With a constant power removal on the cold leg, the power removal must be controlled by the hot leg. 0.3 HP single phase water pump, AMT Model 368A, into the hot side of the HXG, and back into the top of the tank, ultimately exiting via a sparger to ensure uniform cold water distribution with the bulk of the tank. The power matching is obtain via a pneumatic throttling valve that increases the system head and thus decreasing the

flow rate. This throttle valve operates with a 20 psi air supply, and outputs an air pressure that varies with a 0 - 20mA control signal. To measure the energy removal, a 0.5" magnetic volumetric flow meter is placed in the system to measure the amount of water flow.

The HXG is a Brazed flat plate type heat exchanger manufactured by GEA, Model FPN10x20L-70. It contains 70 chevron plates oriented in a counter flow direction, and is capable of up to 51kW heat transfer performance. During single phase experiments, this heat exchanger operates in a counter flow operation with hot water from the water tank and cold water from the building supply. During two-phase experiments, it acts as a steam condenser by a pipe that pulls the steam into the hot side while cooling it to the liquid phase by the cold water from the building supply

6.3 Structural Considerations

Since the facility was custom built in it's entirety, and the design was based only on a few key specifications (e.g. 2" diameter riser, P/D = 4), leaving many design decisions to the researchers discretion. Of these decisions, they fell into two categories: structural safety and practical logistics. Safety decisions included accounting for the thermal expansion and hence structural integrity of the test section and high temperature obstacles. Practical considerations included radiant heater mounting, whose design was key in ensuring a uniform heat flux deposition on the test section riser tubes. Additionally, an optimization study was performed that minimized the variation in heat flux distribution, while also minimizing losses to the surrounding. A detailed explanation of these decisions will be given, with structural and logistical reasons outlined, in the following sections.

6.3.1 Thermal Expansion

The thermal expansion of the facility is a phenomenon that cannot be ignored. Preliminary analytical calculations showed the expected temperatures of the fin center lines will meet or exceed 380 °C, while the cooler water tube, just 3.5" away, will be maintained at a cold 100 °C. For a 304L stainless steel alloy, this temperature difference would cause a 4.8 m

unrestrained fin to elongate 2.06 cm greater than an unrestrained water tube. With box fixed to a combined and common elongated length, thermal stresses will be introduced. The expansion of an unrestrained material is given by Eq. 6.1.

$$\delta = \alpha \Delta T L \tag{6.1}$$

For a system of co-restrained tube and fin, manipulations of strengths of materials equations and compatibility relationships (Beer, 2006) can be used to calculate the final thermal stress experienced by the fin, with a similar procedure carried out for the tube stress.

$$\sigma_{fin} = \frac{(\alpha E^2 A_{tube}(\Delta T_{fin} - \Delta T_{tube}))}{E(A_{tube} + A_{fin})} \tag{6.2}$$

Thermal modeling was performed on the experimental design to obtain new center line temperatures for P/D ratios ranging from 6 to 4, given expected heat flux and power levels. Analytical solutions were obtained for each of 3 configurations, and validated by an ANSYS simulation, where exact dimensions, material properties, and simulation boundary conditions modeled. Results given below in Table 6.2.

Table 6.2: Thermal induced stress for varying P/D ratios, Analytical vs ANSYS

P/D [-]	Fin Center [°C]	δT [mm]	Analytical [MPa]	ANSYS [MPa]
5	387.11	4.04	404.54	435.26
4	304.53	4.27	324.24	339.38
3	207.38	4.58	184.55	198.45
2	131.59	4.78	71.97	77.66

Designs with a P/D of 5 and 4 show thermal stresses that exceed or were close to the materials yield strength (290 MPa). Designs with P/D of 4 fell within safe limits. The design was further modified by incorporating notches at the tops of the fins, at the intersection point with the tube. This area was identified as having the highest stress concentration, thus a notch allowing room for expansion was cut. This decision was made to add a level of safety

and accommodate any high power and temperatures transients that may occur. To reduce costs, off the shelf tubes were used, 2" Sch40 304L stainless steel, and fins were custom sheared from the same material. At the UW facility, this test section assembly is repeated 3 times, yielding 3 total tubes, 2 full fins, and 2 half fins. The total height is 4.8 m with a total width of 72 cm. Engineering drawings of the notched fins and test section is given in Appendix C.

6.3.2 High Temperature Supports

The mounting of the radiant heaters poses a structural design challenge, with the front surface of the heater reaching a maximum of 1,100 °C during operation. The yield stress of 316 stainless steel versus temperature is shown in Figure 6.9. It can be seen that at higher temperatures, the yield stress drops to dangerously low values, reaching 103 MPa at 1,000 °C.

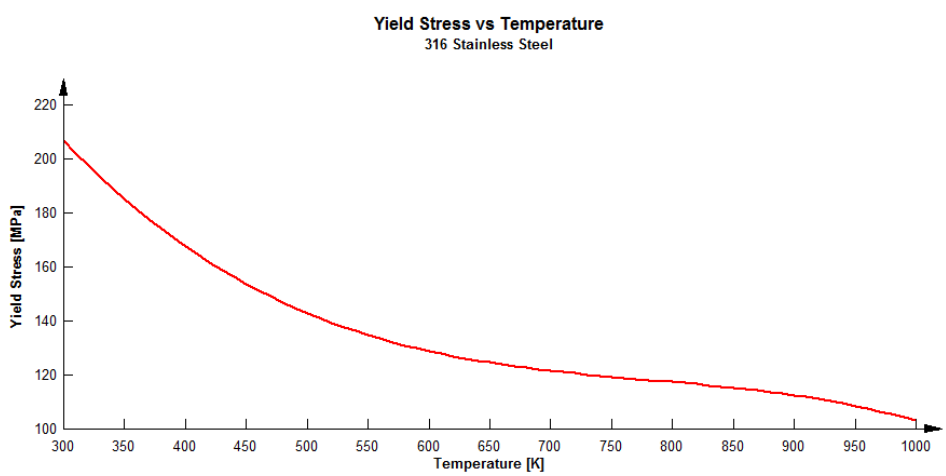

Figure 6.9: 316 Stainless steel yield stress versus temperature

The design analysis began with a simplified analytical calculation, the bending of a beam under a point and distributed load, Appendix B. It was found that for a simple beam under point loading, 1.31 lbf would reach the yield stress, while a more representative uniformly distributed load would reach the yield stress at 3.64 lbf. The analysis was then refined by a ANSYS thermal simulation, imposing a prototypical temperature distribution in the bolt

and conduction and convection boundary conditions.

6.3.3 Heater Spacing

To ensure optimal heater placement, a parametric study was performed that varied the heater placement configuration while optimizing two primary variables: uniform heat deposition into the test section, and minimal heat loss to the surroundings.

A two-dimensional simulation was performed in ANSYS workbench where a uniform heat flux boundary condition was imposed on the surface of the heaters, and heat flux and temperature parameters were measured on the 3 riser tube surfaces. A Goal Driven Optimization study was performed, with a high priority placed on uniform temperature and heat flux, and a medium priority on heat loss to the surroundings. A summary of all the design points is given in Table 6.3.

Table 6.3: Goal driven optimization results for heating geometry and position

Design Point	Heater-Heater Gap [inch]	Heater-Tube [inch]	Δ T [K]	Δq $[W/m^2]$	Q_{loss} [W]
1	0.25	4	19.87	193.88	920
2	1.75	4	9.43	121.33	918
3	2.5	4	2.40	88.61	920
4	0.25	8	8.36	111.92	968
5	1.75	8	3.26	74.57	969
6	2.5	8	1.10	55.86	992
7	0.25	12	2.54	70.19	1115
8	1.75	12	1.05	64.58	1117
9	2.5	12	0.76	57.90	1128

The final design point, 6, was obtained with a heater - heater gap of 2.5", and a heater to tube spacing of 8". This design point resulted in a Δ T across the riser tube walls of 1.10 °C while loosing 55.89 W/m2 to the surrounding walls, totaling just under a kilowatt of heat loss through the insulation box.

6.4 Data Acquisition

The RCCS facility is heavily instrumented to assist in data acquisition and evaluation of the heat removal performance. Thermocouples record surface and water temperatures and volumetric flow meters monitor water flow rates. The power controllers receive and transmit a signal that allows for control and monitoring of supplied heater power. All the data acquisition devices feed into a National Instruments DAQ. A SCXI-1349 chassis houses 4 expansion cards:

1. 1102: Analogue Input x32 TC
2. 1102: Analogue Input x20 TC, x6 TE10P return signal
3. 1124: Analogue Output x6 TE10P analogue control signal
4. 1163R: Digital Relay TE10P 120V power

A total of sixty four thermocouples are placed throughout the facility at key points, measuring temperatures of: fin and tube surfaces, interior network water, HXG inlets and outlets, tank bulk, and safety values.

The test section is most heavily instrumented, with 51 of the total thermocouples placed on or inside of. 12 TCs are welded on the front tube surface, 16 on the front fin surface, 8 on the rear fin surface, and 15 inside the riser tubes measuring the water temperature. 7 thermocouples are placed on the network plumbing, measuring the test section inlet and outlet temperature, 4 of the bulk water storage tank, and 1 on the outlet of the tank. 4 TCs measure the HXG hot and cold inlet and outlet. Finally, 4 TCs are placed in the rear heater cavity to ensure safety operating temperatures. Detailed locations of all TCs are given in Appendix C.

Two magnetic flow rate meters are used to measure the volumetric flow rate in the system and on the hot leg of the HXG. A 3” meter, model Flocat IFC 090, is placed at the bottom of the network plumbing, prior to the entrance to the test section. A smaller, 0.5”, meter is

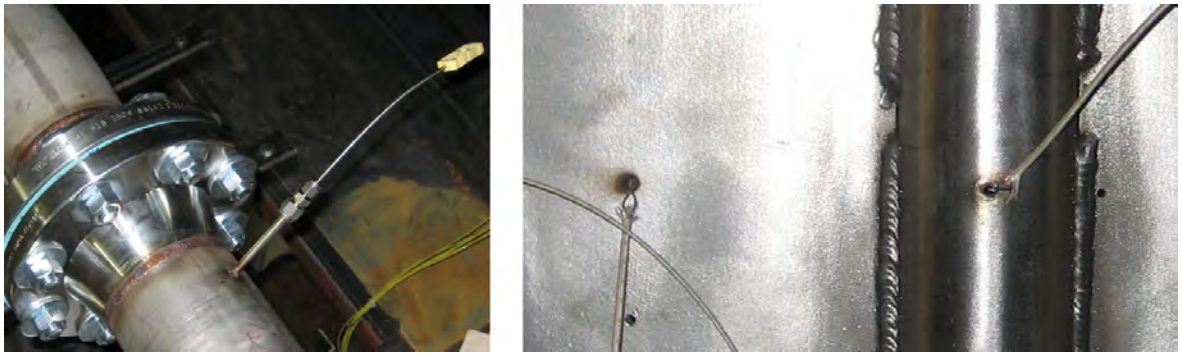

Figure 6.10: Internal water temperature, tube and surface temperature TC

placed on the hot leg of the heat exchanger network to measure flow that is pulled out of the tank and into the heat exchanger.

6.4.1 Ultrasonic Velocity

The UVP instrument, shown below in Figure 6.11 used in this research was manufactured by Met-Flow S.A., and consists of three components: the measurement probe, the main unit, and the user interface. The measurement probe is a small (typically 8mm diameter) piezoelectric transducer and is connected to the main unit by a magnetically-shielded cable. Electrical signals from the transducer are processed and digitized by the main unit. These signals are then sent to a computer from the main unit by the user interface software, where the data is stored and analyzed.

Figure 6.11: UVP instrument (left) and standard ultrasonic transducers (right)

Ultrasonic velocity profiles (UVP) measurements in each of the individual riser tubes were performed by five transducers (TDX) mounted axially inline with the riser tube, Figure **??**. The face of the TDX is mounted flush with the inner surface of the header via a compression fitting that provides a water tight seal. A cable from the TDX to the data acquisition unit provides the signal to the proprietary software, UDV-Duo.

Theory of Operation

The ultrasound Doppler velocimetry (UDV) system, manufactured by Met-Flow, operates on the premise of measuring both time-of-flight and the Doppler shift, including the sign of the shift, at the instant of the echo reception. A single probe acts as both the receiving and transmitter. The UVP measures an instantaneous velocity profile in liquid flow along the ultrasonic beam axis. This non-invasive position of the TDX emits a cylindrically shaped burst of ultrasound-waves into the flow field of interest. The characteristic acoustic velocity in the medium defines the medium itself, and a fraction of the emitted wave are reflected from reflectants in the flow, typically in the form of impurities or introduced tracer particles. After the waves are emitted, the TDX changes to a receiving mode, capturing both time of flight and the Doppler shift. It is the Doppler shift that provides information to deduce the velocity.

The echo from the transmitted signal reaches the listening transducer after some time delay, t.

$$t = \frac{2\ x}{c} \tag{6.3}$$

t time delay between transmitted and received signals

x distance of scattering particle from transducers

c speed of sound in the medium

If the particle is in motion along the acoustic axis of the transducer, the frequency of the ultrasonic wave becomes 'Doppler shifted' between emission and reception by the transducer.

This so-called Doppler effect was named after Austrian Scientist Christian Doppler, who noted that that the frequency perceived by a stationary observer was higher than the actual frequency emitted by a source moving toward the observer. This change in frequency can be measured and ultimately provide not only the velocity of the moving particle but also the direction of the movement. Thus, the velocity magnitude and direction (indicated by the sign of the Doppler shift frequency) of the scattering particle can be determined. A detail explanation and presentation of governing principles in provided in the appendix.

The corresponding data output from the system is in the form of an nxm matrix, with a velocity value at each channel for a corresponding time. The reduction of data depended on the flow regime to be recorded. For laminar flow conditions, an averaging technique was used, and for turbulent flow conditions, a maximum technique was used. The averaging technique, Figure 6.12, was performed as follows: the velocity for a given time was averaged over all channels, yielding a data set that gave a single averaged velocity value versus time, and then all of these velocities were averaged a 2nd time to determine a bulk velocity for the entire measurement. The maximum technique was performed by taking the maximum recorded velocity over all channels for a given time. Then, as with the previous method, the maximum values were averaged over all times to determine a bulk velocity for the entire measurement.

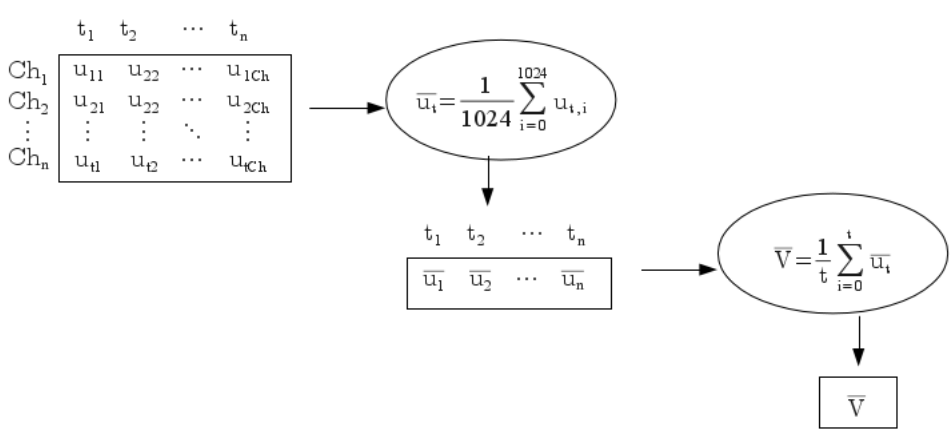

Figure 6.12: Averaging post-processing technique for UDV

Method Validation

The UDV system was validated against two separate tests. These were performed outside and separate from the RCCS facility to confirm the working operation and correct data reduction procedure. The TDX was placed at the bottom of a test section, inline with the flow. The flow was introduced from the top, with a bulk water storage tank supplying the hydrostatic head. The first test was performed with a 1.0" diameter PVC tube, 12" in length, and the 2nd test was a 2.0" diameter PVC tube, 48" in length. These two tests represented both laminar and turbulent test conditions. Velocity results from the setups were validated against the known flow rate, which was a mass weight averaged of the flow by an electronic scale. For any given test, a series of 3 measurements were taken to ensure accurate scale readings. The reading from the scale, in kilograms, was back calculated to a mass flow rate by recording the time of flow collection with a stop watch. To calculate the actual velocity inside the test section (for comparison to the UDV system), known geometry and material properties were used. Results from both test sections are given below in Table 6.4. It can be seen that for laminar test conditions, the averaging technique from the 1st test section compared extremely well, while for turbulent conditions, the maximum technique in the 2nd test section provided better results.

Table 6.4: Validation results for UDV testing

	Average	Maximum	Actual Velocity	*Re*
1" Dia. Test Section	**92.022**	120.816	**92.593**	*2458*
	150.432	188.445	**149.765**	*3975*
2" Dia. Test Section	48.273	**92.875**	**93.244**	*4950*
	52.261	**92.145**	**93.426**	4959

6.4.2 RBI Optical Probe

In order to observe changes in hydrodynamics conditions in two phase flow regime, a double tip intrusive optical probe was used, 6.13. Manufactured by RBI Instrumentation, France, the optical probe is capable of providing accurate measurements of different parameters. Using statistical methods, local measurements such as void fraction, bubble diameter and interfacial area at superficial gas velocities can be computed and analyzed. Key components of the RBI optical device include:

1. A double tip optical fiber probe: Designed with a prism configuration, the optical probe is used for phase detection based on the discrete changes in refractive index of two phases i.e. Snells Descartes law of refraction.
2. An Opto-electronic unit: Connected directly to the double tip optical fibers, the Opto-electronic unit receives the feedback response and integrates the phase indicator functions of the emitted light using a thresholding operation method.
3. Data acquisition box: The data acquisition box collects and converts the analog signals into TTL signals which are then amplified and transformed into output signals of 0V and 5V corresponding to water and air accordingly.

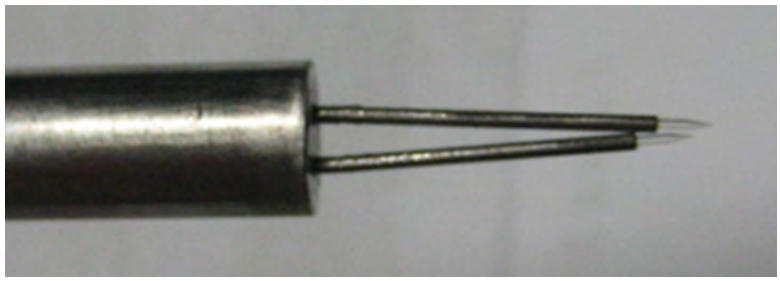

Figure 6.13: Dual tip RBI probe, 0.5mm sapphire tips visible

Prior to the commencement of its full scale use, the spatial location of each fiber was defined and the phase indicators were set. A separate effect test was carried using a 1" vertical column of stagnant water. The optical probe was fixed at the top of the column.

Injecting compressed air with known flow rate from the bottom of the test column, air bubbles were generated and flowed in the direction of the optical probe. Local measurements of the void fraction, bubble rise velocity and bubble diameter were computed and analyzed. This dataset was compared to theoretical calculations for the bubble rise velocity coupled with some visualization studies. Results from the separate effect tests showed less than 2% difference.

The positioning of the optical probe was technically guided by our judgment of expected two-phase flow region within the UW natural circulation loop as shown in Figure 6.14, 6.15 i.e. points on lowest pressure.

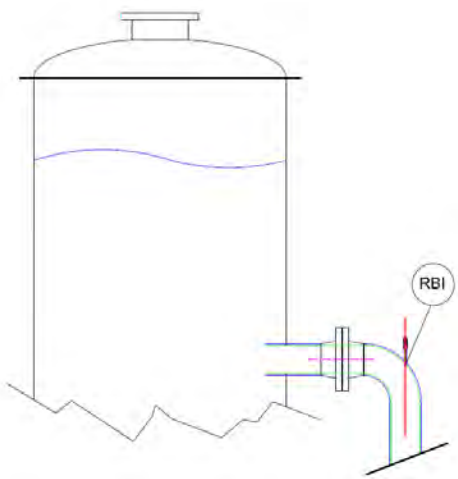

Figure 6.14: AutoCAD drawing of tank, RBI installation

Figure 6.15: Intalled RBI at vertical section into tank

In addition to data from other thermal-hydraulic processes, key physical parameters such as local void fraction α and bubble rise velocity will guide our understanding of the integrated system behavior and determination of flow distribution under two-phase flow conditions. Increasing void fraction could have significant changes on the dynamics of the system and affect the heat transfer characteristics. Using the optical probe, we can also deduce the liquid and superficial gas velocities. Data from each optical fiber was sampled at

about 2MHz and acquired over an average of multiple 10 sec periods.

6.4.3 Calibration

Calibration of the thermocouples was performed by a circulating hot water bath. Each thermocouple to be calibrated was removed from the test section and placed together with a Platinum RTD, model 5624. Upon reaching the desired calibration temperature, each thermocouple was compared against the known RTD temperature. Respective data points for each thermocouple were defined in LabVIEW, empirically to the reference RTD temperature, then extrapolated to the desired maximum. The final result reduced the uncertainty in the thermocouples from +/- 1.1 °C to +/- 0.2 °C.

Calibration of the magnetic flow rate meters were assumed from the factory, with the only configuration performed being a zero point set during a stagnant flow condition. The variation is water purity (tap, filtered tap, 20 M Ω) was found to have no effect on the stability or accuracy of the meter, however an offset zero point was observed, which was accounted for in post processing. Each data acquisition device has an associated uncertainty, which is summarized in Table 6.5.

Table 6.5: Data aquisition measurement uncertainty

Device	Model	Uncertainty in Measurement
Interior TCs	HKMQ-IN-125G-12	0.2 C (with RTD calibration)
Surface TCs	HH-K-20	1.1 C OR 0.4% (Factory)
3" Flow Meter	Flocat IFC 090	+/- 0.3% of measured value OR +/- 0.2% of measured value +1mm/s
0.5" Flow Meter	Rosemount 8712C	+/- 0.25% + 1mm/s (for .04-6ft/s) +/- 0.25% + 1.5mm/s (for greater than 6ft/s)

The magnetic flow rate meters followed a relative error, a percentage of the measured flow rate, plus an absolute error. The deviation from the measured flow velocity over the expected flow range is shown in Figure 6.16 for the large Optiflux 1000 meter.

The interior thermocouples, Type K, part HTMQIN-125G-12 were purchased with "Spe-

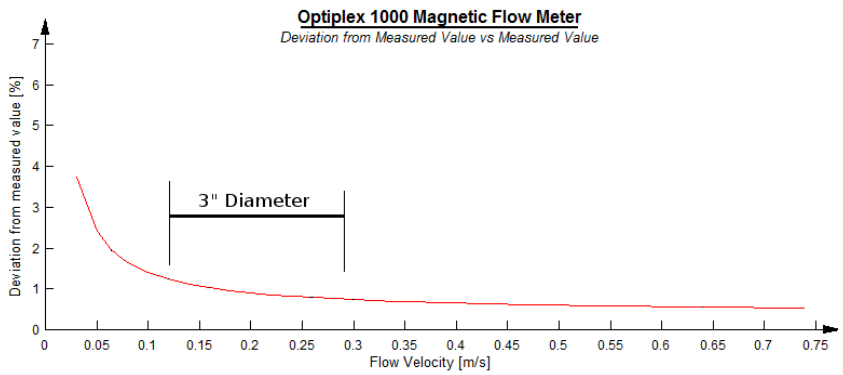

Figure 6.16: Deviation from measured value, Optiflux 1000

cial Limits" of error in their calibration. Thus, from the factory, the Omega TC's are accurate to within +/- 1.1 °C. Surface mount thermocouples were purchased on a bulk spool, 50' in length, and of the standard limits of error, accurate to within +/- 2.2 °C. The primary calculation of interest in the simplified steady-flow thermal energy equation, Eq. 6.4

$$Q = \dot{m}C_p(T_{out} - T_{in}) \tag{6.4}$$

To obtain the uncertainty in this calculation, from the measured data acquisition, an expansion into the variables of interest must be performed, namely the measured velocity.

$$\dot{m} = U_m A\rho \tag{6.5}$$

Which can be rewritten in terms of the measured velocity.

$$Q = U_m A\rho C_p(T_{out} - T_{in}) \tag{6.6}$$

Propagation of error for the desired thermal energy, Q, is dependent on i variables, the velocity, inlet and outlet temperature.

$$\sigma_Q^2 = \sum_i \left(\frac{\partial Q}{\partial X_i}\right)^2 \sigma_i^2 \tag{6.7}$$

The full propagation of error is given below

$$\sigma_Q^2 = \left(\frac{\partial Q}{\partial U_m}\right)^2 \sigma_{U_m}^2 + \left(\frac{\partial Q}{\partial T_{out}}\right)^2 \sigma_{T_{out}}^2 + \left(\frac{\partial Q}{\partial T_{in}}\right)^2 \sigma_{T_{in}}^2 \tag{6.8}$$

The relative errors for each are given below in Eq. 6.9 6.11.

$$\left(\frac{\partial Q}{\partial U_m}\right) = A\ C_p \rho (T_{out} - T_{in}) \tag{6.9}$$

$$\left(\frac{\partial Q}{\partial T_{out}}\right) = A\ C_p \rho U_m \tag{6.10}$$

$$\left(\frac{\partial Q}{\partial T_{in}}\right) = -A\ C_p \rho U_m \tag{6.11}$$

Thus, the full uncertainty equation for the thermal energy in the test section in given by

$$\sigma_Q = \sqrt{A^2\ C_p^2 \rho^2 [(T_{in} - T_{out})^2 (\sigma_{rel} U_m + \sigma_{\text{abs}})^2 + 2U_m^2 |\sigma_T|^2]} \tag{6.12}$$

As a sample case, a volumetric flow rate of 8 GPM was measured at a Δ T of 4 °C. This would yield an energy of 8,409.89 +/- 601.86 Watts, or 7.14 %.

6.5 Operation

The experimental facility is controlled by a LabVIEW program, which is subsequently connected to the NI Chassis for reading of data acquisition devices. Nearly every operation can be performed from the computer, with the exception of manually activating the hot and cold leg water pumps. The LabVIEW code, refined over one year of testing and operation, incorporates such features as online monitoring of energy balances, time averaged values, safety features, and automated controls. Screen shots of the program are given in Appendix D. The order of operations for a typical run are summarized below

1. Specify run number, e.g. Run024, and enter test conditions and notes on 'Logging' tab. This will automatically write a text file with test conditions and notes for later reference.
2. Enable logging with a defined recording frequency. This will begin writing a .csv file to the current directory and will write all data acquisition values.
3. Initialize heaters. Turn on the 120V power, 'enable' each controller, specify the total desired power and ramp time. Once the 'Begin Ramp' in enabled, a ramp to the specified power over the desired duration will begin.
4. The ramp will automatically stop after the time frame, and now the system will be fully operational. During this time, experimental testing may begin, either by a steady state condition or continued operation until two-phase
5. Upon conclusion of the test, the heaters are ramped down for safety and thermal conditions over a duration of 360 seconds. When the ramp down concludes, the test is complete and the logging may continue for post-test data collection, or halted, concluding the test in it's entirety.

A sample test output logging file is given in Appendix E.

Chapter 7

Experimental Results

Results from experimental data sets will be presented in the following section. Attention will first be given to a characterization of the facility: identifying nominal behavior patterns, repeatability validation, energy balance calculations, heat loss methods, and data uncertainty. Then, a summary of the single-phase tests performed at steady state will be presented, following by results at two-phase saturation conditions. Finally, an in-depth review of the theory and results from the key data acquisition instruments will be made.

7.1 Characterization

7.1.1 Heat Loss

Heat loss measurements of the RCCS facility were determined using a 3 tier approach, which coupled experimental data and heat transfer correlations.

Tier 1: Hand measurements with IR thermometer

Tier 2: Water temperatures via LabVIEW data logging

Tier 3: Cross check with energy balance calculations

Tier 1 heat loss calculations began with surface measurements at 64 locations via a hand held IR thermometer, *Model 62.* Forty of these measurements were on the surface of the heater box, 12 on the surface of the angle iron supports, and 12 on the surface of the network insulation. Detailed locations on IR measurements on the test facility are given in figures in Appendix F.

From these 64 temperature measurements, a representation was made in ANSYS to help visualize the temperature distribution, Figure 7.1. Significant heat losses are observed at

the top of the insulated heater box. Due to the geometry of the open cavity, all the hot air inside the box rises to the top, leaving the cooling air to stagnant at the bottom.

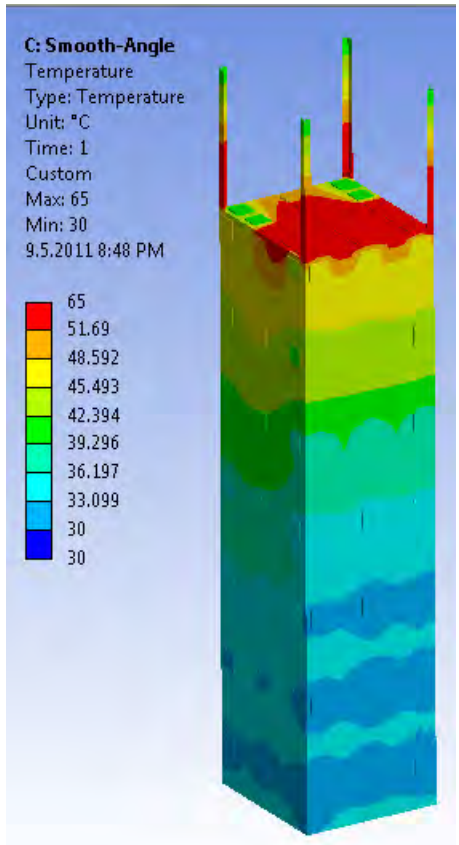

Figure 7.1: Temperature profile of heated enclosure

To determine the heat loss to the ambient air off the heater box and support structures, a convective heat transfer formula was used. Each measurement was used as a bulk surface temperature for a known surface area, and using correlations from ASHREA for ambient heat transfer coefficients from room air, the heat loss could be determined. The heater box is divided into 40 individual areas, summing to the total area of 10.7218 m^2. A higher density of measurement locations is concentrated at the top of the heater box, where the highest temperatures are seen and largest gradients observed. The angle iron supports were divided into 4 measurement areas per angle iron, each with a full size of 1.5”x1.5”x18”.

$$Q_{lossheaterbox} = h_{convambient}\ A_i\ (T_{surface} - T_{ambient}) \tag{7.1}$$

Tier 2 heat loss calculations were obtained by recording times of IR measurements, and cross referencing them with internal water temperature and mass flow rate data recorded from LabVIEW. A resistant network of the total heat transfer from the bulk internal water, through the piping, network insulation, and finally to a recorded surface measurement was drafted to assist in the calculation, Figure 7.2. Material properties for the KFlex insulation and 304L Sch. 40 pipe were pulled from manufacturers resources.

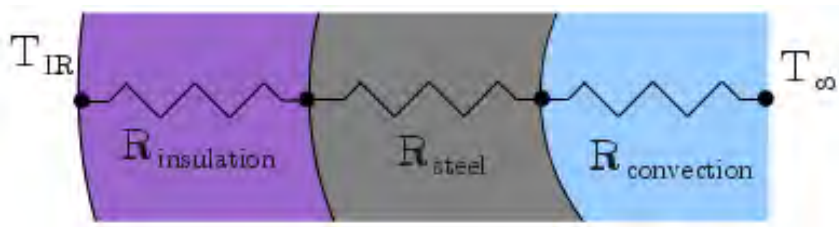

Figure 7.2: Resistance network for network heat loss

The internal convective heat transfer coefficient was determined by the aid of EES. With water temperatures and a mass flow rate recorded from LabVIEW, thermal parameters such as the Prandtl Reynolds, and thermal conductivity were calculated in EES. Then, correlations for internal forced flow for fully developed flow in a tube yielded the Nusselt number, and finally the convective heat transfer coefficient, h. The total resistance network was then determined over the temperature range of measured insulation surface temperature, and recorded bulk water temperature.

1) Resistance due to conduction through stainless steel pipe

$$L_i = [length_i]m \tag{7.2}$$

$$r_i = [radius_i]m \tag{7.3}$$

$$k_i = Conductivity(304L) \tag{7.4}$$

$$R_{condsteel,i} = \frac{\ln(r_o/r_i)}{2\pi L_i \ k_i} \tag{7.5}$$

2) Resistance due to conduction through insulation

$$L_i = [length_i]m \tag{7.6}$$

$$r_i = [radius_i]m \tag{7.7}$$

$$k_i = Conductivity(Insulation) \tag{7.8}$$

$$R_{condinsulation,i} = \frac{\ln(r_o/r_i)}{2\pi L_i \ k_i} \tag{7.9}$$

3) Resistance due to convection inside stainless steel pipe

$$k_i = Conductivity(TC_i) \tag{7.10}$$

$$\mu_i = Viscosity(TC_i) \tag{7.11}$$

$$Re_i = \frac{4\dot{m}_i}{\pi r_i \mu_i} \tag{7.12}$$

$$Pr_i = Prandtl(TC_i) \tag{7.13}$$

$$Nu_i = 0.0265 {Re_i}^{4/5} {Pr_i}^{0.3} \tag{7.14}$$

$$h_i = Nu_i \ k_i/r_i \tag{7.15}$$

$$R_{conv,i} = 1/(2\pi r_i \ L_i \ h_i) \tag{7.16}$$

4) Total heat loss

$$Q_{loss,i} = \frac{TC_i - T_{surface,i}}{R_{conv,i} + R_{condsteel,i} + R_{condinsulation,i}} \tag{7.17}$$

A flow diagram for Tier 1 and Tier 2 methods is given in Figure 7.3.

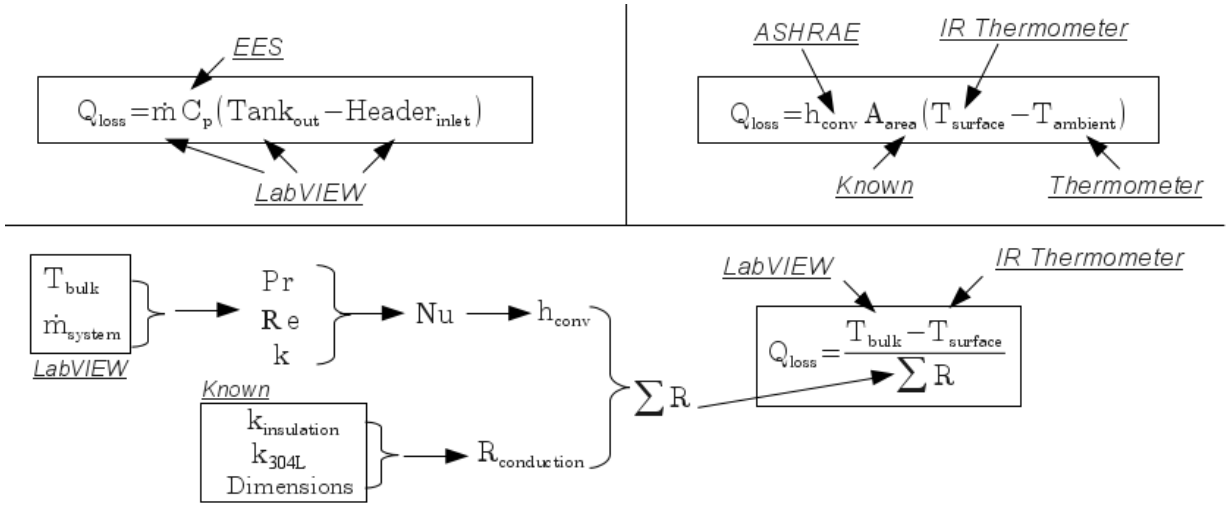

Figure 7.3: Flow chart for heat loss calculation

The 3rd and final tier of heat loss measurements is a cross check with energy balance data. The total heat loss from the 1st and 2nd tier calculations were compared with the difference of the supplied heater power to the calculated energy of the test section and hot leg power removal. A summary of measured heat losses from is given in Table 7.1.

Table 7.1: Heat losses during steady state and two-phase conditions. Percent heat losses from total energy at various integral powers. Contributions from facility components.

	T_{bulk} = 30 °C	Saturation
4.63 kW	20.92%	-
7.27 kW	16.70%	-
9.91 kW	12.96	-
12.5 kW	11.70%	19.75%
15.19 kW	11.53%	17.59%
	T_{bulk} = 30 °C	Saturation
Heated Enclosure	88.20%	43.20%
Network Piping	5.80%	53.20%
Support Structures	6.00%	3.60%

7.1.2 Repeatability

Several experiments to determine the repeatability of the RCCS facility were performed, with one set at single phase steady-state conditions and another at saturation.

Steady state repeatability experiments used baseline conditions of a 22 °C inlet temperature and 9.91 kW power supply. Care was taken to ensure identical initial conditions, except for Run004 which started at zero mass flow rate (versus 0.2 kg/s for Run005 and Run010). Table 7.2 gives the system conditions and resulting parameters, and Figure 7.4 show the compared mass flow rates. The mass flow rate and test section energies show excellent repeatability, to within +/- 2.2 percent. The interior water temperatures show excellent repeatability as well. The bump that can be seen during Run004 is due to an undershooting of the HXG hot leg removal. The inlet temperature exceed the desired value, thus the heat removal was configured to be greater than the supplied power to bring the temperature back down to the goal 22 °C.

Repeatability tests at saturation were performed with 80% initial tank volumes, 70 °C bulk temperature, and 15.19 kW of supplied heater power, Figure 7.5. Given the extreme sensitivity of the facility during two-phase, measurements of the initial tank volume were measured to within 0.25" and at the same system temperature to ensure both equal volume and mass. As with the single phase repeatability tests, a one hour ramp was initiated before reaching the full power of 15.19 kW.

A complete set of figures for single and two phase repeatability data sets are given in Appendix X.

Table 7.2: Initial conditions and test parameters for single phase repeatability

	Repeat #1	Repeat #2	Repeat #3
Run Number	Run004	Run005	Run010
Max Power Input Applied	9,917 W	9,917 W	9,917 W
Heat Flux Applied	6.06 kW/m^2	6.06 kW/m^2	6.06 kW/m^2
Max Power Input Actual	10,002.9 W	10,014.3 W	10,002.9 W
System Volume	80 %	80 %	80 %
Initial Riser Inlet Temperature	15.6 °C	16.0 °C	16.8 °C
Initial Δ T between headers	0.4 °C	0.2 °C	0.2 °C
Tank average temperature	16.4 °C	16.1 °C	16.9 °C
Power Ramp time	60 min	60 min	60 min
Steady State Time	66 min	90 min	130 min
Total Test Time	273 min	383 min	396 min

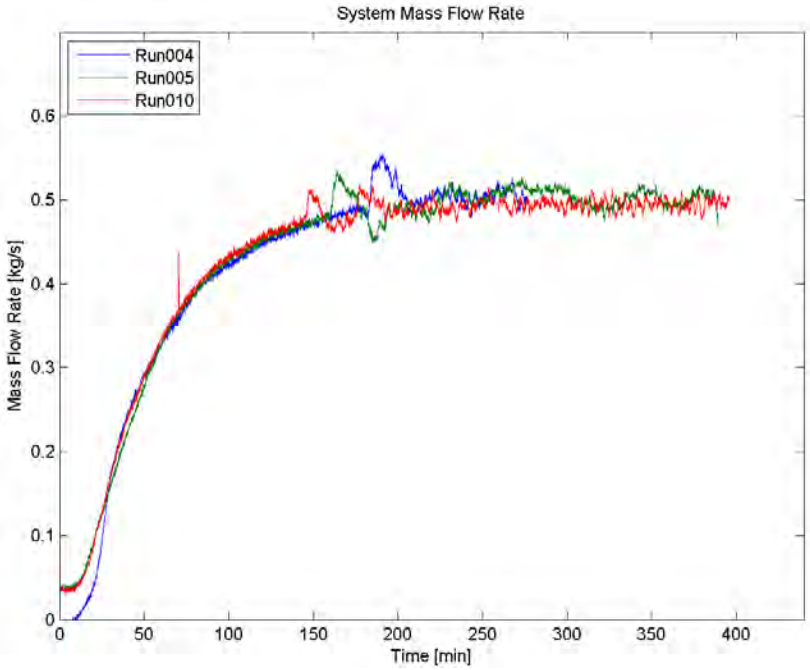

Figure 7.4: Repeatability of single phase experiments. Mass flow rate, Run004,005,010

Table 7.3: Test conditions and results from two-phase repeatability tests

	Repeat #1	Repeat #2
Run Number	Run052	Run058
Heater Power	14.826 W	14.830 W
Heat Flux	9.29 kW/m^2	9.29 kW/m^2
Test Duration	622.5 min	542.2 min
Boiling Duration	261.4 min	260.9 min
Total Condensed	18.16 gal	19.10 gal
Condensation Rate	4.16 gph	4.39 gph
System Volume	80 %	80 %
Riser Inlet	93.66 C	93.95 C
Riser Outlet	96.71 C	96.97 C
Mass Flow Rate	1.01 kg/s	1.00 kg/s
Void Fraction	1.19	1.14
Pressure Drop	257.09 Pa	256.61 Pa
Hydrostatic Pressure	9.44 psi	9.41 psi
Tank Gas Space	13.28 mmHg	13.49 mmHg

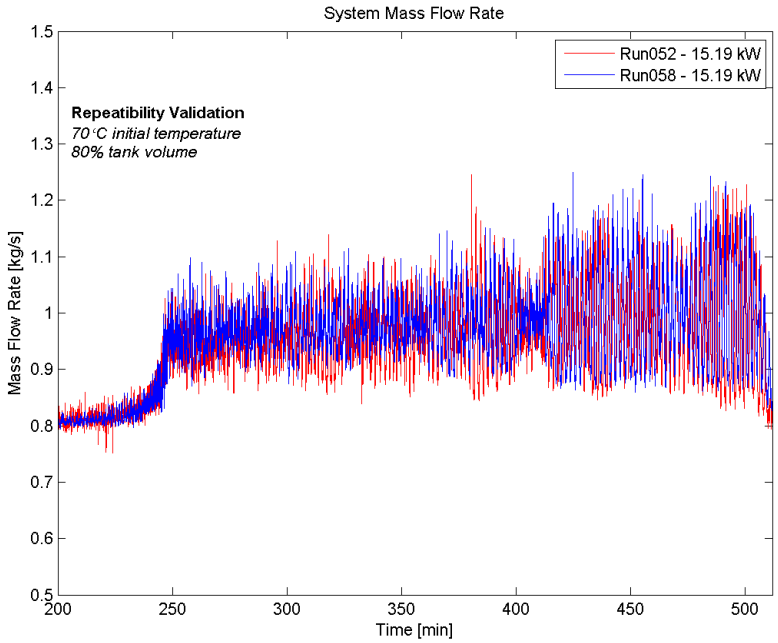

Figure 7.5: Repeatability of two phase experiments. Mass flow rate, Run052,058

7.1.3 Uncertainty

Error analysis and uncertainty in the experimental data and the subsequent calculations began with propagation of error from manufacturers specifications on the data acquisition equipment.

The energy equation was first expanded to include the individual contributions, and to isolate the measured velocity, the only parameter with a defined error from the mass flow rate meter.

$$\dot{m}C_p(T_{out} - T_{in}) -> \dot{U}_\infty \; A \; \rho \; C_p(T_{out} - T_{in}) \tag{7.18}$$

From this equation, each variable has it's error propitiated following standard propagation of error derivations. After performing the partial derivatives with respect to each variable, Table 7.4, Eq. 7.19 gives the full uncertainty for the energy in the test section.

Table 7.4: Uncertainty in calculated energy balance

Mass Flow Rate	$\sigma_{uM} = \sigma_{rel} \; U_m + \sigma_{abs}$	$\left(\frac{\partial Q}{\partial U_m}\right) = A \; C_p \; \rho \; (T_{out} - T_{in})$
Inlet Temperature	$\sigma_T = 0.5 \; °C$	$\left(\frac{\partial Q}{\partial T_{out}}\right) = A \; C_p \; \rho \; U_m$
Outlet Temperature	$\sigma_T = 0.5 \; °C$	$\left(\frac{\partial Q}{\partial T_{in}}\right) = A \; C_p \; \rho \; U_m$

$$\sigma_Q = \sqrt{A^2 \; C_p^2 \; \rho^2[(T_{in} - T_{out})^2)\sigma_{rel} \; U_m + \sigma_{abs})^2 + 2 \; U_m^2 \; \sigma_T{}^2]} \tag{7.19}$$

The uncertainty for a typical experimental run at single-phase steady-state is shown in Figure 7.6. The actual uncertainties from the previous figure, Run010, 9.9 1kW linear power, are given below.

- Average Test Section Energy: 8,512.6 +/- 607 [W] (7.23%)
- Average Hot Leg Energy: 8,385.23 +/- 162 [W] (1.15%)
- Average Heater Power: 10,021.8 +/- 243 [W] (2.42%)

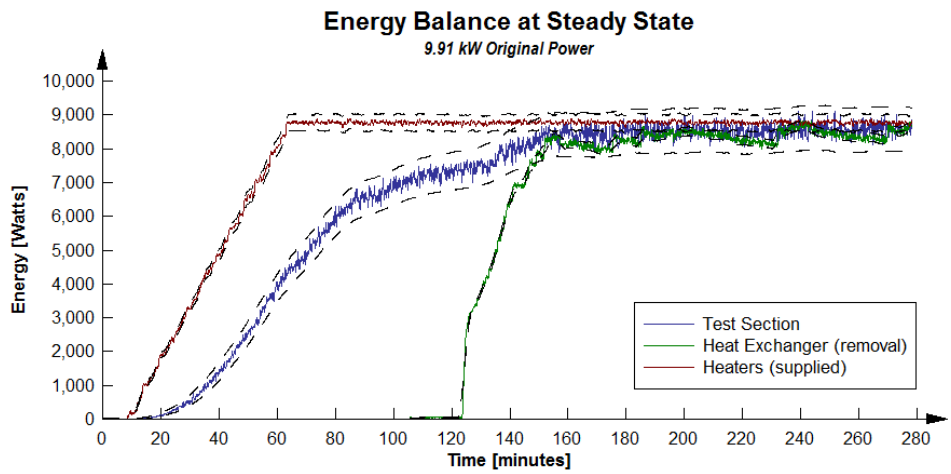

Figure 7.6: Energy balance and uncertainty, Run010. 9.91kW linear

7.1.4 Nominal Behavoir

The time history of a typical experimental run experiences predictable and consistent characteristics that are unique to both natural circulation driven system and the specific facility. An explanation of each will be provided below.

Prior to the start of an experiment, the fluid inside the downcomer and riser tubes is quiescent, that is there is flow rate in the system. Depending on previous conditions, there may or may not be a thermal stratification of fluid temperature between the lower and upper portions of the loop. Upon powering of the heaters, the water inside the riser tubes begins to heat and increase in temperature. At some critical point, or critical Rayleigh number, the temperature causes a higher density inside the heated portion of the riser tubes. At this point, the cold downcomer has sufficient driving hydraulic head to push the lower density water in the riser tubes, thus creating a system flow. The buoyancy force inside the riser tubes overcomes the retarding influence of viscous forces, and is pushed up by the colder fluid. This point can be predicted by looking at the density differences and Rayleigh number.

After the onset of natural circulation, the outlet temperature will continue to rise at some linear rate. However, a period of lag will be exhibited by the inlet temperature during this period. This is shown visually in Figure 7.7. The explanation of this lag in temperature

rise is due to the period of time it takes for the heater outlet temperature to enter the tank, become entrained into the downcomer, and then reenter the test section inlet. This system volume, calculated between the riser outlet and riser include (to include the upper networking, portion of the tank below the inlet, downcomer, and lower network) is 26 gallons. Integrating the mass flow rate during this period, excellent agreement can be found with the time it takes for the volume of fluid to reach the riser inlet with the time that a temperature rise can be seen at the inlet.

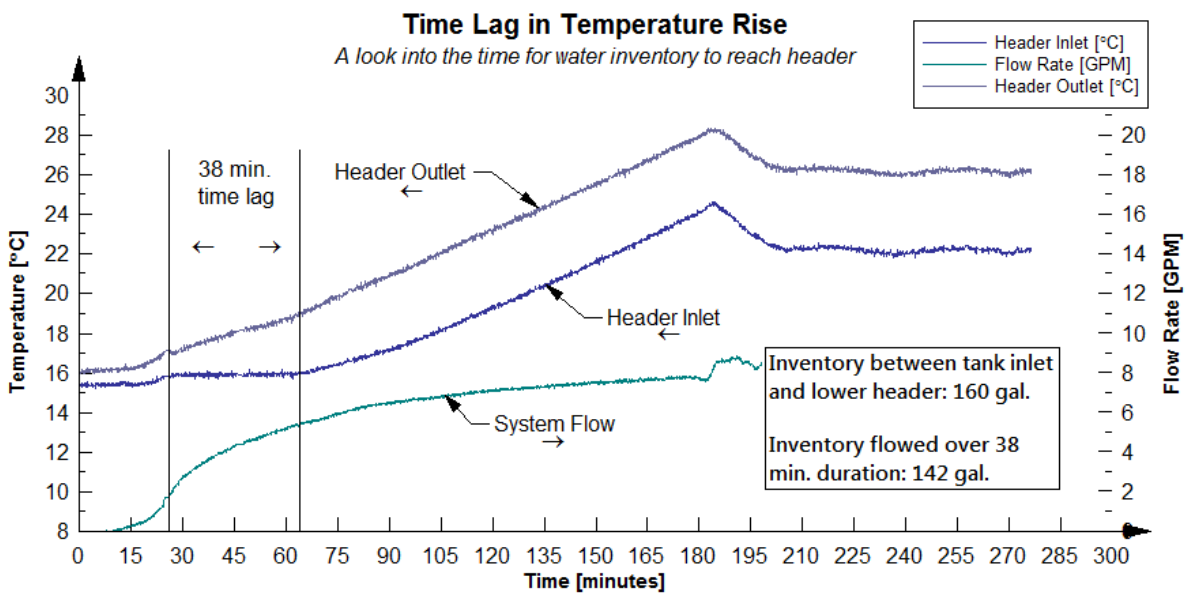

Figure 7.7: Analysis of time lagged inlet temperature

At the conclusion of a given test, the heaters are gradually power down over a period of 360 seconds, and then finally turned off. The system experiences an immediate decrease in mass flow rate, however due to the large thermal inertia of the test section, the water inside the riser tubes continues to increase, Figure 7.8. Eventually all the residual heat is absorption in the heat capacity of the water, and the system begins to cool down. At this point, very interesting effects are seen within the three riser tubes. Since the outer tubes cool at a slightly faster rate, due to the heat losses to the atmosphere, circulation within the riser tubes can be observed.

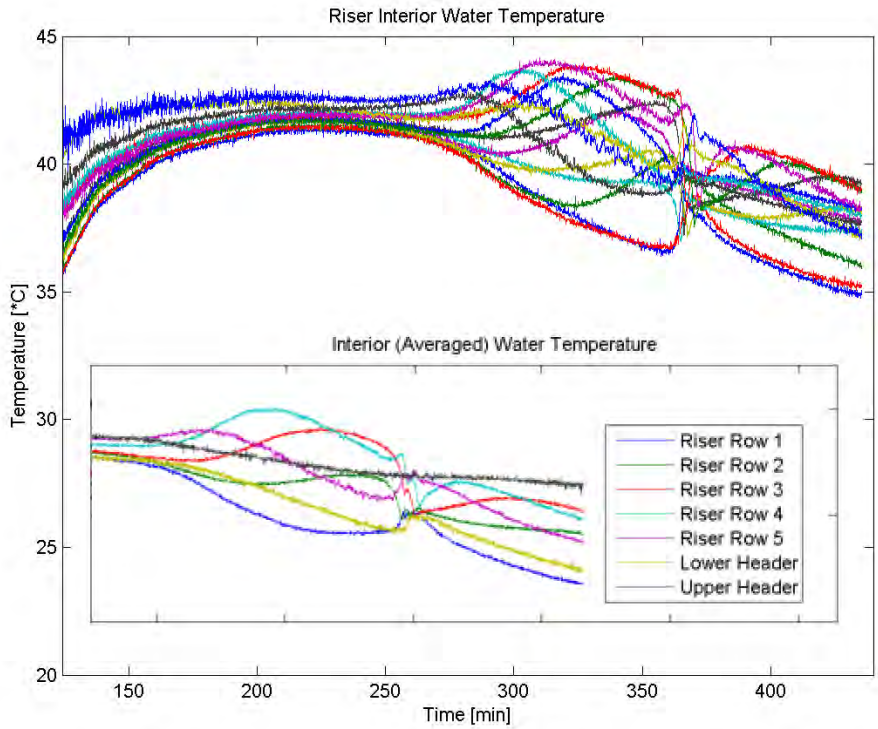

Figure 7.8: Cool down behavior, temperatures in riser tubes. 150 minutes after heater shutdown, from a steady-state power of 9.91kW

After the initial heat up, and when the desired reference value is reached for a steady-state experiment (e.g. Tinlet = 30 °C), the HXG is turned on and power matching begins in the attempt for reaching a steady-state. At the point of initiation, a perturbation in the system mass flow rate can be seen, Figure 7.9. This is caused due to a sudden introduction of higher density fluid (cold water returning from the HXG) into the system, causing a temporary increase in hydraulic driving head from the water storage tank and downcomer. The result is a short term spike in the mass flow rate of the system. However, after some time has passed where the new, colder fluid is mixed with the system, this perturbation settles and the system returns to it's normal behavior.

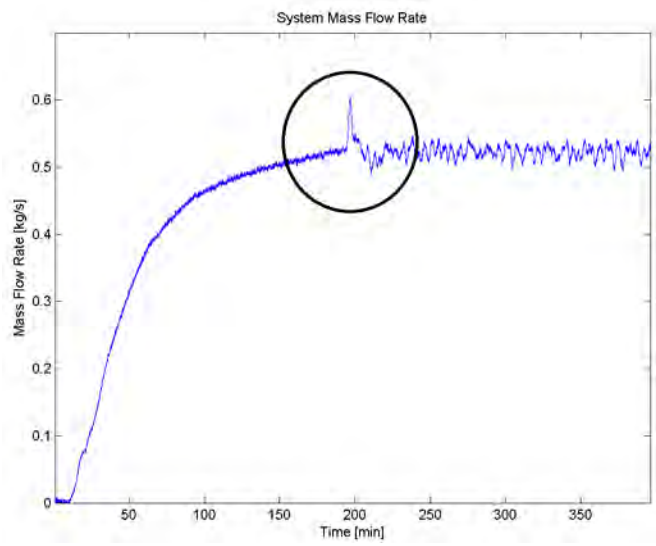

Figure 7.9: Spike in mass flow rate due to initiation of HXG

During a typical test, the thermocouples at the lower and upper portions of the test section show very different behavior. Besides the obvious difference in bulk temperature, the thermocouples towards the upper sections show significantly higher time-temperature fluctuations. This is due to the fully developed turbulent flow that is seen in the top portion, with average Reynolds number of 6,300. A comparison is given in Figure 7.10.

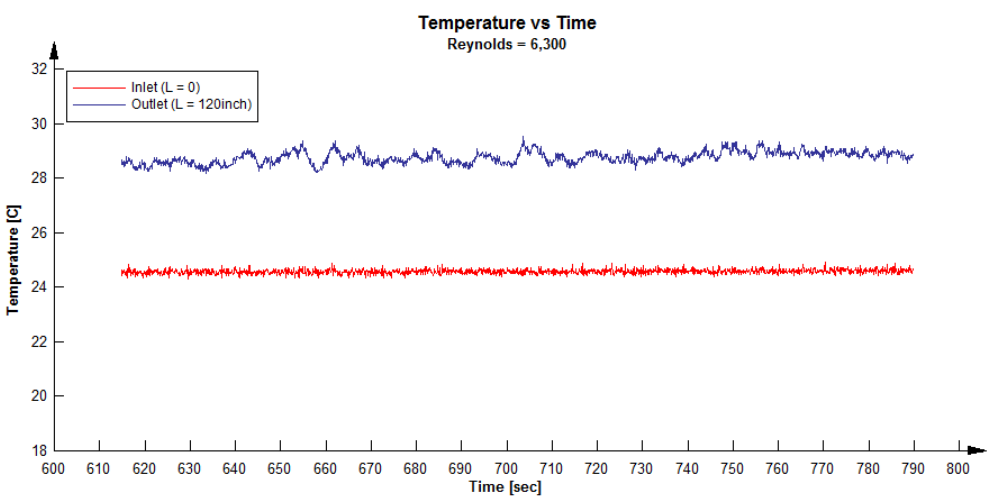

Figure 7.10: Oscillations in TC readings near exit of riser tubes, turbulent regime

The pressure drop in the test section was measured by a differential pressure transducer long the adiabatic chimney, between the outlet header of the heated test section and tank inlet. A separate test was performed that ramped the power from 0 to 15.19 kW to observe a system mass flow rate that reached 0.7 kg/s. The pressure drop was then compared against the mass flow rate, Figure 7.11. The time history begins with an initial period of startup and system stabilization, upon which they enter a laminar regime and finally transitioning into a turbulent state.

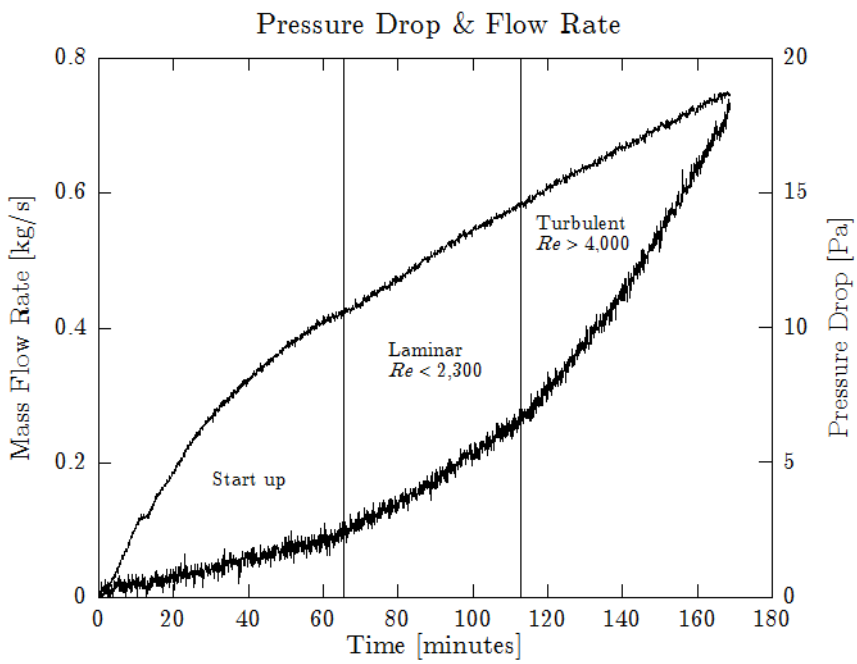

Figure 7.11: Time evolution of the frictional pressure through through the adiabitc chimney, outlet header to tank inlet

Temperatures of the radiant heaters were recorded by a Type-K ceramic thermocouple, positioned on the back surface of each heater bank. At the power levels investigated, Figure 7.12 shows the time evolution of the heater surface temperature, with maximum steady-state values tabulated.

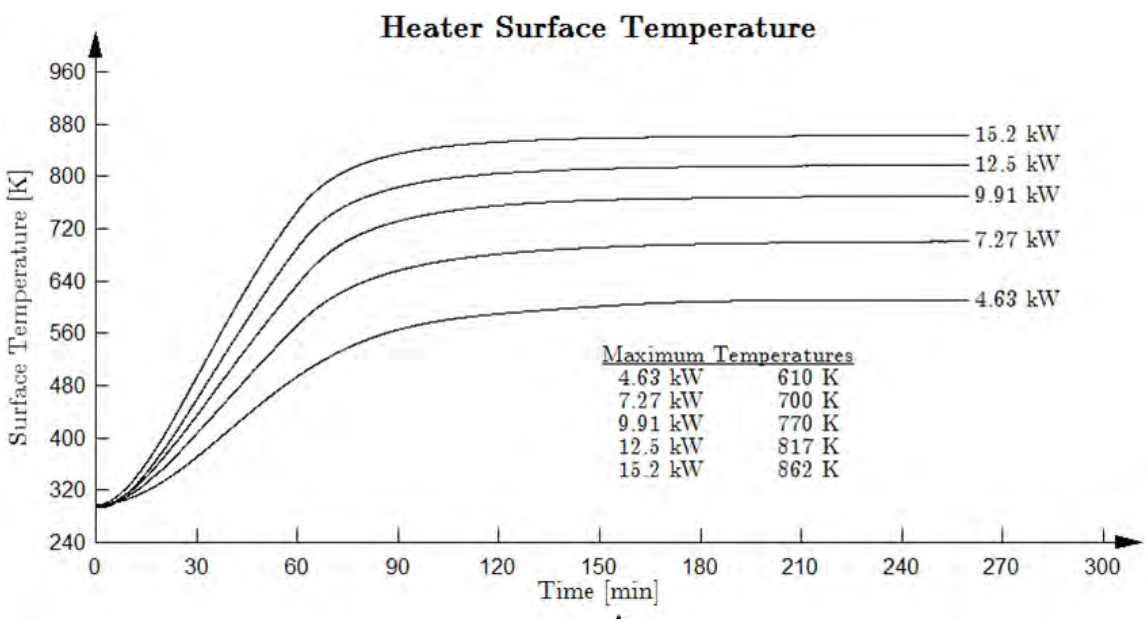

Figure 7.12: Radiant heater surface temperatures, with maximum steady state values noted

7.1.5 Heating Rate

During the shakedown runs, exact calibration and understanding of the heater controllers had not yet be obtained. Only after the shakedown runs were complete and true power controls were obtained, it was found that what was thought to be a gradual increase to 1.0kW turned out to be a fast rise to 15W over a 4 minute duration.

While such a fast heating rate is not desired for structural reasons, it showed very interesting data. Figure 7.13 shows the interior riser water temperatures as a function of time during this shakedown run with a high heating rate. Unlike other runs, where the water temperature follows a gradual and steady rate, this figure shows a stagnant water condition inside the water tubes. The water becomes heated at a fast enough rate where the mass flow rate has not yet been initialized. A temperature gradient forms, and upon reaching a critical Rayleigh number where buoyancy forces dominate, a natural circulation flow rate begins and the temperatures normalize to the system temperature.

This behavior can be explained by natural circulation driven flow. Hotter, less dense fluid rises relative to its initial location, while colder, denser fluid sinks. Changes in temperature

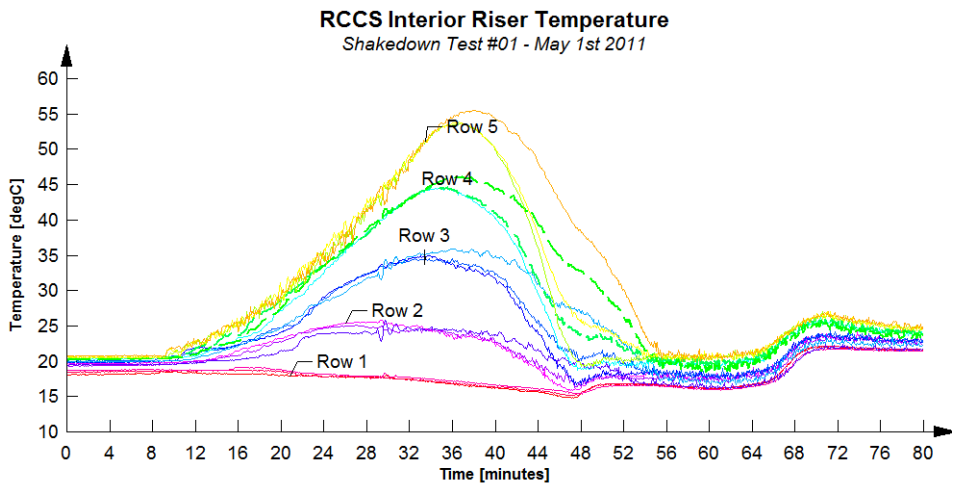

Figure 7.13: Riser interior water temperatures during a fast power rate, 0-15kW in 4 minutes

within a fluid induce changes in density, creating a buoyancy driven flow (Bejan, 2004).

The previous figure can be paralleled to Bejan's explanation. Starting from t=0min, the heaters were activated and a ramp to 15kW began over the duration of 4 minutes. At approximately t=12min, a temperature distribution in the riser tubes can be observed, with an increasing gradient until approximately t=36min. At this time, a critical point is reached, the buoyancy forces of the hot fluid in the riser tubes over comes the frictional force in the system, allowing the cold driving head in the downcomer to initiate a system flow. After approximately 20 minutes, at t=56min, the system reaches an equilibrium where the cold fluid has reached the riser tubes and begins it's normal operation.

This critical point can be defined by the Grashof number, Eq. 7.20, providing an explanation of the ratio of buoyancy forces to viscous forces. Recalling that the Reynolds number provides a measure of the inertial forces to viscous forces, the two can be combined to predict the effects of free and forced convection. Generally, the combined effects of free and forced convection must be considered when $\mathrm{Gr}/\mathrm{Re}^2 \approx 1$. If $\mathrm{Gr}/\mathrm{Re}^2 \leq 1$, then free convection effects may be neglected, and conversing if $\mathrm{Gr}/\mathrm{Re}^2 \geq 1$ then forced convection effects may be neglected.

$$Gr_L = \frac{g\beta(T_s - T_\infty)L_c^3}{\nu^2} \tag{7.20}$$

The transition in a free convection boundary layer depends on the relative magnitudes of buoyancy and viscous forces in a fluid. For vertical flat plates, this critical Rayleigh number is defined by Eq. 7.21.

$$Ra = GrPr = \frac{g\beta(T_s - T_\infty)x^3}{\nu\alpha} \approx 10^9 \tag{7.21}$$

For Nusselt correlations, few exists for vertical cylinders in natural circulation driven flow, thus the following relationship exists, which if valid, allows the use of vertical plate correlations to be used instead of vertical cylinder.

$$D \geq \frac{35L}{Gr_L^{1/4}} \tag{7.22}$$

If this criterion is satisfied, the following correlations for vertical flow against a flat plate can be used.

$$Nu = 0.59Ra_L^{1/4} \qquad (10^4 \leq Ra_L \leq 10^9) \tag{7.23}$$

$$Nu = 0.1Ra_L^{1/3} \qquad (10^{13} \leq Ra_L \leq 10^{20}) \tag{7.24}$$

$$Nu = \left(0.825 + \frac{0.387Ra_L^{1/6}}{[1 + (0.492/Pr)^{9/16}]^{8/27}}\right)^2 \qquad (entire\ range) \tag{7.25}$$

In addition, a modified version of the Gnielinski correlation for the natural convective Nusselt number, suitable for the calculation of forced convective heat transfer, is given in Eq. 7.26 These correlation is valid for both transition and turbulent pipe flows ($2300 \leq Re \leq 5x10^6$). R. Yang (2006) considered that the Rayleigh number can be used to represent the

effect of free convection caused by buoyancy on convective heat transfer in the heated tube under natural circulation. By adopting the Rayleigh number to modify the conventional correlation used for the calculation of heat transfer in forced circulation, he proposes a new correlation for the determination of convective heat transfer in natural circulation

$$Nu_0 = \frac{(\mathrm{Re} - 1000)Pr\mathrm{f}/2}{1.0 + 12.7(Pr^{2/3} - 1)\sqrt{\mathrm{f}/2}} \tag{7.26}$$

$$\frac{Nu}{Nu_0} = Ra^{-0.011} \tag{7.27}$$

Available temperature measurements of the bulk fluid and riser wall are coarsely limited, with five axial locations for each riser tube, yielding a single bulk and wall temperature at each position. For a uniform heat flux distribution, such a calculation with would suffice; however the geometric configuration of the riser and fin assembly, coupled with a directional heat flux, results in an extremely non-uniform temperature gradient in riser tube walls. The convective and radiative portion of the heater power causes a moderate temperature on the front surface of the tube walls; however it is the conduction from the fins to the cooler water tube where the highest temperature occurs, Figure 7.14.

A curve fit to thermal simulation matched data, which solved for the radial tube wall temperature at each node, and data from the 5 water thermocouples was linearly interpolated to obtain axial water temperature at each node.. A modified version of the Gnielinski correlation for the natural convective Nusselt number, and a numerical solver written in MATLAB aided in obtaining a local heat transfer coefficient at each node.

The Nusselt number, Nu, and convective heat transfer coefficient, h, were evaluated from 20 sets of experimental data, with energies ranging from 3.7 to 12.25 kW. Validation of the data was performed by comparison of the total energy from numerical results and Newtons Law of Cooling, to experimental results by an energy balance of the inlet and outlet temperature and mass flow rate through the test section. Excellent agreement was found for the total energy in the test system, within +/-4 percent for sixteen of the tests,

and +/- 8 % for the remaining four. The local coefficients for a sample test at 10.35 kW is shown in Figure 7.14, where the radial dependence shows a trend that follows the complex and non-uniform temperature profile predicted by thermal simulations.

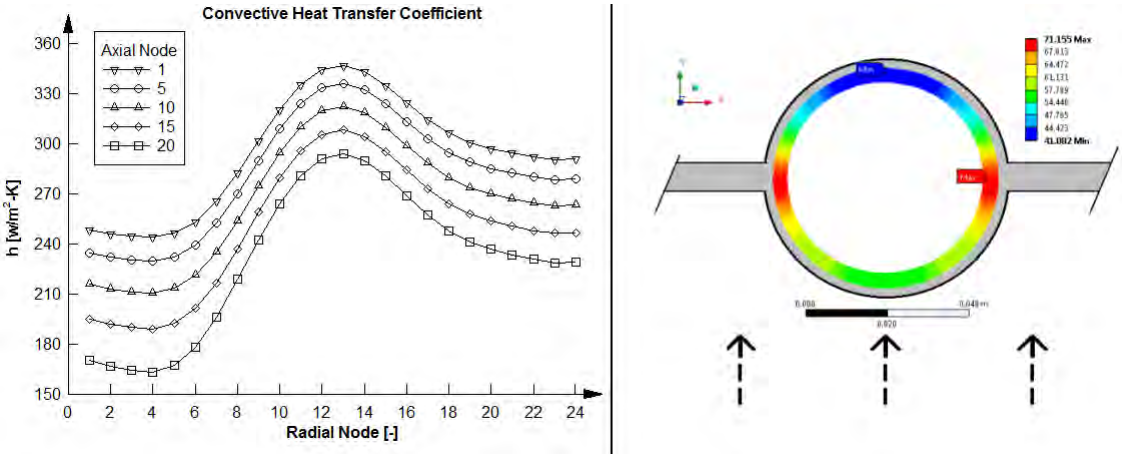

Figure 7.14: Left: Radial dependence on convective heat transfer coefficient Right: Interior tube wall temperature (color), riser tube and fin geometry (gray), heat flux direction (arrows)

7.2 Single Phase Steady-State

The steady-state behavior of the RCCS was investigated by a series of experimental runs where the facility operated at a steady state condition, or that the power supplied was match by the power removed. The purpose of these experiments were to examine the thermal hydraulic behavior of a steady state system at varying experimental parameters. Three primary parameters were examine during eight runs: power level, power shaping, and system volume. Each experiment followed a strict and systematic procedure, which was kept consistent between runs to ensure quality of data. An example log is given below in Figure 7.15.

Figure 7.15: Sample log from steady state experiments

09:10 AM	**Initiate Power**
	• Start 1 hour ramp to desired power level
10:10 AM	**Conclude ramp**
	• Record key test section parameters • Hold power at constant value
12:43 PM	**Reach desired state**
	• Upon reaching desired 30°C, prepare HXG • Record key test section parameters • Turn on Cold Water Supply/ Pump
12:40 PM	**Turn on HXG**
	• Set an initial hot leg mass flow rate • System energy will experience a fast drop • Allow 20 minutes to stabilze
01:00 PM	**Match heat removal**
	• Adjust hot leg flow rate to obtain energy balance • Take care to make fine adjustments, with time to stabilize
01:26 PM	**Obtain power match**
	• Record key test section parameters • Record hot leg removal parameters (flow rate, ΔT, energy, etc) • Hold for 2 hours
03:30 PM	**Conclude experiment**
	• Record final test section parameters • Record final room temperature • Turn off hot / cold pumps, cold water supply • Ramp down heaters over 120 seconds

While great care was taken to ensure identical starting conditions, it was found that obtaining zero flow conditions with a uniform temperature distribution in the test section was extremely difficult. Thus, on average, the experiments were performed with starting

conditions of mass flow that ranged between 0 and 0.1 kg/s, and test section temperature rise of 0 - 2 °C. This was later found to have no effect on the final response at steady-state, it was merely an influence on the approach behavior.

All tests in this section were run to satisfy steady-state criteria of 30.0 +/- 0.5 °C lower header inlet temperature, constant system mass flow rate, and constant Δ T between lower and upper headers during a period of 2 hours of steady-state flow. During steady-state, for all tests mentioned, the system would be analyzed for an overall energy balance; including power sent from the heaters, power delivered to the system water, power removed by heat exchanger, and power lost from the system. It should be re-stated here that the power delivered to the system water should be equal to the power removed by the heat exchanger during steady-state.

The heater power was determined using the signal return from the Eurotherm power controllers and the voltage measured from the supply breakout box. The supply voltage was found to fluctuate between 201V - 211V on any given day. For the tests performed in this thesis, the supply voltage was assumed to be 206 +/-5V.

7.2.1 Integral Behavior at Varying Power

The steady-state behavior at four varying power levels were investigated for it's effects on such parameters at temperature rise, mass flow rate, and heat loss. The baseline power levels was chosen as the GA MHTGR 750 kW nominal decay power and 1.5 MW accident heat load. Scaled to the 1/4 scale experimental facility, these power levels were 4.63 kW and 9.91 kW, respectively. Two additional powers were selected, a middle and higher power: 7.27 kW and 12.55 kW. A table showing the initial and boundary conditions is provided in Table **??**.

A subsidiary goal for these tests was to ensure that the facility could sustain these power inputs for extended periods of time without reaching a critical temperature range anywhere that may damage instrumentation. This would confirm whether or not continuation to extended two-phase studies of flashing flow in the risers and network piping could be performed

Table 7.5: Initial Conditions and Test Parameters for Power Level Variation Runs

	Nominal	Intermediate	Decay	Extrapolated
Max Power Input Applied	4630 W	7275 W	9917 W	12560 W
Heat Flux	2.83 kW/m^2	4.44 kW/m^2	6.06 kW/m^2	7.67 kW/m^2
Max Power Input Actual	4686.35 W	7265.44 W	10015.26 W	12406.49 W
System Volume	80%	80%	80%	80%
Initial Riser Inlet Temperature	19.5 °C	19.1 °C	17.0 °C	19.6 °C
Initial Δ T between headers	1.2 °C	0.8 °C	0.2 °C	1.0 °C
Tank average temperature	21.5 °C	20.2 °C	17.0 °C	21.2 °C
Power Ramp time	60 min	60 min	60 min	60 min
Steady State Time	130 min	132 min	130 min	130 min
Total Test Time	570 min	450 min	420 min	360 min

without a partial re-design to protect equipment. Also note that each run may have a different overall time, but each was kept at steady-state for at least two hours. The difference in total run time exists because reaching the target steady-state was more difficult for the lower power runs because the system heated up slower.

After successfully producing a steady-state flow scenario, a full energy balance of the system was necessary to know how much of the input heat was being transferred to the RCCS, and how much was being lost from the system. A summary of the runs is given in Table 7.6, with figures of ΔT and energy following.

Table 7.6: Summary of power level investigation at steady state

	Inlet	Δ T	Flow Rate	Heaters	Test Section	HXG	Losses
	[°C]	[°C]	[kg/s]	[W]	[W]	[W]	[W]
Nominal	30.25	2.42	0.372	4,686	3,778	3,633	1,053
Intermediate	29.98	3.18	0.448	7,265	5,979	6,058	1,207
Decay	29.99	3.83	0.523	10,015	8,402	8,289	1,736
Extrapolated	29.9	4.37	0.582	12,406	10,646	10,370	2,036

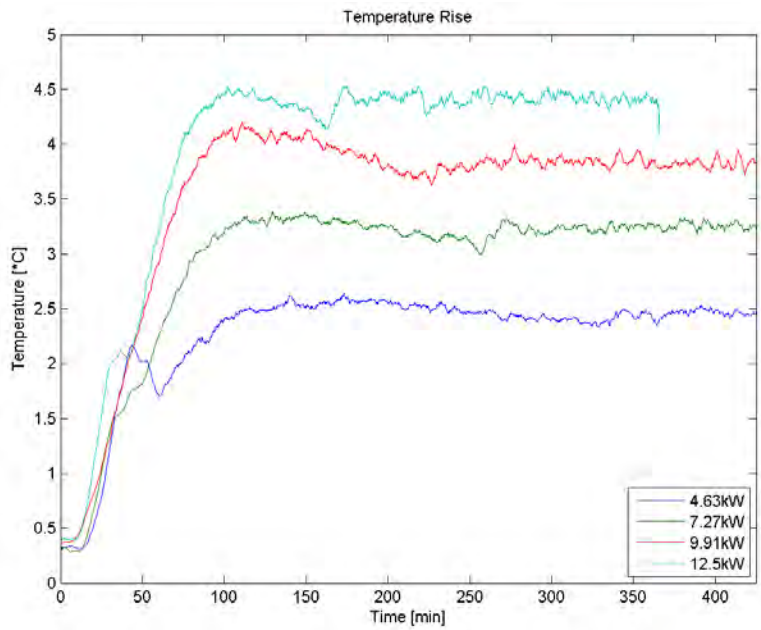

Figure 7.16: Comparison of temperature rise for steady state power variations

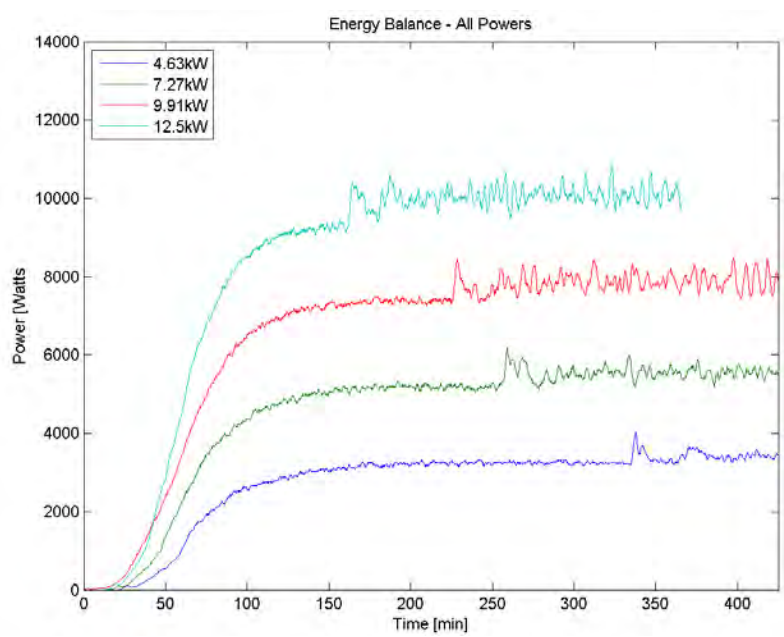

Figure 7.17: Comparison of test section energy for steady state power variations

UDV Measurements

Ultrasonic velocity measurements were taken in the RCCS for two series of test configurations of varying power levels: linear heat flux and asymmetric radial shaping. The linear power tests were conducted at 5 varying levels: 4.62, 7.27, 9.91, 12.5, and 15.2 kW. During each tests, a steady state condition was reached and held for a duration of at least 60 minutes, at which point ultrasonic velocity measurements were made in each riser tube, in both the upper and lower header. Table 7.7 shows the velocities from each test compared to the calculated velocity from the magnetic flow rate meter. Since the magnetic meter measures the system fl ow rate, a division by three to determine the velocity in a given single riser tube was made.

$$V_{magnetic} = \frac{G_{system/3}}{A_{riser}} \tag{7.28}$$

$V_{magnetic}$ Back calculated average velocity $[m/s]$

G_{system} Measured volumetric flow rate $[m^3/m]$

A_{riser} Cross sectional area of riser tube $[m^3]$

Results shown in Table 7.7 include: UVP velocity measurements in the lower header (UVP$_L$ presented below using the P_{max} method), UVP velocity measurements in the upper header (UVP_U), uncertainty with UVP measurements (u$_{UVP}$), back-calculated velocity values from in-line magnetic flow meter (V$_{mag}$), uncertainty with magnetic flow meter measurements (umag), and percent difference between back-calculated velocity values and UVP velocity measurements in both lower and upper headers (Δ_L and Δ_U), respectively. More uncertainty details associated with the UW facility are given in Appendix H.

Table 7.7: Ultrasonic velocity compared to magnetic flow meter, linear heating

	UVP_L	UVP_U	u_{UVP}	V_{mag}	u_{mag}	Δ_L	Δ_U
Power	[mm/s]	[mm/s]	[mm/s]	[mm/s]	[mm/s]	[%]	[%]
4.63 kW	66.24	64.98	+/- 0.696	65.45	+/- 0.196	1.20%	-0.70%
7.27 kW	80.63	79.42	+/- 0.693	79.92	+/- 0.240	0.90%	-0.60%
9.91 kW	94.5	99.81	+/- 0.937	95.96	+/- 0.288	-1.50%	3.90%
12.5 kW	101.68	107.66	+/- 0.705	104.69	+/- 0.314	-2.90%	2.80%
15.2 kW	112.33	112.07	+/- 0.561	113.53	+/- 0.341	-1.10%	-1.30%

7.2.2 Axial Power Shaping

With all previous experiments performed at a linear power shape, an additional test was run with a cosine power profile by varying the power to each of the 6 zones. The heat flux off of a real RPV wall exhibits an axial skew, with a sinusoidal power profile that is a cosine function of the axial position, z. This cosine shape was very coarse in natural, due to the limited number of control zones. A true cosine is shown against the actual cosine power shape, Figure 7.18. The cosine profile scaled with that of a true cosine while preserving the baseline integral power level.

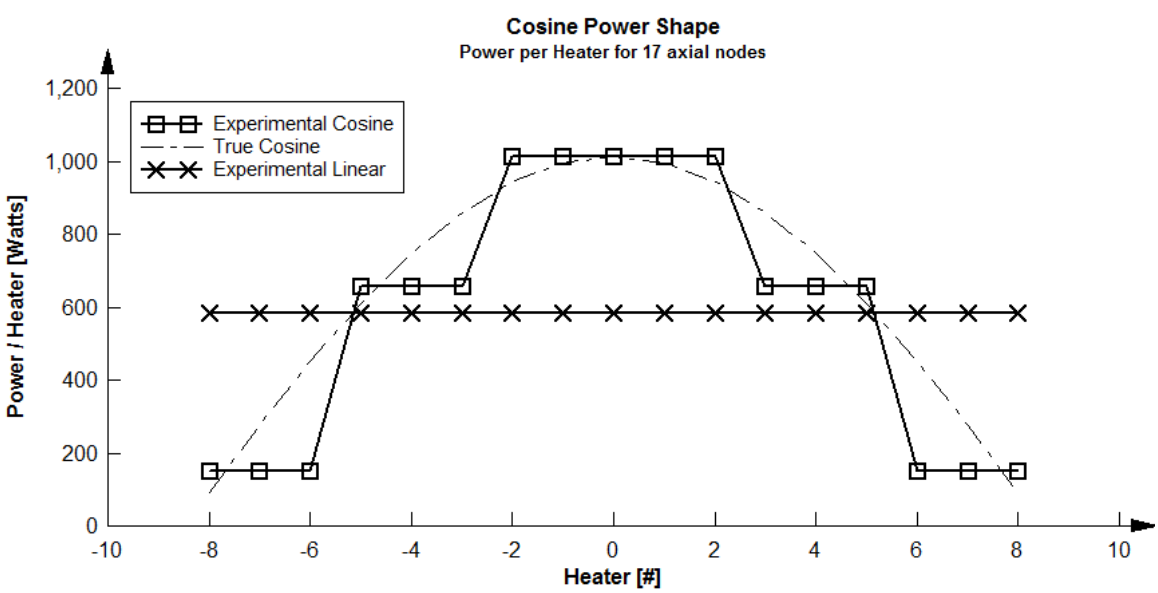

Figure 7.18: True vs actual cosine power profile

Results showed little to no difference in the performing capabilities of the heat removal by the RCCS, the energy balances, mass flow, water temperatures, and heat removal rates were repeatable regardless of the axial profile. The only differences observed were with the surface temperatures of the tube and fin, Figure 7.19. With the cosine profile, both the fin surface and tube walls experienced increased temperatures shortly after the center line, with only a gradual riser near the end of the heated length. While the heat removal performance was unaffected, this must be considered when designing for local hot spots on the RCCS walls.

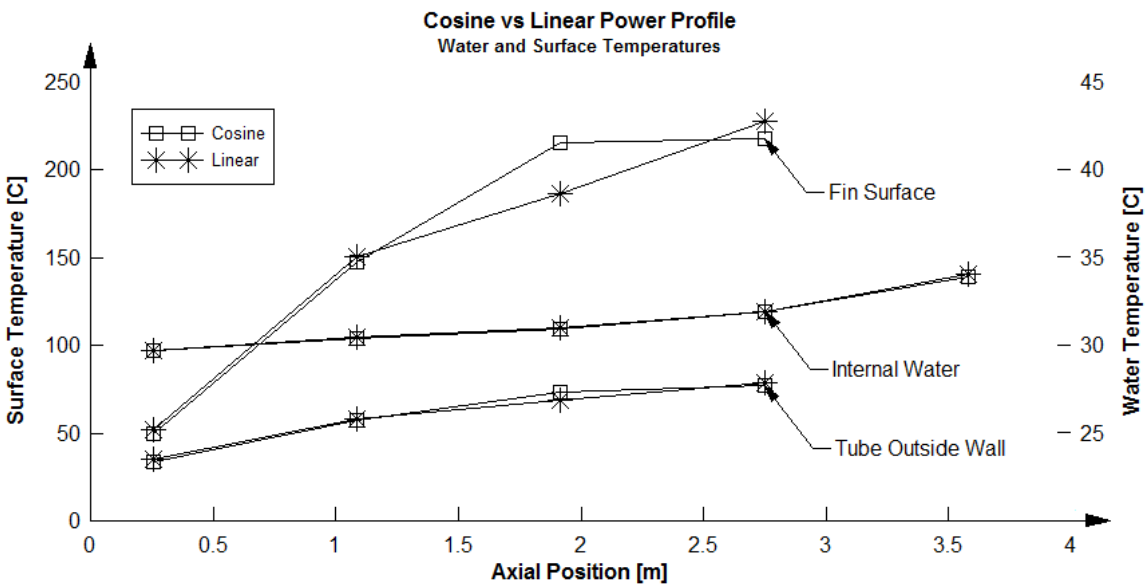

Figure 7.19: Fin surface temperature, steady state with linear and cosine power shoping

These results suggest that an axial decay heat profile on the reactor vessel wall does not affect overall RCCS heat removal performance. However, power shape should not be completely ignored because it does introduce the possibility of local hot spots being created within the reactor cavity, and may affect local flow velocities within individual risers.

7.2.3 Asymmetric Power Shaping

A series of tests were performed with an asymmetric heating profile, which was accomplished by turning off either the A or B bank of heaters. The power for a given test was equal to

previous values, however directed at a given bank in its entirety. As with before, the system was allowed to reach a steady state, and after 60 minutes velocities in each riser tube were recorded. Since the flow distribution was not known, a division of the system flow rate by three was no longer applicable. Instead, validation was made possible by calculating the total flow rate is each riser tube, and summing them for a total. This total was then compared to the total flow rate recorded from the system magnetic flow meter, Table 7.8.

Table 7.8: Comparison of flow rates in individual riser tubes during asymmetric heating

			UDV Indiv. Riser *[gpm]*			UDV Total	Magnetic
Run	**Power**	**Radial**	***Left***	***Center***	***Right***	*[gpm]*	*[gpm]*
Run025	7.27 kW	Left	2.67	2.59	2.36	7.61	7.63
Run026	9.91 kW		3.20	2.96	2.62	8.78	8.79
Run027	7.27 kW	Right	2.30	2.32	2.96	7.57	7.76
Run028	9.91 kW		2.73	2.92	3.48	9.13	9.01

Excellent agreement was found, with the largest different seen in Run027 at 2.43%. The flow distribution was significantly more uniform that originally expected, with a distribution of 37.4%, 33%, and 29.6% for the 'left' heating cases, and 30.1%, 31.3%, and 38.6% for the 'right' heating cases

From Right Asymmetric heating cases, the UDV differed from the measured magnetic flow rate by an average of 0.15 GPM, or 0.5%. Similarly for the 'Left' asymmetric heating cases, differences of a mere 0.1 GPM, 0.3% were observed with the UDV.

The view factors from Heater A, to each of the three riser tubes, is given in Table F.13 along with their view lengths. A derivation is presented in the appendix.

Noting the results from previous Table 7.8, the flow distribution does not follow the expected skew in view factors. Thus, it can be observed that the radiative heat transfer only places a fraction of the total heat transfer inside a given riser tube. It is due to the convective natural circulation of air inside the cavity that causes a flattening of the heat flux distribution. The convective contribution is not unlike that of a real design, and thus provides a mitigating support in areas where uniform positioning of the cooling tubes is not possible, such as at corners and support structures

Table 7.9: Analytical view factors from Heater A to Riser N

	F_{A-1}	F_{A-2}	F_{A-3}
W_1	11.7489	11.7489	11.7489
L_1	11.7174	19.7199	28.1315
L_2	15.3124	8.7486	9.8404
L_3	8.7486	9.7533	16.8969
L_4	7.9968	11.7174	19.7199
	0.438	**0.298**	**0.058**

7.2.4 Initial System Inventory

A test was run at a reduced water storage tank volume, 40% from the baseline 80%. The only effect this had on the system behavior was during the ramp to steady state. The average rate of rise of the inlet temperature for the 40% full case between 70 - 140 minutes is 7.93 +/-0.96 °C/hr, while the average rise rate of the inlet temperature for the 80% full case between 80 - 200 minutes is 4.84 +/- 1.45 °C/hr. This faster heat up for the 40% case was expected because it had less thermal mass to heat up with an equal power input. This behavior suggests that system volume is expected to have a greater impact on the performance of the system during the transient heat-up following steady-state flow. Remaining parameters, such as the mass flow rate and energy balance were extremely repeatable.

7.2.5 Sparger & Tank Mixing

he entirety of the previous results were performed with a HXG return line that entered the water storage tank, and emptied the cool water near the tank outlet. A change to this return system was made by the addition of a sparger, where the HXG return line emptied near the top of the water tank. This sparger allowed the diffusion of the cold water into the bulk of the water inventory, and hence a substantively increased mixing before being entrained back into the tank outlet. A comparison of the mass flow rates with and without the sparger is given in Figure 7.20, with variability in the data outlined in Table 7.10.

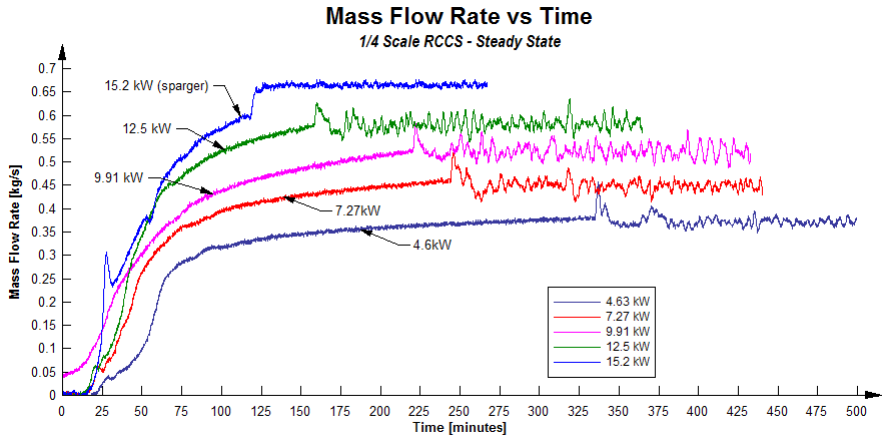

Figure 7.20: Comparison of steady state with and without sparger in mixing tank

Table 7.10: Fluctuations with and without sparger in tank

	No Sparger	Sparger
Riser Inlet	+/- 0.22 °C	+/- 0.12 °C
Riser Outlet	+/- 0.18 °C	+/- 0.16 °C
Mass Flow	+/- 0.013 kg/s	+/- 0.008 kg/s
Energy	+/- 620 W	+/- 436 W

7.2.6 Steady State Summary

A total of 12 experimental tests were performed at steady-state conditions, with primary test variable that included power level, axial profiling, and initial system volumes of water storage tank inventory. Each test concluded with satisfactory results, proving linearity and repeatability. Δ T and overall system flow rate (Figure 7.21), and power transferred to the test section all scale and increase linearly with reactor vessel decay power level.

Experimental system repeatability was found, for the three-tube RCCS, to be limited only by the uncertainty of the measurement devices used, concluding 2.4% for power input, 2.2% for power delivered to the test section, and 9.8% for validating heat loss estimations. Axial power shaping has no effect on the overall heat removal performance of the RCCS at single phase, only affecting local temperatures of RCCS components. Thus, it was concluded that

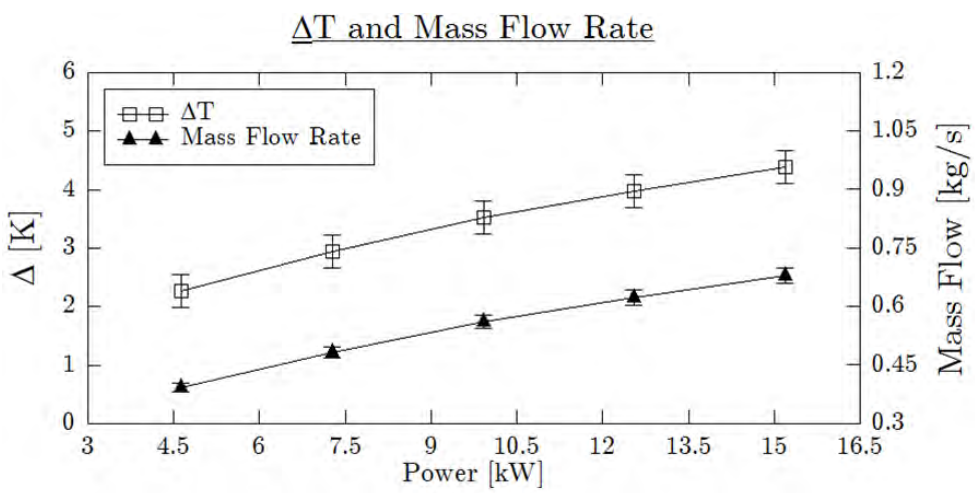

Figure 7.21: Linearity of mass flow rate and Δ T with increasing power

system volume effects the RCCS heat removal only during transient operation. A summary of key thermal hydraulic behavior is given in Table 7.11.

Table 7.11: Summary of single phase, steady-state experiments

Num.	Power	Type	Temperature			Mass Flow	Energy			Heat Loss
			Inlet	Outlet	ΔT		Test Section	Hot Leg	Heater	
-	*kW*	-	*°C*	*°C*	*°C*	*kg/s*	*Watts*	*Watts*	*Watts*	*Watts*
4	9.91	Repeatability	22.46	26.37	3.91	0.511	8,360	7,705	10,003	1,086
5	9.91	Repeatability	22.65	26.63	3.97	0.508	8,451	8,209	10,014	989
6	9.91	Power Decay	29.99	33.82	3.83	0.524	8,402	8,289	10,015	1,140
7	4.63	Power Nom	30.25	32.67	2.42	0.373	3,778	3,633	4,686	791
8	7.27	Power Mid	29.98	33.16	3.18	0.449	5,979	6,058	7,265	999
9	12.5	Power High	29.90	34.27	4.37	0.582	10,646	10,370	12,406	1,272
10	9.91	Repeatability	22.56	26.61	4.05	0.502	8,515	8,368	10,003	1,030
11	9.91	Cosine	29.88	33.73	3.85	0.523	8,418	8,304	9,921	1,147
12	9.91	40% Vol.	30.14	34.09	3.96	0.508	8,407	8,490	10,019	1,201

An additional 11 experiments were performed with a focus on ultrasonic velocity measurements within the riser tubes, Table 7.12. Local velocities are presented for linear and asymmetric heating profiles in Table 7.13. Notations for UDV01-03 at header inlet, UDV04-05 at outlet. Riser 1: UDV01+04, Riser 2: UDV02+UDV05, Riser 3: UDV06.

Table 7.12: Summary of steady state values and energy balance from UDV testing

Num.	Max Power	Type	Temperature [C]		Energy [W]		
-	kW	-	Inlet	Outlet	Test Section	HXG	Heater
Run021	9.91	Linear	31.39	34.89	8,222.97	7,663.34	9,996.90
Run022	12.5	Linear	32.10	36.07	10,359.90	9,822.74	12,410.20
Run023	4.63	Linear	28.72	30.99	3,727.12	3,579.67	4,680.22
Run024	7.27	Linear	26.88	29.89	5,909.66	5,823.56	7,255.55
Run025	7.27	Radial L	29.68	32.65	6,018.63	6,001.48	7,255.53
Run026	9.91	Radial L	30.58	34.17	8,494.41	8,440.17	9,991.11
Run027	7.27	Radial R	30.69	33.56	5,952.20	5,639.87	7,249.80
Run028	9.91	Radial R	30.67	34.20	8,381.20	8,008.11	10,013.60
Run029	15.2	Linear	30.49	34.88	12,254.20	11,873.30	14,821.80
Run032	9.91	Radial L	26.49	30.15	8,551.83	8,331.84	10,000.10
Run033	9.91	Radial L	26.38	30.09	8,507.98	8,279.52	10,026.70

Table 7.13: Summary of flow rate measurements from UDV and magnetic flow rate meter

Num.	Power	Type	Magnetic		UDV Measured [mm/s]				
-	kW	-	[kg/s]	[mm/s]	UDV01	UDV02	UDV03	UDV04	UDV05
Run021	9.91	Linear	0.562	95	94.51	n/a	n/a	-99.81	n/a
Run022	12.5	Linear	0.623	106.04	101.77	n/a	n/a	-102.07	n/a
Run023	4.63	Linear	0.392	65.91	66.23	n/a	n/a	-64.98	n/a
Run024	7.27	Linear	0.469	79.71	80.63	n/a	n/a	-79.91	n/a
Run025	7.27	Rad. L	0.486	n/a	86.79	82.07	76.1	-86.22	-77.55
Run026	9.91	Rad.l L	0.566	n/a	104.07	89.73	82.64	-103.17	-87.79
Run027	7.27	Rad. R	0.495	n/a	74.72	78.36	95.05	-72.42	-97.44
Run028	9.91	Rad. R	0.568	n/a	88.81	97.54	110.25	-92.49	-116.54
Run029	15.2	Linear	0.668	113.82	112.14	-115.46	n/a	-115.46	n/a
Run032	9.91	Rad. L	0.558	n/a	104.63	95.49	82.88	-106.67	-97.71
Run033	9.91	Rad. L	0.548	n/a	102.68	95.6	83.31	-111.83	-93.54

7.3 Two-Phase Conditions

The behavior of the facility at two phase was investigated by allowing the system to continue heating until the water temperature reached saturation. The steady-state heat removal system was modified to remove the hot leg loop, and instead connecting a steam line from the top of the water storage tank to the hot supply of the HXG. The cold leg remained as with the steady-state runs, and steam condensation was collected in a storage tank. Due to the large water inventory, a typical run from room temperature to saturation requires a heat up time ranging from 14 - 18 hours, and thus typically split over the course of two days.

The time response of two phase parameters are fundamentally dynamic, and tightly coupled with several physical phenomena present within the loop. As the system evolves with time, the release of steam causes a loss of inventory and subsequently a change in the storage tank water level. In addition to decreasing the driving hydrostatic head from the cold downcomer, this reduction in pressure lowers the saturation temperature and allows bubbles to form lower in the heated portion of the network plumbing, increasing the effects of flashing. These effects will be investigated, among others, for their influence on the behavior and performance of the experimental facility at two-phase conditions.

7.3.1 Baseline Procedure & Conditions

Initial scoping tests at two-phase conditions indicated that the RCCS behavior can be dramatically affected by minimal variations in initial and boundary conditions. The extreme sensitivity exhibited by the facility required establishing a rigid procedure and strict set of initial conditions if high quality and repeatable data was to be obtained.

Two-phase testing began with defining baseline conditions which were derived from expected operating parameters of the full scale concept design and logistical considerations for experimental practices. An initial 80% tank inventory (measured to within 4mm), ¡70 °C bulk system temperature, and a 60 minute ramp to 15.19 kW (9.29 kW/m2) of supplied heater power defined each baseline test. The heat up period from 70 °C allows the sys-

tem time to recover and stabilize from any nonuniformities present, and spans a nominal 5 hours before reaching boiling conditions. To repeatedly capture the approach to boiling, a thermocouple, placed at the steam outlet of the water storage tank, triggers the cold leg of the condensation system once it exceeds 10 °C above ambient. With this trigger, control parameters are held constant for a 4 hour minimum duration, after which the heaters are ramped down over a 10 minute period and power shut off. This procedure was maintained for several experiments to confirm procedures and established repeatability bounds for the facility.

Key thermal hydraulic behavior of the 1/4 scale water cooled RCCS at baseline two-phase conditions is presented in the form of system mass flow, temperatures, pressure measurements, Figure 7.22. During the 4 hour period at boiling, the baseline conditions of 15.19 kW and 80% initial tank volume experienced an average mass flow rate of 0.98 kg/s, with max/min occurring at 1.24 and 0.81 kg/s. Of the 15,190 watts sent to the Eurotherm heater controllers, an average of 14,826 +/- 360 watts transmitted electrically, while 12,680 +/- 1,169 watts were calculated in the test section. This results in an average of 2,146 watts lost in the environment, or 86% efficiency. Of the total loss, 1,436 watts were calculated to originate from the heated enclosure based on IR temperature measurements.

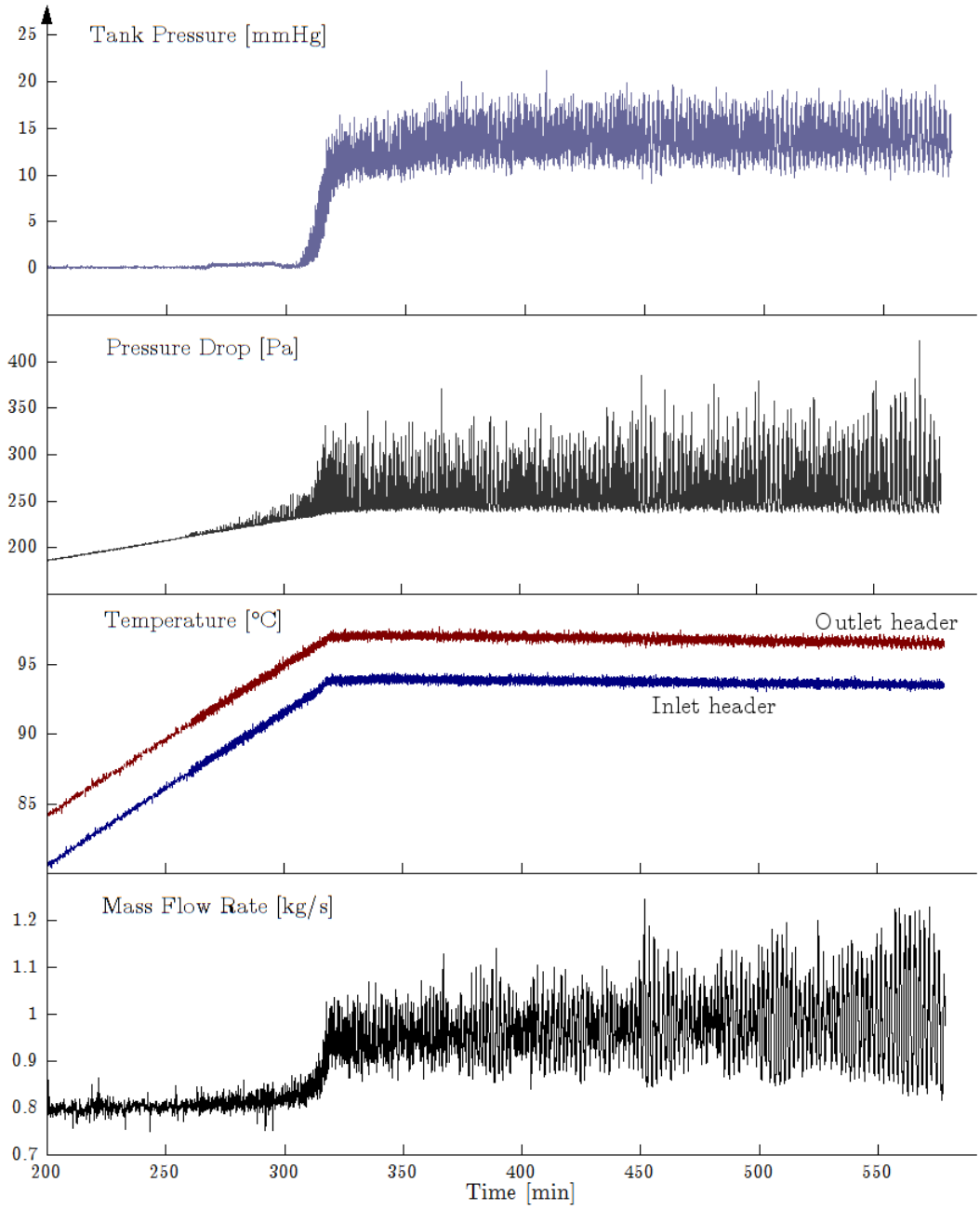

Figure 7.22: Primary measured system parameters for 15.19 kW baseline two-phase

The behavior at baseline conditions of 15.19kW and 80% tank inventory volume shows first signs of shows chaotic, nucleate boiling dominate flow oscillations immediately upon reaching saturation conditions. This remains the primary mechanisms for fluctuations in the system behavior for an nominal 30 minutes, at which point the system begins to experience

periodic oscillations induced by flashing in the adiabatic chimney. These two phenomena continue in parallel, with multimode effects from the combined nucleate boiling and flashing. With continued time, the flashing becomes more and more dominate, eventually completely suppressing the localized fluctuations observed at the start of boiling. Each of these three stages are shown in Figure 7.23 at various points in the baseline condition experiment.

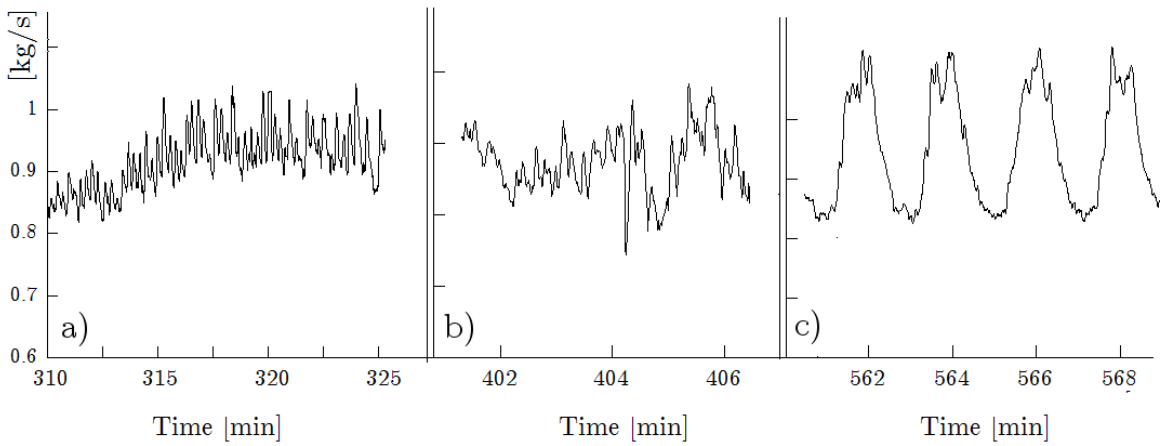

Figure 7.23: Mass flow rate vs time. a) Chaotic nucleate boiling at initiation of boiling, b) multimode nucleate / flashing, c) flashing dominated. 15.19 kW baseline experiment

Local void fraction measurements were recorded with the optical RBI probe placed near the inlet of the header. Results, averaged over a 10 second interval, are presented in Figure 7.24 for the baseline 15.19 kW case. It can observed that the average void fraction rarely drops to 0, a behavior that would otherwise suggest periodic slug flow. At the baseline power, the void fraction suggests that continuous nucleate boiling is present, with a peak void fraction of 4.68%. Histograms for the void fraction and gas bubble velocity are presented in Figures 7.25 - 7.26.

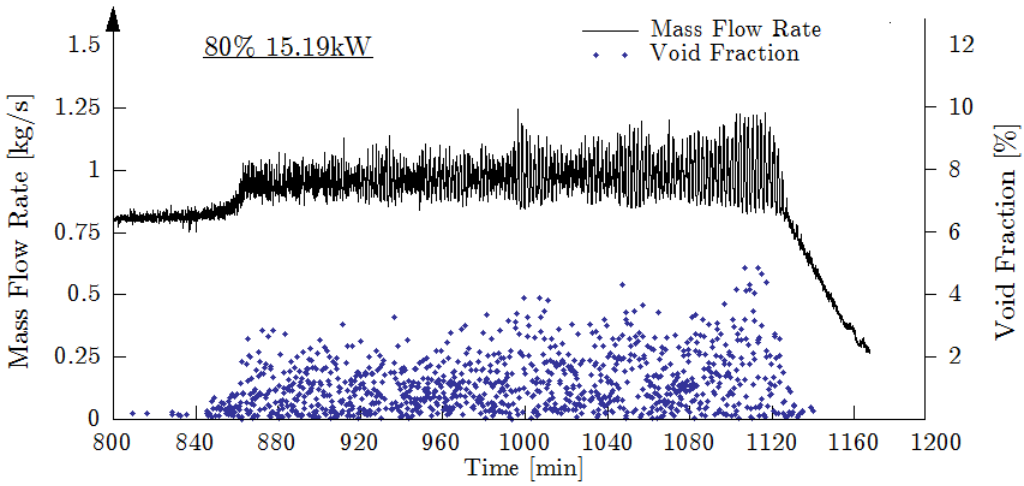

Figure 7.24: Void fraction averaged over 10 second period, shown with mass flow rate overlay

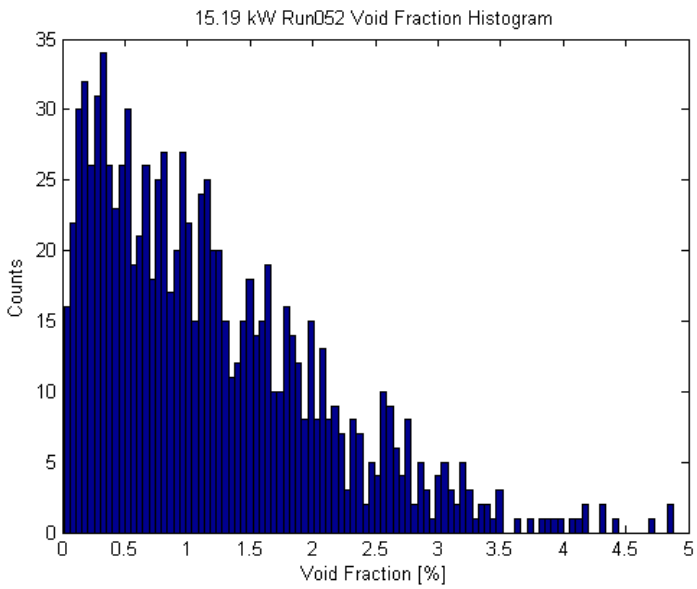

Figure 7.25: Void fraction histogram, 15.19 kW

Coupling between many of the system parameters is evident when observing the data on smaller time scaling, Figures 7.27. The pressure drop yields the first sign of a system oscillation, triggering a flow excursion evident in the system flow rate. Static pressures follow changes in flow rate exactly, while the tank pressure lags behind as steam is generated and travels upward through the water storage tank and into the steam vent.

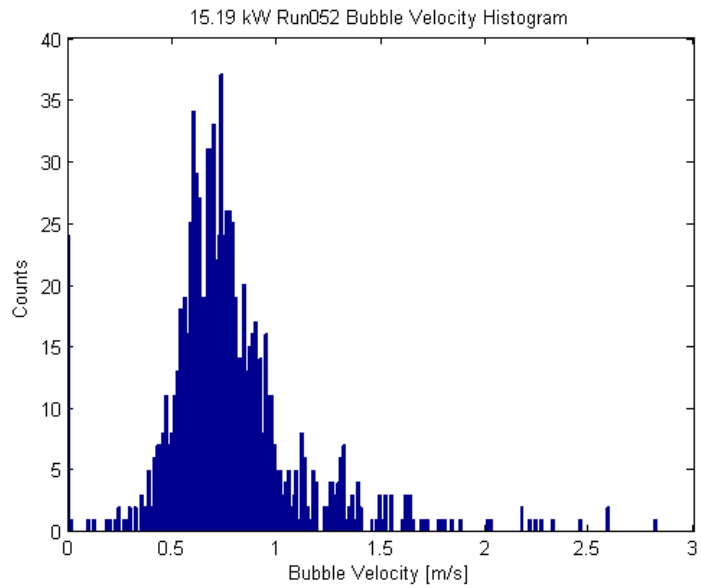

Figure 7.26: Gas bubble velocity histogram, 15.19 kW

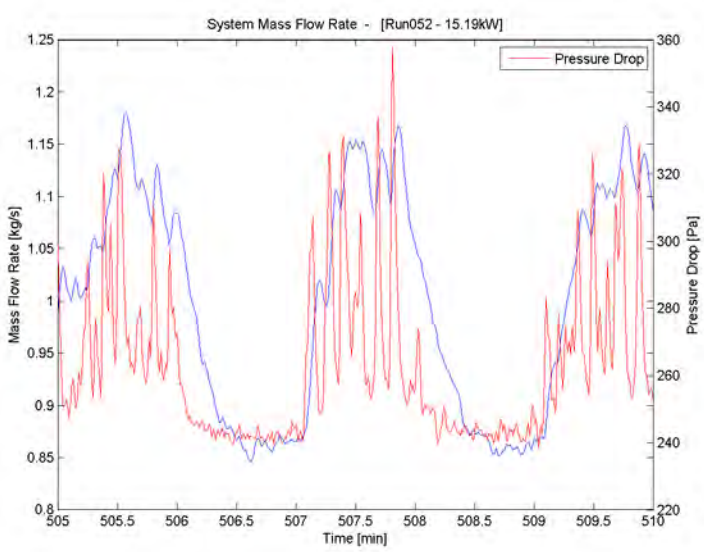

Figure 7.27: Coupling of pressure drop and mass flow rate for baseline conditions

7.3.2 Power Investigation

Three additional tests were performed at 12.55, 17.84, and 20.49 kW of supplied heater power, which resulted in a total heat flux deposition of 7.67, 10.90, and 12.52 kW/m2, respectively. Following baseline procedures, each test varied only in supplied power while maintaining all other parameters equal. From first inspection, the temperature at the header inlet remained constant among all four tests, and only differed during the approach to boiling, Figure 7.28.

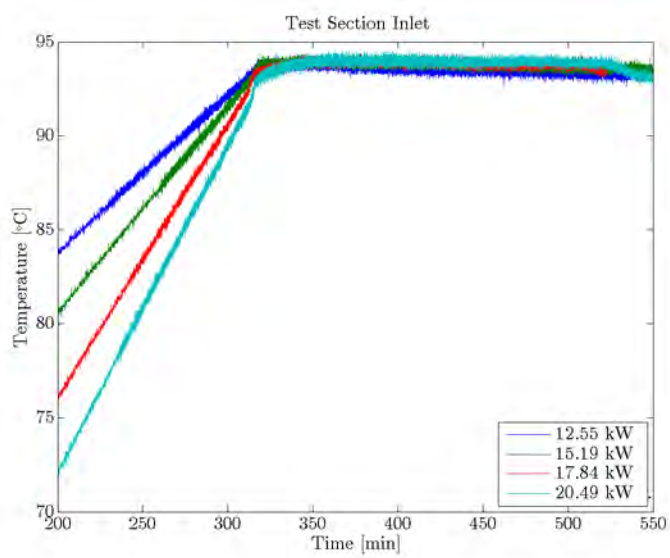

Figure 7.28: Growing amplitude of system flow rate excursions at varying powers

Each of the investigated power levels resulted in instabilities, which followed similar trends and behavior, however differed dramatically in magnitude, Figure 7.29. Flashing phenomena was the dominate mechanism for instabilities for the two highest powers observed, where large flow excursions occurred immediately upon the onset of boiling. At the lowest power of 12.55 kW, fluctuations were attributed to nucleate boiling, and flashing effects were not observed. The baseline power of 15.19 kW experienced a multimode behavior, with contributions from both mechanisms, and a gradual shift towards larger influence from flashing as the elapsed elapsed in time.

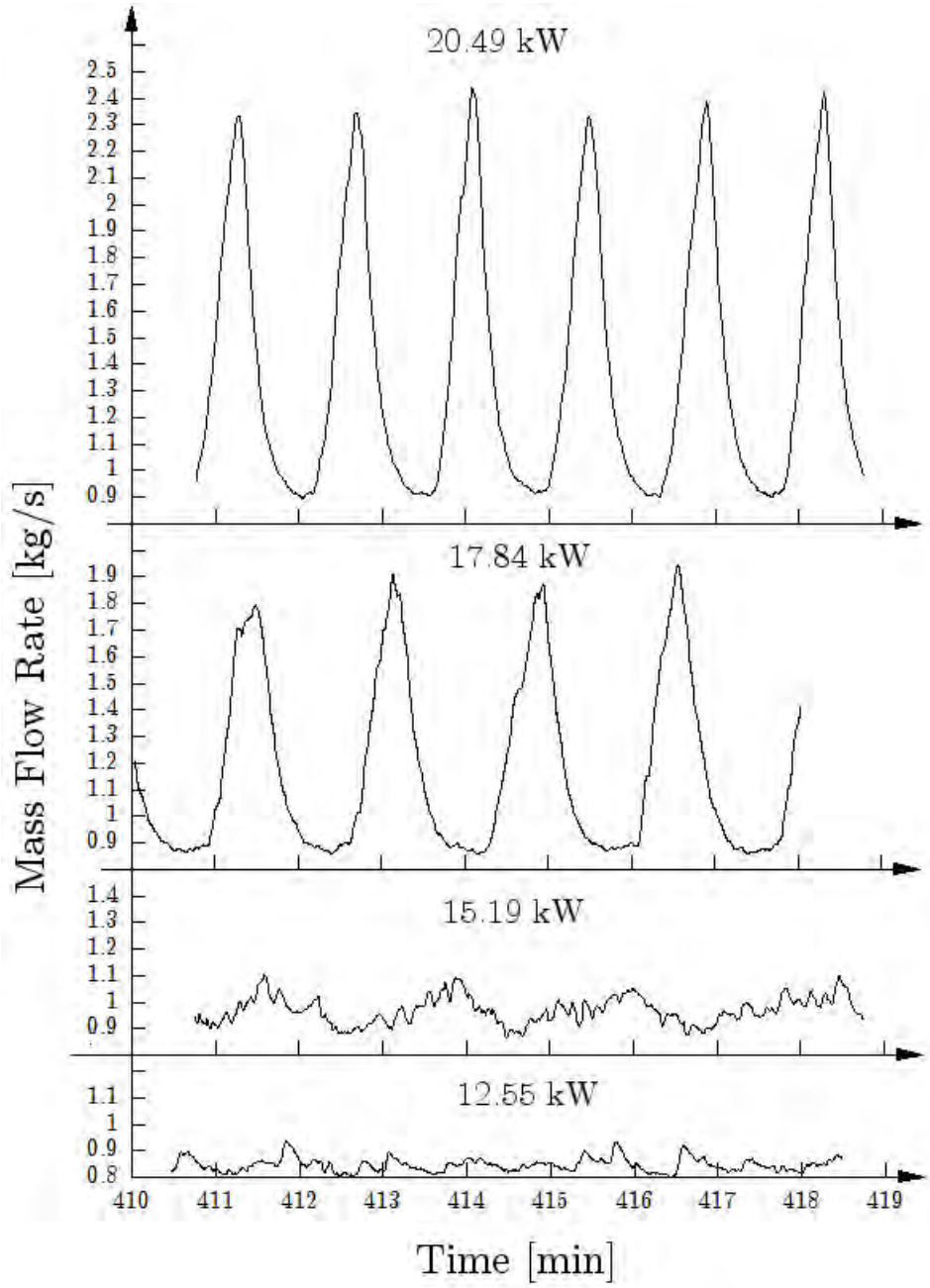

Figure 7.29: Growing amplitude of system flow rate excursions at increasing powers

Phase Portraits

The phase portrait in the plane of pressure drop and mass flow rate is presented in Figures 7.30, and depicts two primary regimes of flow behavior: chaotic oscillations due to intermittent periods of nucleate transition boiling observed at low power, and periodic oscillations due to flashing observed at higher powers. The slug and churn flow regimes initiated after flashing induce large peak, and stable baseline flow rates, while the intermittent bubbles created from nucleate boiling are insufficient in sustaining a stable baseline, and result in a varying time-dependent flow rate baseline.

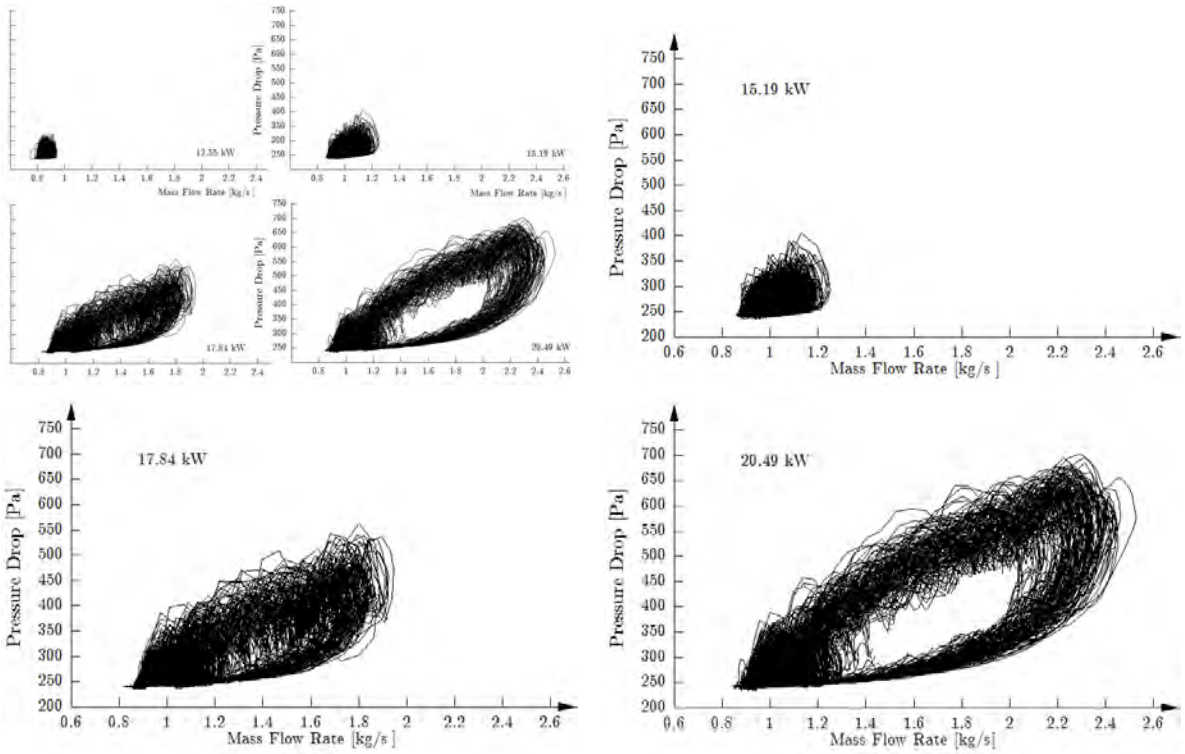

Figure 7.30: Phase portraits, pressure drop and mass flow rate at varying powers

Summary of Results

A summary of key parameters measured from the tests performed at powers of 12.55, 15.19, 17.84, and 20.49 kW are summarized below in Table 7.14.

Table 7.14: Results from two-phase testing, power investigation

	Run #	**Run054**	**Run052**	**Run059**	**Run061**
	Power	12.55 kW	15.19 kW	17.84 kW	20.49 kW
Duration	*Full Test*	606.82	622.51	542.24	608.99
	Boiling	226.05	261.464	196.34	212.487
Condensed	*Total*	12.29	18.16	17.33	21.88
	Rate	3.26	4.16	5.29	6.17
Mass Flow	*Avg*	0.84	1.01	1.40	1.65
	Max	0.94	1.15	2.02	2.52
	Min	0.74	0.81	0.82	0.84
	$\Delta m/m$	0.26	0.41	1.46	1.99
	Period	-	120.59	104.37	86.30
Void Fraction	*Mean*	0.92	1.18	3.07	6.36
	σ	0.85	0.89	3.57	8.12
Gas Velocity	*Mean*	0.76	0.83	0.79	0.85
	σ	0.97	0.65	0.86	0.85
Pressure Drop	*Avg*	247.54	257.08	284.96	314.82
	Max	422.26	422.26	623.64	702.25
	Min	235.01	236.23	234.46	233.67
Hydrostatic	*Avg*	9.36	9.44	9.51	9.64
	Max	9.46	9.53	9.71	9.91
	Min	9.27	9.29	9.30	9.30
Gas Space	*Avg*	9.07	13.28	19.21	25.79
	Max	19.61	21.13	31.09	41.41
	Min	3.62	5.08	4.84	4.41

7.3.3 Inlet Restriction

Of the test matrix established, one subset was to create conditions representative of the full scale prototype design, specifically matching the temperature rise, ΔT across the heated riser section. An orifice plate was placed at the inlet header to minimize influence on the two-phase flow above the heater portion, sized to obtain a 11.5 °C temperature rise. Nominally 4.067" in diameter, the inlet was reduced to 0.903", 7.31.

Figure 7.31: Orifice plate installed at inlet header

Following baseline procedures and conditions, the system at 80% volume underwent a 1 hour ramp to 15.19 kW and held at boiling for a duration of 4 hours. The temperature rise across the heated section due to the constricting effect of the orifice plate requires a subsequent decrease in system flow rate for a constant power. The result had pronounced effects, with high frequency flow excursions and pressure drops exceeding the limitations of the transducer installed on the upper networking, Figure 7.33

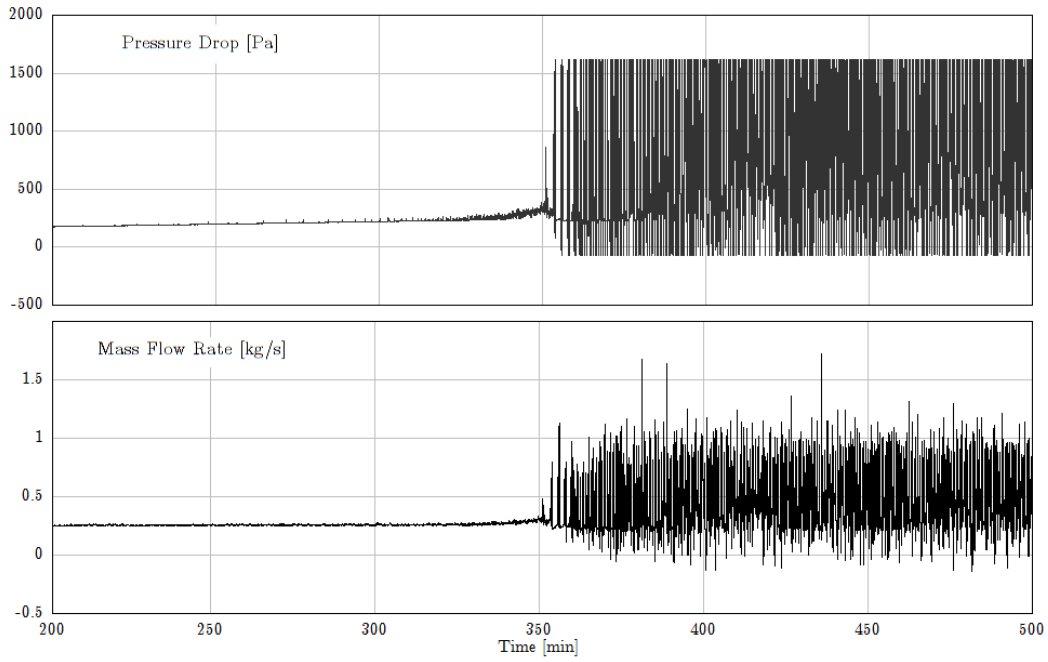

Figure 7.32: Mass flow rate and upper network pressure drop, Run066 (Basline+orifice). Saturation of pressure drop was due to exceeding range of the device

The measured flow oscillation period showed a significant increase in frequency from baseline conditions, with flow excursions occurring an average of every 25 seconds, compared to 120 seconds. Fundamentally the oscillations exhibit a difference shape as well, with sharp falls and rises before settling and repeating, while the baseline test exhibited smooth, a sinusoidal shape, Figure 7.33. Additionally, this test was unique in introducing flow reversals into the system at boiling. The reduced flow rate allowed more heat to enter a given volume of fluid, resulting in a large void creation. The extreme resistance of the orifice plate prevents the cold downcomer rushing in to fill the now low pressure region, and can result in flow reversals by the hot fluid in the risers exiting and temporarily traveling through the lower network portions. In addition to exceeding the limitations of the pressure transducer, it experience negative pressure drops at points within the measurement span, -50 - 1,600 Pa. The behavior was unique to the orifice plate test, as none of the other tests at varying powers or tank inventors experienced such behavior, Figure 7.34 7.35.

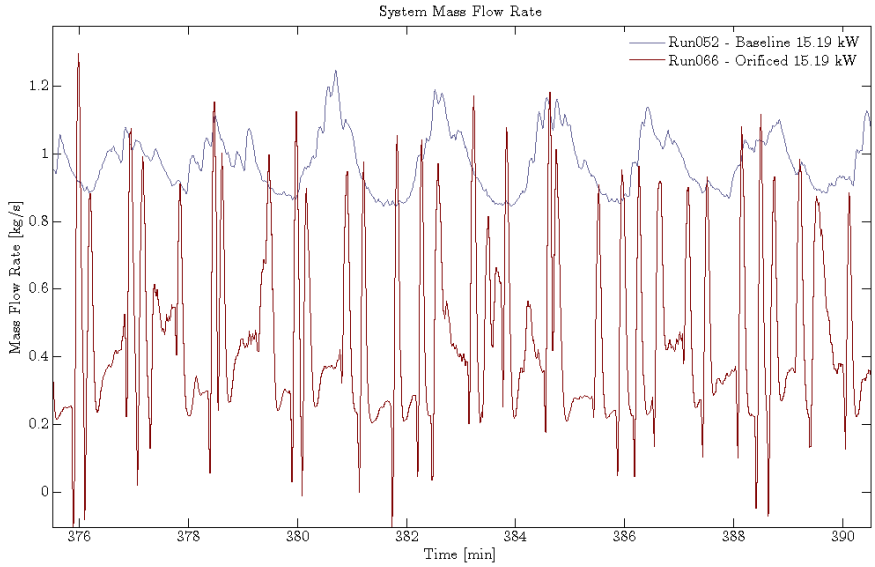

Figure 7.33: Mass flow rate detail. Orifice installation resulted in non-regular, sharp spike in the flow rate. Occasional flow reversal observed. Baseline exhibited periodic sinusoidal shape oscillations.

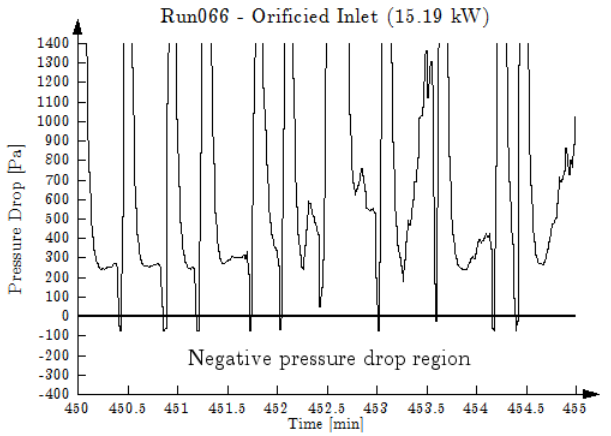

Figure 7.34: Orifice plate installed

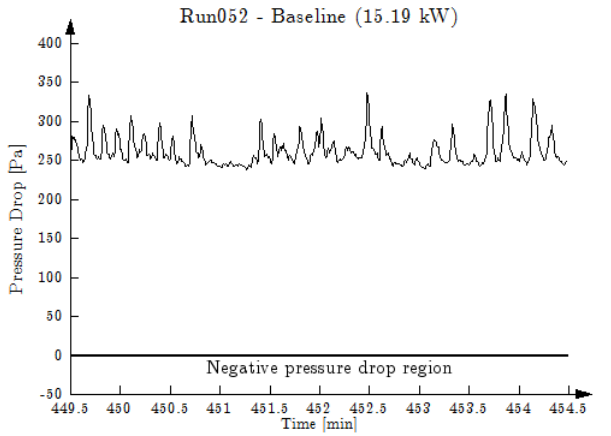

Figure 7.35: Baseline (no orifice plate)

7.3.4 Discussion

The natural circulation loop at the University of Wisconsin - Madison is unique in regards to an extended unheated riser and chimney lengths and very low frictional losses. All the powers investigated, bulk flow enters the heated section and exits the channel without ever changing phase and reaching a boiling condition. As the fluid rises in elevation through the unheated sections, it may reach its local saturation temperature and instantaneously flashes. This process of vapor generation is not created by heat from the outside, but instead a change in operating conditions due to the decrease in hydrostatic head. Additionally, the effect of operating a low pressure (atmospheric) further augments this effect, resulting in a high respectability due to flashing at normal conditions.

If the inlet flow velocity is reduced by creating a flow restriction, such as an orifice plate, boiling can occur within the heated section. The results seen with the orifice test are characteristic of geysering induced density wave oscillations, and exhibit a 'sharf fin' oscillation in the pressure drop. The boiling will initiate in the heated section as smaller bubbles, expanding, often times violently, as they rise in elevation through the unheated portions. The main difference with flashing instability is that the vapor is produced first in the heated section in case of geysering, whereas in flashing the vapor is formed by the decrease of the hydrostatic head as water flows up.

Bibliography

[1] Abram, T., Ion, S., "Generation-IV nuclear power: A review of the state of the science", Energy Policy, 36, 4323 - 4330 (2008).

[2] Albiston, S.M. "Experimental and CFD Single Phase Heat Transfer Studies of NGNP Water Reactor Cavity Cooling System." MS thesis. University of Idaho (2011)

[3] Albiston, S.M. "Natural Convective Flow in RCCS Rise Tubes Experiment". CAES-028. (2010): 1-14.

[4] Alfonsi, G., "Analysis of Streamwise Velocity Fluctuations in Turbulent Pipe Flow with the Use of an Ultrasonic Doppler Flowmeter." Flow, Turbulence and Combustion. 67. (2001): 137-142.

[5] Aritomi, M., Chiang, J. H., & Mori, M. (1993, June). Geysering in parallel boiling channels. Nuclear Engineering and Design, 141 (12), 111121.

[6] Aritomi, M., Chiang, J. H., Nakahashi, T., Wataru, M., & Mori, M. (1992).Fundamental study on thermohydraulics during start-up in natural circulation boil- ing water reactors, (I). Journal of Nuclear Science and Technology, 29 (7), 631 - 641.

[7] Aspen Aerogels. Pyrogel XT. Flexible Industrial Insulation for High-Temperature Applications. Data Sheet. (2012)

[8] Bakhmet'ev, A. 2009. Experimental Validation of the Cooling Loop for a Passive System for Removing Heat. Atomic Energy

[9] Bau, H. H., K. Torrance 1981. Transient and steady behavior of an open, symmetrically-heated, free convection loop. International Journal of Heat and Mass Transfer 24 (4): 597609

[10] Bau, H.H., and K.E. Torrance. "Transient and Steady Behavior of an Open, Symmetrically-Heated, Free Convection Loop." Int. J. Heat Mass Transfer. 24.4 (1981): 597-609.

[11] Bejan, A. (2004). Convection Heat Transfer (3rd ed.). Hoboken, New Jersey: John Wiley & Sons.

[12] Bejan, A. Convection Heat Transfer (3rd ed.). New Jersey: John Wiley & Sons. (2004).

[13] Bejan, A., and J.L. Lage. "The Prandtl Number Effect on the Transition in Natural Convection along a Vertical Surface." J. Heat Transfer. 112. (1990): 787-790.

[14] Ben, N., G. Lohnert, M. Buck, W. Bernnat 2006. The impact of design on the decay heat removal capabilities of a modular pebble bed HTR. Nuclear Engineering and Design 236 (5-6): 648–656.

[15] Borowsky, J., and T. Wei. "Simultaneous Velocimetry/Accelerometry Measurements in a Turbulent Two-Phase Pipe Flow." Experiments in Fluids. 41. (2006): 13-20.

[16] Bour, J., & Mihaila, A. (1966). The oscillatory behavior of heated channels. An analysis of the density effect. Part I: the mechanism (nonlinear analysis). Centre dEtudes Nucleaires de Grenoble, Report CEA, 3049 .

[17] Boure, J., A. Bergles, L. Tong 1973. Review of two-phase flow instability. Nuclear Engineering and Design 25 (2): 165–192.

[18] Brimley, W., W. B. Nicoll, A. B. Strong 1976. Flow oscillations in fixed-pressure-drop flow-boiling systems with random excitation. International Journal of Heat and Mass Transfer 19 (12): 1379-1386.

[19] Broring, S., J. Fischer, T. Korte, S. Sollinger, "Flow Structure of the Dispersed Gasphase in Real Multiphase Chemical Reactors Investigated by a New Ultrasound-

Doppler Technique." The Canadian Journal of Chemical Engineering. 69. (1991): 1247-1256.

[20] C.P. Tzanos, M.T. Farmer, Feasibility Study for Use of the Natural Convection Shutdown

[21] Camarasa, E., C. Vial, S. Poncin, G. Wild, N. Midoux, and J. Bouillard. "Influence of Coalescence Behaviour of the Liquid and of Gas Sparging on Hydrodynamics and Bubble Characteristics in a Bubble Column." Chemical Engineering and Processing. 38. (1999): 329-344.

[22] Carlson, J., and A. Grennberg. "Ultrasonic Measurements of Particle Concentration in a Multiphase Flow." IEEE Ultrasonics Symposium. (1999): 757-760.

[23] Catton, I. "Natural Convection in Enclosures." Proc. 6th Int. Heat Transfer Conf., Toronto. 6. (1978): 13-31 (as cited in Incropera et al., 2007).

[24] Chapin, D., S. Kiffer, and J. Nestell. "The Very High Temperature Reactor: A Technical Summary." MPR Associates, Inc. Rev. 0. Alexandria (2004).

[25] Charmeau, A., Ahmed, B., Wysoki, A., Wei, H.-C., Rose, M. P., Cunningham, B. W., et al. (2009). High Resolution Calculation of Heat Transfer in HTGR Reactor Cavity Cooling Systems. ICAPP2009, paper 9382. Tokyo, Japan.

[26] Chato, J.C. "Natural Convection Flows in Parallel-Channel Systems." Journal of Heat Transfer. 85.4 (1963): 339-345.

[27] Cheng, Lap-Yan Analysis of Depressurization Accident for a 2,400 MW Gas Cooled Reactor - Effects of the Reator Cavity Cooling System.(2005)..

[28] Chexal, V.K., and A.E. Bergles. "Two-Phase Instabilities in a Low Pressure Natural Circulation Loop." AIChE Symp Ser. 69.131 (1973): 37-54.

[29] Chung, B.J., J.H. Heo, M.H. Kim, and G.U. Kang. "The Effect of Top and Bottom Lids on Natural Convection Inside a Vertical Cylinder," Int. J Heat Mass Transfer. 54. (2011): 135-141.

[30] Churchill, S.W., and H.H.S Chu. "Correlating Equations for Laminar and Turbulent Free Convection from a Vertical Plate." Int. J. Heat Mass Transfer. 18. (1975): 1323-1329.

[31] Cimbala, J.M. , J.S. Brenizer, Jr., A.P. Chuang, S. Hanna, C. T. Conroy, A.A. El-Ganayni, and D.R. Riley. "Study of a Loop Heat Pipe Using Neutron Radiography." Bettis Atomic Power Laboratory Report. B-T-3386 (1999)

[32] Cushing, V. "Magnetoelectric Flowmeter." The Review of Scientific Instruments. 35.4 (1964): 496-499.

[33] D'Auria, F., G. Galassi 2010. Scaling in nuclear reactor system thermal-hydraulics. Nuclear Engineering and Design 240 (10): 3267–3293.

[34] DAuria, F., & Galassi, G. (1990, November). Characterization of instabilities during two- phase natural circulation in typical PWR conditions. Experimental Thermal and Fluid Science, 3 (6), 641-650

[35] Davies, R.M., and G.I. Taylor. "The Mechanics of Large Bubbles Rising through Liquids in Tubes." Proc. of Roy. Soc. London. 200, Ser. A (1950): 375-390.

[36] Deev, A.V., T. Rasheed, M.C. Welsh, M.M.K. Khan, and M.G. Rasul. "Measurement of Instantaneous Flow Velocities in a Concentric Reducer Using Particle Image Velocimetry: Study of Scale Deposition." Experimental Thermal and Fluid Science. 33. (2009): 1003-1011

[37] Desrayaud, G., G. Lauriat 2009. Flow reversal of laminar mixed convection in the entry region of symmetrically heated, vertical plate channels. International Journal of Thermal Sciences 48 (11): 2036–2045.

[38] Dijkman, F. 1971. Void fraction and stability of natural circulation water boiling in a vertical annulus heated internally: I. Axial phase and amplitude distribution of void fraction with uniform heat flux. Nuclear Engineering and Design 15: 77–95.

[39] Dumitrescu, D. T. "Stromung and Einer Luftbluse in Senkrechten rohr." Z. Angew. Math.Mech. 23.3 (1943): 139-149

[40] Durga Prasad, G. V., M. Pandey, M. S. Kalra 2007. Review of research on flow instabilities in natural circulation boiling systems. Progress in Nuclear Energy 49 (6): 429–451.

[41] Durrfeld, Heinz, "Mathematisches model zur untersuchung der temperatur-verteilung in strahlrohrbeheitzen ofen", Doctor-Ingenieurs dissertation, Rheinisch-Westfulischen Technischen Hochschule, Aachen. (1975)

[42] Eckert, S., A. Cramer, and G. Gerbeth. "Velocity Measurement Techniques for Liquid Metal Flows." Magnetohydrodynamics - Historical Evolution and Trends . (2007): 275-294

[43] Eckert, S., and G. Gerbeth. "Velocity Measurements in Liquid Sodium by Means of Ultrasound Doppler Velocimetry." Experiments in Fluids. (2002): 1-15.

[44] Eckert, S., G. Gerbeth, and V.I. Melnikov. "Velocity Measurements at High Temperatures by Ultrasound Doppler Velocimetry Using an Acoustic Wave Guide." Experiments in Fluids. 35. (2003): 381-388.

[45] Eckert, S., G. Gerbeth, V.I. Melnikov, C.-H. Lefhalm, and J. Knebel. "Application of Ultrasound Doppler Velocimetry to Flows of Hot Metallic Melts." 3rd International

Symposium on Ultrasonic Doppler Methods. 9-11 Sep 2002. Ed. Dr. G. De Cesare. Lausanne. (2002): 77-82.

[46] Eckert, S., P.A. Nikrityuk, D. Rabiger, K. Eckert, and G. Gerbeth. "Efficient Melt Stirring Using Pulse Sequences of a Rotating Magnetic Field: Part I. Flow Field in a Liquid Metal Column." Metallurgical and Materials Transactions. 38B. (2007): 977-988.

[47] Epoxies.com. 50-3100. High Thermal K Heat Transfer Epoxy Resin. Technical Bulletin. (2005). June 2012.

[48] FlatPlate. FPN10X20L-70. Hydronic Product & Application Catalog. (2010).

[49] Forsberg, C. W. 2006. Alternative Passive Decay-Heat Systems for the Advanced High-Temperature Reactor.

[50] Fukudo, K., Hasegawa, S. Analysis of two-phase flow instability in parallel multichannels.. Journal of Nuclear Science and Technology 16 (1979) 190 - 199.

[51] Geisler, T. "Ultrasonic Velocity Profile Measurements in Experimental Hydraulics." Diploma Thesis. Graz University of Technology (2001): 39-40.

[52] Generation IV International Forum, 2002. A Technology Road Map for Generation IV Nuclear Energy Systems, GIF-002-00. Issued by the U.S. DOE Nuclear Energy Research Advisory Committee and The Generation IV International Forum.

[53] Ghiaasiaan, S. M. (2007). Two-phase flow, boiling, and condensation: In conventional and miniature systems (1st ed.). Cambridge University Press.

[54] Goswami, N., S. Paruya 2011. Advances on the research on nonlinear phenomena in boiling natural circulation loop. Progress in Nuclear Energy 53 (6): 673–697.

[55] Guanghui, S., J. Dounan, K. Fukuda, G. Yujun 2002. Theoretical and experimental study on density wave oscillation of two-phase natural circulation of low equilibrium quality. Nuclear Engineering and Design 215 (3): 187–198.

[56] Haque, H., W. Feltes, G. Brinkmann 2006. Thermal response of a modular high temperature reactor during passive cooldown under pressurized and depressurized conditions. Nuclear Engineering and Design 236 (5-6): 475–484.

[57] Heat Removal Test Facility (NSTF) for Initial VHTR Water-Cooled RCCS Shutdown, Technical

[58] Henry, R. E. and Fauske, H. K., 1971, "The Two-Phase Critical in One-Component Mixtures in Nozzles, Orifices, and Short Tubes," Transactions of the ASME, Journal of Heat Transfer, p. 179

[59] Hosokawa, S., and A. Tomiyama. "Multi-Fluid Simulation of Turbulent Bubbly Pipe Flows." Chemical Engineering Science. 64. (2009): 5308-5318.

[60] I. Tiselj, G. Cerne, Some Comments on the Behavior of the RELAP5 Numerical Scheme at

[61] Incropera, F.P., D.P. DeWitt, T.L. Bergman, A.S. Lavine. Fundamentals of Heat and Mass Transfer (6th ed.). New Jersey: John Wiley & Sons. (2007). 371-376

[62] INEEL, RELAP5-3D Code Manual, INEEL-EXT-98-00834, revision 2.4, 2005

[63] Ishida, T., K. Akagawa, T. Fujii, H. Kutuna, K. Hashimoto, M. Ishizuka, Y. Futamura 1987. Characteristics of natural circulation flow in a bend loop with a U-shape-type cooler. Nuclear Engineering and Design 99: 413–421.

[64] Ishii, M., S. T. Revankar, T. Leonardi, R. Dowlati, M. L. Bertodano, I. Babelli, W. Wang, H. Pokharna, V. H. Ransom, R. Viskanta, J. T. Han 1998. The three-level

scaling approach with application to the Purdue University Multi-Dimensional Integral Test Assembly (PUMA). Nuclear Engineering and Design 186 (1-2): 177 - 211.

[65] Ito, D. H., Kikura, M. Aritomi, and M. Mori. "Study on Ultrasonic Velocity Profile Measurement in Vapor-Water Two-Phase Flow." 6th International Symposium on Ultrasonic Doppler Methods. 9-11 Sep 2008. Prague. (2008): 77-80.

[66] J. A. Trapp and V. H. Ransom, "A Choked-Flow Calculation Criterion for Nonhomogeneous, Nonequilibrium, Two-Phase Flows," International Journal of Multiphase Flow, 8, 6, 1982, pp. 669-681.

[67] Jaballah, S., Sammouda, H., & Belghith, A. (2007). Effect of Surface Radiation of the Natural-Convection Stability in a Two-Dimensional Enclosure with Diffusely Emitting Boundary Walls. Numerical Heat Transfer , 495-516.

[68] Jain, K., M. Petrick, D. Miller, S. Bankoff 1966. Self-sustained hydrodynamic oscillations in a natural-circulation boiling water loop. Nuclear Engineering and Design 4 (3): 233–252.

[69] Jain, V., A. Nayak, P. Vijayan, D. Saha, R. Sinha 2010. Experimental investigation on the flow instability behavior of a multi-channel boiling natural circulation loop at low-pressures. Experimental Thermal and Fluid Science 34 (6): 776–787.

[70] Jang, B.-I., M. H. Kim, G. Jeun 2011. Experimental and computational investigation of a natural circulation system in Regional Energy Reactor-10MWth. Nuclear Engineering and Design 241 (6): 2214–2223.

[71] Jeng, H.R., and C. Pan. "Analysis of Two-Phase Flow Characteristics in a Natural Circulation Loop Using the Drift-Flux Model Taking Flow Pattern Change and Subcooled Boiling into Consideration." Annals of Nuclear Energy. 26. (1999): 1227-1251. Print.

[72] Jiang, S., X. Yang, and Y. Zhang. "Description of Typical Flow Instabilities in the Natural Cirulation System." 10th International Conference on Nuclear Engineering. Arlington. (2002): 44-51. Print.

[73] Jiang, S.Y., X.X. Wu, S.R. Wu, J.H. Bo, Y.J. Zhang, and P. Han. "Experimental Study on Flashing Concerned Instability in a Natural Circulation System at Nuclear Heating Reactor Conditions." Kerntechnik. 62.4 (1997): 148-153

[74] K-Flex. Insul-Sheet. Flexible Closed Cell Sheet Insulation Designed for the HVAC/R Industry. Technical Data Sheet. (2010). Web. June 2012.

[75] Kakac, S., & Bon, B. (2008, February). A review of two-phase flow dynamic instabilities in tube boiling systems. International Journal of Heat and Mass Transfer , 51 (34), 399-433.

[76] Kaliatka, A., Uspuras, E., Benchmark analysis of main circulation pump trip events at the Ignalina NPP using RELAP5 code, Nuclear Engineering and Design, Volume 202, Issue 1, 1 November 2000, Pages 109-118,

[77] Kazansky, V., V. Dubovsky, G. Ziskind, and R. Letan. "Chimney-Enhanced Natural Convection from a Vertical Plate: Experiments and Numerical Simulations." International Journal of Heat and Mass Transfer. 46. (2003): 497-512.

[78] Kikura, H., T. Hayashida, D. Ito, M. Aritomi, and M. Mori. "Applications of Linear Ultrasonic Array Transducer to Two-Phase Flow Measurements." 6th International Symposium on Ultrasonic Doppler Methods. 9-11 Sep 2008. Prague. (2008): 95-98.

[79] Kinsler, L.E., A.R. Frey, A.B. Coppens, and J.V. Sanders. Fundamentals of Acoustics (4th ed.). Hoboken: John Wiley & Sons, Inc. (1999): 126; 526-528.

[80] Kolin, A. "Approaches to Blood-Flow Measurement by Means of Electromagnetic Catheter Flow Meters." IEEE Transactions on Magnetics. 6.2 (1970): 308-314.

[81] Koster, J.N. "Visualizing Convection and Solidification in Metallic Alloys." JOM. (1997): 31-35.

[82] Kumar, N., J. Doshi, P. Vijayan 2011. Investigations on the role of mixed convection and wall friction factor in single-phase natural circulation loop dynamics. Annals of Nuclear Energy 38 (10): 2247–2270.

[83] Kyung, I. S., S. Y. Lee 1994. Experimental observations on flow characteristics in an open two-phase natural circulation loop. Nuclear Engineering and Design 150 (1): 163–176.

[84] Lauda-Brinkmann. RM6 S. Operating Instructions: Compact Low Temperature Thermostats. (1996). Web. June 2012.

[85] Lee, J. D., C. Pan 2005. Nonlinear analysis for a double-channel two-phase natural circulation loop under low-pressure conditions. Annals of Nuclear Energy 32 (3): 299–329.

[86] Lee, S. Y., D. W. Lee 1991. Linear analysis of flow instabilities in an open two-phase natural circulation loop. Nuclear Engineering and Design 128 (3): 317–330.

[87] LeFevre, E.J. "Laminar Free Convection from a Vertical Plane Surface." Proc. Ninth Int. Congr. Appl. Mech, Brussels. 4.168 (1956)

[88] Liang K., Experimental and Analytical Study of Direct Contact Condensation of Steam in Water, Unpublished PhD thesis. Massachusetts Institute of Technology, (1991).

[89] Lisowski, D. et al., "Experimental Studies of NGNP Reactor Cavity Cooling System with Water," Proceedings of ICAPP, 11116, Nice, France. ICAPP (2011).

[90] Lisowski, D.D., S.M. Albiston, A. Tokuhiro, M.H. Anderson, and M.L. Corradini. "Results from a Scaled Reactor Cavity Cooling System with Water at Steady State." ICAPP. 24-28 June 2012. Chicago (2012)

[91] Lisowski, D.D., S.M. Albiston, R.M. Scherrer, T.C. Haskin, M.H. Anderson, A. Tokuhiro, and M.L. Corradini. "Experimental Studies of NGNP Reactor Cavity Cooling System with Water." ICAPP. 2-5 May 2011. Nice (2011)

[92] Lock, G.S.H., and F.J. deB. Trotter. "Observations on the Structure of a Turbulent Free Convection Boundary Layer." Int. J. Heat Mass Transfer. 11. (1968): 1225-1232.

[93] Lu, D., Z. Xiao, B. Chen 2010. A new method to derive one set of scaling criteria for reactor natural circulation at single and two-phase conditions. Nuclear Engineering and Design 240 (11): 3851–3861.

[94] M.T. Farmer, D.J. Kilsdonk, C. P. Tzanos, S. Lomperski, and R.W. Aeschlimann, Topical

[95] MacGregor, R.K., and A.P. Emery. "Free Convection through Vertical Plane Layers - Moderate and High Prandtl Number Fluids." J. Heat Transfer. 91.3 (1969): 391-403.

[96] Maiani, M., W. J. M. de Kruijf, W. Ambrosini 2003. An analytical model for the determination of stability boundaries in a natural circulation single-phase thermosyphon loop. International Journal of Heat and Fluid Flow 24 (6): 853–863.

[97] Manera, A., H.-M. Prasser, D. Lucas, and T.H.J.J. van der Hagen. "Three-Dimensional Flow Pattern Visualization and Bubble Size Distributions in Stationary and Transient Upward Flashing Flow." International Journal of Multiphase Flow. 32. (2006): 996-1016.

[98] Marcel, C. P., Rohde, M., & Van Der Hagen, T. (2009, November). Experimental and numerical investigations on flashing-induced instabilities in a single channel. Experimental Thermal and Fluid Science, 33 (8), 1197-1208.

[99] Marcel, C. P., Rohde, M., & Van Der Hagen, T. (2010, October). Experimental investigations on flashing-induced instabilities in one and two-parallel channels: A comparative study. Experimental Thermal and Fluid Science, 34 (7), 879-892.

[100] Marcel, C., M. Rohde, T. Van der Hagen 2008. Fluid-to-fluid modeling of natural circulation boiling loops for stability analysis. International Journal of Heat and Mass Transfer 51 (3-4): 566–575.

[101] Mashiko, T., T. Segawa, M. Sano, Y. Tsuji. "Simultaneous Measurements of Velocity Fields in Thermal Turbulence by USV and PIV." Flow Measurement and Instrumentation. 17. (2005): 107-112.

[102] Mathews, T. S., M. Ramakrishnan, U. Parthasarathy, A. J. Arul, C. S. Kumar 2008. Functional reliability analysis of Safety Grade Decay Heat Removal System of Indian 500 MWe PFBR. Nuclear Engineering and Design 238 (9): 2369–2376.

[103] Meister, J.J. "Mesure par echographie Doppler et modelisation theorique de leffet de troubles cardiaques sur la pression et le debit arteriels." These No. 504, Ecole Polytechnique Federale de Lausanne. (1983).

[104] Mertol, A., A. Lavine, R. Greif 1984. A study of the variation of the pressure in a natural circulation loop. International Journal of Heat and Mass Transfer 27 (4): 626–630.

[105] Met-Flow. Users Guide UVP Monitor Model UVP-DUO. Release 5 (2002): 3.1-3.15.

[106] Microtherm Group. Super A. Microtherm Super A - Ultra High Temperature Microporous Insulation. Data Sheet. Web. June 2012.

[107] Minagawa, H., T. Ishida, and T. Yasuda. "Contact Measurement of Turbulent Intensity of the Pipe Flow Using UVP." 6th International Symposium on Ultrasonic Doppler Methods. 9-11 Sep 2008. Prague. (2008): 127-130.

[108] Misale, M., P. Garibaldi, J. Passos, G. G. de Bitencourt 2007. Experiments in a single-phase natural circulation mini-loop. Experimental Thermal and Fluid Science 31 (8): 1111–1120.

[109] Misale, M., P. Garibaldi, L. Tarozzi, G. Barozzi 2011. Influence of thermal boundary conditions on the dynamic behaviour of a rectangular single-phase natural circulation loop. International Journal of Heat and Fluid Flow 32 (2): 413–423.

[110] Munoz-Cobo, J. L., O. Rosell, R. Mir, A. Escriv, D. Ginestar, G. Verd 2000. Coupling of density wave oscillations in parallel channels with high order modal kinetics: application to BWR out of phase oscillations. Annals of Nuclear Energy 27 (15): 1345–1371.

[111] Murakawa, H., H. Kikura, and M. Artitomi. "Application of Multi-Wave TDX For Multi-Phase Flow Measurement." 4th International Symposium on Ultrasonic Doppler Methods. 6-8 Sep 2004. Sapporo. (2004): 111-114.

[112] Murakawa, H., H. Kikura, and M. Artitomi. "Application of Ultrasonic Multi-Wave Method for Two-Phase Flow." 5th International Symposium on Ultrasonic Doppler Methods. 12-14 Sep 2006. Zurich. (2006): 23-26.

[113] Murakawa, H., H. Kikura, and M. Artitomi. "Measurement of Liquid Turbulent Structure in Bubbly Flow at Low Void Fraction Using Ultrasonic Doppler Method." Journal of Nuclear Science and Technology. 40.9 (2003): 644-654.

[114] Nakos, J.T. "Uncertainty Analysis of Thermocouple Measurements Used in Normal and Abnormal Thermal Environment Experiments at Sandias Radiant Heat Facility and Lurance Canyon Burn Site." Sandia National Laboratories Report. SAND2004-1023 (2004): 1-82

[115] Nayak, A. K., & Vijayan, P. K. (2008). Flow instabilities in boiling two-phase natural circulation systems: A review. Science and Technology of Nuclear Installations, 2008 , 1-15.

[116] Nayak, A. K., P. K. Vijayan, D. Saha, V. Venkat Raj 1995. Mathematical modelling of the stability characteristics of a natural circulation loop. Mathematical and Computer Modelling 22 (9): 77–87.

[117] Nayak, A., P. Dubey, D. Chavan, P. Vijayan 2007. Study on the stability behaviour of two-phase natural circulation systems using a four-equation drift flux model. Nuclear Engineering and Design 237 (4): 386–398.

[118] Neal, L., Zivi, S., & Wright, R. (1967). The mechanisms of hydrodynamic instabilities in boiling channel. (EURATOM Report, Pro-ceedings of Symposium on Two-Phase Flow Dynamics, Eindhoven)

[119] NSTF Facilities Plan for Water-Cooled RCCS: Normal Operational Test, Technical Report,

[120] Omega Engineering. 5TC-TT-K-24-72. Ready-Made Insulated Thermocouples. Technical Bulletin. Web. June 2012.

[121] Omega Engineering. FTB2001. FTB2000 Series Turbine Flow Rate Sensor Operating and Installation Instructions. (1992) Web. June 2012.

[122] Omega Engineering. QF-127210/240-T. High Temperature Cloth-Faced Infrared Panel Heaters. Technical Bulletin. Web. June 2012.

[123] Ostrach, S. "An Analysis of Laminar Free Convection Flow and Heat Transfer About a Flat Plate Parallel to the Direction of the Generating Body Force." National Advisory Committee for Aeronautics, Report 1111. (1953).

[124] Park, H.-S., K.-Y. Choi, S. Cho, S.-J. Yi, C.-K. Park, M.-K. Chung 2008. Experimental study on the natural circulation of a passive residual heat removal system for an integral reactor following a safety related event. Annals of Nuclear Energy 35 (12): 2249–2258.

[125] Personal Correspondence with Paul Bayless, INL (2011)

[126] Peterson, P. F., V. E. Schrock, R. Greif 1998. Scaling for integral simulation of mixing in large, stratified volumes. Nuclear Engineering and Design 186 (1-2): 213–224.

[127] Pinheiro Rosa, M., M. Podowski 1994. Nonlinear effects in two-phase flow dynamics. Nuclear Engineering and Design 146 (1-3): 277–288.

[128] Porta, P.A., D.P. Cutin, and J.G. McInerney. "Laser Doppler Velocimetry by Optical Self Mixing in Vertical-Cavity Surface-Emitting Lasers." IEEE Photonics Technology Letters. 14.12 (2002): 1719-1721

[129] Prud'homme, M., L. Robillard, P. Vasseur 1987. A study of laminar natural convection in a non-uniformly heated annular fluid layer. International Journal of Heat and Mass Transfer 30 (6): 1209–1222.

[130] Ransom, V. H., W. Wang, M. Ishii 1998. Use of an ideal scaled model for scaling evaluation. Nuclear Engineering and Design 186 (1-2): 135–148.

[131] Rao, N., B. Maiti, P. Das 2005. Pressure variation in a natural circulation loop with end heat exchangers. International Journal of Heat and Mass Transfer 48 (7): 1403–1412.

[132] Rao, Y.F, K. Fukuda, and T. Koga. "Experimental and Numerical Study of Two-Phase Flow Instabilities in Natural-Circulation Boiling Channels." Fifth International Conference on Nuclear Energy. 26-30 May 1997. Nice (1997): 1-18

[133] Report, ANL-GENIV-079, 2006

[134] Resolution Calculation of Heat Transfer in HTGR Reactor Cavity Cooling Systems. ICAPP2009, paper 9382. Tokyo, Japan.

[135] Ridouane, E. H., C. M. Danforth, D. L. Hitt 2010. A 2-D numerical study of chaotic flow in a natural convection loop. International Journal of Heat and Mass Transfer 53 (1-3): 76–84.

[136] Rizwan-Uddin 1994. On density-wave oscillations in two-phase flows. International Journal of Multiphase Flow 20 (4): 721–737.

[137] Rizwan-Uddin, J. Dorning 1986. Some nonlinear dynamics of a heated channel. Nuclear Engineering and Design 93 (1): 1–14.

[138] Satoh, A., Okamoto, K., & Madarame, H. (1998, September). Instability of single-phase natural circulation under double loop system. Chaos, Solitons & Fractals, 9 (9), 1575-1585.

[139] Satou, A., H. Madarame, K. Okamoto 2001. Unstable behavior of single-phase natural circulation under closed loop with connecting tube. Experimental Thermal and Fluid Science 25 (6): 429–435.

[140] Seki, N., S. Fukusako, and H. Inaba. "Visual Observation of Natural Convective Flow in a Narrow Vertical Cavity." J. Fluid Mech. 84. (1978): 695-704

[141] Seyed Khalil Mousavian, Mario Misale, Francesco D'Auria, Mahmoud A. Salehi, Transient and stability analysis in single-phase natural circulation, Annals of Nuclear Energy, Volume 31, Issue 10, July 2004, Pages 1177-1198, ISSN 0306-4549, DOI: 10.1016/j.anucene. 2004.01.005.

[142] Sim, Y. S., R. Y. Park, S. Kim 2007. Development of a new decay heat removal system for a high temperature gas-cooled reactor. Annals of Nuclear Energy 34 (10): 803–812.

[143] Simoneau, J.-P., J. Champigny, B. Mays, L. Lommers 2007. Three-dimensional simulation of the coupled convective, conductive, and radiative heat transfer during decay heat removal in an HTR. Nuclear Engineering and Design 237 (15-17): 1923–1937.

[144] Song, J. 2008. Performance and scaling analysis for a two-phase natural circulation loop. International Communications in Heat and Mass Transfer 35 (9): 1084–1090.

[145] Soong, Y., I.K. Gamwo, A.G. Blackwell, F.W. Harke, and E.P. Ladner. "Ultrasonic Characterizations of Slurries in a Bubble Column Reactor." Ind. Eng. Chem. Res. (1999): 2137-2143..

[146] Sorrell, F.Y., T.B. Curtin, and M.D. Feezor. "An Electromagnetic Current Meter-Based System for Application in Unsteady Flows." IEEE Journal of Oceanic Engineering. 15.4 (1990): 373-379.

[147] Squire, H.B., in S. Goldstein, Modern Developments in Fluid Dynamics, Vol. II, Dover, New York. (1965): 641-643

[148] Swapnalee, B., P. Vijayan 2011. A generalized flow equation for single phase natural circulation loops obeying multiple friction laws. International Journal of Heat and Mass Transfer 54 (11-12): 2618–2629.

[149] Taitel, Y., D. Bornea, and A.E. Dukler. "Modelling Flow Pattern Transitions for Steady Upward Gas-Liquid Flow in Vertical Tubes." AlChE Journal. 26.3 (1980): 345-354

[150] Takeda, Y. "Measurement of Velocity Profile of Mercury Flow by Ultrasound Doppler Shift Method." Nuclear Technology. 79.1 (1987): 120-124.

[151] Takeda, Y. "Velocity Profile Measurement by Ultrasound Doppler Shift Method." Int. J. Heat and Fluid Flow. 7.4 (1986): 313-318

[152] Takeda, Y. "Development of an Ultrasound Velocity Profile Monitor." Nuclear Engineering and Design. 126. (1991): 277-284

[153] Thielman, J., P. Ge, Q. Wu, L. Parme 2005. Evaluation and optimization of General Atomics' GT-MHR reactor cavity cooling system using an axiomatic design approach. Nuclear Engineering and Design 235 (13): 1389–1402.

[154] Thome, J. (2004). Chapter 12: Two-phase flow patterns. In Wolverine engineering data book III (pp. 12-1-12-34). Wolverine Tube Inc

[155] Tong, L. S., & Tang, Y. S. (1997). Boiling heat transfer and two-phase flow (2Sub ed.). CRC Press.

[156] Tzanos, P., Farmer, M.T. Feasibility Study for Use of the Natural Convection Shutdown Heat Removal Test Facility (NSTF) for Initial VHTR Water-Cooled RCCS Shutdown.(2006)..

[157] Vijayan, P., A.. The limits of conditional stability for single-phase natural circulation with throughflow in a figure-of-eight loop. Nuclear Engineering and Design 136 (3): 361–380.

[158] Vijayan, P., H. Austregesilo 1994. Scaling laws for single-phase natural circulation loops. Nuclear Engineering and Design 152 (1-3): 331–347.

[159] Vijayan, P., M. Sharma, D. Saha 2007. Steady state and stability characteristics of single-phase natural circulation in a rectangular loop with different heater and cooler orientations. Experimental Thermal and Fluid Science 31 (8): 925–945.

[160] Wang, C., Zhong, Z, eta al., "Prediction of jet penetration depth based on least square support vector machine", Powder Technology 203(2), 404 - 411 (2010).

[161] Wang, J., J. Li, J. Jackson 2004. A study of the influence of buoyancy on turbulent flow in a vertical plane passage. International Journal of Heat and Fluid Flow 25 (3): 420–430.

[162] Yang R., Liu R., Zhong Y., Lui T., "Experimental study on convective heat transfer of water flow in a heated tube under natural circulation", Nuclear Engineering and Design, 236, 1902 - 1908 (2006).

[163] Yun, G., G. Su, J. Wang, W. Tian, S. Qiu, D. Jia, J. Zhang 2005. Two-phase instability analysis in natural circulation loops of China advanced research reactor. Annals of Nuclear Energy 32 (4): 379–397.

[164] Zheng, Y., L. Shi, Y. Dong 2009. Thermohydraulic transient studies of the Chinese 200 MWe HTR-PM for loss of forced cooling accidents. Annals of Nuclear Energy 36 (6): 742–751.

[165] Zvirin, Y. 1985. Natural circulation loops with parallel channels - transient behavior. Nuclear Engineering and Design 84 (1): 73–81.

NUCLEAR ENERGY UNIVERSITY PROGRAMS

Experimental Studies of NGNP Reactor Cavity Cooling System with Water

PI: Corradini, Michael - University of Wisconsin, Madison

Collaborators:
Anderson, Mark - University of Wisconsin, Madison
Hassan, Yassin - Texas A&M University
Tokuhiro, Akira - University of Idaho

Project Number: 09-202

Initiative/Campaign: Gen IV/Methods

Abstract

This project will investigate the flow behavior that can occur in the reactor cavity cooling system (RCCS) with water coolant under the passive cooling-mode of operation. The team will conduct separate-effects tests and develop associated scaling analyses, and provide system-level phenomenological and computational models that describe key flow phenomena during RCCS operation, from forced to natural circulation, single-phase flow and two-phase flow and flashing. The project consists of the following tasks:

- Conduct separate-effects, single-phase flow experiments and develop scaling analyses for comparison to system-level computational modeling for the RCCS standpipe design. A transition from forced to natural convection cooling occurs in the standpipe under accident conditions. These tests will measure global flow behavior and local flow velocities, as well as develop instrumentation for use in larger scale tests, thereby providing proper flow distribution among standpipes for decay heat removal.
- Conduct separate-effects experiments for the RCCS standpipe design as two-phase flashing occurs and flow develops. As natural circulation cooling continues without an ultimate heat sink, water within the system will heat to temperatures approaching saturation , at which point two-phase flashing and flow will begin. The focus is to develop a phenomenological model from these tests that will describe the flashing and flow stability phenomena. In addition, one could determine the efficiency of phase separation in the RCCS storage tank as the two-phase flashing phenomena ensues and the storage tank vents the steam produced.
- Develop a system-level computational model that will describe the overall RCCS behavior as it transitions from forced flow to natural circulation and eventual two-phase flow in the passive cooling-mode of operation. This modeling can then be used to test the phenomenological models developed as a function of scale.

Supplement C.1: UW RCCS Facility

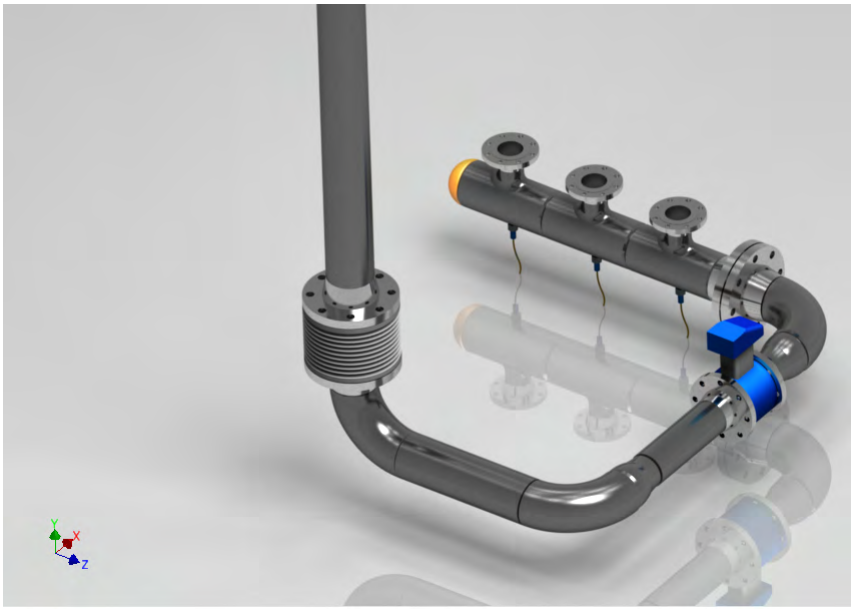

Supplement C.2: Model of experimental facility lower network

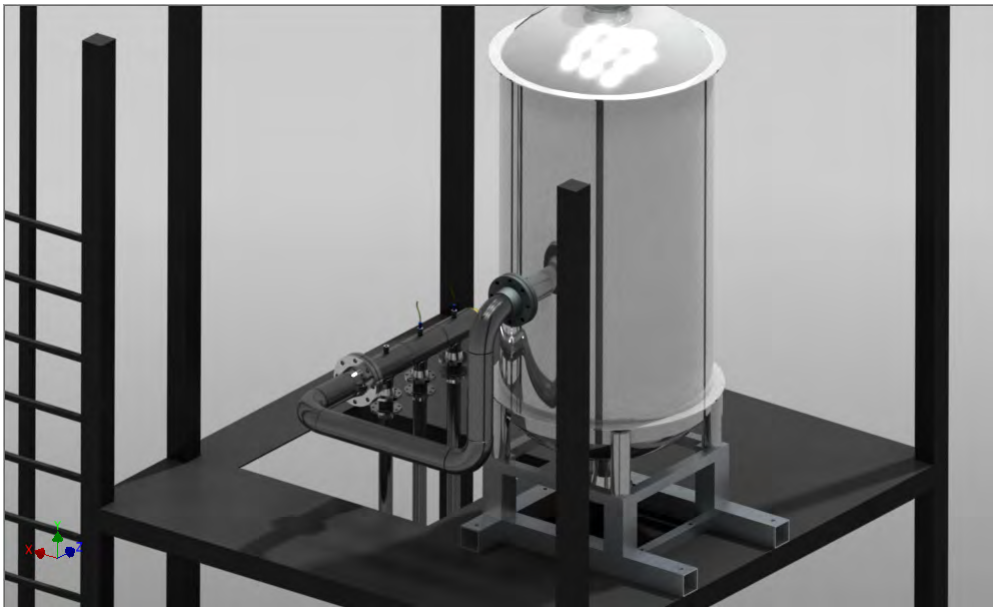

Supplement C.3: Model of experimental facility upper network and tank

Supplement C.4: View along test section prior to installation within structure

Supplement C.5: Bottom view of test section installed within structure; with brace that allows for axial extension without lateral movement

Supplement C.6: Downcomer support "a-frame" spring and turnbuckle provide support while allowing for axial extension

Supplement C.7: {
View down test section with heater box frame surrounding, also insertion points for interior thermocouples

Supplement C.8: Single heater module with six heaters attached to zircal-18 insulation

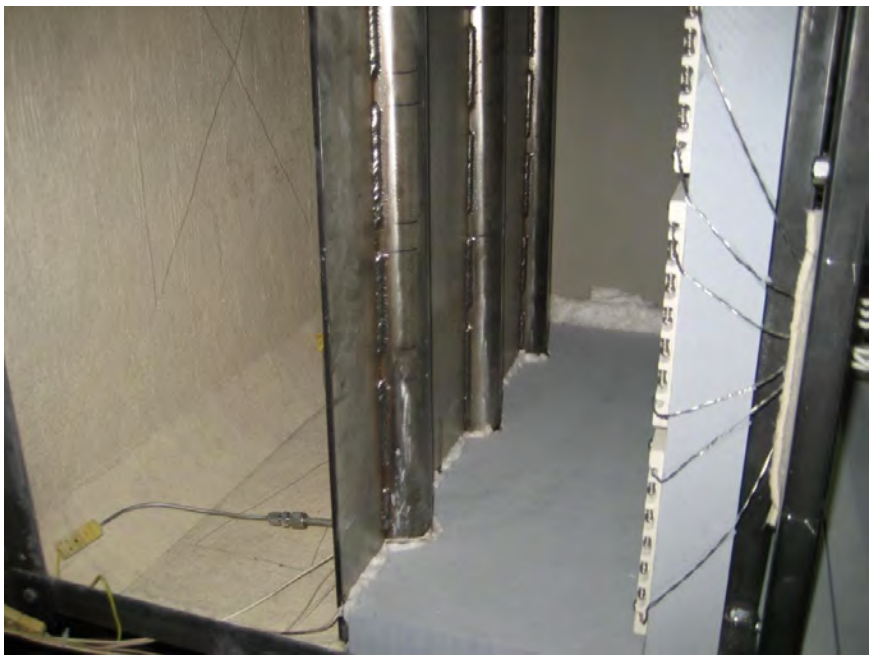

Supplement C.9: {
Front view of test section within heater box with insulation and thermocouples installed

Supplement C.10: Storage tank and upper network plumbing

Supplement C.11: {
Bottom network plumbing with insulation, also shown is system magnetic flow meter, as well as emergency drain line

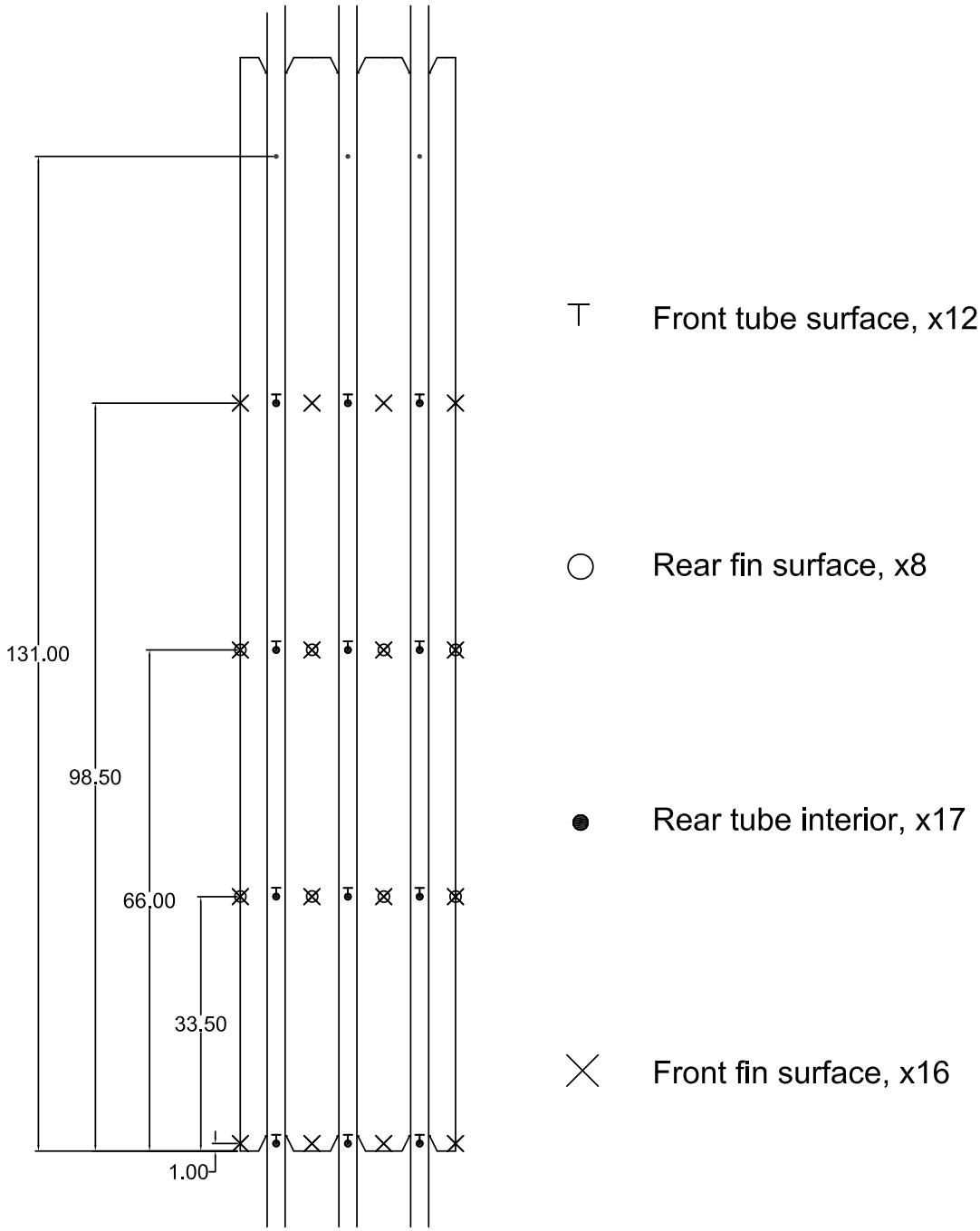
131.00
98.50
66.00
33.50
1.00
Front tube surface, x12
Rear fin surface, x8
Rear tube interior, x17
Front fin surface, x16

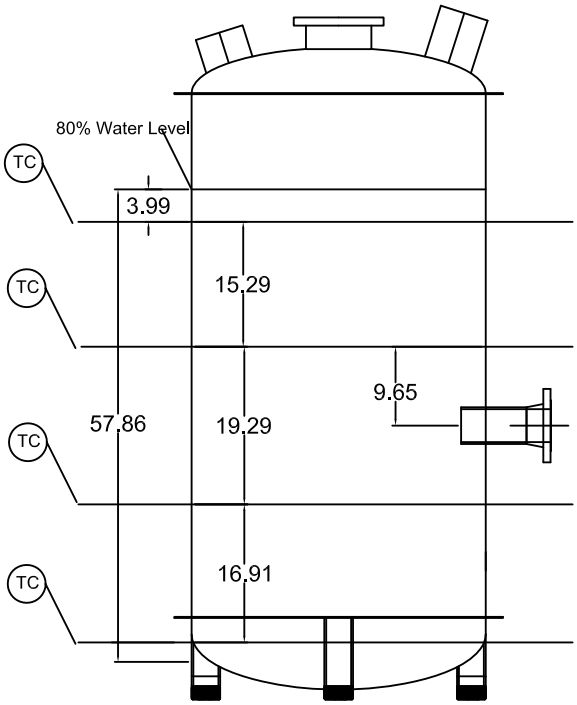
80% Water Level
TC
TC
TC
TC
3.99
15.29
9.65
57.86
19.29
16.91

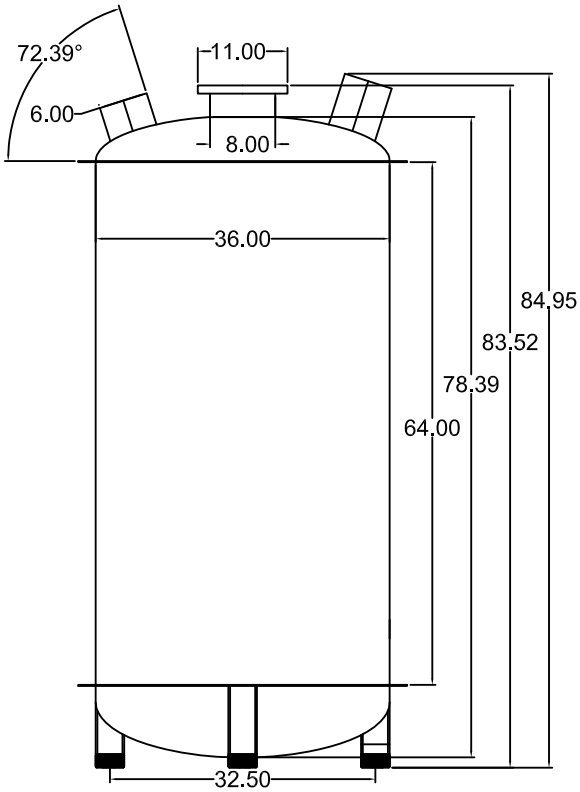
72.39°
11.00
6.00
8.00
36.00
84.95
83.52
78.39
64.00
32.50

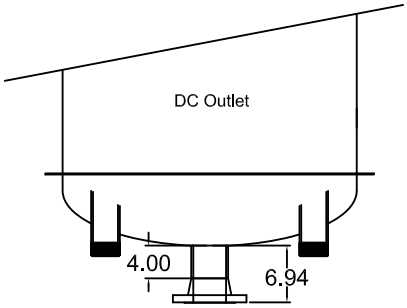
DC Outlet
4.00
6.94

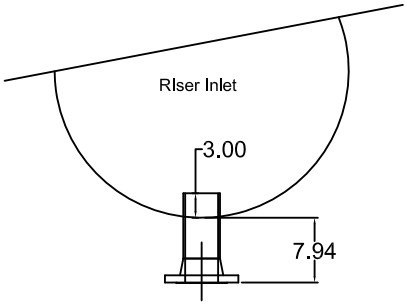
RIser Inlet
3.00
7.94

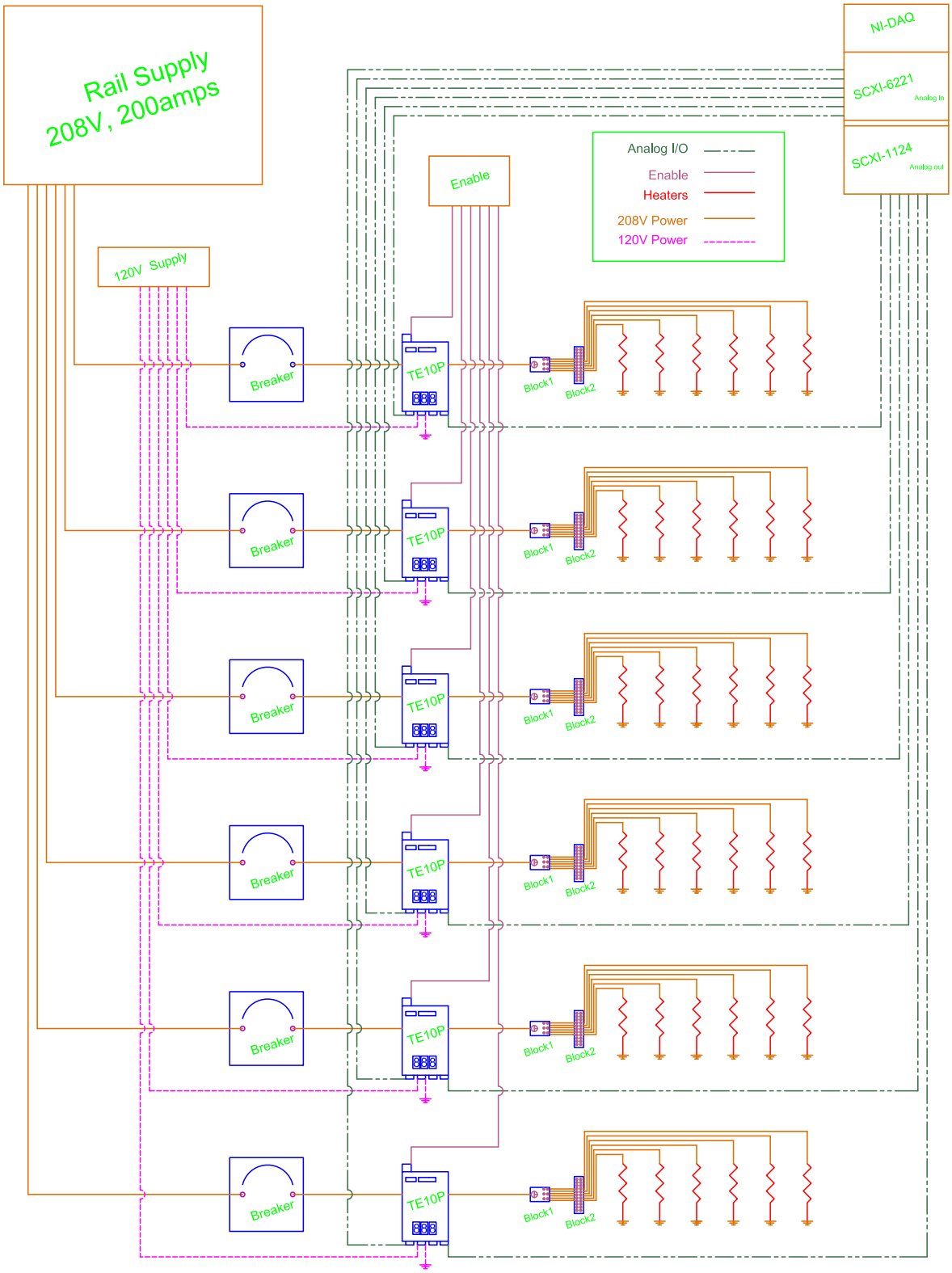
Rail Supply
208V, 200amps
NI-DAQ
SCXI-6221
Analog In
SCXI-1124
Analog out
Analog I/O
Enable
Heaters
208V Power
120V Power
Enable
120V Supply
Breaker
TE10P
Block1
Block2

RCCS Operational Binder Last Updated: September 19th 2011

Equipment List, 1/4

A. Flowmeters

1) *Device*: Large Magnetic Flow Meter
Description: 3.0" / 80mm magnetic bare face flow rate meter
Quantity: x1
Manufacture: Flocat (Krone)
Model: Optiflux 1000, C-RK20-C006. 80Mm/3" - PFA-HC-PN150 PSI
Serial N°: A05 16102
Date Installed:

2) *Device*: Convertor for Large Magnetic Flow Meter
Description: Processing unit for Large Magnetic Flow Meter
Quantity: x1
Manufacture: Flocat (Krone)
Model: C-RK75-A004
Serial N°:
Date Installed:

3) *Device*: Small Magnetic Flow Meter
Description: 0.5" / 15mm magnetic wafer style flow rate meter
Quantity: x1
Manufacture: Rosemount
Model: 8711
Serial N°: 0880096262
Date Installed:

4) *Device*: Convertor for Small Magnetic Flow Meter
Description: Processing unit for Small Magnetic Flow Meter
Quantity: x1
Manufacture: Rosemount
Model: 8712C
Serial N°: 0860115806
Date Installed:

RCCS Operational Binder Last Updated: September 19th 2011

Equipment List, 2/4

B. Thermocouples

5) *Device*: Surface Thermocouple
Description: Welded thermocouples for surface measurement.
Specifications: 20 gauge, Type K
Quantity: Bulk spool (75 feet)
Manufacture: Omega
Model: HH-K-20-50
Serial N°: *n/a*
Date Installed:

6) *Device*: Interior Thermocouple
Description: Manufactured thermocouples for internal water measurement.
Specifications: 1/8th in diameter, 12" long, Type-K. Inconel, Special limits of error. Grounded
Quantity: x19
Manufacture: Omega
Model: HKMQIN-125G-12
Serial N°: *n/a*
Date Installed:

RCCS Operational Binder Last Updated: September 19th 2011

Equipment List, 3/4

C. National Instruments Data acquisition

7) *Device*: NI Chassis
Quantity: x1
Manufacture: National Instruments
Model: SCXI-1000
Serial N°: 15B7005
Date Installed:

8) *Device*: TC/Analogue Input Card for NI Chassis
Quantity: x2
Manufacture: National Instruments
Model: SCXI-1102
Serial N°:
Date Installed:

9) *Device*: Analogue Output Module for NI Chassis
Quantity: x1
Manufacture: National Instruments
Model: SCXI-1124
Serial N°:
Date Installed:

10) *Device*: Digital SSR Module for NI Chassis
Quantity: x1
Manufacture: National Instruments
Model: SCXI-1163R
Serial N°:
Date Installed:

11) *Device*: Computer PCI Card for NI Chassis
Quantity: x1
Manufacture: National Instruments
Model: PCI-6221
Serial N°:
Date Installed:

RCCS Operational Binder Last Updated: September 19th 2011

Equipment List, 4/4

D. Power Controllers

12) *Device*: Eurotherm Power Controller
Description: Thyristor power units to control active power
Quantity: x6
Manufacture: Eurotherm
Model: TE10P
Serial N°: US193133-1-1-05-05, US19495-1-3-09-05, US19495-1-1-09-05, US19495-1-2- 09-05, US19977-1-2-01-06, US19977-1-3-01-06, US19977-1-1-01-06
Date Installed:

E. Lab Computer

13) *Device*: Computer
Description: Lab computer for NI-DAQ hookup
Specifications:
Quantity: x1
Manufacture: Dell
Model: Inspiron 560 Minitower
Serial N°: 5TQBDP1
Date Installed:

F. RTD Calibration Reference

14) *Device*: RTD Probe
Description: Platinum RTD
Specifications: 0 – 961 °C
Quantity: x1
Manufacture: Fluke – Hart Scientific
Model: 5624
Serial N°: 0409
Date Installed:

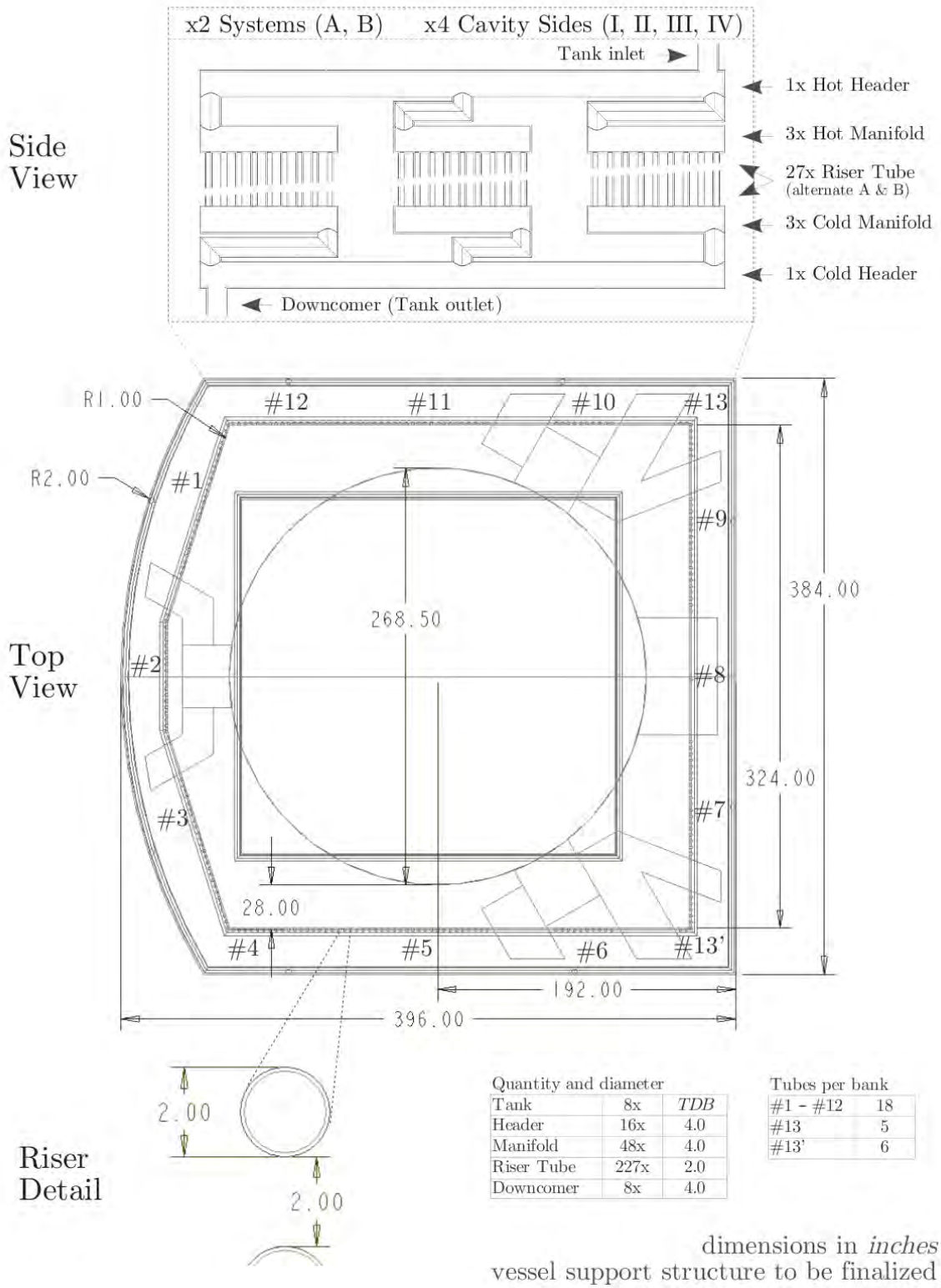

Quantity and diameter

Tank	8x	*TDB*
Header	16x	4.0
Manifold	48x	4.0
Riser Tube	227x	2.0
Downcomer	8x	4.0

Tubes per bank

#1 - #12	18
#13	5
#13'	6

Full scale water RCCS concept, RPV

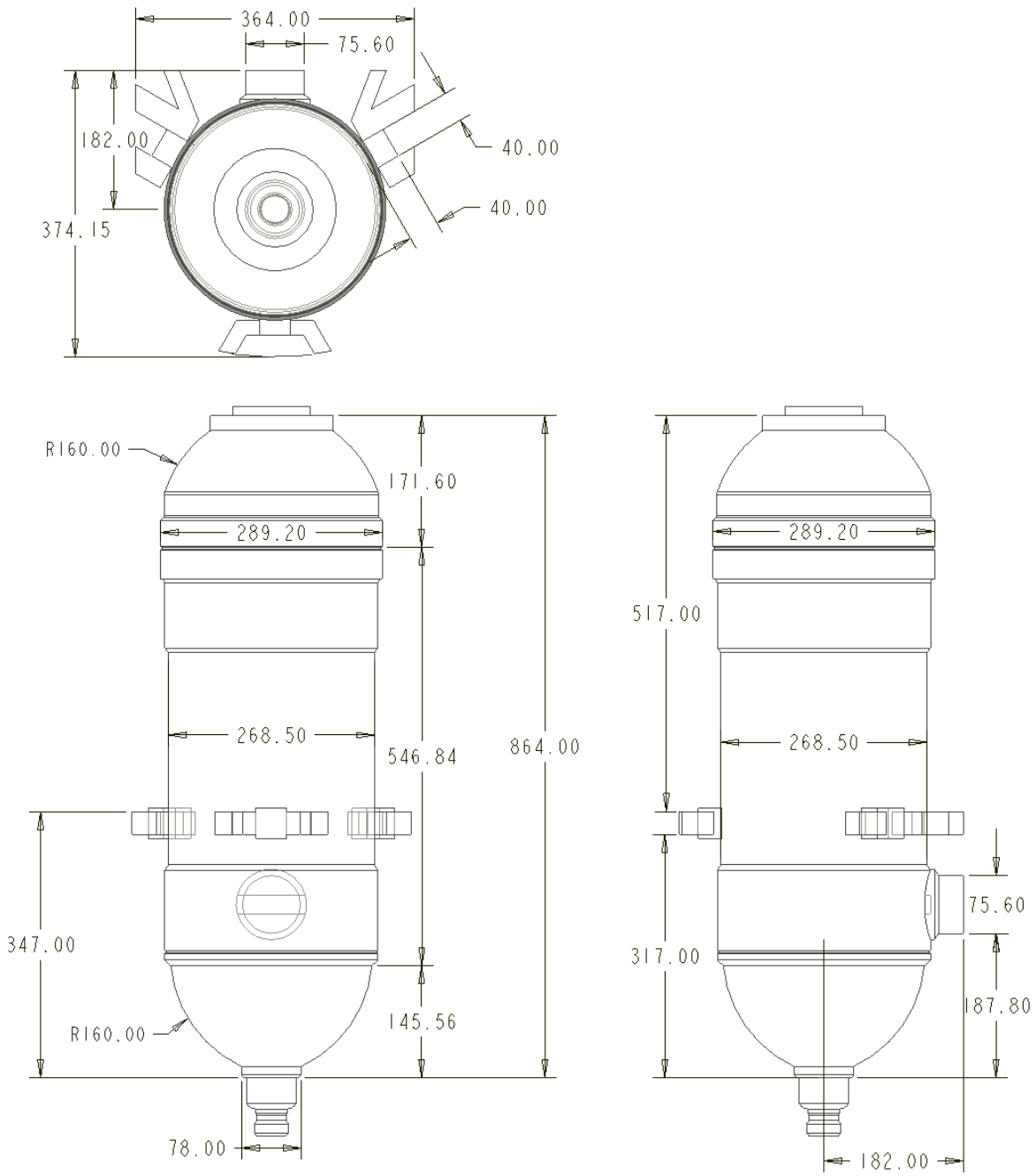

Full scale water RCCS concept, RPV

Full scale water RCCS concept

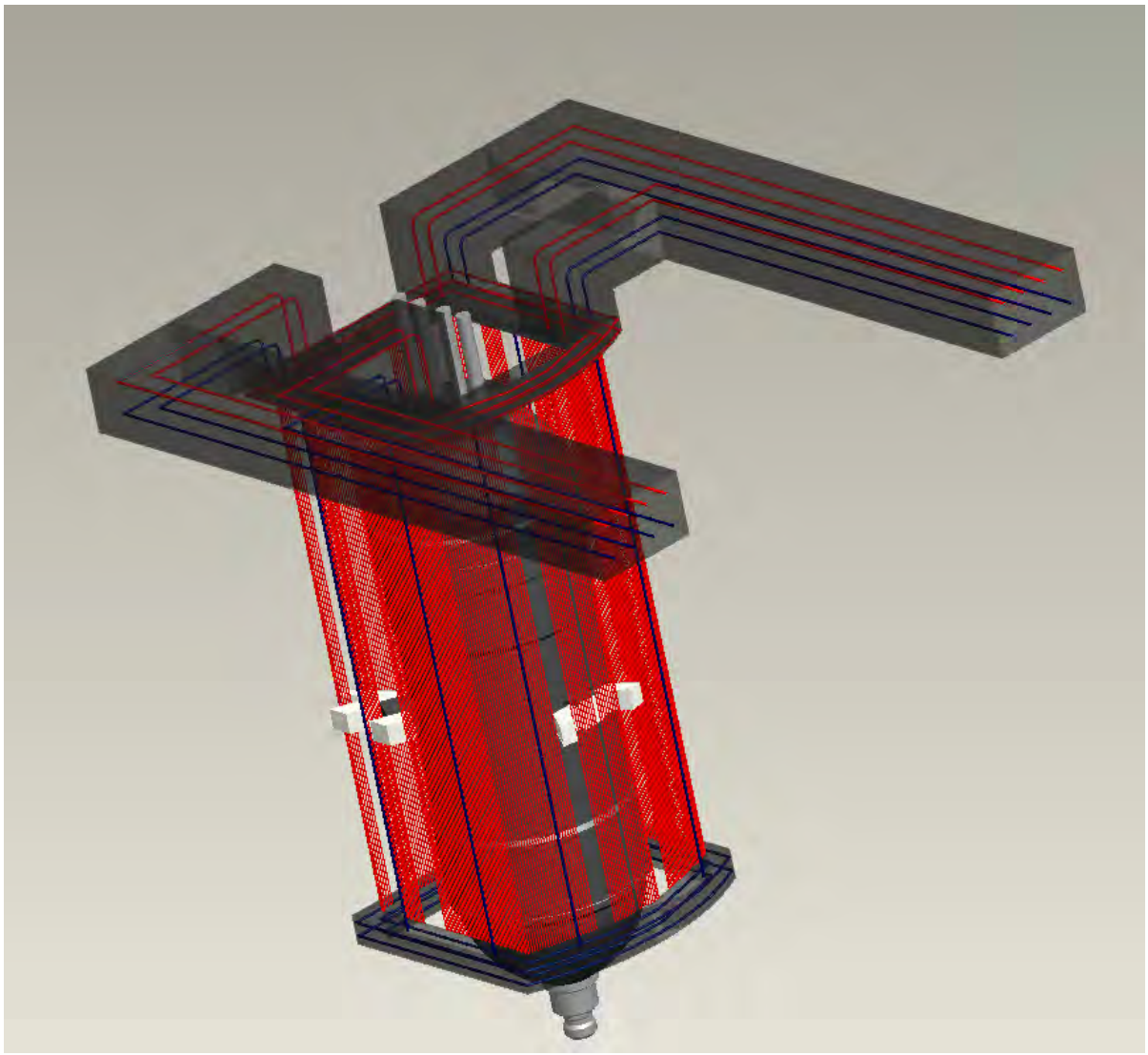

Full scale water RCCS concept, RPV

Analytical View Factors

From the original heat source, a radiative heat flux from the radiant heaters is imposed on the riser tube walls and cooling panels. During linear heating, this is imposed uniformly on the test section walls, with aid of natural convection due to the large temperature gradients. The energy is then transferred via conduction from both cooling fins and tube walls into the working fluid. With a skewed heating profile, the deposition is no longer uniform but with accordance to view factor calculations. A simplification of the of the heater and test section geometry will be made for hand calculations for view factors: two infinitely long parallel plates of different widths contained in a parallel plane, Figure F.12 (Heinz, 1975).

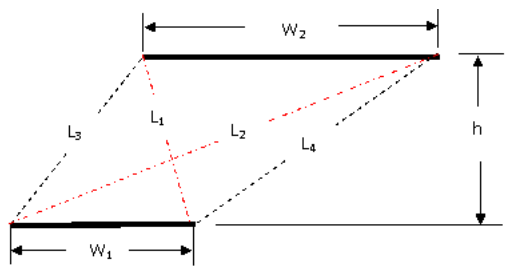

Supplement F.12: View factors for two parallel plates, a simplification of the RCCS geometry

The analytical solution for the view factor from *Surface 1* to *Surface 2* is given in Eq. F.29.

$$F_{1-2} = \frac{L_1 + L_2 - L_3 - L_4}{2w_1} \tag{F.29}$$

Supplement F.13: Analytical view factors from Heater A to Riser N

	F_{A-1}	F_{A-2}	F_{A-3}
W_1	11.7489	11.7489	11.7489
L_1	11.7174	19.7199	28.1315
L_2	15.3124	8.7486	9.8404
L_3	8.7486	9.7533	16.8969
L_4	7.9968	11.7174	19.7199
	0.438	**0.298**	**0.058**

RBI Theory

The double tip optical probe is vertically positioned opposite the direction of flow. Under two-phase flow conditions, i.e. water and air, the intrusive double tip probe penetrates the bubbles. A fraction of incident light beams strike the walls of the fiber (refractive index n_1=1.762) at a 45 degree angle. At a critical angle,θ_{crit} when no light is transmitted or refracted into the surrounding medium, the refraction angle must be 90 degree normal to the surface.

$$n_1 sin(\theta_i) = n_2 sin(\theta_r) \tag{F.30}$$

where n_1, n_2 are the refractive indices of the incident material and surrounding medium respectively and θ_i, θ_r are the incident and refractive or reflective angles respectively. The critical angle $\theta_{crit} = sin^{-1}(n_2/n_1)$ for air and water are then calculated as 34.6° and 49° respectively. Therefore, when the ray of light strikes the interface of the sapphire fiber ($n_1 = 1.762$) and air ($n_2 = 1.0$) , the light is completely reflected back into the Opto-electronic unit i.e. $\theta_i > \theta_{crit}$ while at the boundary of the fiber and water ($n_2 = 1.33$), a fraction of the incident light is refracted i.e. $\theta_i < \theta_{crit}$. Each of the two fiber tips have a radius $r = \mu m$ .Spacing between the centers of both fibers is measured to be $450\mu m$ while the distance between tips is $500\mu m$.

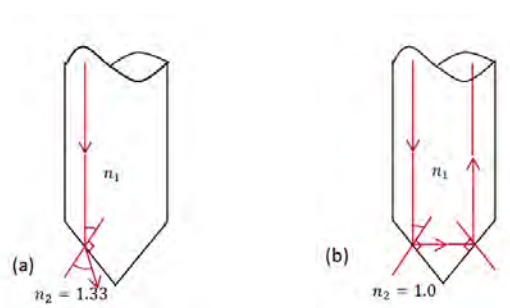

Supplement F.14: Operating principle of the two phase optical probe

Capable of operating under high temperature and pressures, the choice of the point

measurement optical device is premised on short response times and small dimensions of contact areas and designed to have minimal flow intrusiveness. This makes it a suitable detector for phase changes compared to resistive and capacitive probes.

Prior to the commencement of its full scale use, the spatial location of each fiber was defined and the phase indicators were set. A separate effect test was carried using a 1" vertical column of stagnant water. The optical probe was fixed at the top of the column. Injecting compressed air with known flow rate from the bottom of the test column, air bubbles were generated and flowed in the direction of the optical probe. Local measurements of the void fraction, bubble rise velocity and bubble diameter were computed and analyzed. This dataset was compared to theoretical calculations for the bubble rise velocity coupled with some visualization studies. Results from the separate effect tests showed less than 2% difference.

Darius D. Lisowski July 20th 2011

Uncertainty Analysis of Energy Balance for RCCS

1a) Simplified Steady-Flow Thermal Energy Equation

$$Q = \dot{m} C_p (T_{out} - T_{in})$$

1b) Mass flow rate expansion

$$\dot{m} = U_m A \rho$$

1c) Rewrite Eq. 1

$$Q = U_m A \rho C_p (T_{out} - T_{in})$$

2a)Propagation of error for a given variable Q dependent on *i* variables

$$\sigma_Q^2 = \sum_i \left(\frac{\partial Q}{\partial X_i} \right)^2 \sigma_i^2$$

2b) Velocity, inlet, and outlet temperature uncertainty propagation

$$\sigma_Q^2 = \left(\frac{\partial Q}{\partial U_m} \right)^2 \sigma_{U_m}^2 + \left(\frac{\partial Q}{\partial T_{out}} \right)^2 \sigma_{T_{out}}^2 + \left(\frac{\partial Q}{\partial T_{in}} \right)^2 \sigma_{T_{in}}^2$$

3a)Errors associated with each variable

$$\sigma_{U_m} = \sigma_{rel} U_m + \sigma_{abs} \qquad \sigma_{U_m} = 0.2\% U_m + 1 \text{ mm/s}$$

$$\sigma_T = \sigma_T \qquad \sigma_T = 0.4^\circ C$$

3b) Relative errors for each variable

$$\left(\frac{\partial Q}{\partial U_m} \right) = A C_p \rho (T_{out} - T_{in})$$

$$\left(\frac{\partial Q}{\partial T_{out}} \right) = A C_p \rho U_m$$

$$\left(\frac{\partial Q}{\partial T_{in}} \right) = -A C_p \rho U_m$$

4) Full uncertainty formula for Q

$$\sigma_Q = \sqrt{A^2 C_p^2 \rho^2 [(T_{in} - T_{out})^2 (\sigma_{rel} U_m + \sigma_{abs})^2 + 2 U_m^2 |\sigma_T|^2]}$$

$$\sigma_Q = \sqrt{A^2 C_p^2 \rho^2 [(T_{in} - T_{out})^2 (0.2\% U_m + 1 \text{ mm/s})^2 + 2 U_m^2 |0.4^\circ C|^2]}$$

UVP Uncertainty for RCCS Measurements

In this appendix, for velocity measurements with the UVP device, both systematic (also called bias) and random (precision) uncertainty were accounted for.

C.1 Systematic

Systematic uncertainty (B) refers to those errors which remain constant during repeated measurements under fixed operating conditions [Figliola and Beasley, 2006]. The design stage uncertainty method was applied to the velocity resolution of the UVP to determine systematic contributions to the overall uncertainty in velocity measurements. This term is simply half the resolution of the measuring instrument. From Equation 15 [Met-Flow, 2002], the velocity range of the UVP instrument was given as,

$$V_{range} = \frac{c^2}{4 f_0 P_{max}} \tag{C1}$$

where c speed of sound in the medium [m/s]

f_0 emitted frequency [Hz]

P_{max} maximum measurable depth [m]

while the velocity resolution from Equation 16 [Met-Flow, 2002] was,

$$\Delta V = \frac{V_{range}}{N_{DU}} = \frac{V_{range}}{256} \tag{C2}$$

where N_{DU} number of „Doppler units" [-]

Then, the systematic uncertainty (95% probability) associated with UVP measurements is given as [Figliola and Beasley, 2006; Equation 5.1]

$$B = \pm \frac{1}{2} \text{resolution} = \pm \frac{\Delta V}{2} \tag{C3}$$

C.1.1 UI Facility

Using Equations C1-C3, the systematic uncertainty associated with single-phase experiments at the UI Facility (B_1) was calculated in Table C.1, assuming constant sound speed (c). All variables were obtained from RCCS experimental data at steady state conditions.

Table C.1 Systematic Uncertainty for Single-Phase Runs (UI)

		c	P_{max}	P_{max}	V_{range}	ΔV	B_1
		[m/s]	[mm]	[m]	[mm/s]	[mm/s]	[mm/s]
Test #1	Sample #1	1555	1299.98	1.300	116.253	0.454	0.227
	Sample #2	1555	999.87	1.000	151.146	0.590	0.295
	Sample #3	1555	700.14	0.700	215.852	0.843	0.422
	Sample #4	1555	400.02	0.400	377.798	1.476	0.738
	Sample #5	1555	150.06	0.150	1007.108	3.934	1.967
Test #2	Sample #1	1555	1025.91	1.026	147.310	0.575	0.288
	Sample #2	1555	141.12	0.141	1070.908	4.183	2.092
Test #3	Sample #1	1555	141.12	0.141	1070.908	4.183	2.092
	Sample #2	1555	141.12	0.141	1070.908	4.183	2.092
	AVERAGE	**1555**	**555.5**	**0.555**	**580.91**	**2.269**	**1.135**

Using the test-averaged velocity resolution, the design-stage uncertainty associated with UVP velocity measurements is approximated to be,

$$(\pm \mathbf{0.227} \leq \mathbf{B_1} \leq \pm \mathbf{2.092})\ \frac{\mathbf{mm}}{\mathbf{s}}$$

C.1.2 UW Facility: Single-Phase

Again using Equations C1-C3, the systematic uncertainty associated with single-phase power variation experiments at the UW Facility (B_2) was calculated in Table C.2, assuming constant sound speed (c). All variables were obtained from RCCS experimental data at steady state conditions.

Table C.2 Systematic Uncertainty for Single-Phase Runs (UW)

	c	P_{max}	P_{max}	V_{range}	ΔV	B_2
Power	[m/s]	[mm]	[m]	[mm/s]	[mm/s]	[mm/s]
4.63 kW	1510	400.15	0.40015	356.1	1.391	0.6955
7.27 kW	1506	399.84	0.39984	354.5	1.385	0.6925
9.91 kW	1517	299.99	0.29999	479.5	1.873	0.9365
12.5 kW	1519	399.88	0.39988	360.6	1.409	0.7045
15.2 kW	1516	499.9	0.4999	287.3	1.122	0.561

Using the test-averaged velocity resolution, the design-stage uncertainty associated with UVP velocity measurements ranges from

$$(\pm\, \mathbf{0.561} \leq \mathbf{B_2} \leq \pm\, \mathbf{0.937})\ \frac{\mathbf{mm}}{\mathbf{s}}$$

C.1.3 UW Facility: Two-Phase

Once more using Equations C1-C3, systematic uncertainty associated with two-phase experiments at the UW Facility (B_3) was calculated below in Table C.3, assuming constant sound speed (c).

Table C.3 Systematic Uncertainty for Two-Phase Runs

c	P_{max}	P_{max}	V_{range}	ΔV	B_3
[m/s]	[mm]	[m]	[mm/s]	[mm/s]	[mm/s]
1641	205.13	0.20513	820.5	3.205	± 1.603

Using the UVP velocity resolution, the systematic uncertainty associated with two-phase UVP velocity measurements (B_3) is calculated as

$$\boldsymbol{B_3} \pm\ \mathbf{1.603}\ \frac{\mathbf{mm}}{\mathbf{s}}$$

C.2 Random

Random error (P) is simply the scatter of measured data from repeated measurements under fixed operating conditions [Figliola and Beasley, 2006]. According to Met-Flow, UVP measurement precision is 0.5% of the measured value.

C.2.1 UI Facility: Single-Phase

Random uncertainty associated with single-phase experiments at the UI Facility (P_1) was calculated in Table C.4, assuming constant sound speed (c). All variables were obtained from RCCS experimental data at steady state conditions, with random uncertainty of ± 0.5% of the measured value.

Table C.4 Random Uncertainty for Single-Phase Runs (UI)

		V_{Tmax}	P_1-T_{max}	V_{Pmax}	P_1-P_{max}	V_{Avg}	P_1-Avg
		[mm/s]	[mm/s]	[mm/s]	[mm/s]	[mm/s]	[mm/s]
Test #1	Sample #1	44.33	± 0.222	38.77	± 0.194	31.76	± 0.159
	Sample #2	45.43	± 0.227	40.25	± 0.201	32.59	± 0.163
	Sample #3	65.98	± 0.330	47.44	± 0.237	31.84	± 0.159
	Sample #4	92.14	± 0.461	41.93	± 0.210	24.32	± 0.122
	Sample #5	67.98	± 0.340	41.83	± 0.209	18.45	± 0.092
Test #2	Sample #1	56.19	± 0.281	45.97	± 0.230	21.58	± 0.108
	Sample #2	79.95	± 0.400	44.98	± 0.225	23.19	± 0.116
Test #3	Sample #1	69.03	± 0.345	43.18	± 0.216	24.40	± 0.122
	Sample #2	60.92	± 0.305	41.08	± 0.205	21.88	± 0.109

Because the profile maximum (Pmax) method provided the best results for UVP measurements, it was used to represent the random uncertainty. Thus, random uncertainty for UVP measurements at the UI facility (P_1) was calculated to range from

$$(\pm \mathbf{0.194} \leq \mathbf{P_1} \leq \pm \mathbf{0.237})\ \frac{\mathbf{mm}}{\mathbf{s}}$$

C.2.2 UW Facility: Single-Phase

Random uncertainty associated with single-phase power variation experiments at the UW Facility (P_2) was calculated in Table C.5, assuming constant sound speed (c). All variables were obtained from RCCS experimental data at steady state conditions.

Table C.5 Random Uncertainty for Single-Phase Runs (UW)

	UVP_{Lower}	P_2-Lower	UVP_{Upper}	P_2-Upper
Power	[mm/s]	[mm/s]	[mm/s]	[mm/s]
4.63 kW	66.24	± 0.331	64.98	± 0.325
7.27 kW	80.63	± 0.403	79.42	± 0.397
9.91 kW	94.50	± 0.473	99.81	± 0.499
12.5 kW	101.68	± 0.508	107.66	± 0.538
15.2 kW	112.33	± 0.562	112.07	± 0.560

From Table C.5, random uncertainty for single-phase UVP measurements at the UW facility (P_2) is show to vary from

$$(\pm \mathbf{0.325} \leq \mathbf{P_2} \leq \pm \mathbf{0.562})\ \frac{\mathbf{mm}}{\mathbf{s}}$$

C.2.3 UW Facility: Two-Phase

The precision of the unique method utilized for two-phase flow analysis as described in Section 3.4.4 was determined by quantifying the associated random uncertainty [Figliola and Beasley, 2006]. First, the sample mean was determined by Equation C4 [Figliola and Beasley, 2006; Equation 4.14*a*],

$$\bar{x} = \frac{x_1 + x_2 + \cdots + x_N}{N} = \frac{1}{N}\sum_{i=1}^{N} x_i \tag{C4}$$

where $\bar{x}$ sample mean value

x_i individual measurement, where i = 1,2,…,N

N total number of samples

Next, the sample standard deviation was given by Equation C5 [Figliola and Beasley, 2006; Equation 4.14*c*] as,

$$S_x = \sqrt{\frac{\sum_{i=1}^{N}(x_i - \bar{x})^2}{N-1}} \tag{C5}$$

Then the standard deviation of the means was then calculated by means of Equation C6 [Figliola and Beasley, 2006; Equation 4.16],

$$S_{\bar{x}} = \sqrt{\frac{\sum_{i=1}^{N}(x_i - \bar{x})^2}{N(N-1)}} = \frac{S_x}{\sqrt{N}} \tag{C6}$$

Last, the random uncertainty in the mean value due to the variation found in the measured set of data was given by Equation C7 [Figliola and Beasley, 2006; Equation 4.18],

$$x' = \bar{x} \pm t_{v,P} S_{\bar{x}} \tag{C7}$$

where x' represents the true value. The variable $t_{v,P}$ is a weighting function used for finite data sects called the "t estimator" and is obtained from a chart developed by William S. Gosset ("Student"s t distribution"). Together, the quantity $\pm t_{v,P} S_{\bar{x}}$ gives the random uncertainty in the mean value caused by the variation within the measured data set. For application to the employed two-phase velocity measurement method, Equation C7 assuming a 95% confidence interval was modified as,

$$x'_L = \bar{x}_L \pm t_{v,95} S_{\bar{x},L} \quad (95\%) \tag{C8}$$

and

$$x'_G = \bar{x}_G \pm t_{v,95} S_{\bar{x},G} \quad (95\%) \tag{C9}$$

where x'_L liquid phase estimate of true mean value

$\bar{x}_L$ liquid phase sample mean value

$S_{\bar{x},L}$ liquid phase standard deviation of the means

x'_G gas phase estimate of true mean value

$\bar{x}_G$ gas phase sample mean value

$S_{\bar{x},G}$ gas phase standard deviation of the means

Associated random uncertainty using Equations C8 and C9 was then accomplished by analyzing cells in velocity profiles that underwent a change from liquid to gas phase in subsequent profiles. First, five separate sets of fifty points were analyzed from data obtained prior to the flow disturbance. Results of this analysis are shown in Table C.6 and C.7, noting that $P_{L,1}$ and $P_{G,1}$ are the random uncertainties ($\pm\, t_{v,95} S_{\bar{x}}$) associated with liquid and gas phase measurements, respectively.

Table C.6 Random Uncertainty from Liquid Phase Analysis before Flow Disturbance

Liquid Phase	$\bar{x}_L$	$S_{x,L}$	$S_{\bar{x},L}$	$t_{v,95}$	P_L	P_L
	[mm/s]	[mm/s]	[mm/s]	[-]	[mm/s]	[%]
Sample#1	41.99	34.15	4.83	2.011	9.71	23.1%
Sample#2	54.67	58.13	8.22	2.011	16.53	30.2%
Sample#3	47.17	52.47	7.42	2.011	14.92	31.6%
Sample#4	60.70	64.69	9.15	2.011	18.40	30.3%
Sample#5	61.67	64.20	9.08	2.011	18.26	29.6%
Average	**53.24**	**54.73**	**7.74**	**-**	**15.56**	**29.0%**

Table C.7 Random Uncertainty from Gas Phase Analysis before Flow Disturbance

Gas Phase	$\bar{x}_G$	$S_{x,G}$	$S_{\bar{x},G}$	$t_{v,95}$	P_G	P_G
	[mm/s]	[mm/s]	[mm/s]	[-]	[mm/s]	[%]
Sample#1	586.79	213.95	30.26	2.011	60.85	10.4%
Sample#2	557.57	235.19	33.26	2.011	66.89	12.0%
Sample#3	576.08	211.14	29.86	2.011	60.05	10.4%
Sample#4	551.03	211.86	29.96	2.011	60.25	10.9%
Sample#5	547.38	223.37	31.59	2.011	63.53	11.6%
AVERAGE	**563.77**	**219.10**	**30.99**	**-**	**62.31**	**11.1%**

Thus, random uncertainty for the liquid phase before the flow disturbance ranges from

$$(\pm\, \mathbf{9.71} < \mathbf{P_{L,1}} < \pm\, \mathbf{18.40})\ \frac{\mathbf{mm}}{\mathbf{s}}$$

while gas phase random uncertainty lies between

$$(\pm\, \mathbf{60.05} < \mathbf{P_{G,1}} < \pm\, \mathbf{66.89})\ \frac{\mathbf{mm}}{\mathbf{s}}$$

Next, seven sets of fifty points were analyzed from data obtained during the flow disturbance. Results of this analysis are shown in Table C.8 and C.9, again noting that $P_{L,2}$ and $P_{G,2}$ are the random uncertainties ($\pm\, t_{v,95} S_{\bar{x}}$) associated with liquid and gas phase measurements, respectively.

Table C.8 Random Uncertainty from Liquid Phase Analysis during Flow Disturbance

Liquid Phase	$\bar{x}_L$	$S_{x,L}$	$S_{\bar{x},L}$	$t_{v,95}$	P_L	P_L
	[mm/s]	[mm/s]	[mm/s]	[-]	[mm/s]	[%]
Sample#1	43.26	56.07	7.93	2.011	15.95	36.9%
Sample#2	52.76	68.97	9.75	2.011	19.61	37.2%
Sample#3	62.56	69.78	9.87	2.011	19.85	31.7%
Sample#4	41.91	56.31	7.96	2.011	16.01	38.2%
Sample#5	43.45	51.92	7.34	2.011	14.77	34.0%
Sample#6	42.36	49.47	7.00	2.011	14.07	33.2%
Sample#7	54.54	60.91	8.61	2.011	17.32	31.8%
AVERAGE	**48.69**	**59.06**	**8.35**	**-**	**16.80**	**34.7%**

Table C.9 Random Uncertainty from Gas Phase Analysis during Flow Disturbance

Gas Phase	$\bar{x}_G$	$S_{x,G}$	$S_{\bar{x},G}$	$t_{v,95}$	P_G	P_G
	[mm/s]	[mm/s]	[mm/s]	[-]	[mm/s]	[%]
Sample#1	684.99	157.77	22.31	2.011	44.87	6.6%
Sample#2	631.99	184.73	26.13	2.011	52.54	8.3%
Sample#3	578.91	172.27	24.36	2.011	48.99	8.5%
Sample#4	623.64	183.80	25.99	2.011	52.27	8.4%
Sample#5	623.01	160.05	22.63	2.011	45.52	7.3%
Sample#6	655.83	152.32	21.54	2.011	43.32	6.6%
Sample#7	657.45	153.75	21.74	2.011	43.73	6.7%
AVERAGE	**636.54**	**166.38**	**23.53**	**-**	**47.32**	**7.5%**

Thus, random uncertainty for the liquid phase during the flow disturbance ranges from

$$(\pm\, \mathbf{14.07} < \mathbf{P_{L,2}} < \pm\, \mathbf{19.85})\ \frac{\mathbf{mm}}{\mathbf{s}}$$

while gas phase random uncertainty lies between

$$(\pm\, \mathbf{43.32} < \mathbf{P_{G,2}} < \pm\, \mathbf{52.54})\ \frac{\mathbf{mm}}{\mathbf{s}}$$

C.3 Combined

C.3.1 Single-Phase Experiments

To determine the overall uncertainty associated with single-phase UVP measurements, the systematic (B) and random uncertainties (P) must be combined [Figliola and Beasley, 2006]. This is accomplished by the root-sum-squares method (RSS) defined by,

$$u_{UVP} = (B^2 + P^2)^{1/2} \tag{C10}$$

Using Equation C10, overall uncertainties for single-phase measurements at the UI and UW facilities were calculated in Table C.10.

Table C.10 Overall Uncertainty of UVP Data from Single-Phase Tests

		UI Facility		UW Facility
Uncertainty		[mm/s]		[mm/s]
Systematic	$B_1 =$	± 2.092	$B_2 =$	± 0.937
Random	$P_1 =$	± 0.237	$P_2 =$	± 0.562
Total	$\boldsymbol{u_{UVP,1}}$	**± 2.105**	$\boldsymbol{u_{UVP,2}}$	**± 1.093**

C.3.2 Two-Phase Experiments

To determine the overall uncertainty associated with two-phase UVP measurements, Equation C10 was again used. Table C.11, gives the overall uncertainty for two-phase UVP measurements before and during the flow disturbance.

Table C.11 Overall Uncertainty of UVP Data from Two-Phase Tests

Uncertainty	Before	[mm/s]	During	[mm/s]
Systematic	$B_3 =$	± 1.603	$B_3 =$	± 1.603
Random_L	$P_{L,1} =$	± 18.4	$P_{L,2} =$	± 19.85
Random_G	$P_{G,1} =$	± 66.89	$P_{G,2} =$	± 52.54
$\textbf{Total}_{L,1\&2}$	$\boldsymbol{u_{UVP,L1}}$	**± 18.47**	$\boldsymbol{u_{UVP,L2}}$	**± 19.91**
$\textbf{Total}_{G,1\&2}$	$\boldsymbol{u_{UVP,G1}}$	**± 66.91**	$\boldsymbol{u_{UVP,G2}}$	**± 52.56**

In conclusion, it is seen that the maximum total error is less than 41% and 11% for the liquid and gas phases, respectively. Also, it is important to note that the uncertainty in the gas phase (±66.91 mm/s) is less than the difference observed between the average gas phase value before (563.77 mm/s) and after (636.54 mm/s) the disturbance.

1) Initial Conditions
   a) Record Initial Conditions and Paramaters ☐

2) Power Preparation
   a) Remove lock from 200A disconnect box ☐
   b) Flip switch to “ON” position ☐
   c) Verify working operation of hot leg pump ☐
   d) Verify working operation of cold leg pump ☐

3) LabVIEW Setup
   a) Enter desired power level ☐
   b) Set desired ramp time ☐
   c) Ensure logging is enabled ☐
   d) Turn on 120V power (x1), Enable switches (x6) ☐

4) Start Power Ramp
   a) Enable Power Ramp in LabVIEW ☐
   b) Record Start Power Conditions ☐

5) End Ramp Conditions
   a) Record End Ramp Conditions ☐

6) Wait and Hold
   a) Allow to reach desired condition (e.g. T_{inlet} = 30°C) ☐

7) Steady-State Preparation
   a) Turn on cold water supply ☐
   b) Turn on 220V cold leg pump ☐
   c) Record Prepare Steady-State Conditions ☐

8) Start Steady-State
   a) Open throttle valve by setting EP-mA control to 7mA ☐
   b) Turn on 120V hot leg pump ☐
   c) Ensure water is flowing by monitoring hot leg meter ☐
   d) Allow 10 minutes for system stabilization ☐

9) Approach Steady-State
   a) Increase hot leg flow rate by increasing EP-mA control ☐

b) until hot leg energy is half of the test section energy ☐
c) Allow 20 minutes for system stabilization ☐

10) Reach Steady-State
a) Increase hot leg flow rate until 90% of test section energy ☐
b) Allow 5 minutes for system stabilization ☐
c) Increasing remaining amount until hot leg energy ☐
d) is matched to test section energy ☐
e) Record Reached Steady State Conditions ☐
f) Hold for desired duration ☐

11) Shutdown Preparation
a) Record End Steady-State Conditions ☐
b) Turn off 220V cold leg pump ☐
c) Turn off cold water supply ☐
d) Turn off 120V hot leg pump ☐
e) Reset throttle valve to closed, 0mA ☐

12) System Shutdown
a) Enter desired time for power ramp down (120 seconds) ☐
b) Enable Ramp Down ☐
c) After heaters have ramped to 0.1% ☐
d) turn off Enable (x6), 120V Power (x1) ☐
e) Flip 200A switch to “OFF” position ☐
f) Reinstall safety lock ☐
g) Save and move logging file to appropriate folder ☐

Darius Lisowski August 14th 2011

RCCS Heat Loss Calculations

Heater Box, Angle Iron

Heater box is divided into 40 individual areas, summing to the total area of 10.7218 m^2. A higher density of measurement locations is concentrated at the top of the heater box, where the highest temperatures are seen and largest gradients observed. The angle iron supports were divided into 4 measurement areas per angle iron, each with a full size of 1.5”x1.5”x18”. To determine the heat loss to the ambient air off the heater box and support structures, a convective heat transfer formula was used. Each measurement was used as a bulk surface temperature for a known surface area, and using correlations from ASHREA for ambient heat transfer coefficients from room air, the heat loss could be determined.

$$Q_{loss,heater\,box} = h_{conv,ambient} A_i \left(T_{surface,i} - T_{ambient}\right)$$

Downcomer

Heat loss from the downcomer was made by an energy balance at the tank outlet and header inlet.

$$Q_{loss,DC} = \dot{m} C_p \left(Tank_{out} - Header_{in}\right)$$

Network Plumbing

12 surface measurements are made on the outer insulation of the network plumbing. Then, a room temperature recording is performed. Lastly, water temperature data from LabVIEW is saved at the same time of surface measurements at the corresponding reference points.

1) Resistance due to conduction through stainless steel pipe

$$L_i = [length_i]\,m \quad , \quad r_i = [radius_i]\,m$$

$$k_i = Conductivity(304L)$$

$$R_{cond-steel,i} = \frac{\ln(r_o/r_i)}{2\pi L_i k_i}$$

2) Resistance due to conduction through insulation

$$L_i = [length_i]\,m \quad , \quad r_i = [radius_i]\,m$$

$$k_i = Conductivity\,(Insulation)$$

$$R_{cond-insulation,i} = \frac{\ln(r_o/r_i)}{2\pi L_i k_i}$$

3) Resistance due to convection inside stainless steel pipe

$$k_i = Conductivity(TC_i) \quad , \quad \mu_i = Viscosity(TC_i)$$

$$Re_i = \frac{4\dot{m}_i}{\pi r_i \mu_i} \quad , \quad Pr_i = Prandtl(TC_i)$$

$$Nu_i = 0.0265\, Re_i^{4/5} Pr_i^{0.3}$$

$$h_i = Nu_i k_i / r_i$$

$$R_{conv,i} = 1/(2\pi r_i L_i h_i)$$

4) Total heat loss

$$Q_{loss,i} = \frac{TC_i - T_{surface,i}}{R_{conv,i} + R_{cond-steel,i} + R_{cond-insulation,i}}$$

	Surface Measurement	Water Temperature
1	Lower Network	TC52
2	Lower Header	TC52
3	Front Fin	*n/a*
4	Rear Fin	*n/a*
5	Upper Header	TC53
6	Upper Network	Average(TC56,TC53)
7	South Riser	TC49
8	Center Riser	TC50
9	North Riser	TC51
10	Tank	Average(TC55,TC56,TC57,TC58)
11	2nd Floor Downcomer	Average(TC54,TC52)
12	1st Floor Downcomer	Average(TC54,TC52)

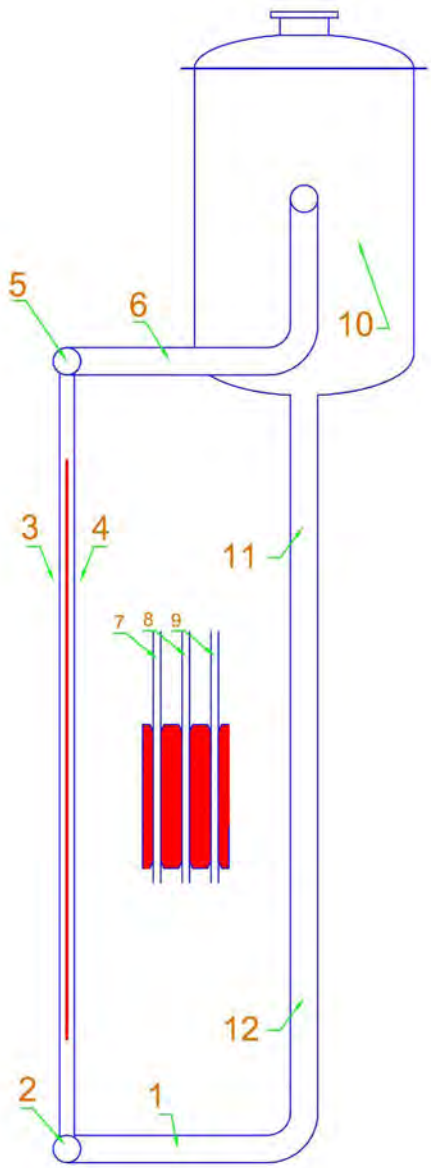

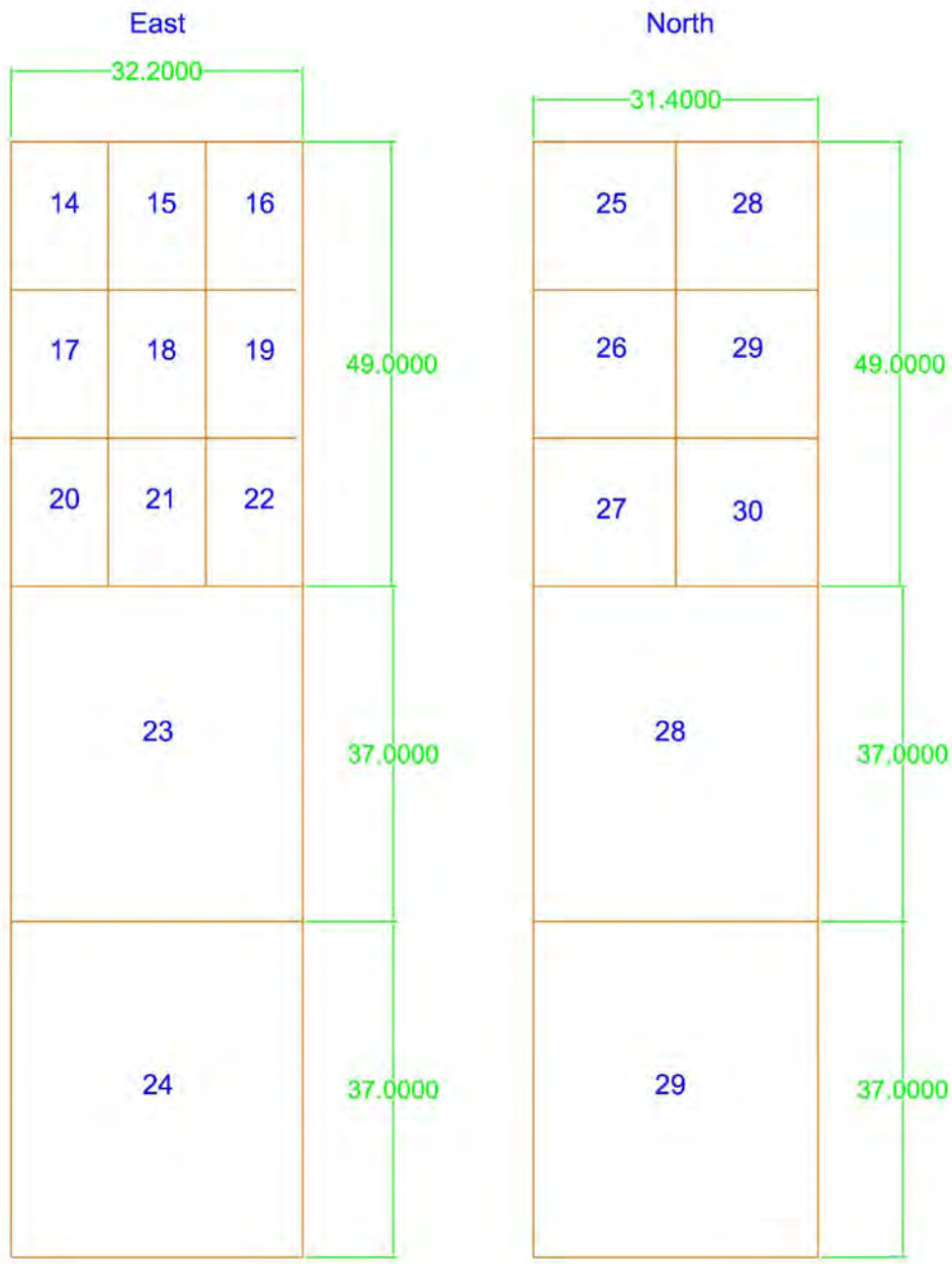
East
32.2000
14
15
16
17
18
19
20
21
22
49.0000
23
37.0000
24
37.0000
North
31.4000
25
28
26
29
27
30
49.0000
28
37.0000
29
37.0000

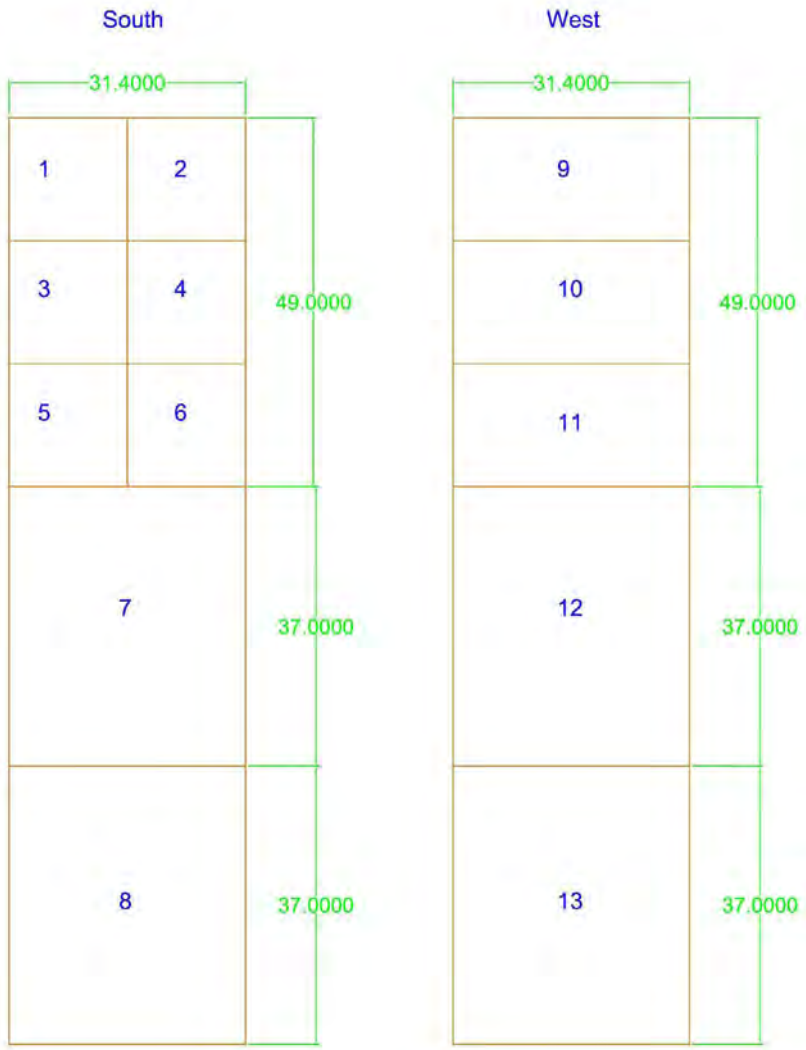
South
West
31.4000
31.4000
1
2
3
4
5
6
7
8
9
10
11
12
13
49.0000
49.0000
37.0000
37.0000
37.0000
37.0000

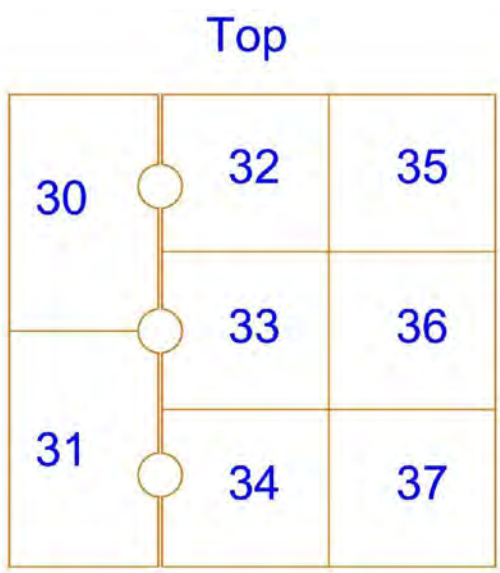
Top
30
31
32
33
34
35
36
37

Appendix XX. UI Facility Experimental Design

It was decided that a shakedown test facility should be constructed at the University of Idaho. This facility was planned to be quickly constructed, to help provide useful feedback and recommendations for the more carefully planned and robustly constructed test facility at the UW Facility. To reduce costs and simplify both design and construction, a single riser tube design was selected. Scaled a little under 1/4, the experiment was designed to represent a small wedge of the reactor cavity in which a single riser tube is located. The original test section was designed and partially constructed by Albiston [Albiston, 2010].

The structural support and framework was constructed out of 3/8" plywood, approximately 13" (H) x 44" (W) x 27" (D) and also conveniently served as an enclosure for the heaters and standpipe. The interior surfaces of the enclosure were pre-coated with a high temperature Rust-Oleum paint to help provide an initial barrier between the plywood and radiant heaters. This inner surface was then lined with aluminum foil to help reflect heat inside the test section onto the standpipe and also serve as an additional insulator between the heaters and plywood.

A 2" diameter, 10" long type K copper pipe was chosen for the single standpipe, and was attached to a 1/8" thick, 116" long aluminum fin with a layer of high temperature thermal epoxy (15 BTU-in/ft^2-hr-°F; 2.16 W/m-K). This riser tube assembly was anchored to the back wall of the plywood cavity via wood screws and metal braces. The rest of the piping network connected to the standpipe consisted of a combination of 3/4" and 2" copper tubing segments connected by various tees and elbows. During normal operation, heat added to the standpipe would cause the density of the water in the standpipe to decrease, thus initiating natural circulation. From the standpipe exit, the tubing network would carry water from the heated portion of the test section to a polyethylene tank located above the enclosure. A 3/4" copper downcomer connected to the bottom of the tank would then guide cooled water back down to the bottom of the standpipe to complete the flow loop. Heat was added to the test section via two rectangular radiant heaters (Omega QF-127210/240-T), capable of a 10 W/in^2 (15.5 kW/m^2) output. Control for these heaters consisted of a manually-adjustable variable percent power controller. To mitigate heat loss to the environment, additional insulation (R-13 fiberglass) was added between the enclosure wall and the riser tube-fin assembly.

After initial testing, several modifications were made to the original design to improve performance. These included replacing the 3/4" tubing segments with 2" CPVC piping (rated to 83 °C). Several unnecessary tees and elbows were also eliminated, enabling water from the standpipe to terminate directly into the storage tank. This design change also provided easy access for instrumentation being inserted into the standpipe. The designs are show below in Figures 2.8.

Figure 2.8 Modified UI Facility Design

These design modifications significantly improved access for the various instrumentation options scheduled for testing. Temperature measurements, via type-K (Omega, 5TC-TT-K-24-72) thermocouples, were taken in three main locations: within the enclosure, on the surface of the riser tube and fin, and inside the riser tube. Measurements within the cavity were accomplished with an assembly comprised of 10 thermocouples, mounted to a wire framework. This thermocouple „tree" could then be adjusted to take temperature measurements of the air at various heights within the enclosure. Figure 2.9 shows the thermocouple tree positioned within the test section cavity.

For measurements on the standpipe, the thermocouples were attached to the standpipe at 30cm increments along the length of the heated section, for a total of 11 measurement locations.

The thermocouples were affixed to the surface by high temperature aluminum tape and sealed with a high temperature heat sink compound. For measurements within the riser tube, a thermocouple probe was constructed from two sections of 1/2" copper tubing connected by a flexible piece of plastic tubing. Twelve thermocouples were fastened (six on each side) to metal guides at two separate locations on the probe, spaced 30cm apart. The spacing between thermocouples is best explained by Figure 2.10 below.

For velocity measurements, a probe was constructed capable of measuring the axial velocity component of the water in the riser tube. Because the UI Facility lacked a dedicated flow meter, data from the axial velocity measurements would serve as a rough check for the mass flow rate while enabling users to gain experience with UVP instrument operation. As stated in Section 1.2, because the flow in the riser tubes is predominately in the axial direction, velocity measurements in the azimuthal and radial directions were neglected. Not only did this simplify data processing and analysis, but it also greatly simplified the design and construction of the test facilities both at UI and UW. The probe was designed to house two ultrasonic transducers within the riser tube, to enable both on and off-axis axial velocity measurements to be taken. Both transducers were attached to a 3" long aluminum tube (3/8" OD, .319" ID), with one positioned in the center and the other offset ~6mm from the pipe wall. To ensure that the electronics in the transducers were sealed from water damage, signal cables were routed through the interior of the pipe. To this end, BNC connectors on the transducers were de-soldered, fed through the aluminum tube and then re-soldered. Silicone sealant was also liberally applied to all the openings near the transducer casing. After modifications described earlier in Section 2.2.1, this probe could be easily inserted into the riser tube through the water tank, located directly above. Thus, by adjusting the tube to various axial positions, velocity measurements could be taken at different locations within the riser tube.

Run010 — steady-state, 9.91 kW, 80% tank volume

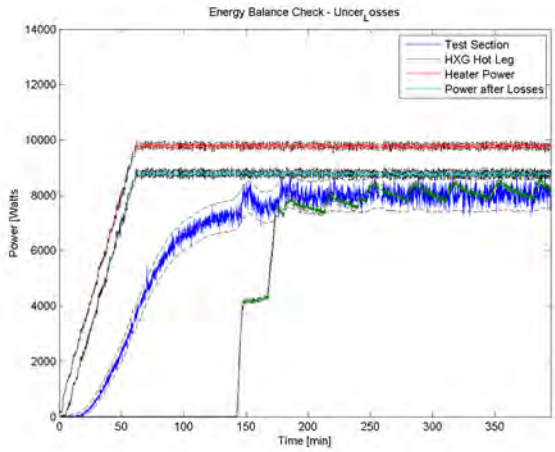

Supplement I.15: Energy balance

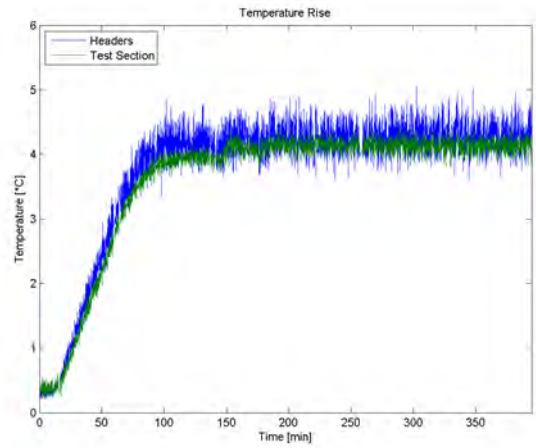

Supplement I.17: Temperature rise

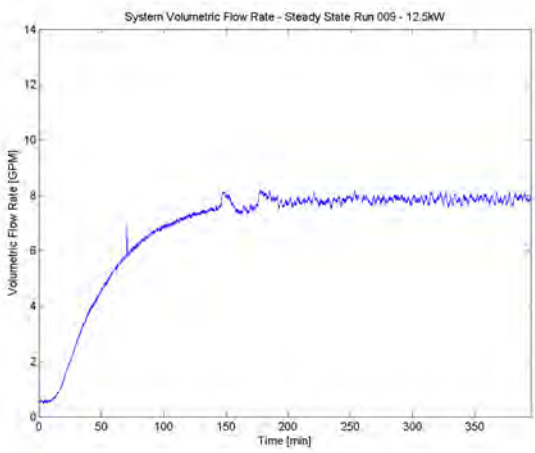

Supplement I.16: Flow rate

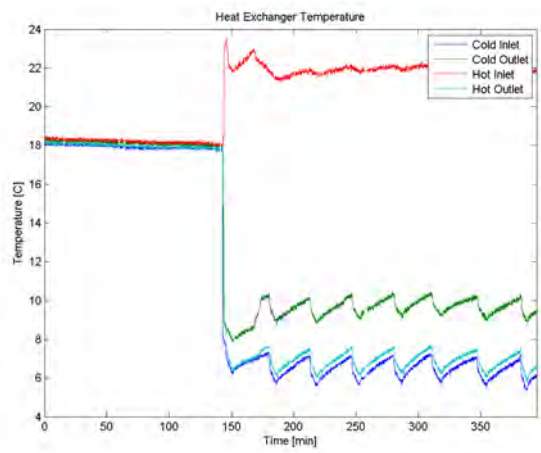

Supplement I.18: HXG Temperatures

Run010 — steady-state, 9.91 kW, 80% tank volume

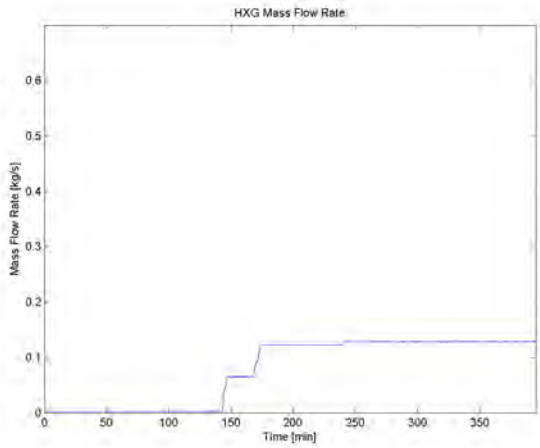

Supplement I.19: HXG flow rate

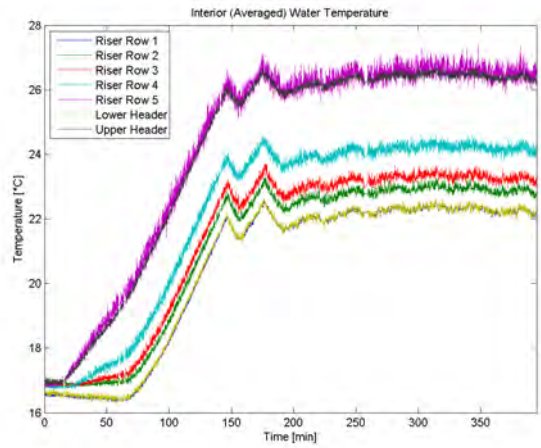

Supplement I.21: Interior riser temperatures

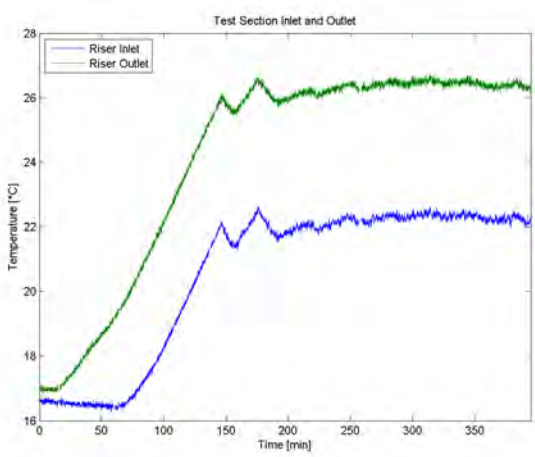

Supplement I.20: Riser water temp.

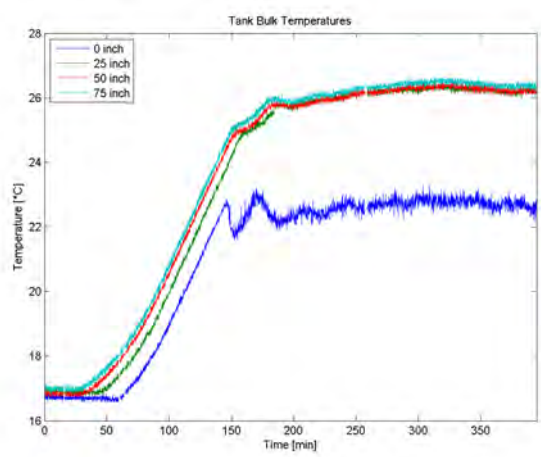

Supplement I.22: Tank Temperatures

Run010 — steady-state, 9.91 kW, 80% tank volume

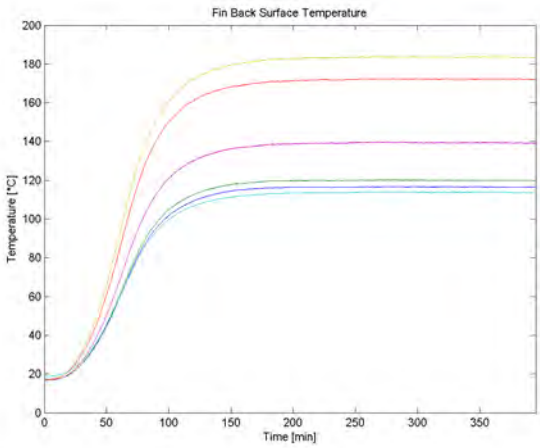

Supplement I.23: Fin back surface temp.

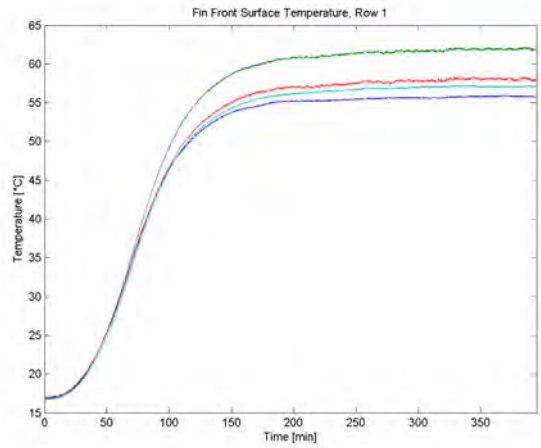

Supplement I.25: Row 1 - Tubes

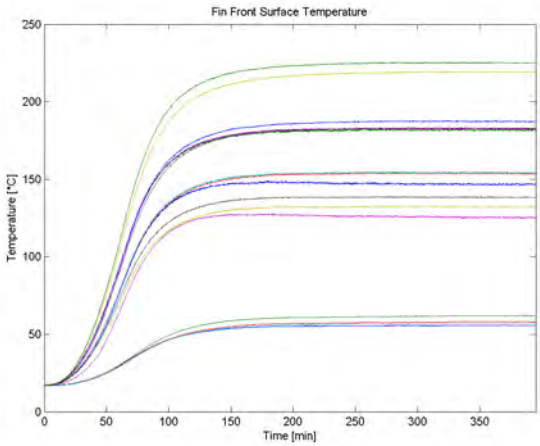

Supplement I.24: Fin front surf. temp

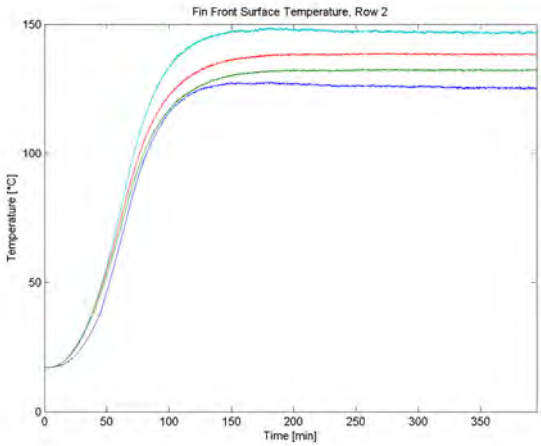

Supplement I.26: Row 2 - Tubes

Run010 — steady-state, 9.91 kW, 80% tank volume

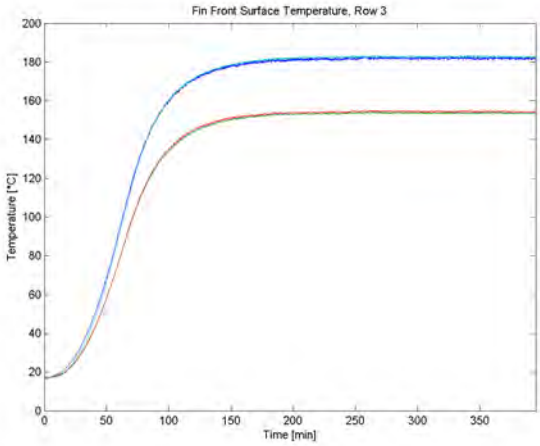

Supplement I.27: Row 3 - Tubes

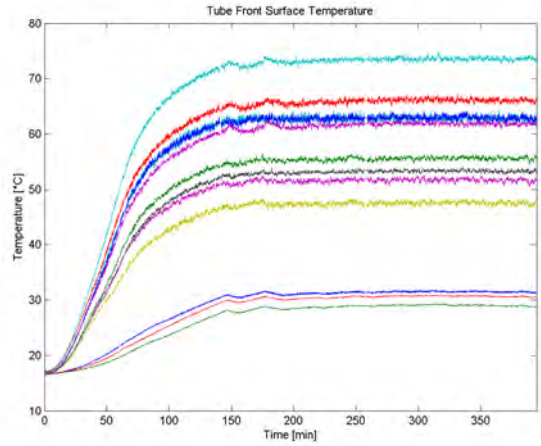

Supplement I.29: Tube front surface

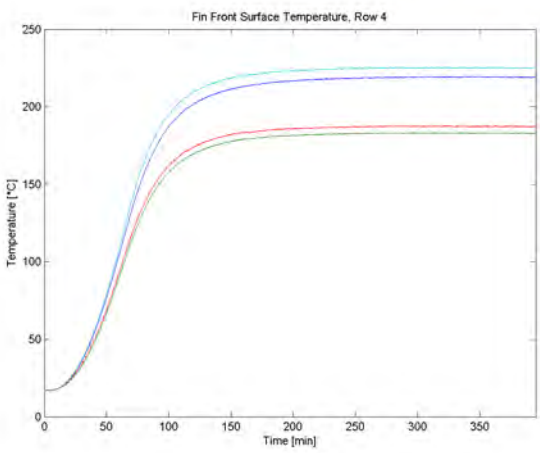

Supplement I.28: Row 4 - Tubes

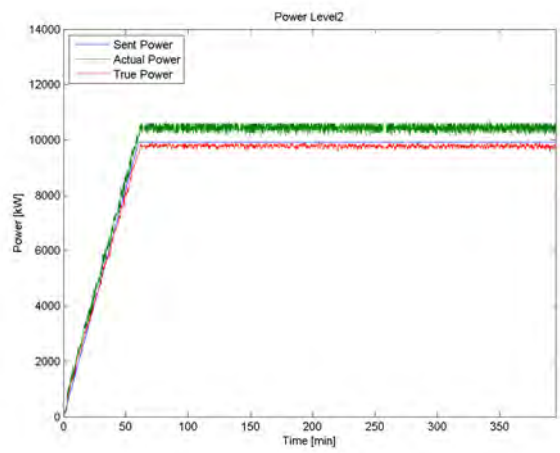

Supplement I.30: Heater power

Run058 — two-phase, 15.19 kW, 70 °C start, 80% tank volume

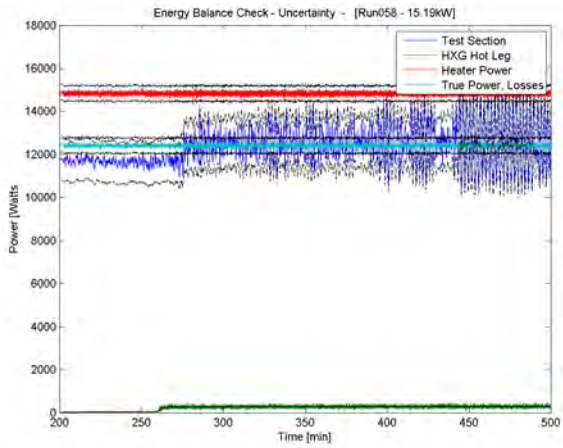

Supplement J.31: Energy Balance

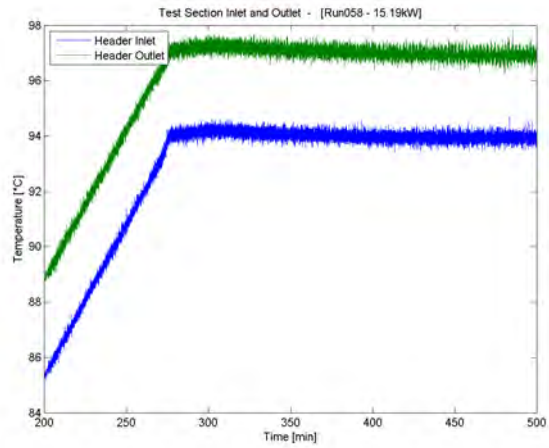

Supplement J.33: Inlet Outlet Temp

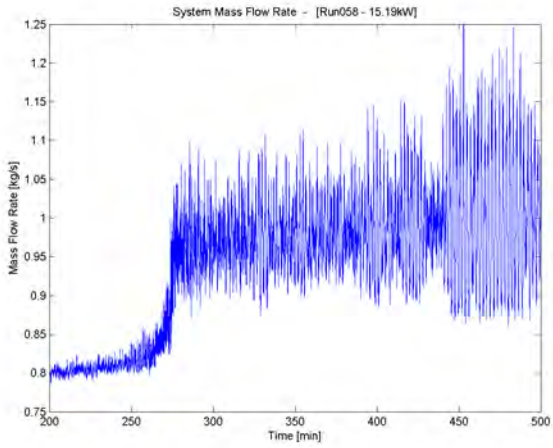

Supplement J.32: Mass Flow

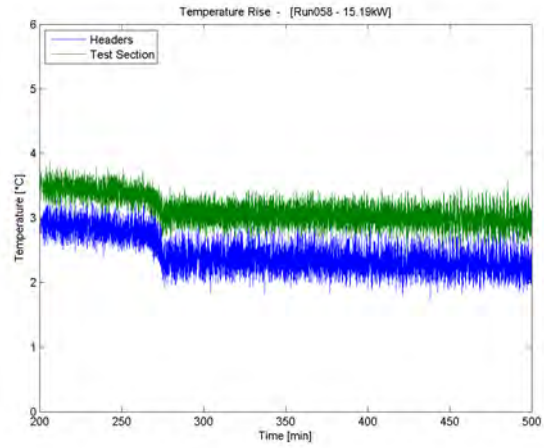

Supplement J.34: Temperature rise

Run058 — two-phase, 15.19 kW, 70 °C start, 80% tank volume

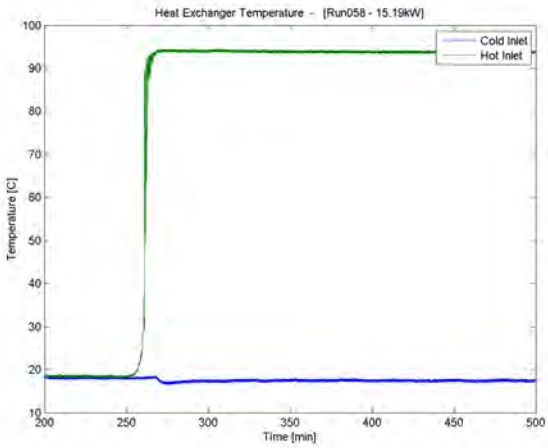

Supplement J.35: HXG temp

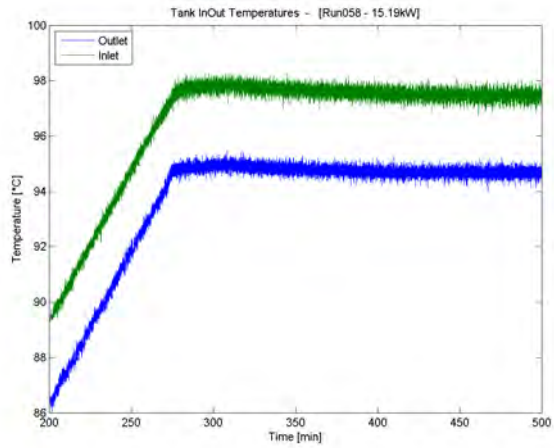

Supplement J.37: Tank Inlet Outlet

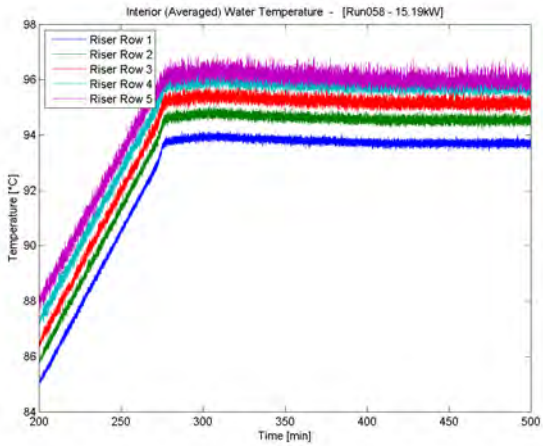

Supplement J.36: Interior riser water

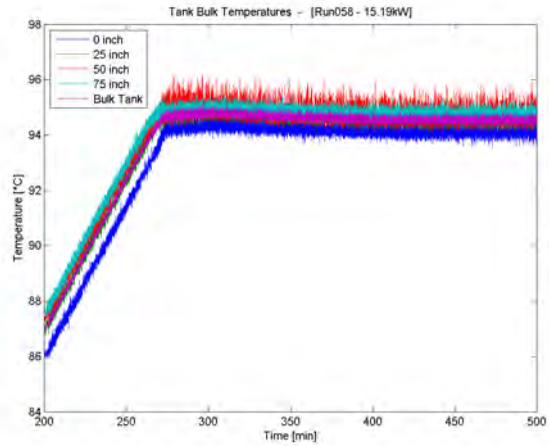

Supplement J.38: Tank Bulk

Run058 — two-phase, 15.19 kW, 70 °C start, 80% tank volume

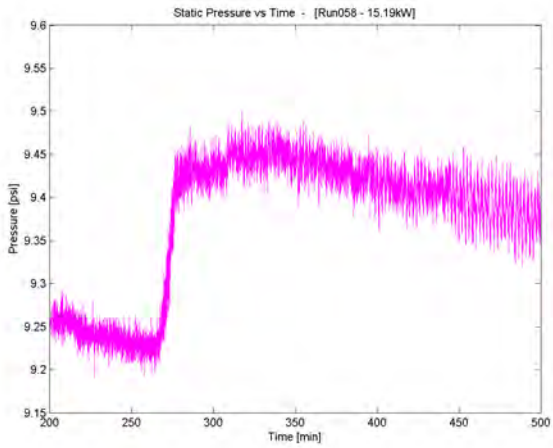

Supplement J.39: Static pressure

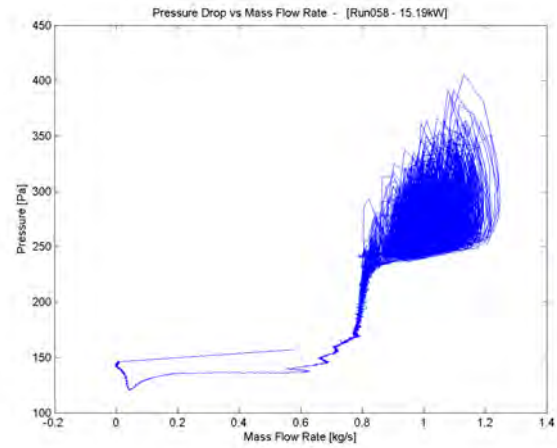

Supplement J.41: Phase portrait

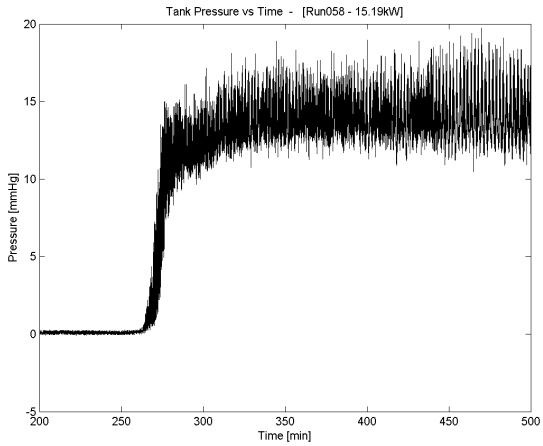

Supplement J.40: Tank pressure

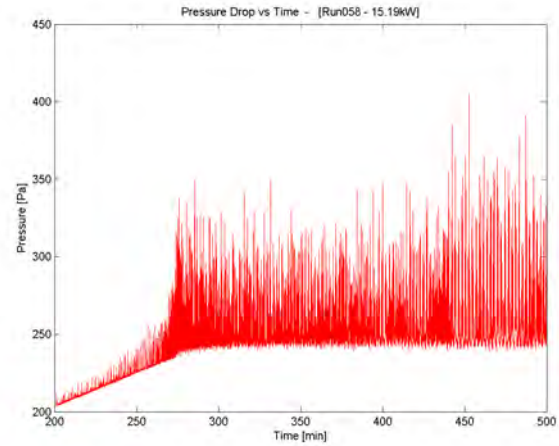

Supplement J.42: Pressure drop

Run058 — two-phase, 15.19 kW, 70 °C start, 80% tank volume

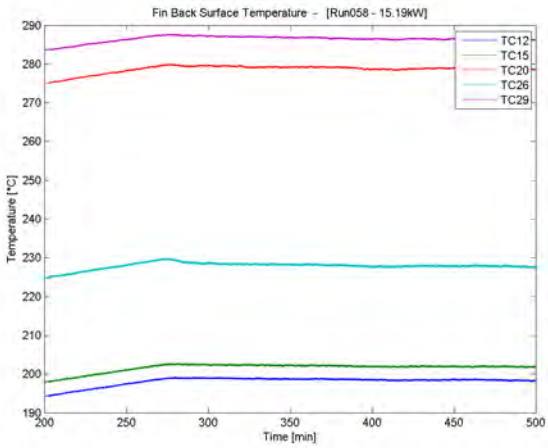

Supplement J.43: Fin back surface

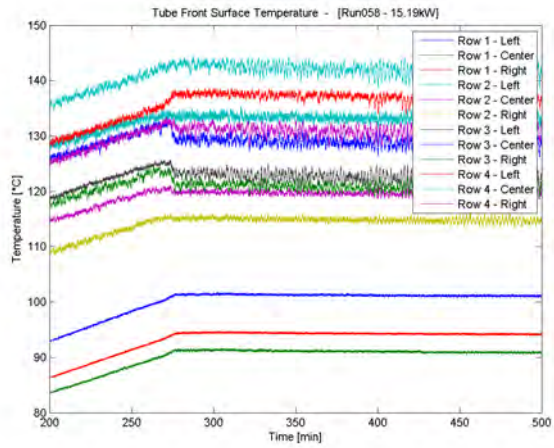

Supplement J.45: Tube front surface

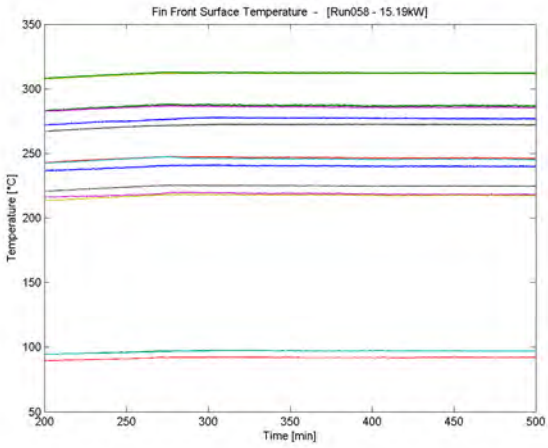

Supplement J.44: Fin front surface

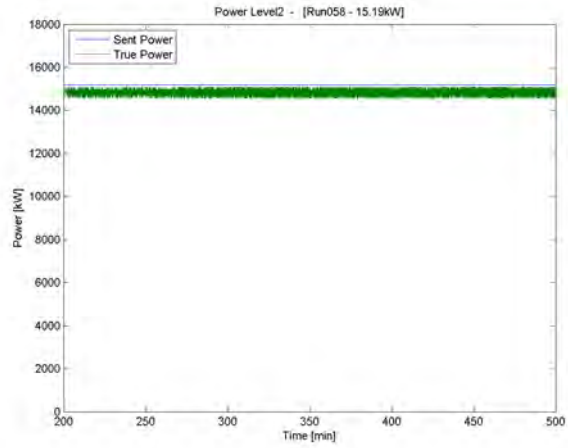

Supplement J.46: Heater power